

**Biomimetic improvement of hydrodynamic performance
of horizontal axis tidal turbines**



By: **Weichao Shi**

Project Supervisors: **Dr Rosemary NORMAN**

Prof Mehmet ATLAR

NEWCASTLE UNIVERSITY

SCHOOL OF MARINE SCIENCE AND TECHNOLOGY

May 2017

A thesis submitted for the degree of Doctor of Philosophy

Abstract

This study explored the potential of further improving the hydrodynamic performance of tidal turbines by applying leading-edge tubercles to the blades inspired by the humpback whales. Within this framework, a wide variety of experimental investigations, supported by numerical studies, has been conducted.

The study first focused on the design of the leading edge tubercles for a tidal turbine blade. Numerical simulation has been conducted for various designs and the best candidate was then applied onto a representative tidal turbine blade, a 3D hydrofoil can be fitted with various leading-edge designs. Experimental test was conducted in a cavitation tunnel and demonstrated significant benefits in terms of improving the lift coefficient and lift-to-drag ratio especially after stall. The results were then validated and complemented by numerical simulations for further detailed analysis. This simulation explicitly showed that the contra-rotating vortices generated by the tubercles formed a vortex fence prevented the tip vortex from inducing the spanwise flow, which meanwhile energized the flow and maintained more attached.

Following that, a set of tidal turbine models with different leading-edge profiles was manufactured and were tested to evaluate the efficiency, cavitation, underwater noise and detailed flow characteristics in the cavitation tunnel. These experimental investigations confirmed that the leading-edge tubercles could: improve the hydrodynamic performance in the low Tip Speed Ratio (TSR) region without lowering the maximum power coefficient; maintain the power coefficient in the low Reynolds number; constrain the cavitation development to within the troughs of the tubercles; hence mitigate the underwater noise levels.

Acknowledgements

Time flies! The journey of my PhD soon reached the end. During the past enjoyable three and a half years, there are too many people needs to be thanked. So allow me to start from the very beginning.

Thanks very much for my parents for bringing me to this world. They were both ordinary Chinese people but did extraordinary things to me. Fulfilling the dream of my father to achieve the highest degree is my responsibility, which he can't achieve only because of poverty and early loss of his father.

Thanks very much for my supervisors and tutors, Prof Mehmet Atlar, Dr Rosemary Norman and Prof Dazheng Wang. Thanks very much for your patient guidance. "You rise me up, so I can stand on mountains; you raise me up to walk on stormy seas." Particular thanks to the life-long trust and friendship between Prof Mehmet Atlar with Prof Dazheng Wang, which formed the bridge to bring me to the U.K.

The utter most thanks to the team in the Emerson Cavitation Tunnel. You guys are superior. To George Politis, Kwang-Cheol Seo, Batuhan Aktas, Serkan Turkmen, Lynna Rosli, Alessandro Carchen, Chang Li, Irma Yeginbayeva, Rod Sampson wish you all the very best for future and hope that our friendship can last forever wherever we are.

And also thanks to all the PhD students in the School of Marine Science and Technology. You guys made my life in Newcastle. Sincere thanks to my very best friends, Yibo, Mingyue, Wenyue, Bowen, Serena, Maria..... Thank you all for all your support.

Of course, thanks to the funding societies, Sasaki Donation and China Scholarship Council. Special thanks to Dr Noriyuki Sasaki and his wife Junko Sasaki for your knowledgeable and generous donation. And thanks to the Chinese government to provide people like me with a priceless opportunity to fulfil our dream.

Having lost my ex-girlfriend is not an easy thing for me to go through at the beginning of my PhD, who supported me six year with her accompany and encouragement. Hope she can find the right person who cares about her for the rest of her life. The last but not the least to my wife. It was a miracle but maybe destined to meet you in Glasgow at the very end of my PhD and to get married in six-month time. You married me for nothing but I want to give you everything. Hope our love can live long and prosperous.

Table of Contents

Abstract.....	i
Acknowledgements	iii
Table of Contents	v
List of Figures.....	ix
List of Tables.....	xviii
Chapter 1 Introduction	1
1.1 Introduction.....	1
1.2 Motivation.....	1
1.3 Aim and objectives	3
1.3.1 Aim.....	3
1.3.2 Objectives	3
1.4 Thesis layout	4
1.5 Summary	5
Chapter 2 Literature Review	6
2.1 Introduction.....	6
2.2 Tidal energy	6
2.2.1 Overview of tidal energy development	6
2.2.2 State-of-the-art HATT devices	10
2.2.3 Challenges for HATTs	14

2.3	Enlightening leading-edge tubercles	16
2.3.1	Review of aero/hydrodynamic mechanism of leading-edge tubercles	18
2.3.2	Biomimetic applications of leading-edge tubercles	24
2.3.3	Further understanding of the aero/hydrodynamic mechanism of leading-edge tubercles.....	30
2.4	Methodology for biomimetic application of leading edge tubercles.....	32
2.4.1	Numerical simulation methods for tidal energy devices.....	32
2.4.2	Experimental investigations of tidal energy devices.....	33
2.5	Summary	39
Chapter 3	Tubercle Design and Optimisation	41
3.1	Introduction	41
3.2	Description of selected tidal turbine geometry.....	41
3.3	Tubercle profile design, optimisation and validation.....	43
3.3.1	Optimisation methodology.....	43
3.3.2	CFD validation and performance evaluation	44
3.4	Optimisation and discussion of results.....	50
3.5	Summary	52
Chapter 4	Experimental and Numerical Investigations of Tubercles Applied on a Simplified Turbine Blade.....	53
4.1	Introduction	53
4.2	3D Blade model and its manufacture	53
4.3	Experimental investigation of 3D blade with the optimised tubercles.....	57

4.3.1	Experimental setup	57
4.3.2	Force measurement results and discussion	60
4.3.3	Flow visualisation results and discussion	72
4.3.4	Further remarks on the combined results of force measurements and flow visualisations	78
4.4	Numerical simulation of 3D blade with the optimised tubercles	79
4.4.1	Methodology of CFD simulation	79
4.4.2	Results and discussions	82
4.5	Summary	90
Chapter 5	Experimental Investigations of Leading-edge Tubercles as applied on Tidal Turbine	92
5.1	Introduction	92
5.2	Description of the tidal turbine models	93
5.3	Open water hydrodynamic performance tests	95
5.3.1	Experimental setup	95
5.3.2	Results and discussions	99
5.3.3	Key findings on the effects of tubercles on open water hydrodynamic performance	106
5.4	Cavitation observation tests	107
5.4.1	Experimental setup	107
5.4.2	Result and discussion	111
5.4.3	Key findings on the effects of tubercles on cavitation performance	118
5.5	Underwater radiated noise measurement tests	119

5.5.1	Experimental setup.....	119
5.5.2	Results and discussions.....	121
5.5.3	Key findings on the effects of tubercles on underwater radiate noise	131
5.6	Detailed flow measurement tests with PIV	132
5.6.1	Experimental setup.....	132
5.6.2	Results and discussions.....	139
5.6.3	Key findings on the effects of tubercles based on detailed flow investigations	160
5.7	Summary	161
Chapter 6	Conclusions & Recommendations for Future Research	163
6.1	Introduction	163
6.2	Overall review of the thesis and contributions to the state-of-the-art	163
6.3	Main conclusions.....	168
6.4	Recommendations for the future research.....	169
Reference	172
Appendix A -	Test results of open water hydrodynamic performance.....	180
Appendix B -	Pictures of cavitation observation	184
Appendix C -	Performance evaluation under wave-current interaction.....	204

List of Figures

Figure 2-1 Worldwide distribution of tidal energy (Ocean Energy Systems, 2016).....	8
Figure 2-2 Distribution of world marine energy commercial projects and testing sites(Ocean Energy Systems, 2016).....	9
Figure 2-3 Vertical Axis Tidal Turbine (VATT) (EMEC, 2013).....	10
Figure 2-4 Horizontal Axis Tidal Turbine (HATT) (EMEC, 2013).....	10
Figure 2-5 AR1000 built by Atlantis Resources (Atlantis, 2015).....	11
Figure 2-6 Tidal turbine built by Alstom (Alstom, 2013).....	12
Figure 2-7 SR2000 2MW floating tidal energy device (Scotrenewables, 2015).....	13
Figure 2-8 BlueTEC floating platform (BlueTEC, 2015).....	14
Figure 2-9 Humpback whale (Wikipedia, 2016).....	16
Figure 2-10 Humpback whale lunging in the centre of a bubble net spiral (Wikipedia, 2016)	17
Figure 2-11 Bubble net feeding of humpback whale (SwiftSwan, 2015).....	17
Figure 2-12 Cross sections of humpback whale flippers (Fish and Battle, 1996).....	17
Figure 2-13 Tested model of the whale flipper models (Miklosovic <i>et al.</i> , 2007).....	18
Figure 2-14 Tested result of 3D humpback whale flippers (Miklosovic <i>et al.</i> , 2007).....	19
Figure 2-15 Tested 2D foil models (Miklosovic <i>et al.</i> , 2007).....	19
Figure 2-16 Tested results of 2D foil models(Miklosovic <i>et al.</i> , 2007).....	20
Figure 2-17 Comparison in Lift coefficient(Johari <i>et al.</i> , 2007).....	21
Figure 2-18 Comparison in Drag coefficient(Johari <i>et al.</i> , 2007).....	21
Figure 2-19 Flow visualisation with tufts at 18°(Johari <i>et al.</i> , 2007).....	21
Figure 2-20 Analysis results for 3D airfoils and 2D airfoils (van Nierop <i>et al.</i> , 2008).....	22

Figure 2-21 Wind turbine with tubercle (Fish <i>et al.</i> , 2011)	24
Figure 2-22 Comparison of the generated power between two turbines with and without tubercles (Bellequant and Howle, 2009).....	25
Figure 2-23 Tidal turbine blades (Top: Control Blade. Middle: 1/3 Tubercled. Bottom: 2/3 Tubercled) (Gruber <i>et al.</i> , 2011)	26
Figure 2-24 Power coefficient (C_p) vs. current velocity for all three blade designs (Gruber <i>et al.</i> , 2011)	26
Figure 2-25 Comparison of peak lift-drag ratio for the three rudders (Weber <i>et al.</i> , 2010)	27
Figure 2-26 Cavitation contrast between the smooth rudder and the tubercle rudder (Weber <i>et al.</i> , 2010)	28
Figure 2-27 Cavitation patterns on various sizes of tubercles (Johari, 2015).....	28
Figure 2-28 Measuring position and the vorticity field from behind the foil where the counter clockwise vortex core (red/upper) is positive and the clockwise vortex core (blue/lower) is negative. $AOA=5^\circ$, $Re = 2230$, image planes are shown for $x'/c=0.4, 0.6, 0.8$ and 1 (a–d). (Hansen <i>et al.</i> , 2016).....	30
Figure 2-29 Turbine mounted on Dynamometer H33 for power coefficient curve test	34
Figure 2-30 Cavitation observed at shallow shaft immersion and designed stream speed (Wang <i>et al.</i> , 2007a).....	35
Figure 2-31 Net noise levels at designed shaft depth in the full scale(Wang <i>et al.</i> , 2007a)	35
Figure 2-32 PIV results on the vertical plane at the crest for wing with variable tubercles at angle of attack equal to 10° (Sisinni <i>et al.</i> , 2012).....	36
Figure 2-33 PIV results on the horizontal plane for wing with variable tubercles at angle of attack equal to 5° (Sisinni <i>et al.</i> , 2012).....	37
Figure 2-34 Turbine model fitted on the dynamometer in KHL.....	38
Figure 3-1 Cross-section profile of S814 (Janiszewska <i>et al.</i> , 1996)	41

Figure 3-2 Scaled tidal turbine model mounted on the dynamometer of Emerson Cavitation Tunnel.....42

Figure 3-3 Experimental result of the performance of S814 at $Re=1+e6$ (Janiszewska *et al.*, 1996).....42

Figure 3-4 Definition of 2D foil with a sinusoidal tubercle44

Figure 3-5 Illustration of boundary conditions.....45

Figure 3-6 Mesh overview (left) and zoom-in view of wing section at the leading edge (right)47

Figure 3-7 Refined mesh by the “solution adaptive mesh” method47

Figure 3-8 Validation for CFD prediction of lift and drag coefficients of S814.....49

Figure 3-9 Validation for CFD prediction of Pressure coefficient distribution at 12° of angle of attack.....49

Figure 3-10 Validation for CFD prediction of Pressure coefficient distribution at 15° of angle of attack49

Figure 3-11 Comparison of 2D foil lift coefficients with different tubercle profiles by varying the wavelength (W) at constant tubercle height ($H=0.05C$).....50

Figure 3-12 Comparison of 2D foil lift coefficients with different tubercle profiles by varying the wavelength (W) at constant tubercle height ($H=0.1C$).....51

Figure 3-13 Comparison of flow separation at 15° angle of attack (Velocity isosurface at 50% of incoming velocity coloured by pressure distribution).....51

Figure 4-1 Leading-edge profile of 3D hydrofoil with tubercles55

Figure 4-2 Tested 3D hydrofoil models with interchangeable leading-edge parts.....56

Figure 4-3 Sketch of the Emerson Cavitation Tunnel (Atlar, 2011)57

Figure 4-4 Setup of 3-component balance (Cussons R102) on the upper lid (Left) and setup of tested foil mounted on the 3-component balance (right).....58

Figure 4-5 Sample of uncertainty analysis results applied on the measured lift and drag coefficients	58
Figure 4-6 Experimental data for Foil "0000" with smooth leading edge at different incoming velocities	62
Figure 4-7 Experimental data for Foil "1111" with leading-edge tubercles at different incoming velocities	63
Figure 4-8 Comparison of experimental data for Foil "0000" and Foil "1111" at 2m/s.....	65
Figure 4-9 Comparison of experimental data for Foil "0000" and Foil "1111" at 3m/s.....	66
Figure 4-10 Comparison of experimental data for Foil "0000" and Foil "1111" at 4m/s.....	67
Figure 4-11 Growth ratio of C_L/C_D for Foil "1111" (with leading-edge tubercles) relative to Foil "0000" (with smooth leading edge)	68
Figure 4-12 Comparison of experimental data for different leading-edge tubercle coverage arrangements	70
Figure 4-13 Comparison of experimental data for foil with minimum leading-edge tubercle coverage ("0001") and for the reference foil ("0000") at 3m/s.	71
Figure 4-14 Comparison of relative growth ratios for C_L/C_D for Foil "1111" (with leading-edge tubercles applied on whole span) and Foil "0001" (with minimum leading-edge tubercles applied around the tip)	72
Figure 4-15 Sectional positions selected along Foil "1111" for flow visualisation using PIV	73
Figure 4-16 3 dimensional effect of typical 3D foil.....	74
Figure 4-17 Cavitating tip vortex observation on reference foil with smooth leading edge (Note a 10mm diameter tip vortex cavitation was generated)	77
Figure 4-18 Computation domain and boundary conditions	79
Figure 4-19 Volumetric mesh control.....	80
Figure 4-20 Generated mesh with volumetric control	81

Figure 4-21 Prism layer mesh.....	81
Figure 4-22 Example of convergence histogram of C_L and C_D	83
Figure 4-23 Mesh sensitivity and turbulence model verification	83
Figure 4-24 Comparative flow separation patterns of two hydrofoils (Iso-surface: $V_x=0\text{m/s}$; $\text{AOA}=16^\circ$).....	84
Figure 4-25 Comparative vorticity of tip vortex and flow separation from two hydrofoil sections, at section $X=0.2\text{m}$	85
Figure 4-26 Comparative vorticity magnitude distributions along two hydrofoils	86
Figure 4-27 Comparative vorticity [i] distributions along two hydrofoils on the suction side	87
Figure 4-28 Comparative details of vorticity [i] distribution at the suction side and tip of two hydrofoils.....	87
Figure 4-29 Comparison of pressure coefficient distributions in trough and crest area ($\text{AOA}=16^\circ$) for two foil sections	89
Figure 5-1 Tested turbine models	93
Figure 5-2 3D design of the turbine with leading-edge tubercles	94
Figure 5-3 Frictional torque measurement with the dummy mass (the yellow coloured shaft fairing) fitted on the dynamometer inside the ECT.....	96
Figure 5-4 Test conditions.....	98
Figure 5-5 Sample of uncertainty analysis	98
Figure 5-6 Influence on turbine performance caused by Reynolds number effect and blade cavitation	99
Figure 5-7 Types of blade cavitation.....	100
Figure 5-8 Performance influenced by pitch angle	101
Figure 5-9 Performance comparison (Pitch= 0° , 2m/s).....	103

Figure 5-10 Performance comparison (Pitch=4°, 2m/s).....	104
Figure 5-11 Performance comparison (Pitch=8°, 2m/s).....	105
Figure 5-12 High-speed cameras to observe any cavitation.	107
Figure 5-13 Test matrix against the full-scale conditions.....	109
Figure 5-14 Detailed comparison of cavitation pattern (Pitch angle=+8°; V=3m/s; TSR=6; Cav _{0.75r} =1.3).....	115
Figure 5-15 Cavitation inception diagram	117
Figure 5-16 Arrangement of the test turbine and hydrophone.....	119
Figure 5-17 Calibration configuration of the Hydrophone (Top), The connection diagram of the hydrophone (Middle) Typical Receiving Frequency Characteristics of B&K 8103(Bottom).	120
Figure 5-18 Comparative total noise levels measured in 1Hz band (Pitch angle=8°, V=2m/s)	124
Figure 5-19 Comparative total noise levels measured in 1Hz band (Pitch angle=8°, V=3m/s)	125
Figure 5-20 Comparative total noise levels measured in 1Hz band (Pitch angle=8°, V=4m/s)	126
Figure 5-21 Detailed comparison of cavitation pattern (Pitch angle=+8°; V=2m/s; TSR=8; Cav _{0.75r} =1.7).....	126
Figure 5-22 Net noise (sound pressure) level of Ref at pitch angle=0°	127
Figure 5-23 Net noise (sound pressure) level of Ref at pitch angle=4°	128
Figure 5-24 Net noise (sound pressure) level of Ref at pitch angle=8°	128
Figure 5-25 Net noise (sound pressure) level of Ref at pitch angle=0° and TSR=4	129
Figure 5-26 Net noise (sound pressure) level of Ref at pitch angle=0° and Vin=4m/s.....	130

Figure 5-27 Net noise (sound pressure) level of Ref at TSR=4 and $V_{in}=4\text{m/s}$ 130

Figure 5-28. Radial positions of 2D PIV measurement planes 133

Figure 5-29. Sample image of 2D PIV 133

Figure 5-30. Stereo PIV measurement plane..... 134

Figure 5-31. Setup of Stereo PIV alongside the test section of Emerson Cavitation Tunnel. 134

Figure 5-32. Typical stereo PIV Images from two different cameras shooting from different perspective angles..... 135

Figure 5-33. Calibration target for stereo PIV system located downstream of the model turbine 135

Figure 5-34 Calibration result of stereo PIV 136

Figure 5-35 Stereo PIV result with a detailed tip vortex structure..... 137

Figure 5-36 Mapping of flow separation area in downstream of turbine blade by using 2D PIV (Case: Ref_4_TSR2_10) 140

Figure 5-37 Volumetric flow field description for stereo PIV measurements 152

Figure 5-38 Velocity distribution for the reference turbine at varied sections, 50mm, 150mm and 250mm downstream of model turbine at TSR2 with the iso-surface of axial velocity = 1.5m/s 154

Figure 5-39 Velocity distribution for the Sin2 turbine at varied sections, 50mm, 150mm and 250mm downstream of model turbine at TSR2 with the iso-surface of axial velocity = 1.5m/s 154

Figure 5-40 Velocity distribution for the Sin8 turbine at varied sections, 50mm, 150mm and 250mm downstream of model turbine at TSR2 with the iso-surface of axial velocity = 1.5m/s 155

Figure 5-41 Iso-surface pair of radial velocity = +/-0.5m/s (Left: Ref; Middle: Sin2; Right: Sin8) 155

Figure 5-42 Iso-surface of vorticity (tangential) = 100 (Left: Ref; Middle: Sin2; Right: Sin8)	155
Figure 5-43. Velocity distribution for the reference turbine at varied sections, 50mm, 150mm and 250mm downstream of model turbine at TSR4 with the iso-surface of axial velocity = 3.3m/s	156
Figure 5-44. Velocity distribution for the Sin2 turbine at varied sections, 50mm, 150mm and 250mm downstream of model turbine at TSR4 with the iso-surface of axial velocity = 3.3m/s	157
Figure 5-45. Velocity distribution for the Sin8 turbine at varied sections, 50mm, 150mm and 250mm downstream of model turbine at TSR4 with the iso-surface of axial velocity = 3.3m/s	157
Figure 5-46. Velocity distribution for the reference turbine at varied sections, 50mm, 150mm and 250mm downstream of model turbine at TSR5 with the iso-surface of axial velocity = 3.3m/s	158
Figure 5-47. Velocity distribution for the Sin2 turbine at varied sections, 50mm, 150mm and 250mm downstream of model turbine at TSR5 with the iso-surface of axial velocity = 3.3m/s	159
Figure 5-48. Velocity distribution for the Sin8 turbine at varied sections, 50mm, 150mm and 250mm the turbine at TSR5 with the iso-surface of axial velocity = 3.3m/s	159
Figure A-1 Performance comparison (Pitch=0°, 3m/s)	180
Figure A-2 Performance comparison (Pitch=0°, 4m/s)	181
Figure A-3 Performance comparison (Pitch=4°, 3m/s)	181
Figure A-4 Performance comparison (Pitch=4°, 4m/s)	182
Figure A-5 Performance comparison (Pitch=8°, 3m/s)	182
Figure A-6 Performance comparison (Pitch=8°, 4m/s)	183
Figure C-1 Schematic of the KHL towing tank	204

Figure C-2 Turbine model and dynamometer fitting onto the towing carriage.....	205
Figure C-3 JONSWAP wave spectra generated in model tests.....	208
Figure C-4 Results of Reynolds number effect test.....	209
Figure C-5 Test result of open water performance in the towing tank.....	210
Figure C-6 Time history and FFT analysis for the regular wave test.....	212
Figure C-7 Amplitudes of torque and thrust in regular waves	215
Figure C-8 Sample of JONSWAP wave profile (Hs=0.15m, Tp=1.581s)	216
Figure C-9 Wave spectrum calibration against encounter wave frequencies (Hs=0.15m, Tp=1.581s).....	216
Figure C-10 Time history and FFT analysis for the irregular wave test (Hs=150mm; Tp=1.581s, N=150RPM and V=0.785m/s).....	218
Figure C-11 Linear turbine response to the wave action.....	220
Figure C-12 RAOs of the reference turbine in regular waves with 250rpm	221
Figure C-13 Comparison of thrust RAO in the regular waves with 250RPM	222
Figure C-14 Comparison of torque RAO in regular waves with 250RPM	222
Figure C-15 RAO(f) of thrust (left) and torque(right) derived from regular and irregular wave test with 150RPM.....	223
Figure C-16 RAO(f) of torque (top) and thrust(bottom) tested at different towing speeds ...	224
Figure C-17 ΔV against the wave frequency as calculated based on two regular wave test data with two different carriage speeds.....	226

List of Tables

Table 2-1 Typical applications of leading edge tubercles.....	29
Table 2-2 Main dimension of the Emerson Cavitation Tunnel.....	34
Table 2-3 Technical data of open water dynamometer H33	34
Table 2-4 General description of the Kelvin Hydrodynamic Lab	38
Table 4-1 Chord distribution of the reference foil	54
Table 4-2 Specifications of Dantec Dynamics Stereo PIV (Particle Image Velocimetry) system	59
Table 4-3 Comparative experimental flow patterns at 3 selected sections for Foil “0000” and Foil “1111” observed at 16° of angle of attack	75
Table 4-4 Comparative experimental flow patterns at 3 selected sections for Foil “0000” and Foil “1111” observed at 24° of angle of attack	76
Table 4-5 Mesh convergence study under 8° angle of attack	82
Table 4-6 Experimental and numerical results of the hydrofoil with and without tubercles at AOA=16°	84
Table 5-1 Main particulars of the tidal stream turbine model.....	93
Table 5-2 Technical data of propeller dynamometer H33	96
Table 5-3 Test matrix	97
Table 5-4 Full-scale design	108
Table 5-5 Full-scale operating conditions for pitch control turbine	110
Table 5-6 Full-scale operating conditions for variable speed control turbine	110
Table 5-7 Tip vortex cavitation.....	112
Table 5-8 Back side cloud cavitation.....	113

Table 5-9 Face side cloud cavitation	114
Table 5-10 Double side cloud cavitation.....	116
Table 5-11 Hydrophone data acquisition settings	120
Table 5-12 Measured hydrodynamic performance data of model turbines in the selected PIV testing conditions.....	138
Table 5-13 2D PIV measurement results of turbines at different radial positions (at TSR=2)	141
Table 5-14 2D PIV measurement results of turbines at different radial positions (at TSR=4)	145
Table 5-15 2D PIV measurement results of turbines at different radial positions (at TSR=5)	149
Table B-1 Cavitation observation results	185
Table C-1 Test matrix for Reynolds number test and open water performance test.....	206
Table C-2 Test matrix for regular and irregular wave test	207
Table C-3 Uncertainty analysis of the wave test	211
Table C-4 Normalized time average C_p and $C_t/10$ in regular wave test at wave amplitude=0.05m and TSR=4	213
Table C-5 Normalized time average C_p and $C_t/10$ in regular wave test at wave amplitude=0.1m and TSR=4.....	213
Table C-6 Percentage of C_p and $C_t/10$ fluctuation in regular wave test at wave amplitude=0.05m.....	215
Table C-7 Percentage of C_p and $C_t/10$ fluctuation in regular wave test at wave amplitude=0.1m	215
Table C-8 Normalized time average C_p and $C_t/10$ in irregular waves (JONSWAP)	219

Table C-9 Percentage of significant values of thrust and torque fluctuation in irregular waves (JONSWAP)..... 219

Chapter 1 Introduction

1.1 Introduction

The main objective of this chapter is to introduce the research study presented in this thesis which involves an investigation into the application of leading edge tubercles on the blades of horizontal axis tidal turbines for hydrodynamic performance improvement. Following this introductory section (Section 1.1), the motivation of the research is given in Section 1.2 which is followed by the aim and specific objectives of the research in Section 1.3. The layout of the presentation of the thesis chapters is given in Section 1.4 while the summary of Chapter 1 is presented in Section 1.5.

1.2 Motivation

Replacing fossil energy with renewable energy has been a goal of the human race for some time. Recently, there has been a growing demand for alternative energy derived from sustainable resources due to global climate changes and threats of an impending energy crisis. The oceans of the world are a largely untapped resource, capable of making a major contribution to the world's ever-increasing energy needs. Among the different marine renewable energy sources, tidal current is a predictable and sustainable energy source resulting from the gravitational effects of the moon and sun (Pelc and Fujita, 2002). Based on the developments over the last 20 years the Horizontal Axis Tidal Turbine (HATT), which is also called "the underwater wind turbine", has reached the stage that it is very close to commercial development (Bahaj *et al.*, 2007; Khan and Bhuyan, 2009).

However, high installation and maintenance cost, the harsh marine environment and limited deployable sites around the world are factors which currently limit the development of this technology. All these challenges focus on a need to make the turbine more efficient and robust so that it can generate more power for a given amount of investment and can survive longer under the harsh marine environment. From the marine hydrodynamic point of view, improving the turbine design is key to solving most of the above highlighted challenges and associated problems.

Recently, the tubercles on the leading edges of humpback whale flippers have drawn the attention of researchers working in the field of tidal energy and wind energy, as these round protuberances have the ability to delay the stall and hence improve the lift-to-drag ratio of

blades (Johari *et al.*, 2007; Miklosovic *et al.*, 2007; Stanway, 2008; Hansen *et al.*, 2009; Weber *et al.*, 2010; Yoon *et al.*, 2011). Many research studies, which are both numerical and experimental in nature, have investigated the influence of the leading-edge tubercles as applied on air fans, wind turbines, rudders and so on (van Nierop *et al.*, 2008; Weber *et al.*, 2010; Swanson and Isaac, 2011; Corsini *et al.*, 2013). According to these studies, blades with leading-edge tubercles can maintain lift coefficients further beyond the stall point in comparison to those without tubercles.

Based on the above findings, the tubercles might be able to provide the tidal turbine blades with the following hydrodynamic advantages:

1. Better lift-to-drag ratio: This particular characteristic might be able to enhance the maximum power coefficient to help the turbine generate more power and make more use of the available energy;
2. Delaying the stall angle: This factor might be able to help the turbine to operate more stably without the sudden loss of the lift which may cause fluctuation in power generation hence lowering the power quality. This loss of lift may in turn cause the vibration and fatigue problems that reduce the lifetime of a tidal turbine;
3. Maintaining the lift under stall: This is another factor which might be very effective in the starting process of a fixed pitch tidal turbine as this process relies on the initial torque of the turbine to overcome the frictional torque and to start spinning. Since the initial torque is very small due to the high angle of attack, maintaining the lift under a high angle of attack is crucial.

The above reviewed developments and technical observations motivated the Author to explore and develop this biomimetic concept further with a view to improving the hydrodynamic performance of tidal turbines.

1.3 Aim and objectives

1.3.1 Aim

Based upon the Author's motivation and the literature review presented in Chapter 2, the aim of the research was set as:

- To explore the feasibility of applying the biomimetic concept inspired by the leading-edge tubercles of humpback whale flippers to tidal turbines to enhance their hydrodynamic performances.

1.3.2 Objectives

In order to achieve the above aim, the following objectives were specified:

- Objective 1: Review the literature on biomimetic applications and the state-of-the-art design and optimisation of tidal turbines to improve their hydrodynamic performance; conduct a comprehensive review to have a broader understanding of the research topic and confirm the knowledge gaps which need to be filled in this area by the current research; propose a suitable research methodology to meet the aim and objectives of the research.
- Objective 2: Design or select a state-of-the-art tidal turbine to use as a reference and explore the effect of the LE tubercles relative to the performance of this reference turbine. Conduct the initial design and optimisation of the turbine blade sections with tubercles to achieve an optimised geometry of the leading-edge tubercle profile.
- Objective 3: Apply the optimised tubercle geometry onto a 3D hydrofoil which is a representative foil with a similar geometry to a tidal turbine blade but with a constant pitch. Conduct both numerical and experimental investigations; and compare the hydrodynamic performance of this foil with that of the traditional wing (without tubercles); achieve the basic understanding of the influence of the tubercles that can be employed on turbine blades.
- Objective 4: Using the reference turbine as the basis, establish and optimise a new, counterpart turbine with the LE tubercles. Conduct comprehensive experimental campaigns to evaluate the comparative hydrodynamic performance characteristics of these turbines. The campaigns are to include: comprehensive flow field visualisations

and measurements using PIV/LDA; torque and thrust measurements; cavitation observations and underwater radiated noise measurements.

1.4 Thesis layout

The above aim and objectives of the research have been achieved by the work conducted in this study, which is presented in the six chapters of the thesis, described as follows:

Chapter 1 introduces the research work presented in the thesis including the motivation of the Author, aim and objectives of the research as well as the layout of the thesis to make a general introduction to the research carried out.

Chapter 2 presents a comprehensive literature review on the state of the art for tidal turbine developments and biomimetic applications for their performance improvement, which targets “Objective 1”. This is to gain a broader understanding of the research topic and hence refine the aim and objectives of the thesis by identifying the knowledge gaps which needed to be addressed in this research.

Chapter 3 focuses on “Objective 2” to design and optimise the tubercles geometry for a blade section, including 3D modelling, mesh generation and CFD simulation. The blade sections, fitted with various size and shapes of leading-edge tubercles, were evaluated in terms of the lift and drag performance. With the aid of this work, an “optimum” design of tubercles can be proposed for further developments.

Chapter 4 is dedicated to improving further the understanding of the LE tubercles through simplified foil experiments to meet “Objective 3”. A 3D foil model with various leading-edge profiles (including tubercles) was designed and fabricated. The model with different leading edges were tested in the Emerson Cavitation Tunnel to compare the detailed flow and hydrodynamic force characteristics. This experimental activity was followed by numerical simulations to further validate and compliment the experimental study especially for thorough understanding of the effect of tubercles.

Chapter 5 presents a series of tidal turbine model tests which were conducted in a cavitation tunnel, to satisfy “Objective 4”. These tests in the cavitation tunnel explored the effect of leading-edge tubercles on the open water performance; cavitation performance; underwater radiated noise level and flow field around and behind the turbines.

Chapter 6 presents an overall review of the research study conducted by scrutinising its aim and objectives as well as the main conclusions drawn from the research work. The chapter also recommends further work for future studies.

1.5 Summary

Chapter 1 introduced the research study presented in this thesis. The motivation, aim and objectives of the research are described as well as the layout of the thesis to make a general introduction to the research study conducted.

Chapter 2 Literature Review

2.1 Introduction

The main objective of this Chapter is to confirm the aim and objectives of this research study further by identifying the current knowledge gaps in the state-of-the art literature regarding the application of leading edge tubercles onto tidal turbines to improve their hydrodynamic performance.

In order to achieve the Chapter objective, in Section 2.2, the current developments of the tidal energy industry have been reviewed to observe the trends in the development of tidal turbines and the means to improve their hydrodynamic performance. Following this, in Section 2.3, the recent progress made on the research involving the fundamental mechanism of leading-edge tubercles and their biomimetic applications for various industry practices, has been reviewed. This is followed by a review of the state-of-the art in experimental and numerical methods that can be used to investigate further details of the tubercles and their applications for the improvement of tidal turbine performances in Section 2.4. The main conclusions of the literature survey conducted in this chapter, including the current knowledge gap(s) to be addressed in confirming the aim and objectives of the thesis, are presented in Section 2.5.

2.2 Tidal energy

2.2.1 Overview of tidal energy development

Tidal energy is a well-known form of marine renewable energy used to generate electricity through turbines driven by the twice daily rising and falling of the tide. It is an attractive form of renewable energy, which is highly reliable, predictable and abundant in coastal regions (Pelc and Fujita, 2002; Charlier, 2003; Li *et al.*, 2010).

According to the report by Ocean Energy System (OES) Technology Collaboration Programme, theoretically, tidal energy can provide 7800TWh/year, from sites mainly located along coastal areas but this strongly relies on the special geographical conditions where the flow velocity can be accelerated, usually between islands (Ocean Energy Systems, 2016). The global distribution of tidal energy is shown in Figure 2-1 while the current commercial marine energy projects and testing sites are presented in Figure 2-2. It can be seen that a number of countries like the United Kingdom, the United States, Canada, France, China and so on, have been involved in the development of tidal energy targeting to secure their energy reserves and to meet the goal for

CO₂ emission reduction agreed in United Nations Framework Convention on Climate Change (Zhang *et al.*, 2014).

However, apart from the rising political initiatives, like “Blue Energy Action needed to deliver on the potential of ocean energy in European seas and oceans by 2020 and beyond” by the European Commission Communication, ocean energy deployments are proceeding at a slower pace than expected because of the economic recession and low oil price (Badcock-Broe *et al.*, 2014; Magagna and Uihlein, 2015). The marine energy market, including tidal energy, is still yet to be established.

Nowadays tidal energy technologies have four main bottlenecks: (1) technology development; (2) finance and markets; (3) environmental and administrative issues and (4) grid availability, where technology issues account for about 35% of the key priorities for the tidal energy industries (Badcock-Broe *et al.*, 2013; Magagna and Uihlein, 2015). Even with the recent progress, no ocean energy technology developed has so far achieved the level of technological readiness required to be competitive with other renewable energy sources or sufficient to ensure commercialisation of the technology. The key issues concern the long-term reliability and the performances in demanding environments; the survivability of the devices, especially during storms or extreme condition; lack of design consensus between overall design and its components. So overcoming the technology issues is fundamental to identifying solutions to the other barriers which are slowing this sector’s development, in particular financial hurdles.

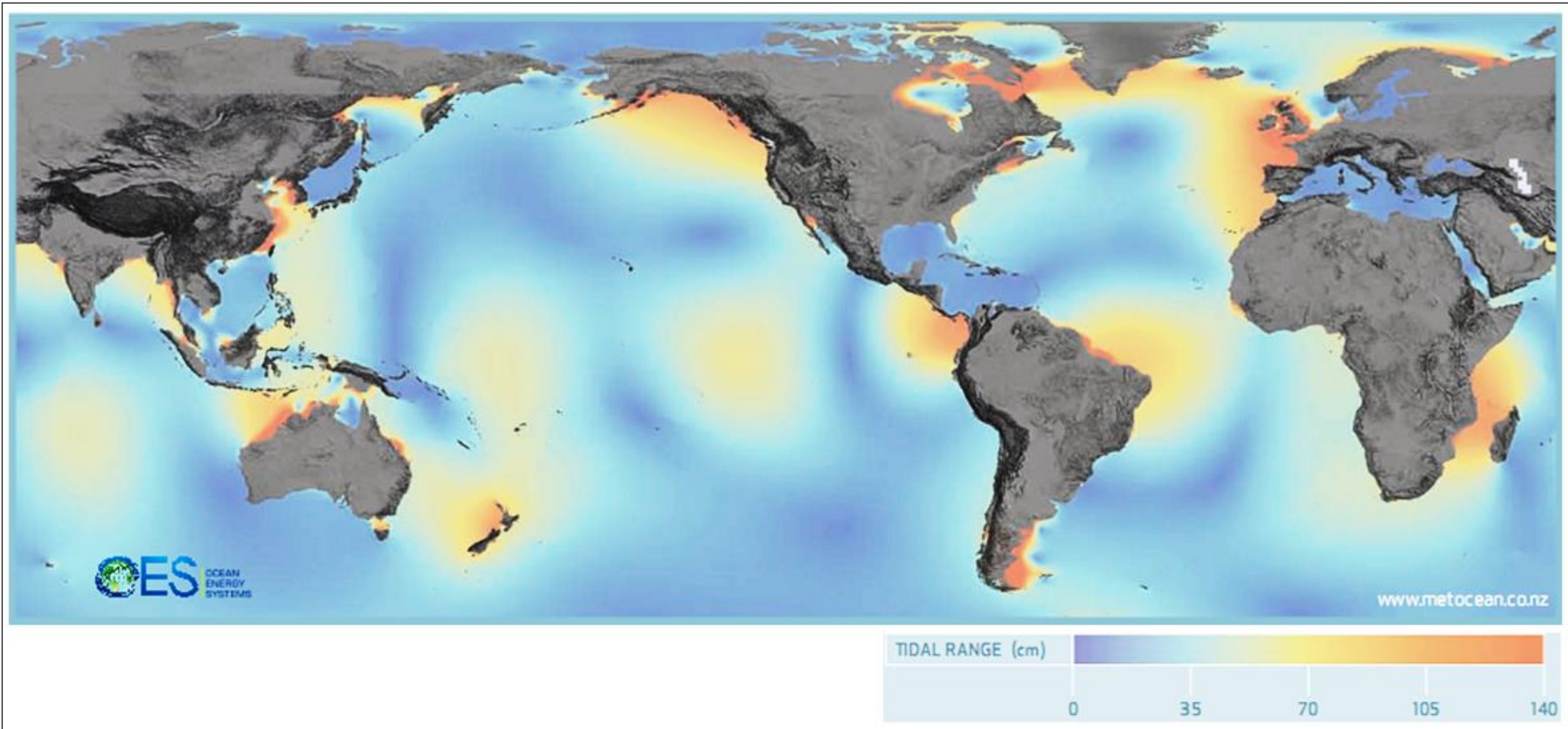


Figure 2-1 Worldwide distribution of tidal energy (Ocean Energy Systems, 2016)

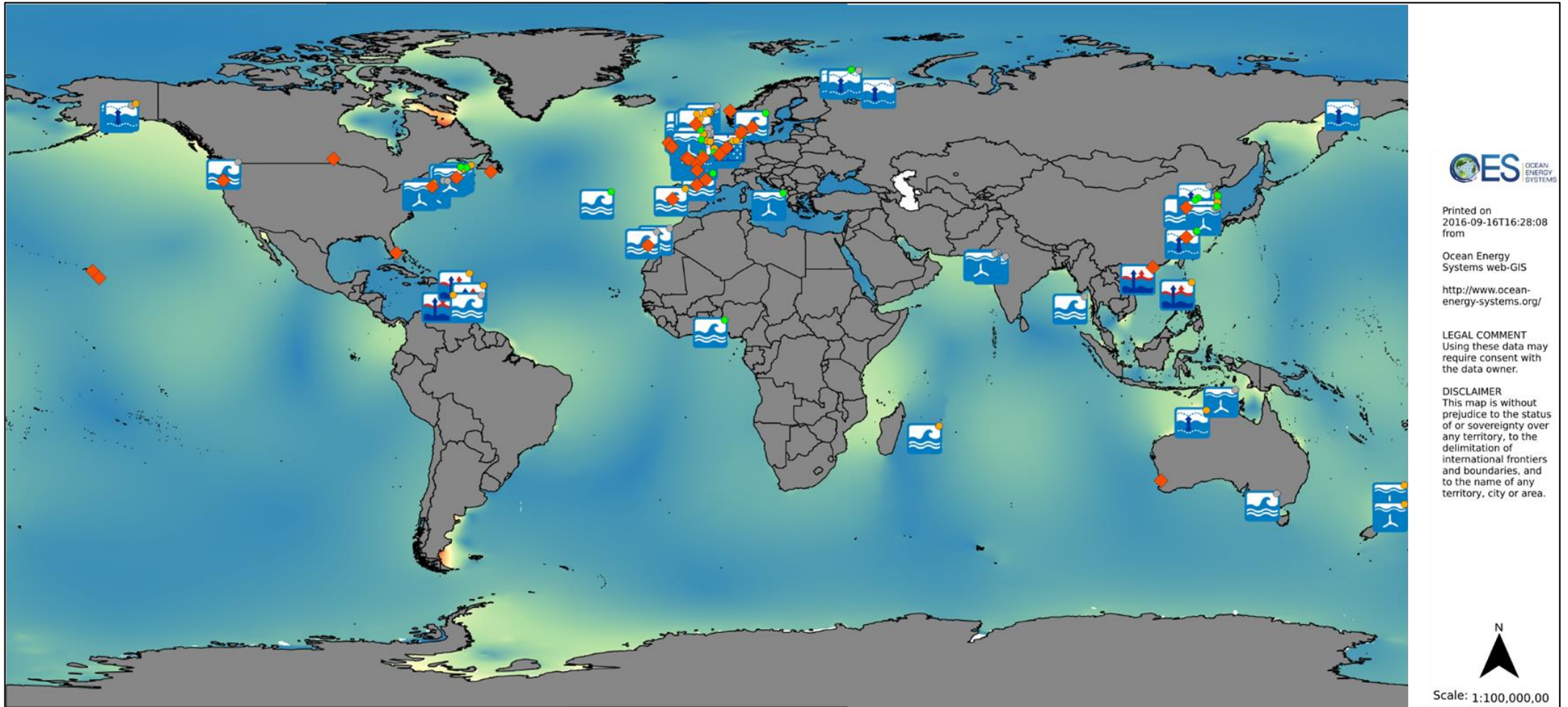


Figure 2-2 Distribution of world marine energy commercial projects and testing sites(Ocean Energy Systems, 2016)

2.2.2 State-of-the-art HATT devices

In terms of the energy conversion technology, turbines are the most mature and widely used technology to harness the kinetic energy of the fast flowing water generated by the ebb and flood tides. They can be generally categorized into horizontal and vertical axis turbines, according to the relative positions of their rotational axis to the incoming flow. A Vertical Axis Tidal Turbine (VATT, Figure 2-3) has its rotational axis perpendicular to the incoming flow whilst a Horizontal Axis Tidal Turbine (HATT, Figure 2-4) is parallel to the incoming flow (King and Tryfonas, 2009).

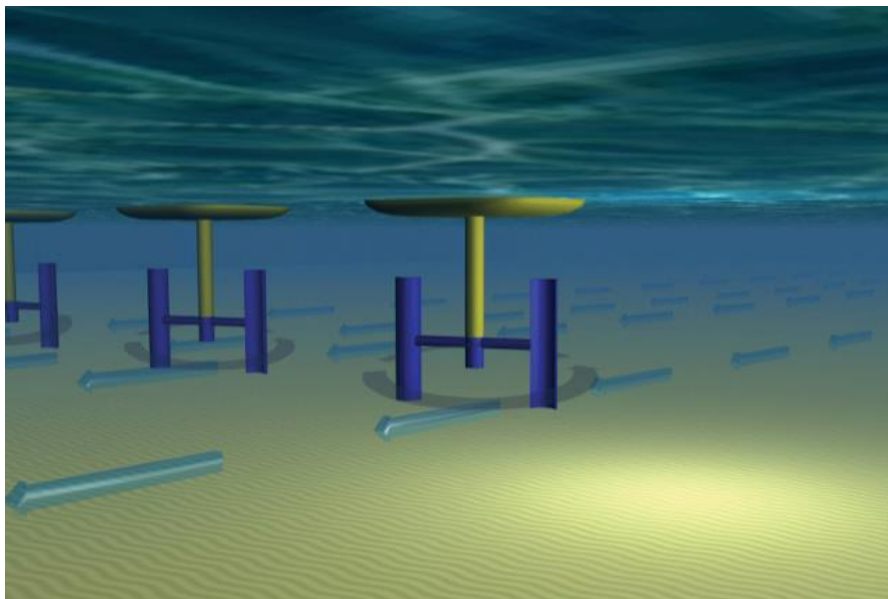


Figure 2-3 Vertical Axis Tidal Turbine (VATT) (EMEC, 2013)

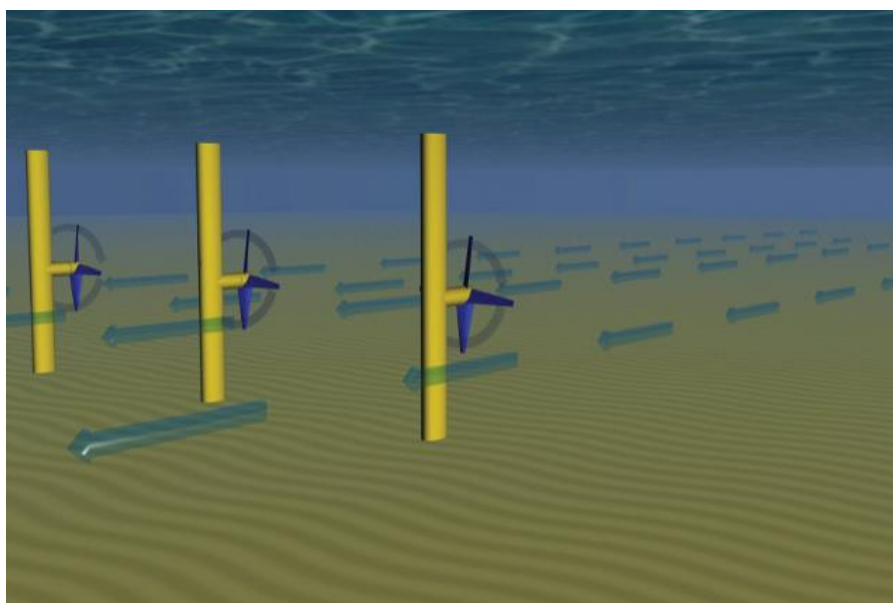


Figure 2-4 Horizontal Axis Tidal Turbine (HATT) (EMEC, 2013)

Through developments over the last 20 years, the HATT, which is also called “the underwater wind turbine”, has reached the stage that it is very close to commercial development (Bahaj *et al.*, 2007; Khan *et al.*, 2009). In fact, many companies, like Atlantis Resources and Alstom already have the technology to provide a tidal energy solution with ratings from 1 to 3MW (Alstom, 2013; Atlantis, 2015). The feasibility of extracting tidal energy is no longer a question. Tidal energy researchers have developed various HATT devices to extract energy from the tidal current. These devices have different control systems to control either the blade pitch angle or the rotational speed to suit the changing incoming velocity in order to maintain the maximum power generating efficiency. They also have different designs of their supporting structures, such as floating platforms, fixed foundations and so on. With respect to the turbine design, contemporary HATTs can be mainly divided into the following four different types of devices with different control mechanism and supporting structures.

HATT with variable speed control and fixed foundation



Figure 2-5 AR1000 built by Atlantis Resources (Atlantis, 2015)

A tidal turbine with variable speed control and fixed foundation is widely used in the current development of tidal current energy devices. One example is the AR1000 built by Atlantis Resources and tested at the European Marine Energy Centre (EMEC), as shown in Figure 2-5. The turbine has three fixed pitch blades with a diameter of 18m and controlled by a variable speed control system. The AR1000 is designed to produce its nameplate capacity of 1MW in

water flows of 2.65m/s and above (Atlantis, 2015). The turbine is supported by a gravity-based foundation working in around 40m deep oceans. This turbine is now scheduled to be installed on CECEP's (China Energy Conservation and Environmental Protection Group) Daishan demonstration site in China.

The rotational speed of this kind of device is continually being adjusted with the varying incoming flow velocity to keep the turbine working at the optimum efficiency. The shaft immersion is also changing because of the tidal effect on the free surface and waves.

HATT with pitch control and fixed foundation

The HATT with pitch control is another type of tidal turbine that is also very popular and similar to the wind turbine, and typically supported by a fixed structure. The pitch angle can be controlled to adapt to the varying incoming velocity. A typical device would be one produced by Alstom and also tested in the EMEC site as shown in Figure 2-6 (Alstom, 2013). Its rotor has three pitch-controlled blades with a diameter of 18m. The unit operates fully submerged, with no surface piercing parts, in a water depth of about 40m.

Instead of maintaining the optimum TSR by changing the rotational speed, this device maintains a constant rotational speed by controlling its blade pitch angle to suit the changing incoming velocity. Because of the fixed foundation, the shaft immersion also changes with the tide and the waves.



Figure 2-6 Tidal turbine built by Alstom (Alstom, 2013)

HATT with variable speed control and floating platform

Aiming to minimise the whole lifecycle cost of electricity production from tidal energy and to be able to operate in deep water, floating platforms are becoming more and more popular in tidal energy. The SR2000 device, as shown in Figure 2-7, produced by Scotrenewables Tidal Power Ltd, can be installed in any water depths of 25m and above due to the flexible mooring system. The SR2000 carries two 16m fixed pitch rotors, giving a rating of 2 x 1MW for a 3m/s current speed and using variable speed control (Scotrenewables, 2015).

Like the other devices with variable speed control, the rotational speed of this kind of device is constantly adjusting with the varying incoming velocity. However, because of its floating platform the shaft immersion does not change greatly with the tide and the waves.

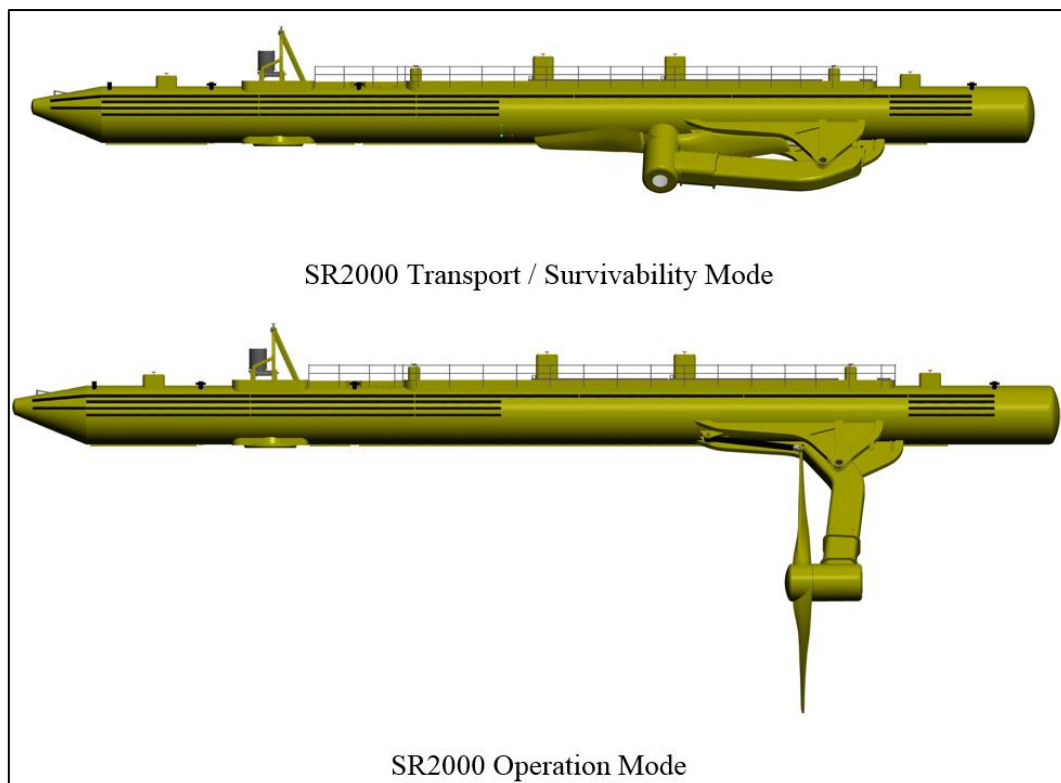


Figure 2-7 SR2000 2MW floating tidal energy device (Scotrenewables, 2015)

HATT with pitch control and floating platform

Similarly, the floating platform can also be used to carry a HATT with pitch control. Bluewater produce a floating platform, BlueTEC, which can carry different kinds of turbine, as shown in Figure 2-8. These turbines can also be controlled by pitch control systems.

The pitch control tidal turbines will maintain a constant rotational speed but change the blade pitch angle to suit the changing incoming velocity. However, the shaft immersion does not change with the tide and the waves.

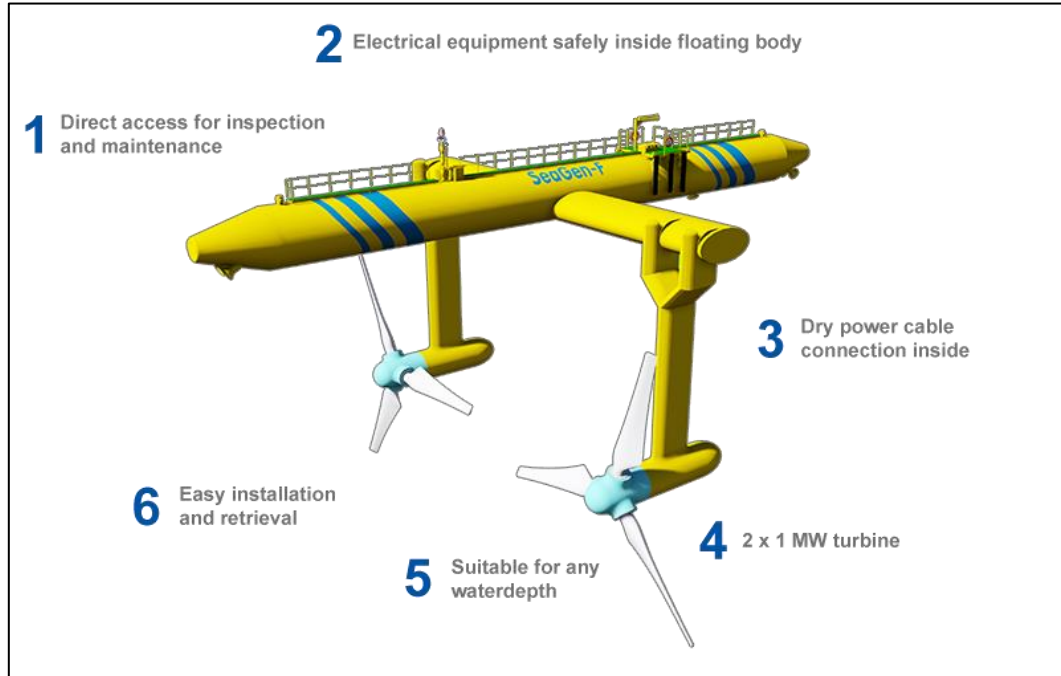


Figure 2-8 BlueTEC floating platform (BlueTEC, 2015)

2.2.3 Challenges for HATTs

Although the commercial projects summarised above have demonstrated the technical solutions to the extraction of energy using HATTs, their reliability, survivability and economics have also been questioned in recent years (Mitchell and Connor, 2004; Douglas *et al.*, 2008).

As it has been commonly acknowledged, the technology of the HATT is mainly inherited from the wind turbine industry. From the turbine blade, generator and the control system through to the grid integration system, most of the systems mimic the technology developed for wind turbines. From the power generation point of view, the main difference between wind turbines and tidal turbines is the density of the operating medium and the velocity range. For instance, the density of the sea water is about 800 times higher than the density of air. The tidal current speed varies periodically from 0m/s to the fastest speed which may vary from 2m/s to 4m/s in

spring tide, in contrast to the rapidly changing wind speed. However, all these factors only result in difference in the sizes of turbines in terms of power generation.

However, there are other issues from which tidal turbines suffer but that do not affect wind turbines. Amongst them is the cavitation issue. Blade cavitation may have significant detrimental effects on the hydrodynamic and structural performance of tidal turbines. Firstly, it can lead to a significant loss of efficiency. Secondly, it may cause erosion on the turbine blade which would result in undesirable damage to the blade structure that is typically a composite material (Harper and Hallett, 2015), and can be easily disintegrated due to this undesirable phenomenon (Hammond *et al.*, 1993).

Apart from the cavitation problem, the complex, harsh marine environment is the key factor explaining why tidal energy costs are high compared to other forms of renewable energy. This is not only because of the costly offshore installation, like drilling and piling, that many companies are trying to avoid by introducing floating structure and other novel designs; it is also because of the maintenance cost resulting from the prevalence of marine organisms (i.e. marine biofouling) which poses a significant impact on the performance and corrosion on the structure. On the other hand, the complex environmental conditions, combined with wind, wave and current, challenge the development of tidal energy as well.

In spite of the above challenges, as stated in Section 2.2.1, tidal energy is a form of renewable energy that is stable and predictable. Unlike wind energy with its very high and variable wind speeds (e.g. 10m/s to 50 m/s) and directions, that require complicated control systems, like pitch control, rotational speed control, yaw control and so on; tidal energy has the scope to simplify the control scheme and hence to improve the economics. All in all, the improvement of this technology to be more efficient, stable and robust will always be the aim of the tidal energy developer.

2.3 Enlightening leading-edge tubercles

Mother Nature always enlightens and amazes us. Recently an investigation has shown that tubercles on the leading edges of the flippers of a humpback whale (*Megaptera novaeangliae*), shown in Figure 2-9, significantly enhance its manoeuvrability during prey capture, by delaying flow separation at large angles of attack over these foils (Fish *et al.*, 2008). This giant species of marine mammal generally ranges from 12-16m. They first attracted the attention from marine biologists for their unusual feeding behaviour. A study conducted in the 1970s to 1980s into their feeding behaviour (Hain *et al.*, 1982) showed their most inventive technique which is known as bubble net feeding (shown in Figure 2-10 and Figure 2-11). First a group of humpback whales swims in a shrinking circle and then they blow bubbles below a school of prey. With the shrinking ring of bubbles the school of fish can be confined in an ever-smaller cylinder. Finally they swallow their prey in the bubble net.

With such unique preying habits, humpback whales surprised the researchers with agile moves in sharp turns and tight circular swimming. Their unusually long flippers show spectacular hydrodynamic design with NACA 63-xxx like cross section which can be seen from Figure 2-12. But in the contrast their leading edge does not seem to be either geometrically or hydrodynamically smooth, instead it has large protuberances which lead to the research reviewed in the following.



Figure 2-9 Humpback whale (Wikipedia, 2016)



Figure 2-10 Humpback whale lunging in the centre of a bubble net spiral (Wikipedia, 2016)

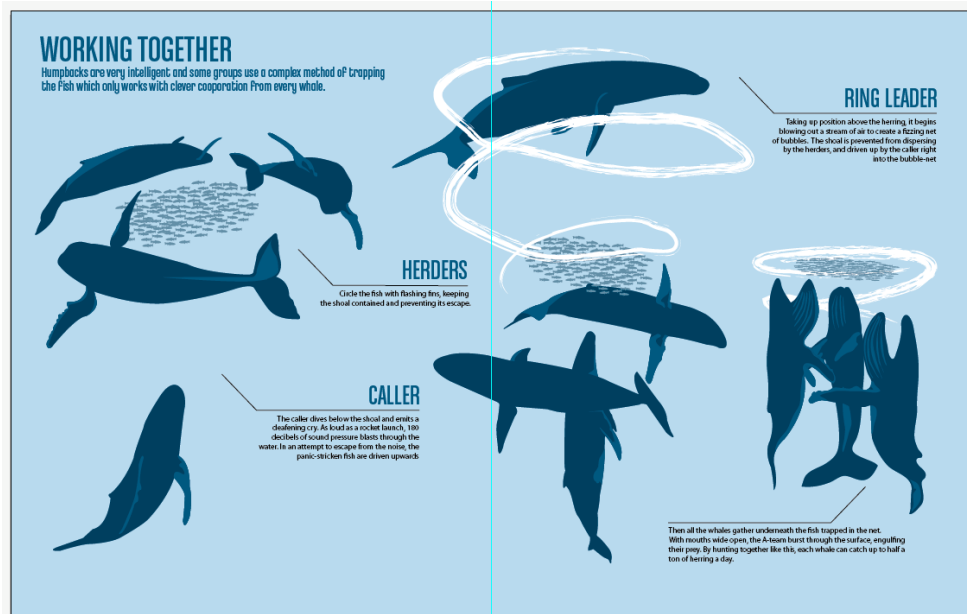


Figure 2-11 Bubble net feeding of humpback whale (SwiftSwan, 2015)

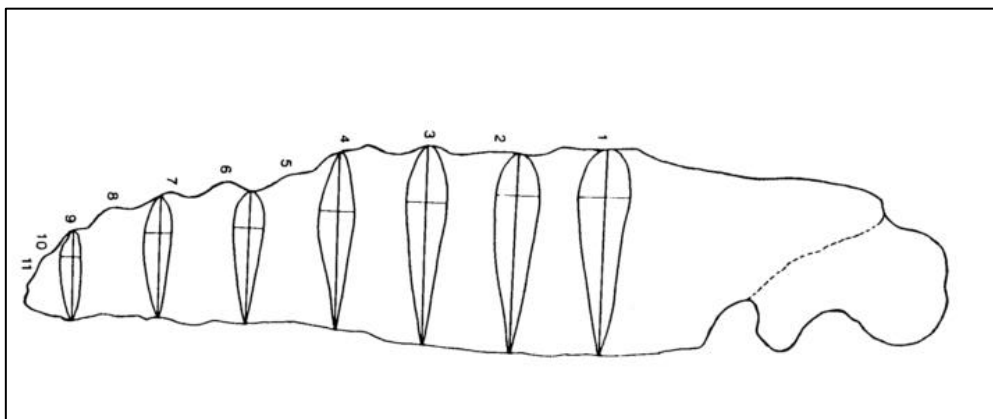


Figure 2-12 Cross sections of humpback whale flippers (Fish and Battle, 1996)

2.3.1 Review of aero/hydrodynamic mechanism of leading-edge tubercles

The first pioneering tests with model humpback whale flippers were carried out in a wind tunnel at effective Reynolds numbers as high as 534,000 to 631,000 by Miklosovic et al in 2007. These tests used replicas of humpback whale flippers with and without tubercles. The results indicated that the addition of leading-edge tubercles to a scale model of an idealized humpback whale flipper would delay the stall angle by approximately 40%, while increasing the lift and decreasing the drag (Miklosovic *et al.*, 2007). The two humpback whale flipper models tested, with and without the tubercles, are shown in Figure 2-13. The comparison of the test results between the two models is shown in Figure 2-14. Because of the promising future of tubercles that this test showed, a series of research on these kind of wings was carried out.

To explore its effects on foil sections, a traditional two-dimensional foil test was also conducted at effective Reynolds numbers of 274,000 to 277,000. However the results from two-dimensional (2D) foils with tubercles are vastly different to those of three-dimensional (3D) foils (Miklosovic *et al.*, 2007). Although the research shows 2D and 3D foils share the same functions of slightly decreasing lift and increasing drag at pre-stall angles of attack but improved lift in their post-stall region, a substantial loss in lift and increase in drag was observed in the 2D test, but not in the 3D foil test. Therefore, the generation of vortices by the tubercles appeared to be beneficial only to 3D foils in the range of Reynolds numbers tested.

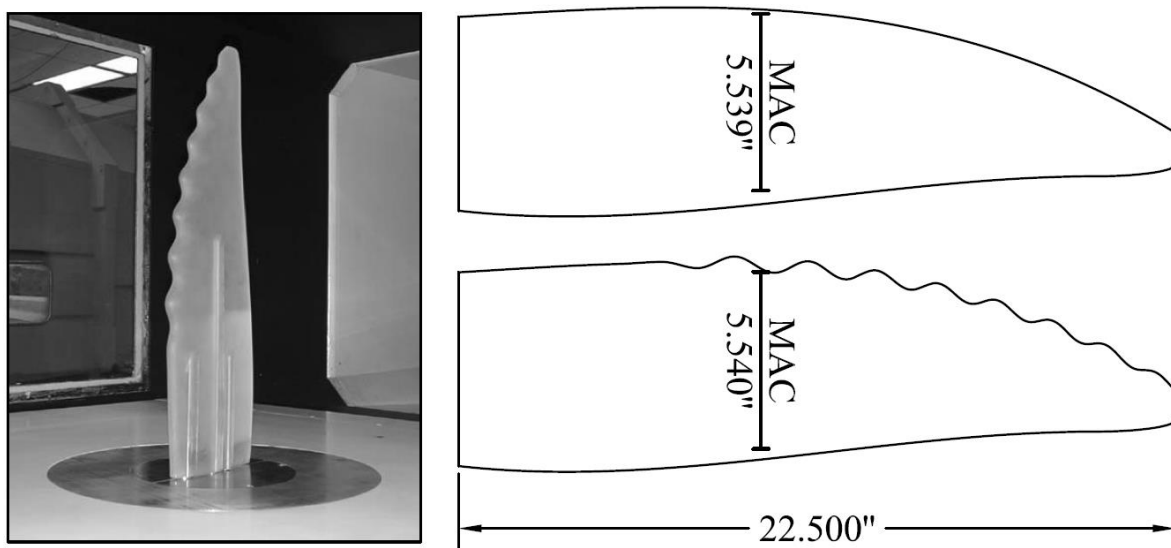


Figure 2-13 Tested model of the whale flipper models (Miklosovic *et al.*, 2007)

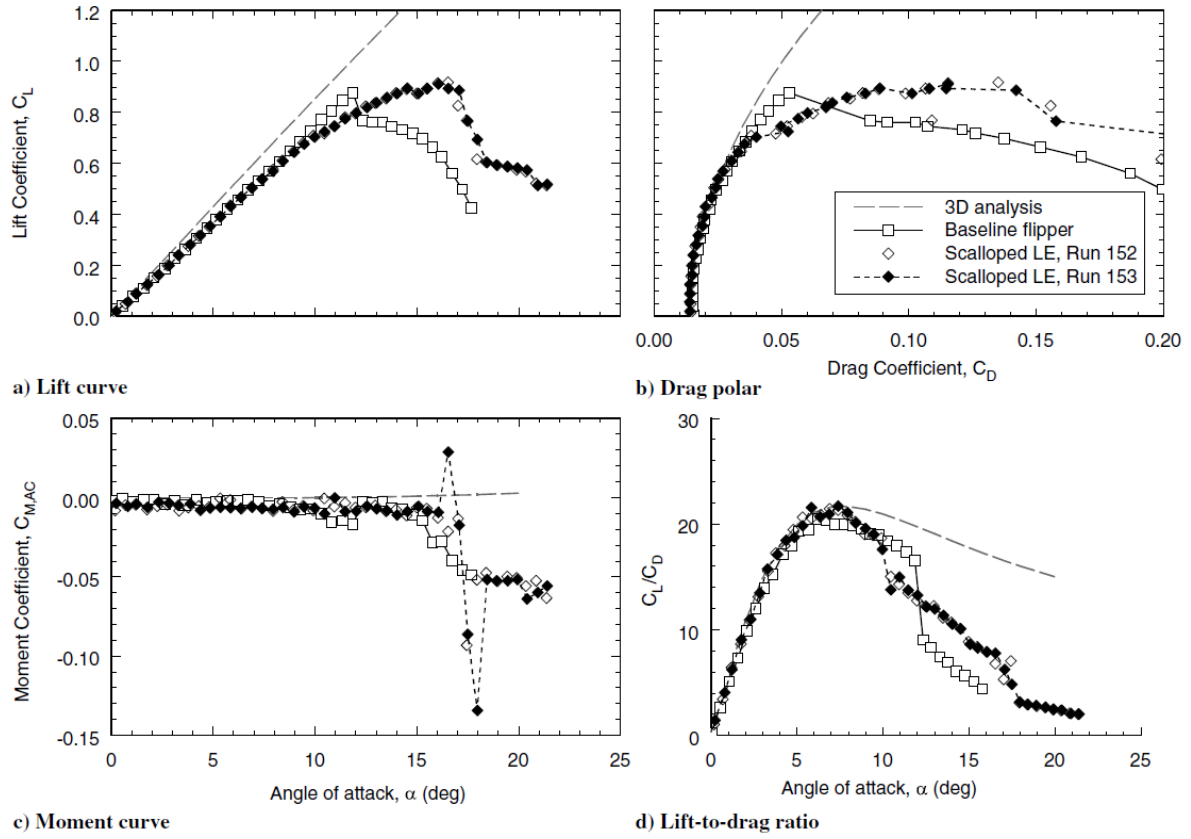


Figure 2-14 Tested result of 3D humpback whale flippers (Miklosovic *et al.*, 2007)

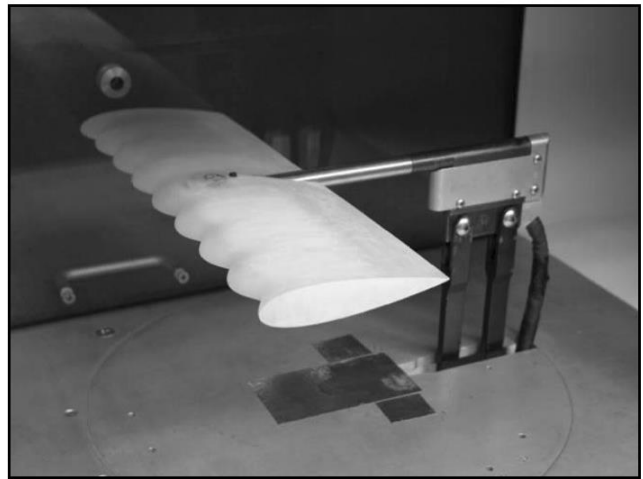
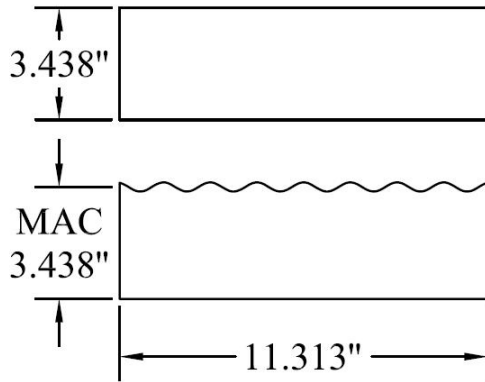


Figure 2-15 Tested 2D foil models (Miklosovic *et al.*, 2007)

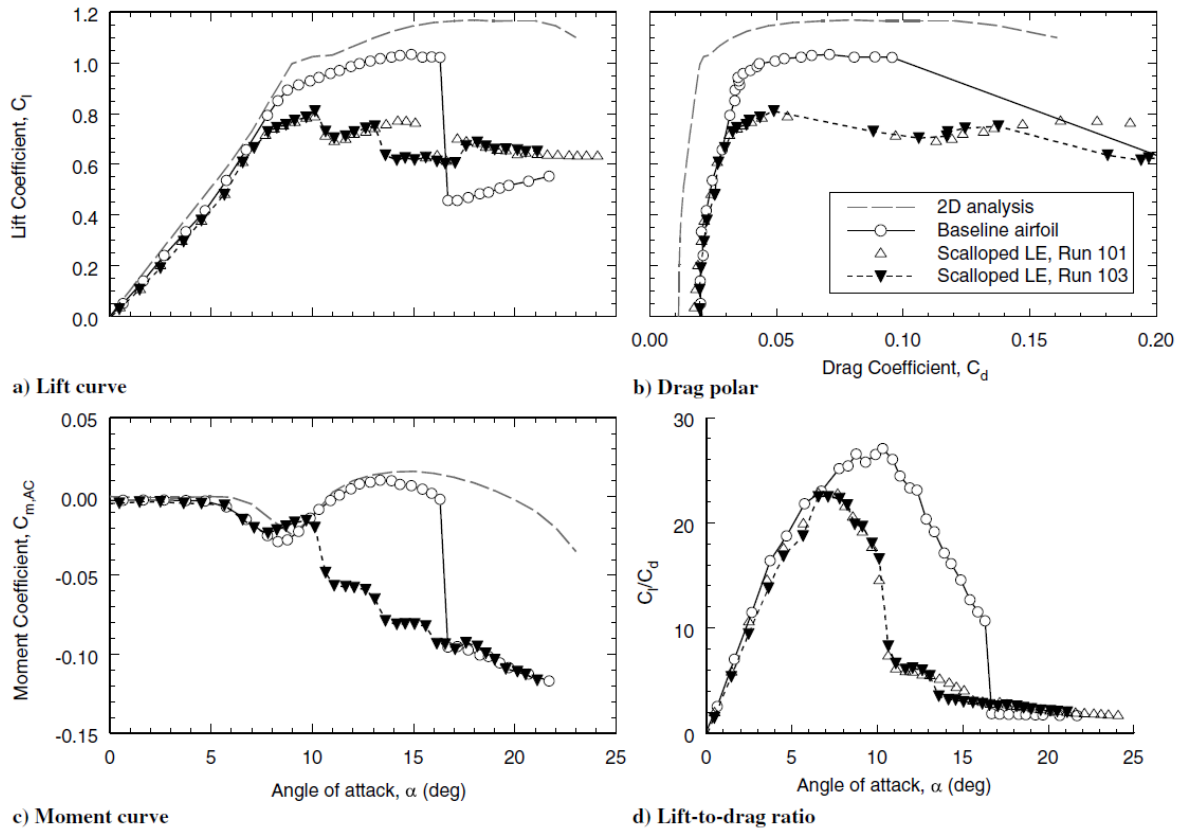


Figure 2-16 Tested results of 2D foil models(Miklosovic *et al.*, 2007)

The above study was conducted in air so, in order to investigate the characteristics in water, Johari et al conducted experiments in the Rhode Island water tunnel of the Naval Undersea Warfare Center (NUWC), which has a 0.30m square cross section under $Re=1.83e+5$ (Johari *et al.*, 2007). Hydrodynamic characteristics of 2D wings with varied sinusoidal leading edges with different parameters were compared. According to Johari et al's report, the foils with the leading-edge protuberances did not stall in the same manner as the baseline foil with the smooth leading edge. Figure 2-17 and Figure 2-18 reveal that the tubercles caused a reduction in the lift coefficient at angles of attack below the baseline foil stall angle. In the post-stall regime, the foils with tubercles had higher lift coefficients. After comparison of various tubercle wings, they found that the wavelength of the wavy edges played a minor role on the force and moment coefficients; on the other hand, the amplitude had a more significant effect (Johari *et al.*, 2007). Moreover, tufts were attached to the foil surface to observe the separation near the surface, as shown in Figure 2-19, and they stated that the flow over the tubercles remained attached well past the angle of attack where the baseline foil stalls.

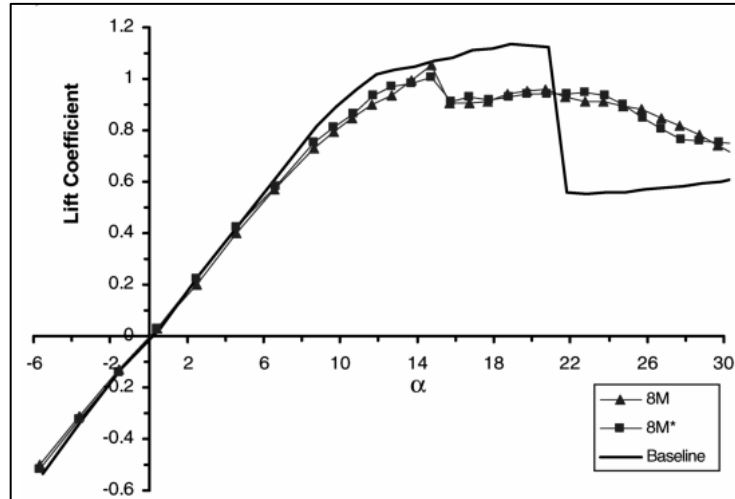


Figure 2-17 Comparison in Lift coefficient(Johari *et al.*, 2007)

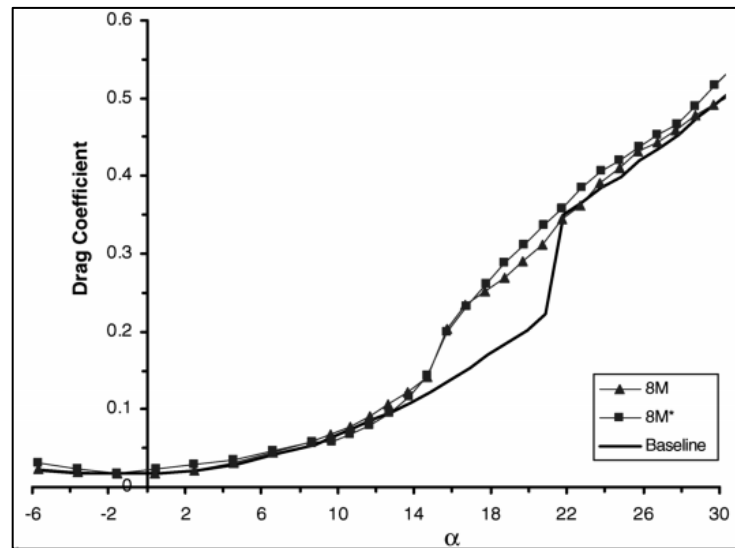


Figure 2-18 Comparison in Drag coefficient(Johari *et al.*, 2007)

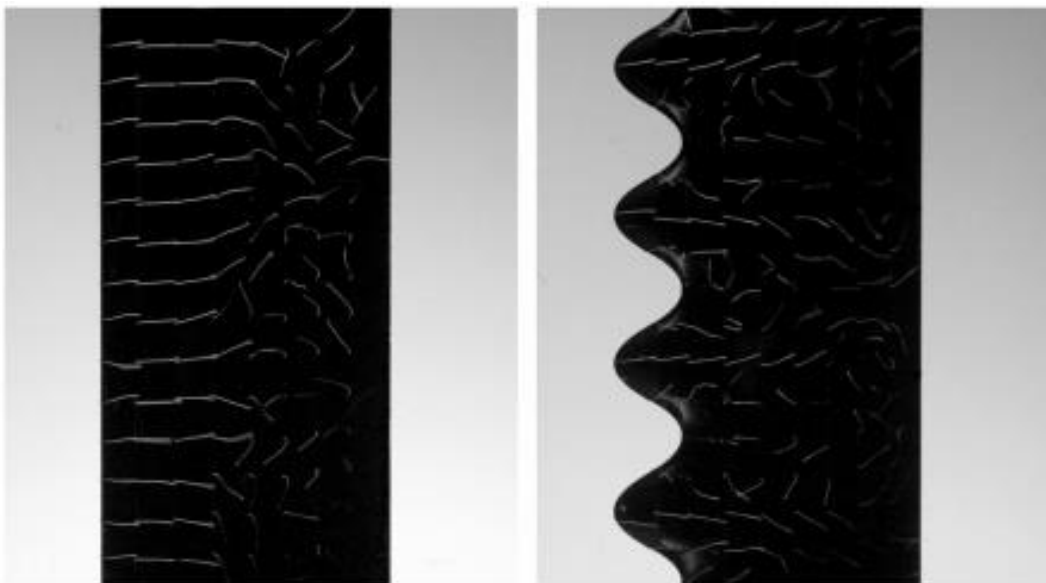


Figure 2-19 Flow visualisation with tufts at 18°(Johari *et al.*, 2007)

One numerical model presented by van Nierop et al, also supported the claim that when the hydrofoil was defined to be an infinite span foil, the advantage of the bumpy leading edge was less obvious. The comparison of the numerical results is presented in Figure 2-20 (van Nierop *et al.*, 2008). Accordingly, the wavy leading edge had a largely three dimensional benefit and this feature could be suitable for tidal turbines. Three dimensional effects at the blade tip would greatly reduce the efficiency of tidal turbines while hardly any useful lift would be generated at the tip regions as a result of 3D flow.

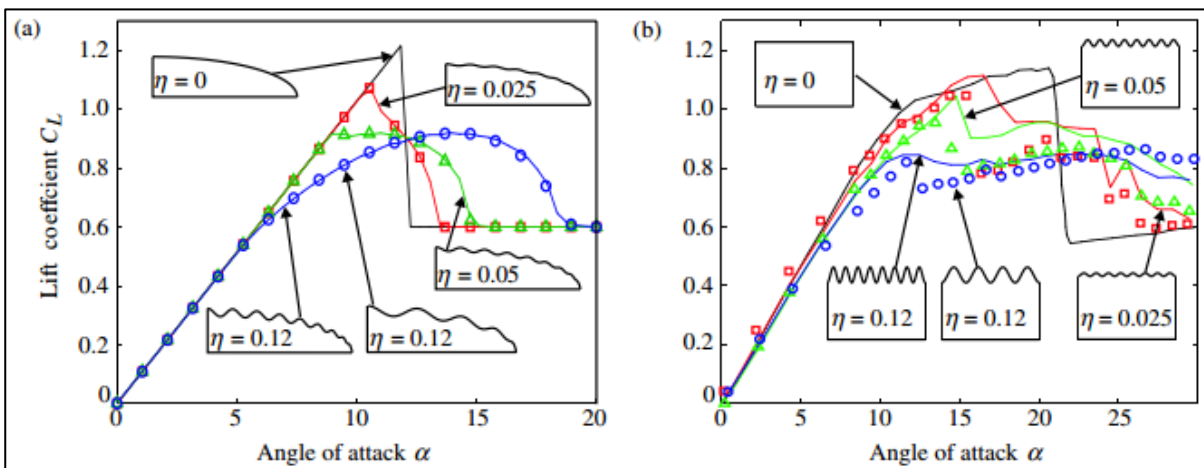


Figure 2-20 Analysis results for 3D airfoils and 2D airfoils (van Nierop *et al.*, 2008)

Stemming from the studies reviewed above, a number of follow up investigations have been conducted to explore the various aspects of leading edge tubercles, as summarised in the following:

- Optimisation of tubercle size: These studies focussed on the optimisation of the sinusoidal tubercle sizes by changing the wavelength and amplitude (Custodio, 2007; Johari *et al.*, 2007; Hansen *et al.*, 2011; Malipeddi, 2011; Chen *et al.*, 2012; Hansen *et al.*, 2012; Huang *et al.*, 2015). Both numerical and experimental methods have been used in these studies.
- Optimisation of the tubercle coverage: The percentage of tubercle coverage also has a certain level of influence on the performance. Researchers have tried to vary the coverage of the tubercles (Yoon *et al.*, 2011).
- Optimisation of the space of tubercles: There are also some studies to investigate the use of non-continuous tubercles and by changing the space between the tubercles and the influence of the tubercles has been also studied (Arai *et al.*, 2010).

- Effect of unsymmetrical foil sections: The effect of tubercles in unsymmetrical foil sections has been studied (Huang *et al.*, 2015).
- Effect of tubercles on swept wings: Investigations on tapered and swept wings have been conducted (Bolzon *et al.*, 2014)

The investigations conducted in the above listed studies generally agreed on the fact that the effects caused by the tubercles on the performance of a 2D foil and a 3D foil were quite different. Studies on the 2D foils were more focused on the optimisation of the tubercle profiles which could be defined by different parameters. Optimised tubercle profiles on these 2D sections could improve the lift coefficient curves further by maintaining the lift after the stall point. However, this was at the cost of a reduction in the maximum lift coefficients since the drag coefficients were increased by these tubercles, at the same time. On the other hand, different performance characteristics have been reported based on the investigations with the leading-edge tubercles on 3D foils which are usually tip tapered. The investigations with the 3D foils also claimed an improvement of the lift coefficient curves by maintaining the lift beyond the stall point which was similar to the effect of tubercles on 2D foils. However, in addition to this, the performance regarding to the lift-to-drag ratio could be enhanced.

Based on the above fundamental observations, potential applications of tubercles on tidal turbine blades could be attractive because: higher lift and lower drag of the blades would result in a higher performance; furthermore, the increase in stall angle of attack would largely enhance the starting performance and hence sustain the power to be generated in lower current speeds, which would enlarge the operational speed range of a turbine at the lower end. The latter would be a great benefit for tidal turbine technology to spread its application more widely over the world's oceans to make more use of lower tidal speeds which vary globally from 0.5 to 4 m/s.

The investigations conducted in the above listed studies generally agreed on the fact that the effects caused by the tubercles on the performance of a 2 dimensional (2D) foil and 3 dimensional (3D) foil were quite different. Studies on the 2D foils were more focused on the optimisation of the tubercle profiles which could be defined by different parameters. Optimised tubercle profiles on these 2D sections could improve the lift coefficient curves further by maintaining the lift after the stall point. However, this was at the cost of a reduction in the maximum lift coefficients since the drag coefficients were increased by these tubercles, at the same time. On the other hand, different performance characteristics have been reported based on the investigations with the leading-edge tubercles on 3D foils which are usually tip tapered.

The investigations with the 3D foils also claimed the improvement of the lift coefficient curves by maintaining the lift beyond the stall point which was similar to the effect of tubercles on 2D foils. However, in addition to this, the performance regarding to the lift-to-drag ratio could be enhanced.

Based on the above fundamental observations, potential applications of the tubercles on the tidal turbine blades could be attractive because: higher lift and lower drag of the blades would result in a higher performance; furthermore, the increase in stall angle of attack would largely enhance the starting performance and hence sustain of power to be generated in lower current speed, which would enlarge the operational speed range of a turbine at the lower end. The latter attraction would be a great benefit for the tidal turbine technology to spread its application wider over the world's oceans to make more use of lower tidal speeds which vary globally from 0.5 to 4 m/s.

2.3.2 Biomimetic applications of leading-edge tubercles

Based on the above findings, various biomimetic applications of leading edge tubercles have been tried, especially by a company named WhalePower which applied the concept on wind turbines to improve their efficiency. Such a turbine blade with leading-edge tubercles is shown in Figure 2-21. Bellequant and Howle conducted an experiment with a wind turbine in 2009. The tests showed that the turbine with tubercles on the leading edge generated more power in the lower wind speed range than the original one, as shown in Figure 2-22 (Bellequant and Howle, 2009).

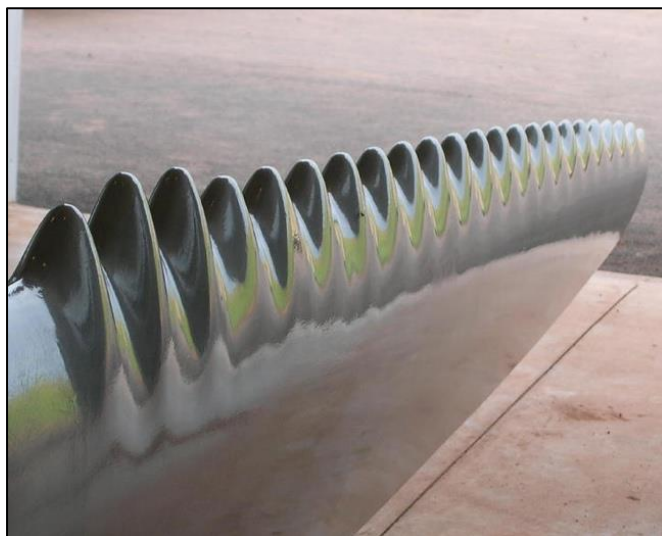


Figure 2-21 Wind turbine with tubercle (Fish *et al.*, 2011)

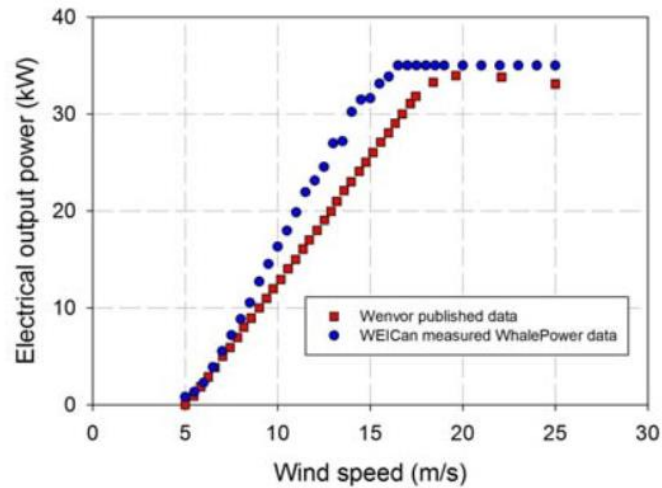


Figure 2-22 Comparison of the generated power between two turbines with and without tubercles (Bellequant and Howle, 2009)

Following the wind turbine application, the tubercle concept was also applied on a tidal turbine for the first time by (Gruber *et al.*, 2011) by using different tubercle designs on a scaled model (as shown in Figure 2-23) and conducting tests in a towing tank. The comparison result demonstrated significant performance improvement, as shown in Figure 2-24.

“The 1/3 tubercled blade outperformed both of the other blade designs in every measured parameter across the full spectrum of velocities tested. At each tip speed ratio, the 1/3 tubercled blade had a 15-85% higher C_p than the control blade. The 2/3 tubercled blade demonstrated higher C_p performance than the control blade, but not as consistently high as the 1/3 tubercled blade.”

However because the power coefficients were rather low (maximum C_p : about 20% for the reference turbine) compared with state-of-the-art tidal turbines (maximum C_p : above 40%), the findings could be questioned on the grounds of whether the performance improvement was due to the effect of the leading-edge tubercles or accidental. This question mark raised over such a limited application (in fact the only application) of leading edge tubercles on a tidal turbine was identified as a significant gap for this research study to explore further.



Figure 2-23 Tidal turbine blades (Top: Control Blade. Middle: 1/3 Tubercled. Bottom: 2/3 Tubercled) (Gruber *et al.*, 2011)

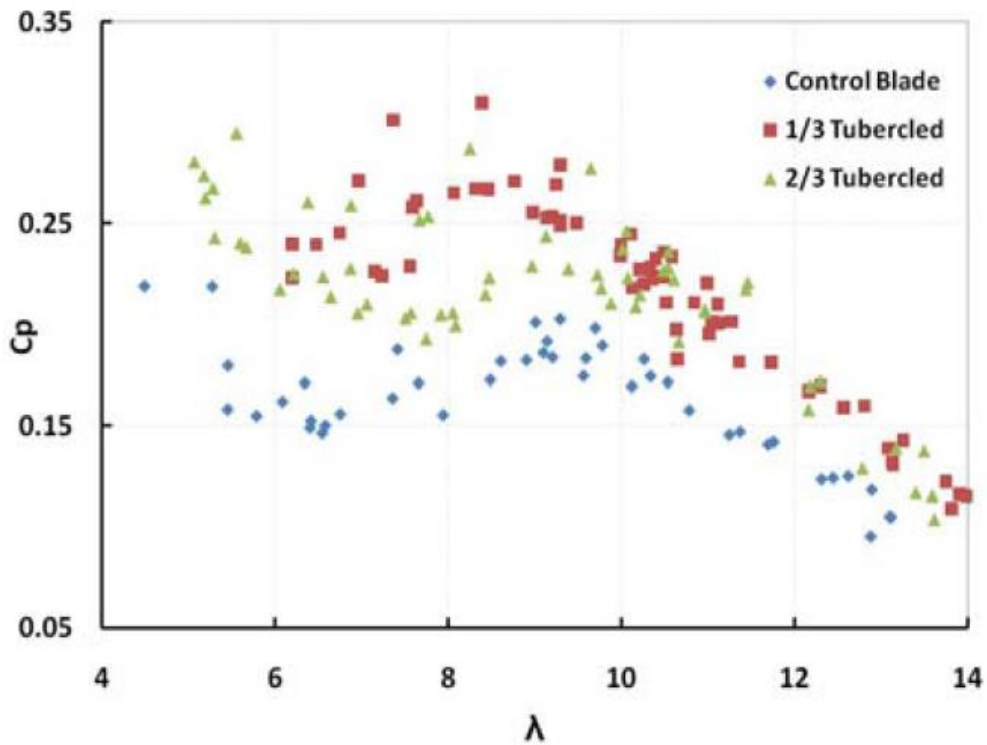


Figure 2-24 Power coefficient (C_p) vs. current velocity for all three blade designs (Gruber *et al.*, 2011)

In a different biomimetic application of leading-edge tubercles, they were applied on rudders and their effects were explored by model tests conducted in a cavitation tunnel to measure lift, drag and cavitation onset by Weber et al, 2010. In this investigation, the performance of rudders with a smooth leading edge and different numbers of tubercles were measured under different Reynolds numbers ranging from $2e+5$ to $9e+5$. As shown in Figure 2-25, rudders with tubercles at lower Reynolds number would generate higher lift-to-drag ratio than the smooth rudder,

although the effect was reversed for the high Reynolds numbers. However, the cavitation trend was in favour of the rudder with the leading edge tubercles as the cavitating regions were restricted to the slots between the tubercles instead of spreading over the entire span. In addition, the diameter of the tip vortex cavitation generated by the biomimetic rudder was smaller than that of the one generated by the smooth rudder as shown in Figure 2-26. Similar findings regarding the cavitation pattern were also found by Johari, as shown in Figure 2-27 (Johari, 2015).

Apart from the above reviewed applications, the following potential applications from different investigators have been tried or imagined as shown in Table 2-1.

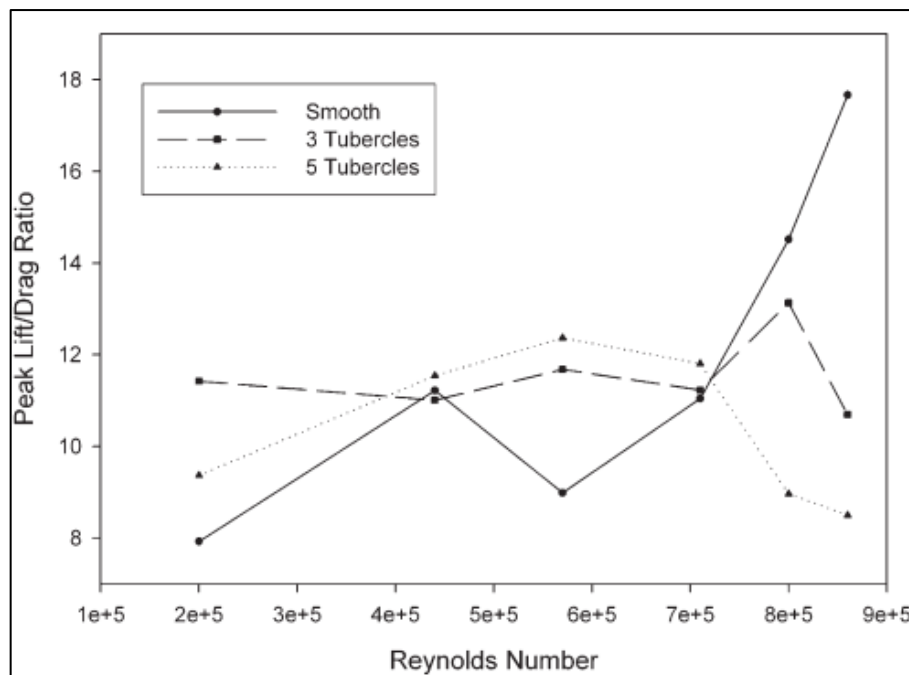


Figure 2-25 Comparison of peak lift-drag ratio for the three rudders (Weber *et al.*, 2010)

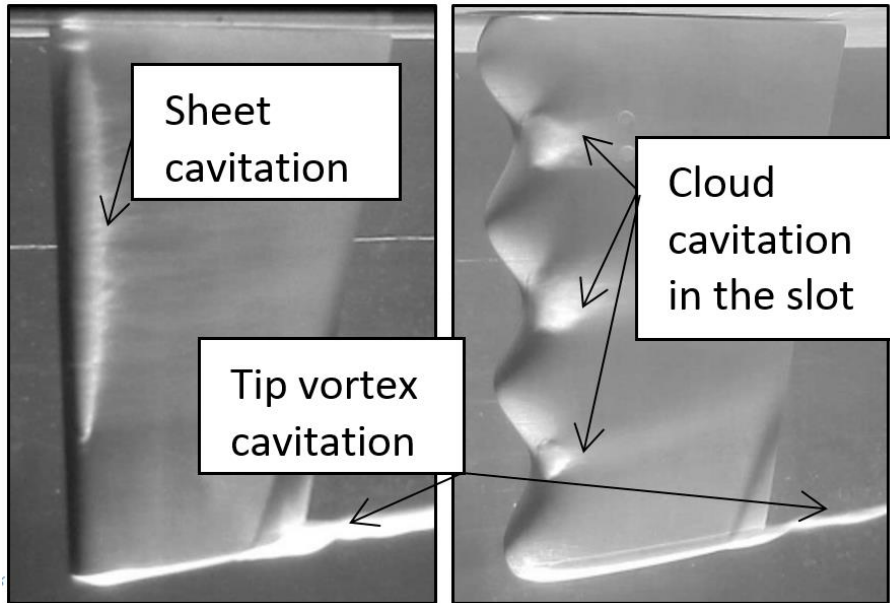


Figure 2-26 Cavitation contrast between the smooth rudder and the tubercle rudder (Weber *et al.*, 2010)

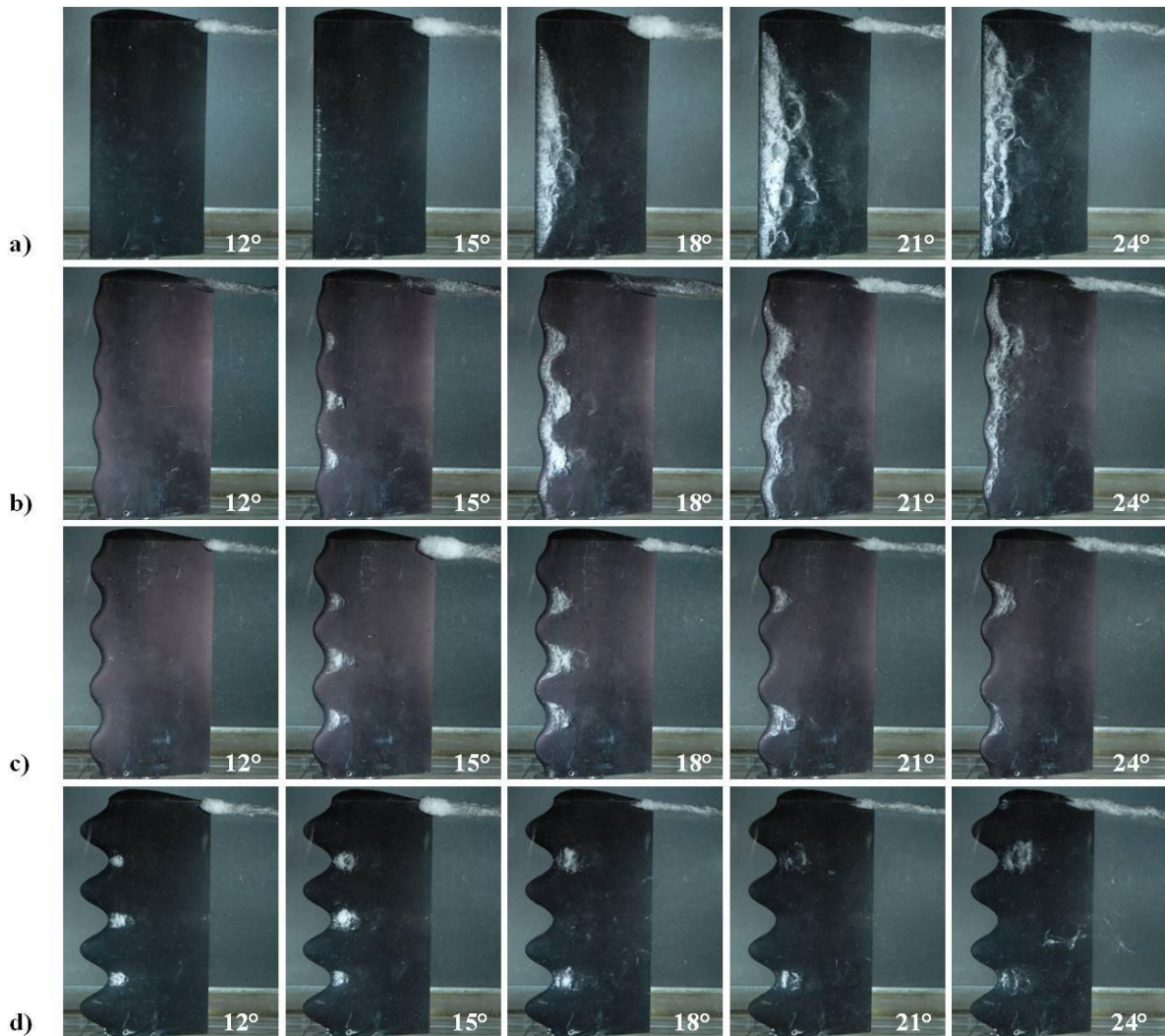


Figure 2-27 Cavitation patterns on various sizes of tubercles (Johari, 2015)

Table 2-1 Typical applications of leading edge tubercles

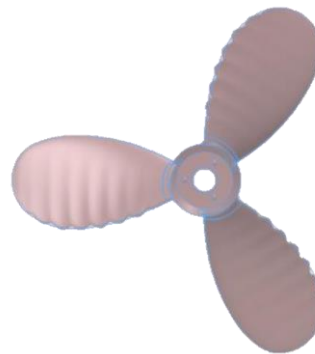
- **Surfboard fins with tubercles (Stuart, 2014)**



- **Modern commercial jet airliner with tubercles (Fish *et al.*, 2011)**



- **Marine propeller (Ibrahim and New, 2015)**



- **Air fans by WhalePower (Whalepower, 2016)**



- **Computer cooling fans by WhalePower (Whalepower, 2016)**



2.3.3 Further understanding of the aero/hydrodynamic mechanism of leading-edge tubercles

The fundamental research conducted to date on tubercles and their applications on foil based machines, as reviewed in Section 2.3.2, has already demonstrated significant benefits with the most evident performance improvement occurring during the post-stall region of the foils (Bolzon *et al.*, 2016). Currently, it is only known that the tubercles create pairs of streamwise counter-rotating vortices, as it has been observed by numbers of researches. For example, (Hansen *et al.*, 2016) used a PIV system to measure the vorticity distribution which clearly demonstrated the presence of the counter-rotating vortices, as shown in Figure 2-28, and many researchers have investigated this both numerically and experimentally (Swanson and Isaac, 2011; Zhang and Wu, 2012; Wei *et al.*, 2015; Hansen *et al.*, 2016).

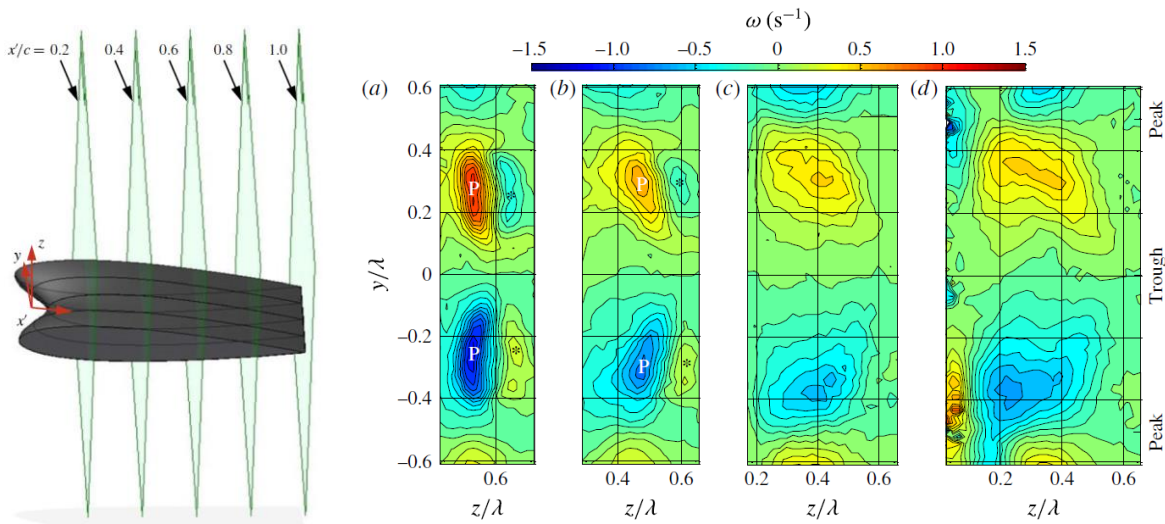


Figure 2-28 Measuring position and the vorticity field from behind the foil where the counter clockwise vortex core (red/upper) is positive and the clockwise vortex core (blue/lower) is negative. AOA=5°, Re = 2230, image planes are shown for $x'/c=0.4, 0.6, 0.8$ and 1 (a–d). (Hansen *et al.*, 2016)

Notwithstanding the above research, a clear and full explanation of the mechanism of tubercles is still under discussion and several possibilities have been argued. The current hypotheses can be summarized as follows (Bolzon *et al.*, 2016):

- **Compartmentalization:** tubercles would create virtual barriers through the streamwise, counter rotating vortices acting like a wing fence to prevent the flow from traveling spanwise but not by adding physical barriers.

- Induced Flow: tubercles produce pairs of these streamwise, counter rotating vortices, and as such a region of common downwash occurs over each peak, while a region of common upwash occurs over each trough. Where downwash occurs, it is suggested that the effective angle of attack is reduced, resulting in an increased stall angle, whereas the opposite will occur where there is upwash.
- Vortex lift: This is a way of producing lift that is less susceptible to stalling. By creating strong vortices over the suction side of a foil or wing, the downwash of the vortices causes the flow to remain attached over the surface, thereby delaying flow separation.
- Boundary layer momentum exchange: Tubercles can energise the flow and increase the momentum of the boundary layer through mixing with the freestream, which will result in a delayed stall.

Even though the above hypotheses have not been fully proved, they have indicated a promising future in applying this concept onto tidal turbines. For example, if the compartmentalization effect can be utilised in tidal turbines, the tip loss (3D effect) will be greatly lowered since it can produce counter rotating vortices to prevent the spanwise flow. On the other hand, since foil sections of tidal turbine blades at different radial positions are operating at different angles of attack, this compartmentalization effect will also prevent the foil sections from influencing each other. Likewise, other effects might be also beneficial, such as the boundary layer momentum exchange effect by which flow can be energised and remain more attached to the blade surface. However, all these hypotheses needs to be explored and discussed in the current research study.

2.4 Methodology for biomimetic application of leading edge tubercles

Although some useful experimental and numerical work on tubercle research have been accomplished so far, the biomimetic application of the tubercle concept on tidal turbines is still ambiguous and the design method for such applications still needs to be established. In order to help the situation thorough research on tidal turbines with tubercles is necessary and this may require a combined use of advanced numerical and experimental methods.

2.4.1 Numerical simulation methods for tidal energy devices

Regarding numerical methods, Computational Fluid Dynamics (CFD) has gradually become the major mathematical tool to solve fluid dynamic problems due to the dramatically enhanced computer technologies and resources available to simulate complicated practical cases.

A number of commercial CFD software packages have been developed during the past few decades, like ANSYS (CFX or Fluent), Star-CCM+, OpenFOAM, etc. Moreover, they have already been applied by researchers to investigate various hydrodynamic aspects of tidal turbines including performance predictions and to support industry for practical applications at full-scale (O'Doherty *et al.*, 2009; Harrison *et al.*, 2010; Jo *et al.*, 2012; Mason-Jones *et al.*, 2012). While conducting CFD simulations, how to improve the accuracy of the predictions is always the hottest issue discussed by researchers.

Above all, the most important task is to fully understand the physical conditions of the simulated cases. Only by fully understanding the simulation conditions can the researchers ensure that the numerical model is based on the real physical model. The grid quality needs to be considered carefully, especially for the mesh within the boundary layer. Due to the variable needs of the different turbulence models for the mesh division, the methods change with the requirement of different turbulence model. Finally, the choice of a suitable turbulence model for the simulation changes too. Since the flow conditions around turbines can be considered as steady state for most of the time, the time saving and computationally cheap steady state approach is always preferred. However there are exceptions for a non-uniform incoming velocity or large vortex being generated by turbines where transient analysis should be employed (Mason-Jones *et al.*, 2013). Accordingly, to make the CFD modelling more accurate, there needs to be not only a full understanding of the turbines but also CFD skill and experience. Even though with the above mentioned key factors for effective numerical simulations, model tests are still

compulsory for most of the cases to validate and calibrate the numerical model, as reviewed next.

2.4.2 Experimental investigations of tidal energy devices

In order to validate the numerical predictions model tests are still the most efficient way and are employed by most of the researchers, even though there is a considerable number of other methods to verify the numerical models and to ensure their accuracy. Model tests can be conducted in traditional hydrodynamic laboratories, like towing tanks, water flumes and cavitation tunnels (Bahaj *et al.*, 2007; Shi *et al.*, 2013; Gaurier *et al.*, 2015). The tests basically include investigation of the performance of turbines, like power coefficients (C_p) and thrust coefficients (C_T), under various conditions. The rotational speed, torque and thrust of the turbines are generally measured by open water dynamometers, which results in the non-dimensional power and thrust coefficients over a range of tip speed ratios (TSRs).

As a part of the former UK National research programme (EPSRC-RNET), Wang *et al.* (2007) conducted an experimental investigation into the efficiency, slipstream, cavitation and noise characteristics of different types of horizontal axis marine tidal turbines which were stall-regulated. The experiments of this research programme were conducted in the Emerson Cavitation Tunnel (ECT) of Newcastle University which is complemented by suitable state-of-the-art equipment for tidal turbines tests. Since this facility was also used for the Author's PhD experiments it will be appropriate to have a brief review of the facility and equipment, although they will be described in Chapter 4&5 in more detail.

The main dimensions of the Emerson Cavitation Tunnel are shown in Table 2-2. The open water dynamometer H33 (Cussons Technology) is used to measure the thrust and torque of turbines, and the main technical data of H33 are given in Table 2-3. On top of the dynamometer, a variable-speed DC motor (64kW at 415 V) is mounted to drive a propeller or to absorb the power generated by a turbine. The turbine is mounted on the vertically driven dynamometer, as shown in Figure 2-29.

Table 2-2 Main dimension of the Emerson Cavitation Tunnel

Description of facility	Vertical plane, closed circulation
Test section size (L×B×H) (m)	3.10×1.26×0.80
Test section area (m ²)	1.008
Contraction ratio	4.271
Main pump power (kW)	300
Main pump rotation speed (RPM)	294
Impeller diameter (m)	1.295
Maximum velocity (m/s)	8
Absolute pressure range (kN/m ²)	7.6 (min) – 106 (max)
Cavitation number range	0.5 (min) – 23 (max)
Model propeller size (mm)	150 - 400

Table 2-3 Technical data of open water dynamometer H33

Type of dynamometer	Kempf & Rammers H33
Rated maximum thrust (N)	±3000
Rated maximum torque (Nm)	±150
Maximum rotation speed (RPM)	4000

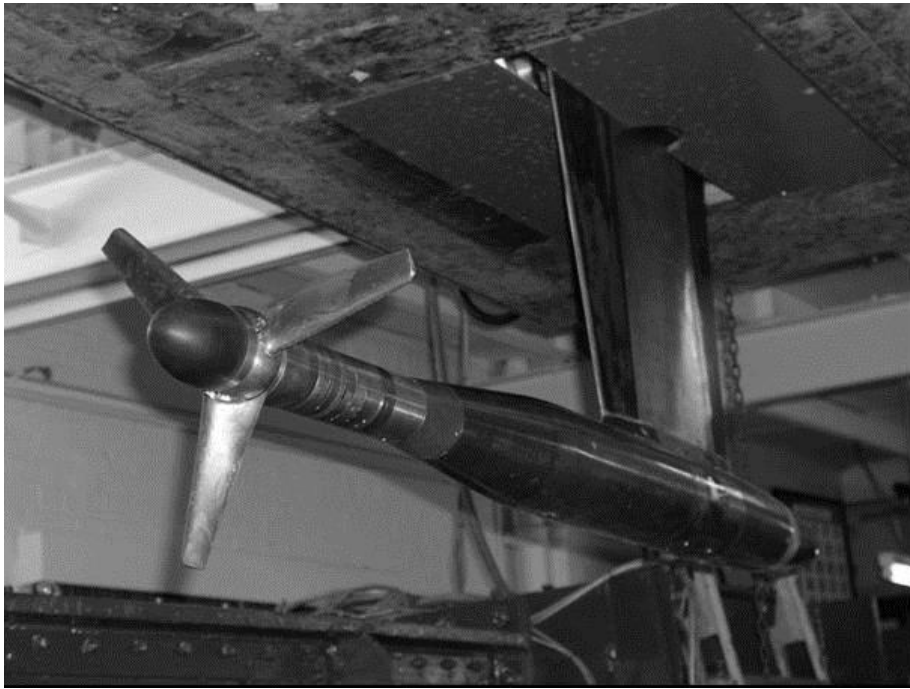


Figure 2-29 Turbine mounted on Dynamometer H33 for power coefficient curve test

In addition to the performance tests to measure the torque and thrust of a turbine, cavitation and underwater radiated noise characteristics can be investigated in this facility by taking advantage of the capability to vary the pressure by applying vacuum on the ECT. Wang et al (2007) explored the potential impact of cavitation and associated underwater radiated noise on ocean environments by observing cavitation and measuring noise levels in the ECT. High speed cameras and a stroboscope were employed to observe the cavitation phenomenon; at the same time, a hydrophone was used to measure the noise level. Figure 2-30 shows the experimental

results of cavitation simulating a shallow depth of submergence of the turbine shaft at the design tip speed while Figure 2-31 shows the noise levels at the designed shaft depth extrapolated to the full-scale turbine.



Figure 2-30 Cavitation observed at shallow shaft immersion and designed stream speed (Wang *et al.*, 2007a)

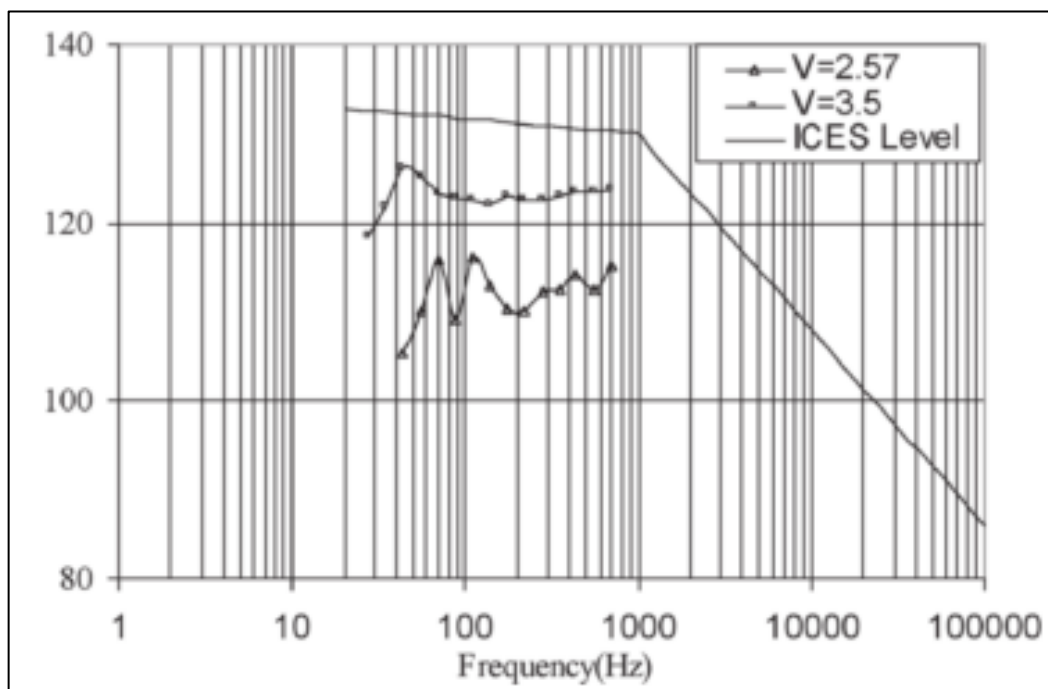


Figure 2-31 Net noise levels at designed shaft depth in the full scale(Wang *et al.*, 2007a)

In contrast to the traditional turbines, turbines with leading-edge tubercles may induce more complex flow structures around the blades and in the slipstream of the turbine. The influence of this flow structure, in particular the effect of the counter rotating vortex structure around the blades, should be investigated. Therefore, a suitable experimental tool to visualise and measure the flow structure would play a vital role to support the CFD simulations. In addressing at this requirement, PIV (Particle Image Velocimetry) is perhaps the most preferred state-of-the-art optical method for advanced visualisation and analysis of such flow structure using instantaneously measured flow velocities. In comparison with other techniques used to measure flows, e.g. Laser Doppler Velocimetry (LDV) and hot-wire anemometry, the main advantage of the PIV is that it produces two dimensional or even three dimensional velocity vectors in a 2D flow field or 3D flow volume, respectively, while the others can only provide the velocity data measured at a point, hence more insight into the real physics of the flow phenomena can be gained.

The ECT is already equipped with a Stereo PIV system (Dantec Dynamics). Stereo PIV can measure the three velocity components of the flow in a plane section using two high-speed cameras. This technology has already been used in research into 3D wings with tubercles (Sisinni *et al.*, 2012). Wings with tubercles do not stall at the crest of the tubercle at the stall angle for wings without tubercles, as indicated in Figure 2-32. On the contrary, as shown in Figure 2-33, the valleys of wings with tubercles were turned into velocity defects where flow separation existed and stall regions developed.

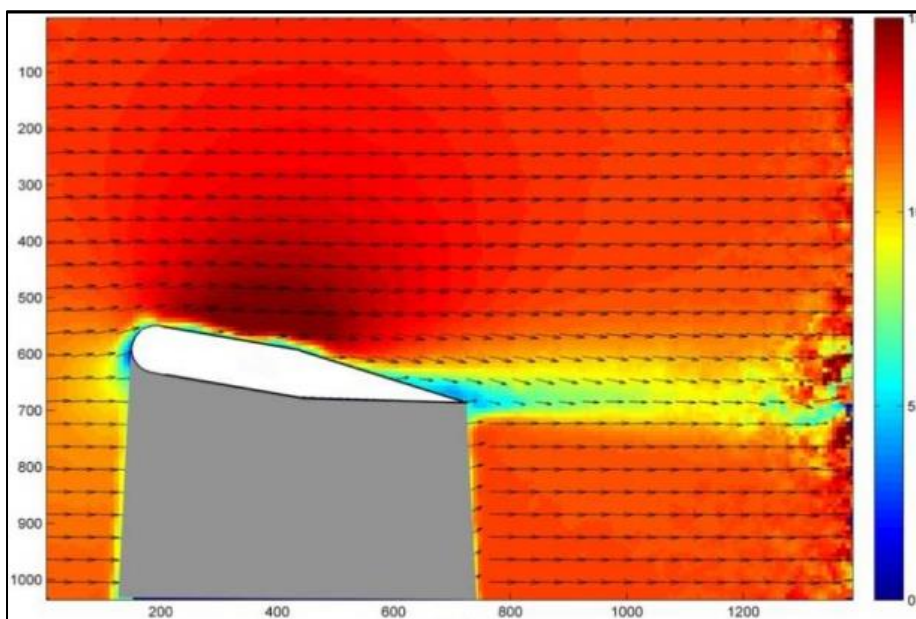


Figure 2-32 PIV results on the vertical plane at the crest for wing with variable tubercles at angle of attack equal to 10° (Sisinni *et al.*, 2012)

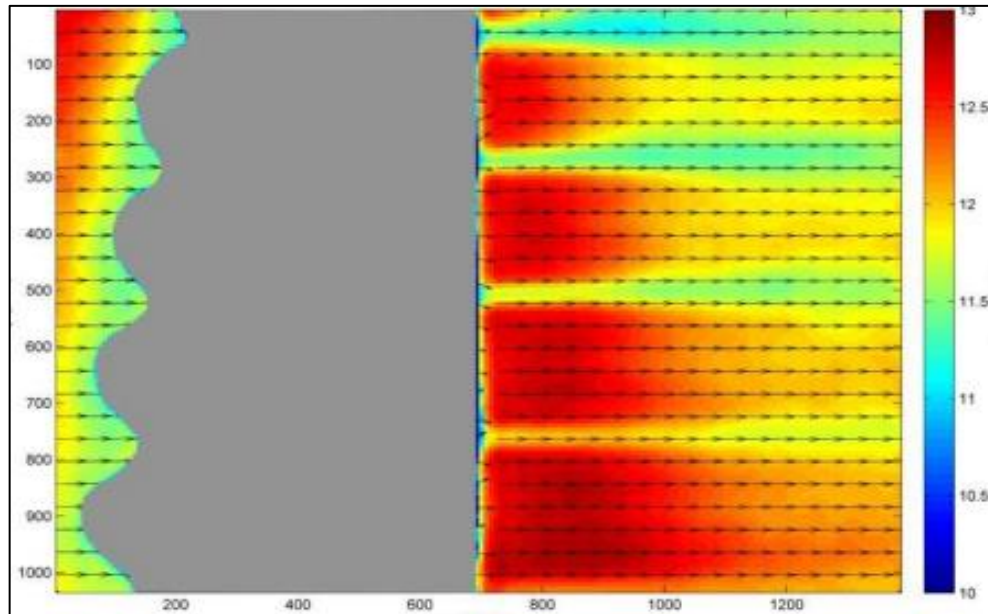


Figure 2-33 PIV results on the horizontal plane for wing with variable tubercles at angle of attack equal to 5° (Sisinni *et al.*, 2012)

By using the above reviewed facility and equipment, the hydrodynamic performance tests, cavitation observations, noise measurements and advanced flow visualisations could be conducted in the Emerson Cavitation Tunnel to complement the aim and objectives of the present research. However, these tests are all about the performance investigations in uniform flow and under steady conditions. On the other hand, a typical tidal turbine will be affected by the presence of waves and their unsteady effects in a real sea environment. To the best of the Author's knowledge there has been no study exploring the effect of waves on the performance of a tidal turbine with leading edge tubercles. In complementing the objectives of this research further, it would be informative to explore the unsteady effect of waves on the performance of the biomimetic turbine with leading edge tubercles. For this purpose there would be a need for a wave making facility and it was found suitable to utilise the Kelvin Hydrodynamic Lab (KHL) of Strathclyde University. In the past, KHL has been heavily involved in testing work for wave and tidal energy devices (Day *et al.*, 2015; Gaurier *et al.*, 2015). The general description of the KHL has been given in Table 2-4.

The open water dynamometer that KHL uses is an in-house built dynamometer driven by a 900W AC motor decelerated by a 10:1 gear box, which is limited to a maximum of 300 RPM, specially designed for tidal turbine testing. The torque and thrust are measured by a torque and thrust transducer with the capability to measure 2000N thrust and 50Nm torque. The dynamometer and the model fitting can be seen in Figure 2-34.

Table 2-4 General description of the Kelvin Hydrodynamic Lab

Tank Type	<ul style="list-style-type: none">• Towing Tank
Tank Dimensions	<ul style="list-style-type: none">• 76m x 4.6m x 2.5m
Carriage Speed	<ul style="list-style-type: none">• Computer-controlled digital drive: max speed 5m/s. Equipped with digitally-controlled oscillating sub-carriage
Wavemaker	<ul style="list-style-type: none">• Variable-water-depth computer-controlled four-flap absorbing wavemaker generating regular or irregular waves over 0.5m height (subject to water depth)• High quality variable-water-depth sloping beach, with reflection coefficient typically less than 5% over frequency range of interest
Data acquisition	<ul style="list-style-type: none">• PC based modular data acquisition/control system• Up to 64 input and 20 output channels, sample rate up to 60kHz



Figure 2-34 Turbine model fitted on the dynamometer in KHL

2.5 Summary

This chapter presented a literature survey to review the development status of tidal energy, the biomimetic-inspired concept of leading-edge tubercles and critical research methodologies for the application of this biomimetic concept to a tidal turbine. The chapter also presented the following conclusions from the survey including the current knowledge gap(s) that will be addressed in this research study to meet the aims and objectives of the thesis:

- Based on this review, it can be seen that technology development is still playing a vital role for tidal energy industry, which is currently limited by reliability, survivability and economics. Whereas the current technology is mainly inherited from the mature wind energy system, the technology dedicated for the tidal energy extraction still needs to be invented, developed and validated.
- Within the context of developing a dedicated technology, a number of biomimetic research projects have demonstrated the potential for performance improvement of foils (as lifting bodies) by the application of leading-edge tubercles. This biomimetic concept can be exploited in various aero and hydrodynamic engineering practises including renewable energy applications. Since a tidal turbine is a typical 3D foil application, there is great scope to explore the potential of this biomimetic concept by using state-of-the-art research methodologies as reviewed in this chapter.
- Having conducted the review, it has been found that the “*extremely limited amount of research available for the application of the leading edge tubercles on a tidal turbine*” is the major research gap that needs to be addressed and bridged. This will require further research, in particular experimental research, to help in understanding the physics of the leading edge tubercles and whether they can improve the turbine performance. Addressing this knowledge gap will enable this research to explore the feasibility of the leading edge tubercles to improve the hydrodynamic performance of a tidal turbine which is the aim of this research study.
- The above stated knowledge gap may be divided into the following components that will be explored in the forthcoming chapters of this study:
 1. How to design leading-edge tubercles for a tidal turbine blade section;

2. How the tubercles influence the hydrodynamic performance of a tidal turbine blade section;
3. Whether leading-edge tubercles can improve the hydrodynamic performance of tidal turbines;
4. If so, which aspect(s) of the hydrodynamic performances are being affected by the leading-edge tubercles; If not, what is the main cause for any particular performance deterioration;
5. Is there any side effect of the leading edge tubercles for the hydrodynamic performance of a tidal turbine system that may need to be compromised?
6. What are the details of the flow mechanisms to cause performance variations of a tidal turbine through the application of leading-edge tubercles?

Chapter 3 Tubercle Design and Optimisation

3.1 Introduction

With the purpose of applying the tubercle concept onto tidal turbine blades, this chapter focuses on the selection and design of suitable tubercle geometry and its numerical optimisation for a representative 2D tidal turbine blade with S814 profile section which was chosen for this study. Within this framework, Section 3.2 of the Chapter elaborates on the selected tidal turbine model and its blade section geometry. This is followed by the selection and design of suitable tubercle geometry and its numerical optimisation in Section 3.3. The results of the optimisation in terms of the foil performance are discussed in Section 3.4 while the overall Chapter conclusions are given in Section 3.5.

3.2 Description of selected tidal turbine geometry

The design study of the tubercles was based on a previous UK National research programme (EPSRC-RNET), in which a tidal turbine was designed based on the S814 profile cross-section from the NREL series, as shown in Figure 3-1 from Wang et al (Wang *et al.*, 2007b) who conducted an experimental investigation into the efficiency, slipstream wash, cavitation and noise characteristics of this turbine. The scaled turbine model is shown in Figure 3-2 as mounted on the open water dynamometer of the Emerson Cavitation Tunnel.

The foil profile (NREL S814) was chosen for 24% thickness for the strong structure property and its good performance of its tolerance of surface imperfections that is a critical property for fouling threatened tidal turbines (Somers, 2004; Barltrop *et al.*, 2006). On the other hand, the aerofoil has a very low drag coefficient and is not sensitive to change of angle of attack around stall angle, as shown in Figure 3-3.

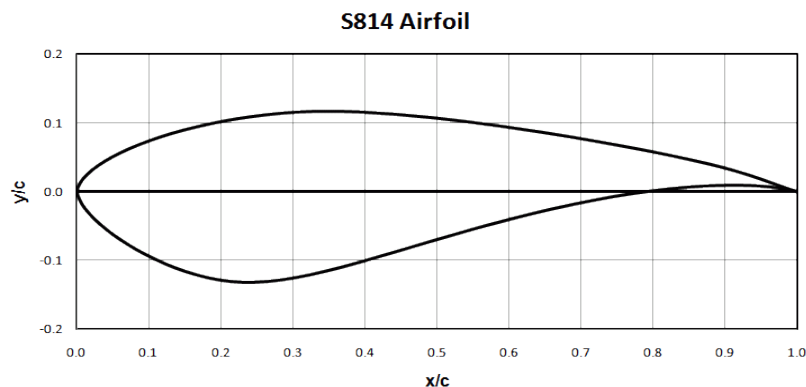


Figure 3-1 Cross-section profile of S814 (Janiszewska *et al.*, 1996)



Figure 3-2 Scaled tidal turbine model mounted on the dynamometer of Emerson Cavitation Tunnel



Figure 3-3 Experimental result of the performance of S814 at Re=1+e6 (Janiszewska *et al.*, 1996)

3.3 Tubercle profile design, optimisation and validation

3.3.1 Optimisation methodology

Previous studies by other researchers on 2D foils were more focused on the optimisation of the sinusoidal shape tubercle profiles defined by different parameters, because of the close pattern with the tubercle on the humpback whales. But the current literature does not display any useful application of the leading-edge tubercles on thick and highly cambered foil sections like the S814 section used in this study.

As reviewed in Chapter 2, the optimised tubercle profiles on these 2D sections could improve the lift coefficient curves further by maintaining the lift after the stall point, but at the cost of a reduction in the maximum lift coefficients because of the increased drag coefficients (Stanway, 2008; van Nierop *et al.*, 2008; Hansen *et al.*, 2009; Hansen *et al.*, 2011; Swanson and Isaac, 2011; Hansen *et al.*, 2012; Hansen *et al.*, 2016). But the tubercles once applied on 3D foil application can maintain the lift and delay the stall with even improved lift-to-drag ratio, which is accredited to the lowered 3 dimensional flow by tubercles. It is ideal to optimise the tubercles directly as applied on 3D foil; nonetheless, to directly optimise the tubercles on the 3D foil can be highly computationally expensive. Therefore, in this Chapter the optimisation process is designed to be computational economical process based on the 2D section to design a tubercle at a moderate penalty of lowering the peak lift coefficient but have the capability to maintain the lift performance after the stall. Later on the as the proposed design applied onto the 3D foil/turbine blade, it can gain 3 dimensional benefits with even improved lift-to-drag ratio.

However, based on the experience from the previous studies, the sinusoidal form was selected as the basis shape to apply on the leading edge of section S814 and the optimisation process was conducted. The investigation into the optimisation of the tubercle profiles was initiated by systematically changing two variants, the Height (H) and the Wavelength (W), of these protrusions based on the sinusoidal form of their shapes. The definitions of these parameters are shown in Figure 3-4. The leading-edge profile is defined as in Equation 3-1.

$$h = \frac{H}{2} \cos \left[\frac{2\pi}{W} s - \pi \right] + \frac{H}{2} \quad \text{Equation 3-1}$$

where h (mm) is the local height of the leading-edge profile of tubercle relative to the reference one which is the smooth leading-edge profile; s (mm) is the spanwise position of foil section.

Two sets of tubercle designs were simulated with two different heights which were assumed to be 5% and 10% of the foil chord length C (mm) and combined with ten wavelength arrangements varying from $0.1C$ to $1C$ in $0.1C$ increments. In order to maintain the maximum thickness, the tubercles were extended forward from the point of the maximum thickness, 25% of chord from the leading-edge.

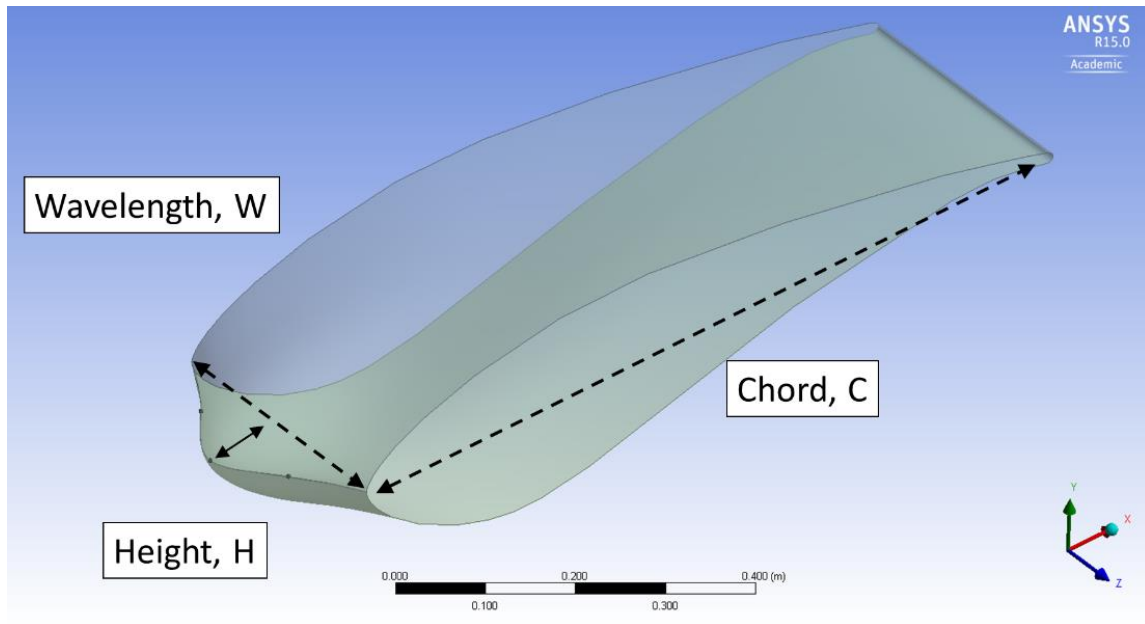


Figure 3-4 Definition of 2D foil with a sinusoidal tubercle

With the changing parameters, the models were built, meshed and evaluated all in the integrated environment of ANSYS-Workbench, which includes ANSYS-Designmodeller as a geometry generator, ANSYS-Meshing as a mesh generator and ANSYS-CFX as a CFD code for performance evaluation. However the most critical component is the CFD code which should provide an accurate prediction for the performance of the foil especially under stall conditions. Therefore in the following sub-section, the chapter first validated the CFD code ANSYS-CFX. Following this, by using the validated code, the performance of 2D infinite foils with varying shapes of tubercles was evaluated to investigate the effect of the shape variations on the lift and drag characteristics of a 2D foil to select the best tubercle profile to be used in combination with the S814 section.

3.3.2 CFD validation and performance evaluation

For validation purposes, the foil test data available from Ohio State University was used (Janiszewska *et al.*, 1996). According to the previous 2D foil studies (Johari *et al.*, 2007; Miklosovic *et al.*, 2007; van Nierop *et al.*, 2008; Weber *et al.*, 2010), the tubercles were found

to be beneficial when the foil was under stall or near stall conditions. However the simulation of a foil performance under stall conditions is a challenging task in CFD simulations (Menter *et al.*, 2003; ANSYS, 2013). Therefore the establishment of a reliable CFD model, in terms of the turbulence modelling, effective mesh generation, etc., is critical for the simulations as discussed next.

Definition of boundary conditions

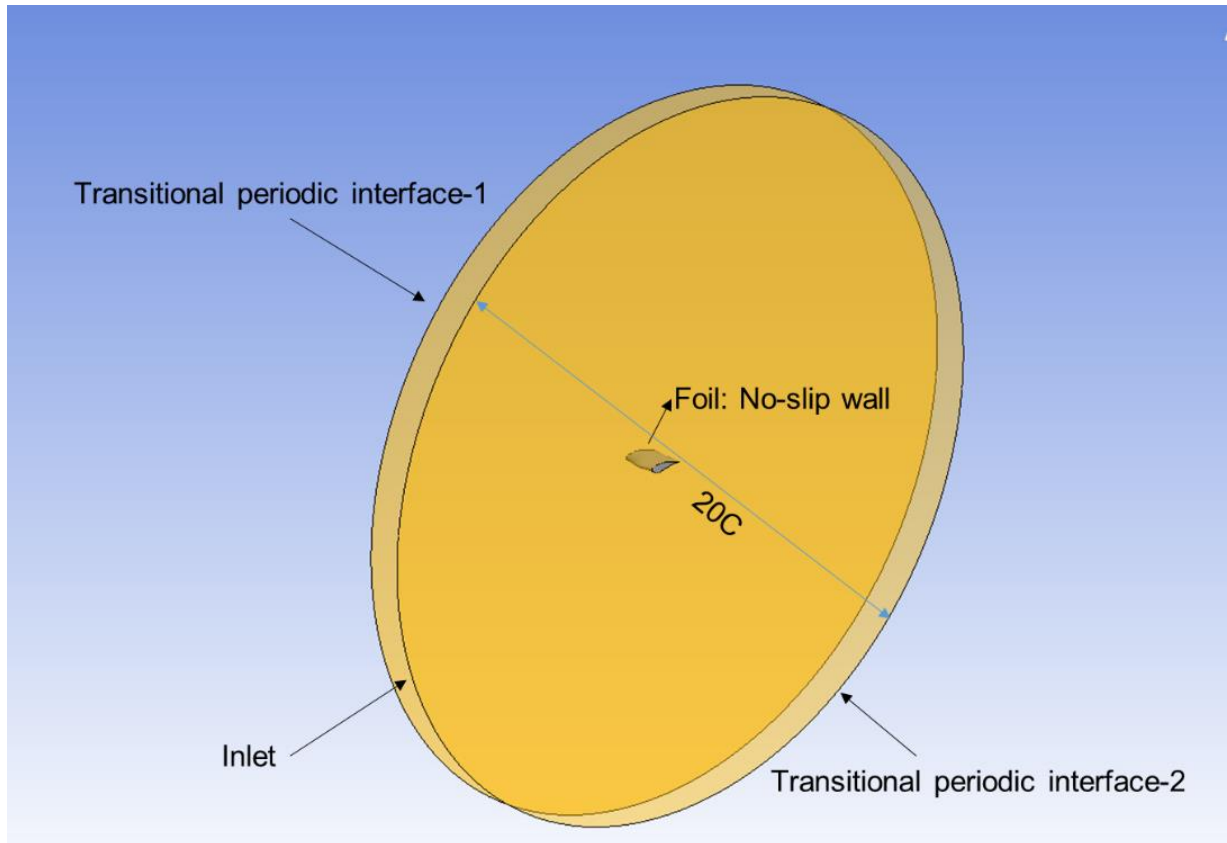


Figure 3-5 Illustration of boundary conditions

The computational domain is a circular zone of which the diameter is set to be 20 times of the foil chord length. The boundary definition has been presented in the Figure 3-5. The outer boundary of the domain is defined as the inlet boundary condition with the function of combining the inlet and outlet. By changing the inflow direction of the inlet, the angle of attack of the foil can be changed. The boundary of the foil section was defined as no-slip wall. For the purpose of simulating the 2D infinite foil, two side boundaries of calculation domain were defined as transitional periodic boundary condition, which treats the flow at transitional periodic interface-1 as though the transitional periodic interface-2 is a direct neighbour. Thus, when calculating the flow through the one periodic boundary adjacent to a fluid cell, the flow conditions at the fluid cell adjacent to the opposite periodic plane are used (ANSYS, 2013). By

using this transitional periodic boundary condition, a section of foil can be treated as if with an infinite span, which is well practiced in 2D foil simulation.

Selection of turbulence models

For flow with large separation, the choice of a turbulence model is very important. Amongst the various CFD models, Large Eddy Simulation (LES) and Detached Eddy Simulation (DES) are recognised to be the solutions for the large separation problems. However, these two models are always regarded as highly time consuming and hardware demanding. Therefore for the optimisation study presented here, a more computationally economical, steady state RANS model was preferred. The industrially acknowledged and recommended K-epsilon and Shear Stress Transport (SST) turbulence models were also investigated in the study (ANSYS, 2013).

Mesh generation

Mesh quality for curved surfaces is another critical issue for CFD simulations. As a first attempt a structured mesh of around 1 million O-type elements was generated by the ANSYS-MESHING module (ANSYS, 2013). The value of the non-dimensional wall parameter, y^+ , was kept as 1 to ensure the required mesh quality within the boundary layer (Menter *et al.*, 2003) and the growth ratio was limited to 1.08. Meanwhile newly developed Solution Adaptive Mesh technology was also used to adapt the mesh automatically based on the flow gradient (ANSYS, 2013). This enabled more effective mesh distribution depending on the requirements.

Figure 3-6 shows the whole mesh and the details of the grid near the foil section before the solution adaptive mesh was processed. However after the process of solution mesh adaption, the number of elements became around 2.5 million or more which depended on the calculation cases. The mesh would be further refined automatically during the simulation itself, as shown in Figure 3-7.

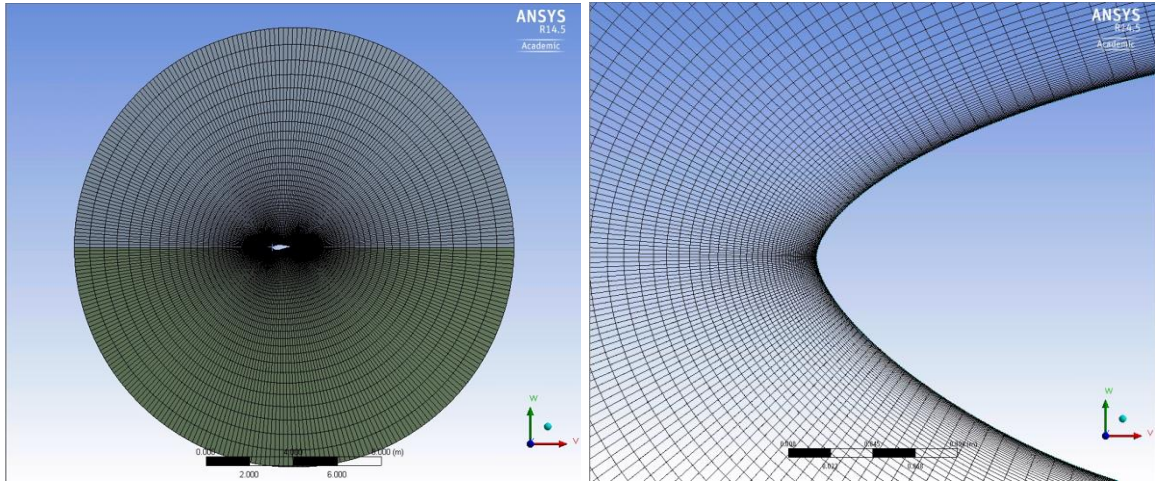


Figure 3-6 Mesh overview (left) and zoom-in view of wing section at the leading edge (right)

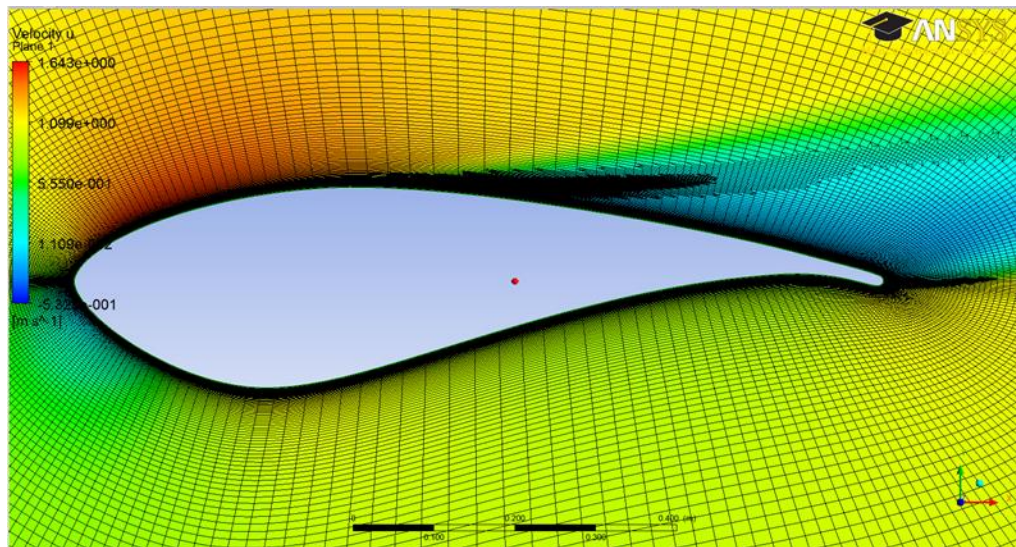


Figure 3-7 Refined mesh by the “solution adaptive mesh” method

Validation of CFD

Figure 3-8 shows the comparison of the CFD predictions with the experimental lift and drag coefficients of the Ohio State University foil. The lift and drag coefficients are defined as given in Equation 3-2 and 3-3, respectively.

$$C_L = \frac{Lift}{\frac{1}{2}\rho V^2 A} \quad \text{Equation 3-2}$$

$$C_D = \frac{Drag}{\frac{1}{2}\rho V^2 A} \quad \text{Equation 3-3}$$

where *Lift* is the lift of the foil which is perpendicular to the incoming flow; *Drag* is the drag of the foil which is aligned with the incoming flow; ρ is the density of the water; V is the inflow velocity; A is the reference area of the foil, which is C (Chord) * W (Wavelength).

The CFD simulations were conducted using both K-epsilon and SST turbulence models. By maintaining the chord length to be constant, the Reynolds number was fixed at 10^6 . As shown in Figure 3-8, both CFD simulations with the two different turbulence models displayed very good agreement with the experiments up to 10 degree of angle of attack (AOA) before the stall occurred. After the stall, the conventional CFD predictions overestimated the lift coefficient especially using the K-epsilon turbulence model. However, once the CFD simulation with the SST turbulence model was combined with the solution adaptive mesh technique (Menter *et al.*, 2003) the prediction for the lift coefficients could be greatly improved, as shown in Figure 3-8(top); similar comparisons are also shown for the drag coefficients (bottom). As shown in Figure 3-8, the predictions with the SST turbulence model combined with the solution adaptive technique show close agreement with the experimental data.

Finally, the comparisons of the CFD predictions with the experimentally measured pressure distribution around the foil in stall condition are shown in Figure 3-9 and Figure 3-10, for two different angles of attack (AOA), both of which again display very good correlations. In these figures pressure coefficient (C_{Pre}) is defined as in Equation 3-4.

$$C_{Pre} = \frac{Pressure}{\frac{1}{2}\rho V^2} \quad \text{Equation 3-4}$$

Based upon the above analysis it was concluded that the SST turbulence model with the solution adaptive mesh has the capability to accurately predict the performance of the foil section and hence it was adopted for the optimisation process which is described next.

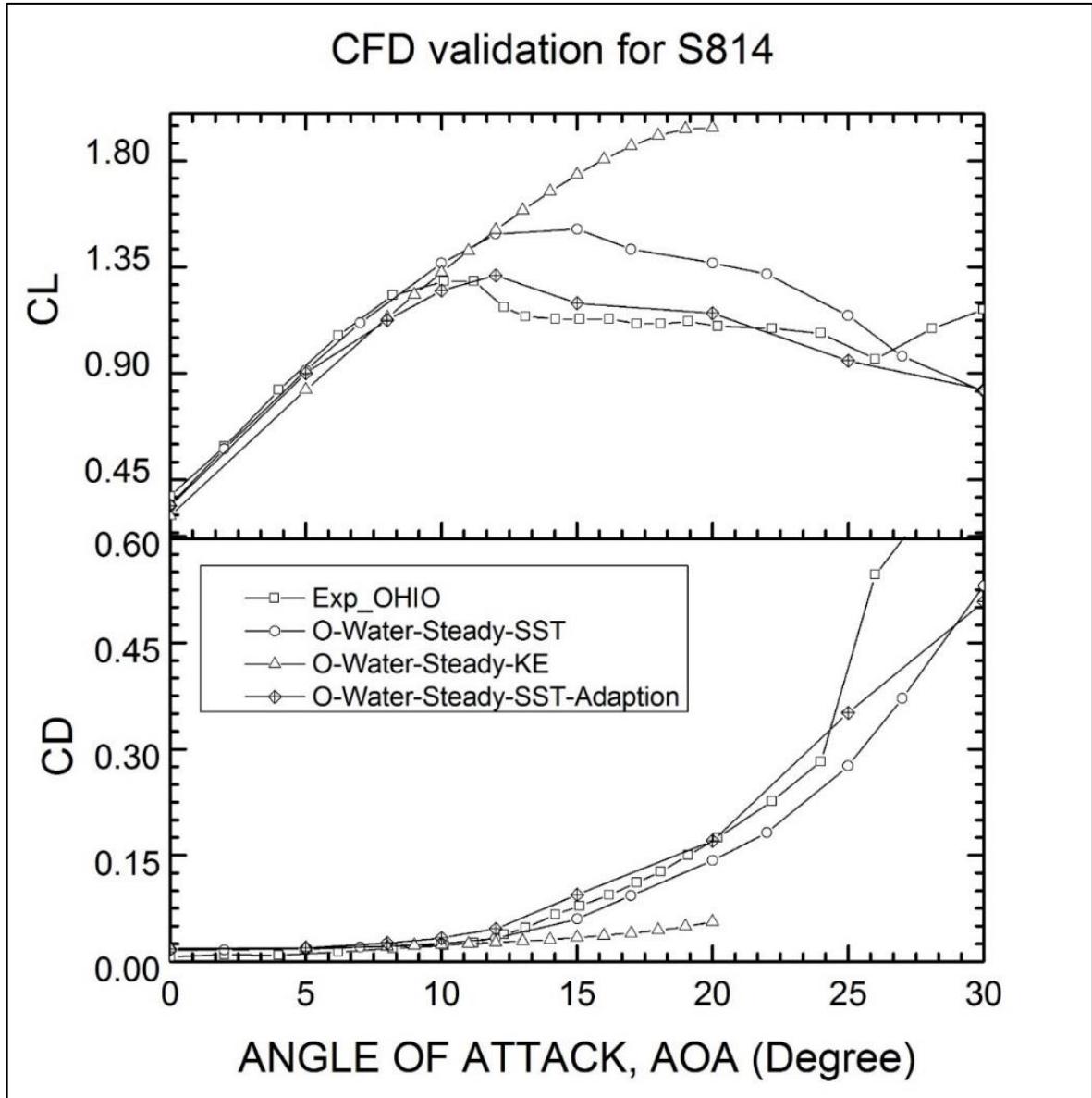


Figure 3-8 Validation for CFD prediction of lift and drag coefficients of S814

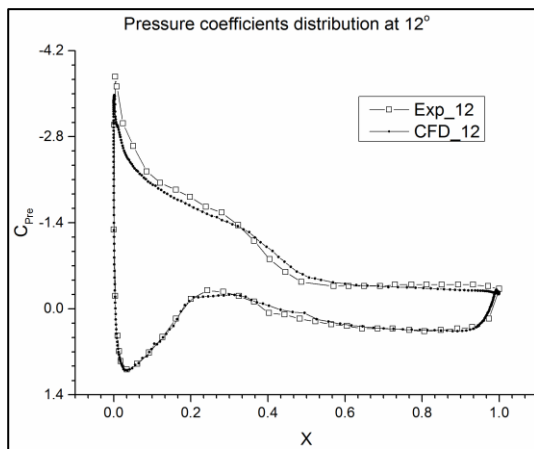


Figure 3-9 Validation for CFD prediction of Pressure coefficient distribution at 12° of angle of attack

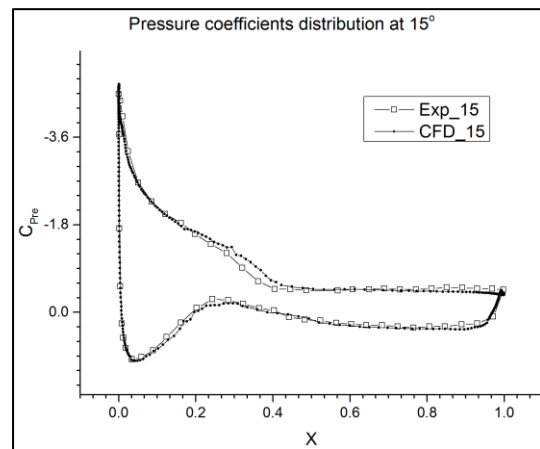


Figure 3-10 Validation for CFD prediction of Pressure coefficient distribution at 15° of angle of attack

3.4 Optimisation and discussion of results

Using the validated CFD model, the lift coefficients of the foil with the S814 profile cross-section and sinusoidal tubercles of differing parameters were simulated. The simulations were focused on the stall conditions, when the AOA was ranging from 8° to 40° . As shown in Figure 3-11 and Figure 3-12, the tubercles on 2D foils maintained higher lift coefficients in the post-stall region ($20^\circ\sim 40^\circ$) while they also reduced the maximum lift coefficient. Increasing the tubercle wavelengths brought the lift coefficients of the foil with the leading-edge tubercles closer to the lift coefficients of the reference or “baseline” foil with the smooth leading edge (i.e. without tubercles). However reducing the wavelengths increased the lift at higher angles of attacks while reducing the maximum value of the lift. By taking into account these trends, the foil having a sinusoidal form of tubercle with the height and wavelength of $H=0.1C$ and $W=0.5C$, respectively, was considered to be a good compromise from the performance point of view and hence was chosen for further analysis to be applied on a 3D foil.

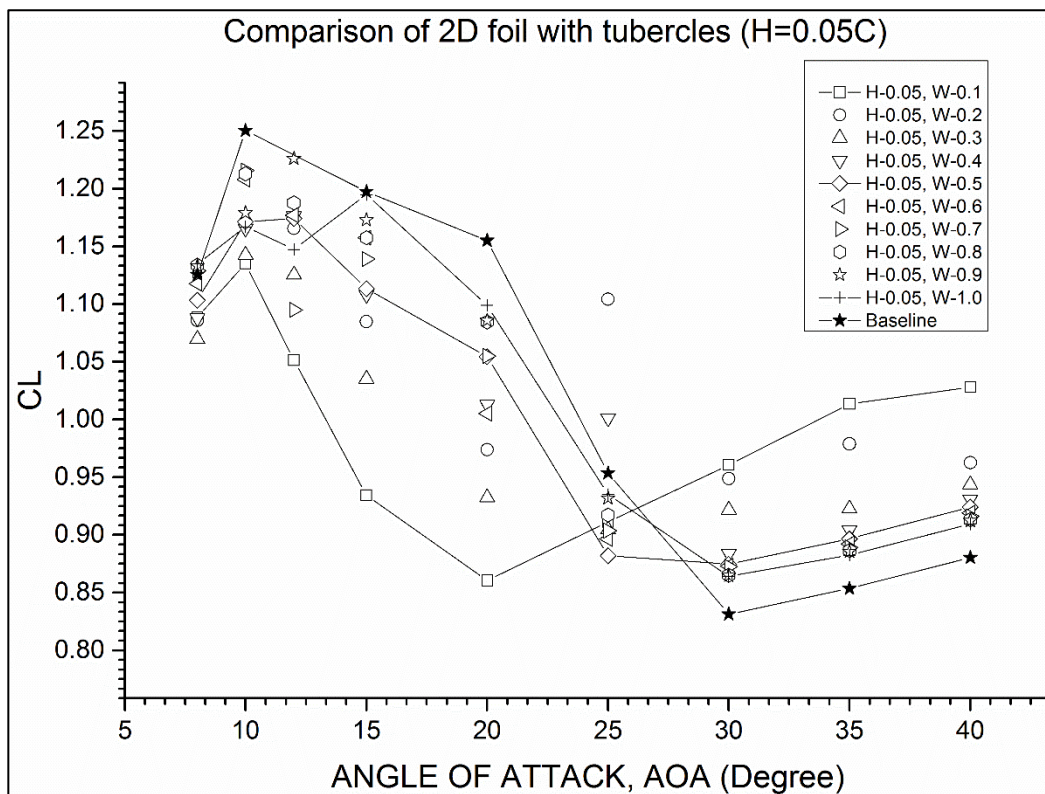


Figure 3-11 Comparison of 2D foil lift coefficients with different tubercle profiles by varying the wavelength (W) at constant tubercle height ($H=0.05C$)

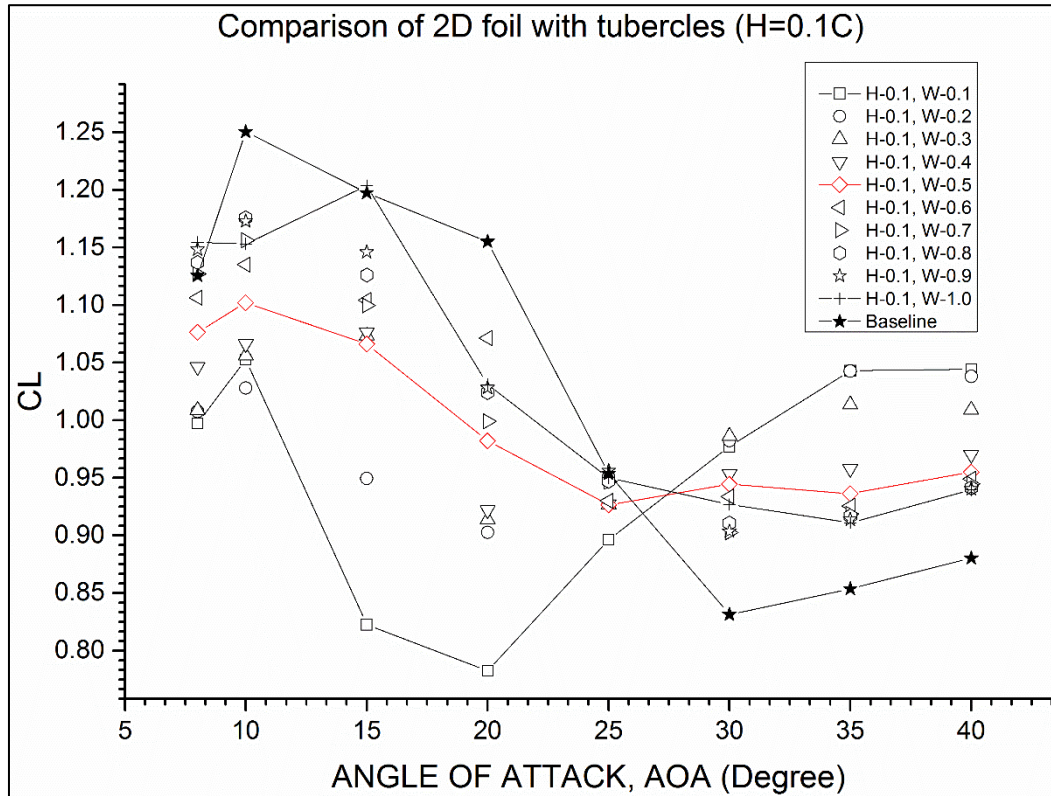


Figure 3-12 Comparison of 2D foil lift coefficients with different tubercle profiles by varying the wavelength (W) at constant tubercle height (H=0.1C)

Post analysis results of the CFD simulations for the case of “Baseline” and that of optimised “H-0.1, W-0.5”, under 15° of angle of attack are shown in Figure 3-13. The velocity iso-surfaces for the case where the velocity is equal to 50% of the incoming velocity, reveal the flow separation patterns and were plotted and coloured base on the pressure distribution. As shown in Figure 3-13 (right), the flow pattern around the foil was favourably affected by the presence of the tubercles as the flow appeared to be more attached to the foil surface following the crest of the tubercles whereas the baseline foil without tubercles displayed separated flow after the leading edge Figure 3-13 (left).

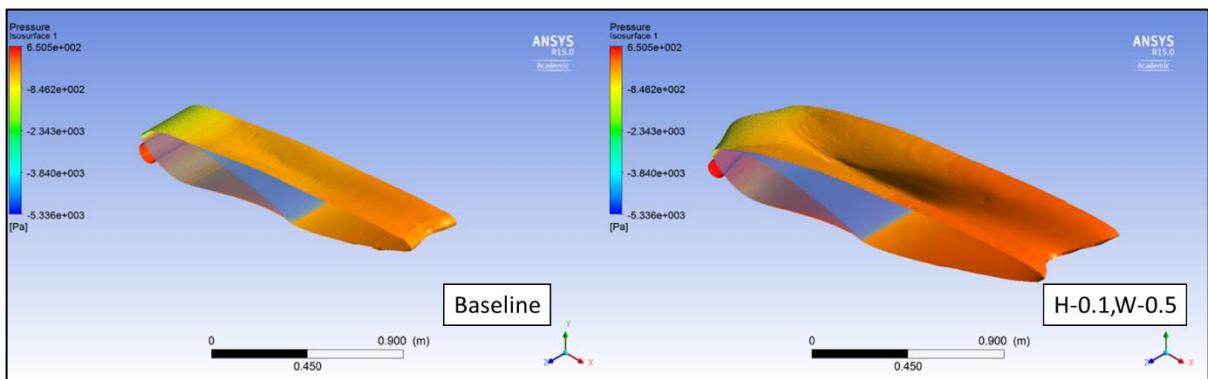


Figure 3-13 Comparison of flow separation at 15° angle of attack (Velocity isosurface at 50% of incoming velocity coloured by pressure distribution)

3.5 Summary

This chapter presented the selection of the profile shape and optimisation for the sinusoidal shape of leading-edge tubercles which were applied on a representative 2D tidal turbine blade with the S814 profile section. The two main tubercle parameters, which are the height and wave length, were optimised in the integrated environment of ANSYS-Workbench CFD tool for the hydrodynamic performance (in terms of lift, drag and flow separation) of the blade. The results of the profile shape selection and optimisation were discussed and following conclusions were drawn:

1. CFD simulation for the flow with great separation is very challenging, but the SST turbulence model with solution adaptive mesh has the capability to accurately predict the hydrodynamic performance of the foil section even under stall conditions.
2. As demonstrated in the optimisation study based on the 2D foil, while the application of leading-edge tubercles could maintain high lift coefficients under post-stall conditions, it could also lower the magnitude of the maximum lift.
3. Based on the optimisation study, a sinusoidal form of leading-edge tubercle profile with $0.1C$ height and $0.5C$ wavelength appeared to be a good compromise among the candidates to be applied on a 3D foil and to be validated by model tests for its performance in the forthcoming chapters of this study.
4. The flow pattern around the foil was favourably affected by the tubercles as the flow was more attached to the foil surface following the crest of the tubercles whereas the baseline foil without tubercles displayed separated flow after the leading edge.

Chapter 4 Experimental and Numerical Investigations of Tubercles Applied on a Simplified Turbine Blade

4.1 Introduction

Having conducted the numerical optimisation of leading-edge tubercles for a 2D foil (with the representative profile section of S814), the next task of the research was to apply the optimum tubercle shapes onto a 3D tidal turbine blade with the same profile section. This Chapter therefore presents the details of this application and discusses the results. In doing so the Chapter provides further understanding of the tubercle concept by conducting fundamental experimental and numerical investigations, as applied to a representative 3D turbine blade.

Following this introduction (Section 4.1), the details of the basis turbine used in this study and its representative 3D blade (hydrofoil) including the selection of the leading edge tubercles are given in Section 4.2. Since the 3D blade was investigated experimentally, Section 4.2 also presents the details of the scaled models of the 3D blade which was tested in the Emerson Cavitation Tunnel (ECT). Section 4.3 presents the details of these experiments which involved the measurement of the lift and drag force characteristics of the 3D blade without and with various combinations of tubercle geometries. Detailed flow observations were also conducted during these tests using the PIV system, as described in Section 4.3. In order to complement the experimental investigations and provide further discussions on the understanding of the tubercle concept application to a turbine blade, a computational fluid dynamics (CFD) investigation was conducted by using commercial RANS software, Star-CCM+, and results are presented and discussed in Section 4.4 in combination with the experimental results. Finally, the overall conclusions obtained from this Chapter are given in Section 4.5.

4.2 3D Blade model and its manufacture

In this section the geometry details of the representative 3D blade, which was tested in the ECT, are given including the details of the tubercle design. As reviewed in Chapter 2, better performance characteristics have been reported based on the previous investigations with the leading-edge tubercles on 3D foils which are usually tip tapered like rudders, stabilizer fins, wings, flippers etc. The investigations with the 3D foils also claim the improvement of the lift coefficient curves by maintaining the lift beyond the stall point which is similar to the effect of tubercles on 2D foils. In addition to this, the performance regarding to the peak lift-to-drag ratio

can be enhanced (Miklosovic *et al.*, 2004; Miklosovic *et al.*, 2007; Stanway, 2008; van Nierop *et al.*, 2008; Weber *et al.*, 2010; Sisinni *et al.*, 2012). A tidal turbine blade is a typical tip tapered 3D foil. The impact of tubercles on tidal turbine blade-type 3D foils, as well as the associated flow mechanisms, are yet to be identified.

The representative 3D foil was based on the blade of the tidal turbine designed by Wang *et al* (Wang *et al.*, 2007b). However, while the foil had the same chord length distribution as the subject tidal turbine blade it had a constant pitch. Based on the limitations imposed by the testing section of the Emerson Cavitation Tunnel, the span of the test foil was specified as 560mm. The chord distribution is given in Table 4-1. The aspect ratio of this hydrofoil is 3.39.

Table 4-1 Chord distribution of the reference foil

Span(mm)	0	70	140	210	280	350	420	490	560
Chord(mm)	225.1	210.08	195.06	180.04	165.02	150	134.98	119.96	104.94

Considering the operating range of the tip speed ratios (TSRs), the range of the angles of attack (AOAs) to be applied on the foil during the tests was specified to be 0° to 40° while the inflow velocities (V) were selected as 2, 3 and 4m/s. Over this inflow velocity range the reference Reynolds number was varied from 0.3×10^6 to 0.6×10^6 and here Re was defined by Equation 4-1. This range was similar to the Re range for the turbine model that was tested by Wang *et al* (Wang *et al.*, 2007b).

$$Re = \frac{VL}{\nu} \quad \text{Equation 4-1}$$

where ν is the kinematic viscosity, m^2/s and L the chord length (L , 150mm) of the foil at the spanwise position of 350mm which corresponds to $0.7r$ of the turbine blade.

According to the optimisation results for the 2D foil, the foil with the tubercles would display the best performance when the height (H) and wavelength (W) of the tubercles were $0.1C$ and $0.5C$, respectively. With the wavelength (W) of the tubercles were set to be $0.5C$, approximately 8 sinusoidal tubercles with successive crests and troughs were evenly distributed along the leading edge. For the design of interchangeable leading edge module, the wavelength of tubercle is set to be 70mm. The leading-edge profile is defined as in Equation 4-2 and shown in Figure 4-1.

$$h = \frac{0.1C}{2} \cos \left[\frac{2\pi}{70} s - \pi \right] + \frac{0.1C}{2} \quad \text{Equation 4-2}$$

where h is the local height of the leading-edge profile relative to the reference blade which has the smooth leading-edge profile, in mm; s is the spanwise position, in mm; C is the local chord length, in mm.

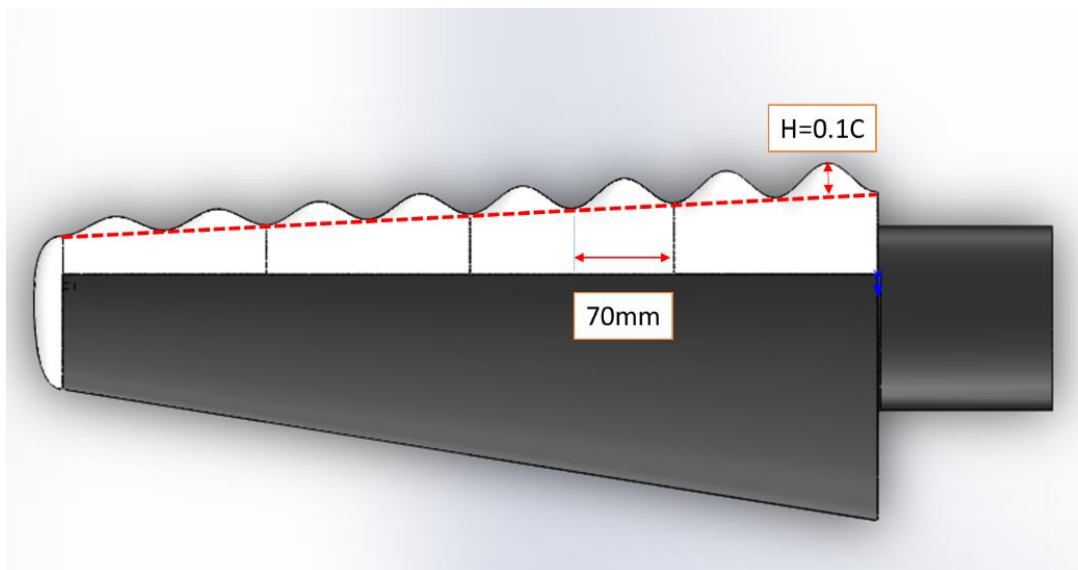


Figure 4-1 Leading-edge profile of 3D hydrofoil with tubercles

Based on the above arrangement, the 3D foil was manufactured in two separate parts and then assembled. The first part was the interchangeable (or removable) leading-edge part of the foil while the second part was the remainder (i.e. main body) of the foil that also supported the whole foil structure. The interchangeable leading-edge was printed using a 3D printer in four segmented pieces from a liquid resin material, Stratasys Vero White Plus RGD835.

As reviewed in Chapter 2, an attempt was made recently to apply the tubercle concept to tidal turbine blades and scaled turbine models with different tubercle designs were tested in a towing tank (Gruber *et al.*, 2011). The blade with only a 1/3 of the span covered with tubercles displayed the best performance amongst the different ranges of the tubercle extensions over the blade span. Therefore what the optimum coverage of the tubercle leading edge is also a question to be resolved.

The interchangeable and segmented manufacture of the leading-edge profiles provided very useful flexibility for testing the different leading-edge arrangements as well as overcoming the size limitation of the 3D printer. The main body of the foil was milled by CNC machine from a carbon fibre reinforced plastic (CFRP) to ensure that the structure would be strong enough and the deformation would be minimal. All of the models with various combinations of leading edge profiles are shown in Figure 4-2.

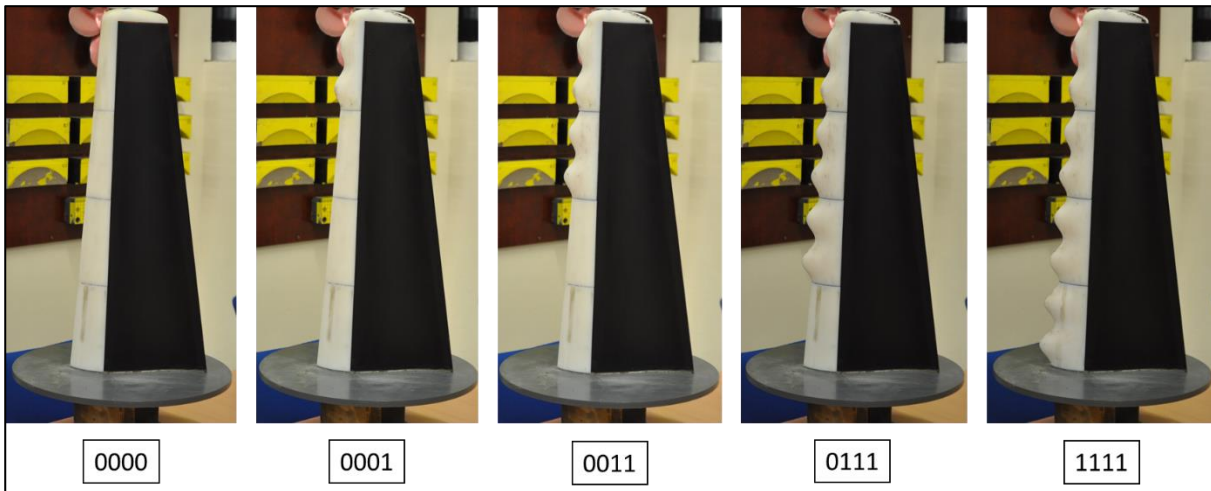


Figure 4-2 Tested 3D hydrofoil models with interchangeable leading-edge parts

The main foil with five different leading-edge combinations, one of which was the smooth leading edge, were tested and corresponding hydrodynamic performances were compared to explore the effect of the four different tubercle arrangements on the foil performance. In order to classify the different leading-edge tubercle combinations, the reference foil with the smooth leading-edge section is represented by legend “0000” while the foil with the leading-edge tubercles covering the whole span was represented by “1111”. Other leading-edge combinations with partial tubercle applications are represented using legend “0001”, “0011” and “0111” for the 1/4, 1/2 and 3/4 coverage of the foil span by the tubercles from tip to root, respectively, as shown in Figure 4-2.

During the test, no turbulence trips, like sand grit, trip wire and so on, have been applied to the models to accelerate the flow transition from laminar flow to turbulent flow. This is due to the following reasons: first, the turbulence trips need to be applied on the leading edge where the tubercles locate, which will bring another factor and make tubercle effect indistinctive; second, the application of turbulence trips on the leading-edge tubercles, i.e. the thickness, the width, the location and other practical details which might bring further uncertainties, needs careful

investigations. For the future study, turbulence trips can be studied with special attentions to guarantee the application of turbulence trips do not influence the effect of these tested devices.

4.3 Experimental investigation of 3D blade with the optimised tubercles

4.3.1 Experimental setup

The experiments were conducted in the Emerson Cavitation Tunnel (ECT) at Newcastle University. The tunnel is a medium size propeller cavitation tunnel with a measuring section of 1219mm×806mm (width × height), as shown in Figure 4-3. The speed of the tunnel inflow varies between 0.5 to 8 m/s and the water temperature is around 12 degree Celsius. Full details of the ECT and its further specifications can be found in (Atlar, 2011).

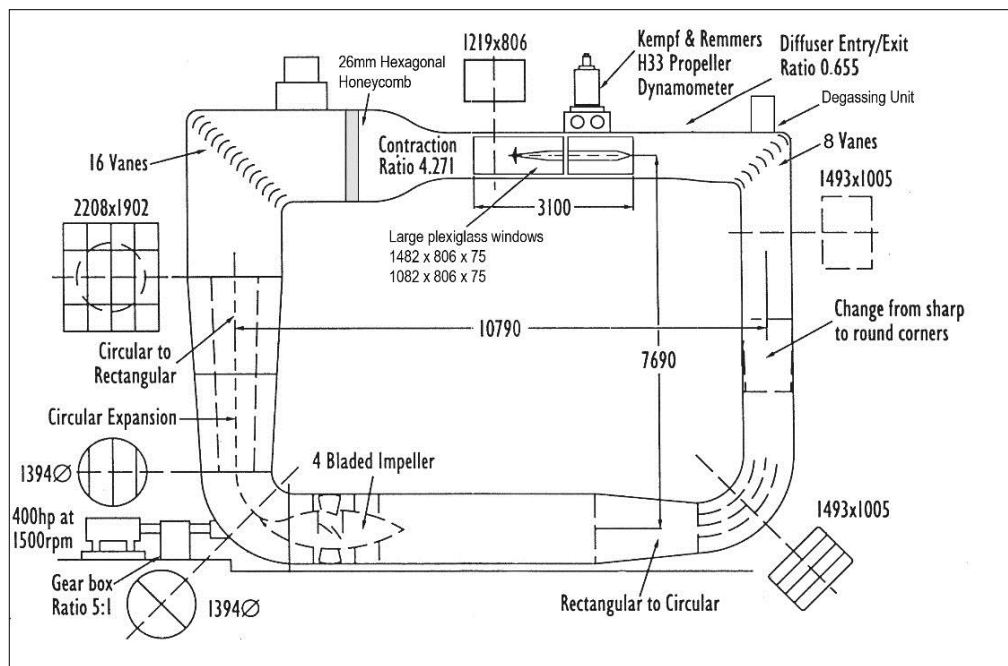


Figure 4-3 Sketch of the Emerson Cavitation Tunnel (Atlar, 2011)

4.3.1.1 Force measurements

The lift and drag performance of the test foil was the primary interest during the experiments as in many foil investigations. During the tests, the forces (X, Y) acting on the foil, which was suspended vertically from the upper lid in the mid-plane of the tunnel measuring section, were measured using a 3-component balance device. This device was a Cussons R102 balance which was specially designed and manufactured for the ECT to be mounted on the top lid of the tunnel using a height and angle adjustment mechanism. The test foil was mounted to the bottom plate of the 3-component balance to transfer the forces to the 3 load cells and a circular plate was

fitted at the root of the blade to prevent the tunnel inflow entering into the cavity, where the balance was housed, as shown in Figure 4-4.

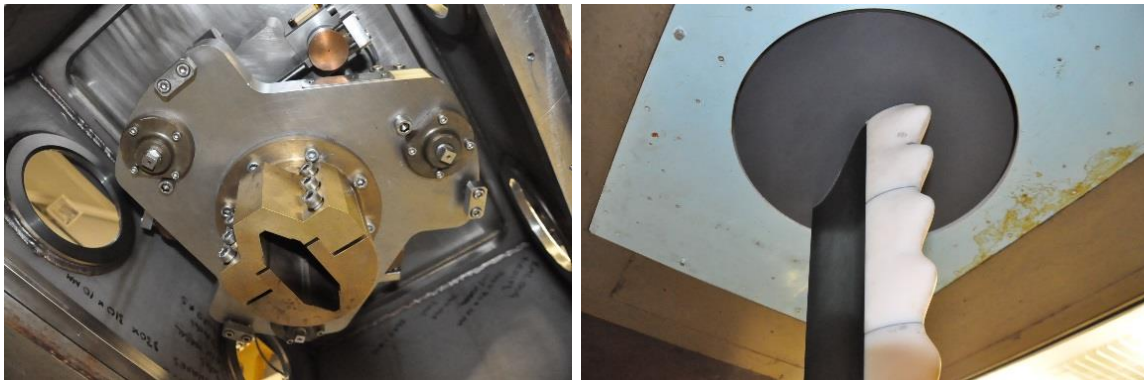


Figure 4-4 Setup of 3-component balance (Cussons R102) on the upper lid (Left) and setup of tested foil mounted on the 3-component balance (right)

The measured lift and drag forces were represented by the following non-dimensional coefficients: C_L and C_D with the reference area (A) of the foil equal to the foil projected area 0.0924 m^2 (resulted in 8.8% blockage ratio). All the measured data was gathered by a National Instruments data acquisition system and analysed instantaneously by LabVIEW. For each measurement point, 500,000 samples were acquired at a 1 kHz sample rate and averaged to calculate the mean value.

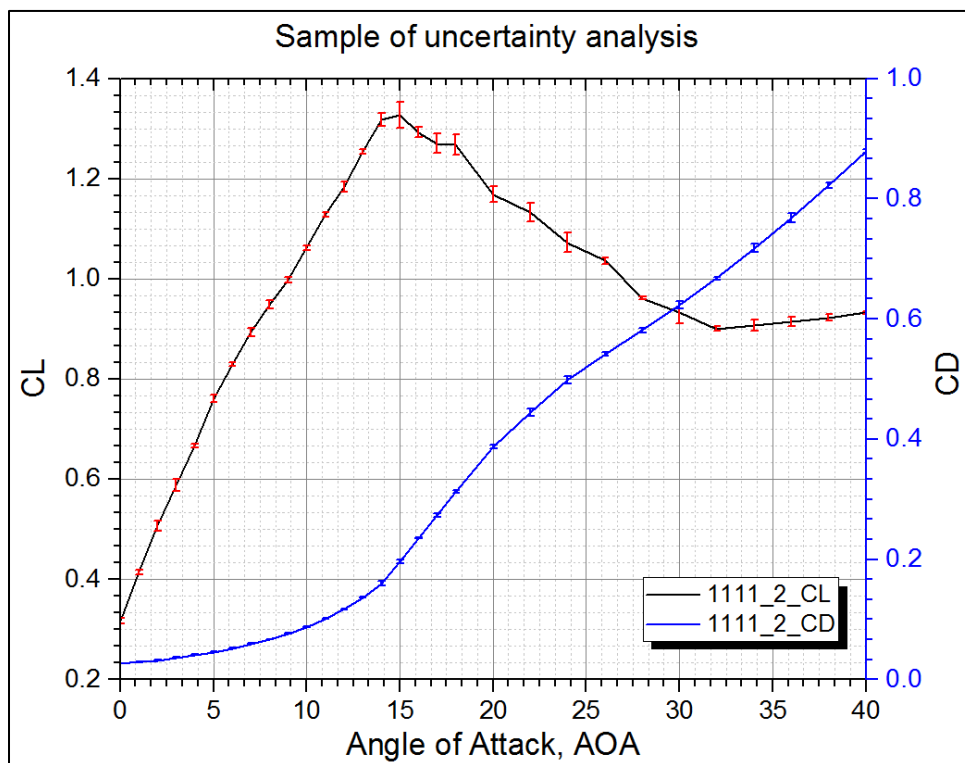


Figure 4-5 Sample of uncertainty analysis results applied on the measured lift and drag coefficients

During the experiments, each test run was repeated three times for uncertainty analysis to guarantee the repeatability. The average results and standard deviation were then plotted and compared. The maximum errors of C_L and C_D were 2.3% and 3.1%, respectively, with mean values of standard deviation of 1.1% and 1.0%, respectively. One example of the uncertainty analysis is presented in Figure 4-5.

4.3.1.2 Flow visualisations

In order to measure and analyse the flow field around the foil, a 2D particle image velocimetry (PIV) system was used, while some still photo images were also taken. The detailed technical specification of the PIV system used, which was a Dantec Dynamics Ltd product, is shown in Table 4-2. During the use of this system, the flow field was illuminated by the planar laser light sheet which was perpendicular to the hydrofoil and highly seeded flow field images were captured by the double framing high-speed CCD camera at a frequency of 500Hz and 0.0004s time interval. Throughout the measurements, a common practice in ECT was followed, according to which 100 double frame image pairs were captured, analysed and averaged to achieve a time-averaged velocity distribution. The adaptive PIV analysis was used for the 2D images from each camera with a grid size of 16x16 pixels. Afterwards, the results of these 100 velocity samples were averaged to achieve the final results.

Table 4-2 Specifications of Dantec Dynamics Stereo PIV (Particle Image Velocimetry) system

Laser	NewWave Pegasus
Wavelength	527nm
Repetition rate per head	1-10K Hz; 2-20K Hz
Energy –Dual Cavity System	10 mJ @ 2000 Hz
Light sheet optics	80x70 high power Nd:YAG light sheet series
Synchronizer	NI PCI-6601 timer board
Camera	NanoSense MK III
Sensor size	1280x1024 pixels
Maximum capture frequency	1000Hz
Maximum images	3300
Seeding particles	Talisman 30 white 110 plastic powder

4.3.2 Force measurement results and discussion

4.3.2.1 Reynolds number effect

First of all, based on the above test set-up, the reference foil “0000” was tested at 2, 3 and 4m/s tunnel velocity to demonstrate the effect of Reynolds number (Re). Because of the practical limitations of the testing facility, a typical full-scale Re range for a tidal turbine, which often ranges from 10×10^6 to 30×10^6 based on the chord length at 0.7 radius, could not easily be met within the model scale test. In the current tests, the Re range was varied from 0.3×10^6 to 0.6×10^6 where the Re was described based on the reference chord length of 150mm at 0.7 radius. It is important that the Reynolds number effect has to be checked prior to any flow tests and certain precautions must be taken to improve the circumstances for very low Re cases.

Figure 4-6 shows the measured lift, drag and lift-to-drag ratio of the reference foil (i.e. Foil 0000) which are represented in terms of the associated coefficients as described in Section 3.2. In this figure the last character with an underscore bar in the legend refers to the tunnel incoming velocity (e.g. 0000_2, where the tunnel velocity is 2 m/s). As shown in Figure 4-6 within the range of the Reynolds numbers tested, the slope and maximum value of lift coefficients decrease gradually with increasing Re. On the other hand, the drag coefficients are nearly identical for different values of Reynolds number. Thus, the lift-to-drag ratios of the reference foil with the smooth leading-edge are reduced with increasing Reynolds number.

On the other hand, the lift coefficient curves of the reference foil present a small hump at around 22° angle of attack under 3m/s and 4m/s while no such a phenomenon has been observed during 2m/s. The test has been repeated numbers of times to confirm the existence of this phenomenon, of which the answer is affirmative. This phenomenon might be because of that flow separation occurred initially after the stall AOA; with the increase of AOAs the turbulent flow reattached to the foil surface which raised the lift coefficients; eventually the flow totally separated from the foil surface. This process can be caused by the flow transition from laminar flow to turbulent flow interact with the flow separation at these specific Reynolds numbers.

The tests conducted for the reference foil (Foil “0000”) were repeated for Foil “1111” which had full leading-edge tubercles and the results are presented in Figure 4-7. As shown in Figure 4-7, unlike in the reference foil case, the lift coefficient of the foil with the leading-edge tubercles increases with the Reynolds number, particularly after a 14° angle of attack (AOA) for 2m/s and 3m/s flow speed. A large gap can be seen between the lift coefficients for 2m/s

and 3m/s. There seemed to be a trend suggesting that the lift-to-drag ratio can be enhanced with increasing Reynolds number and hence the foil with the leading-edge tubercles may have a better performance at a higher range of Reynolds number.

Reynolds number effect on "0000"

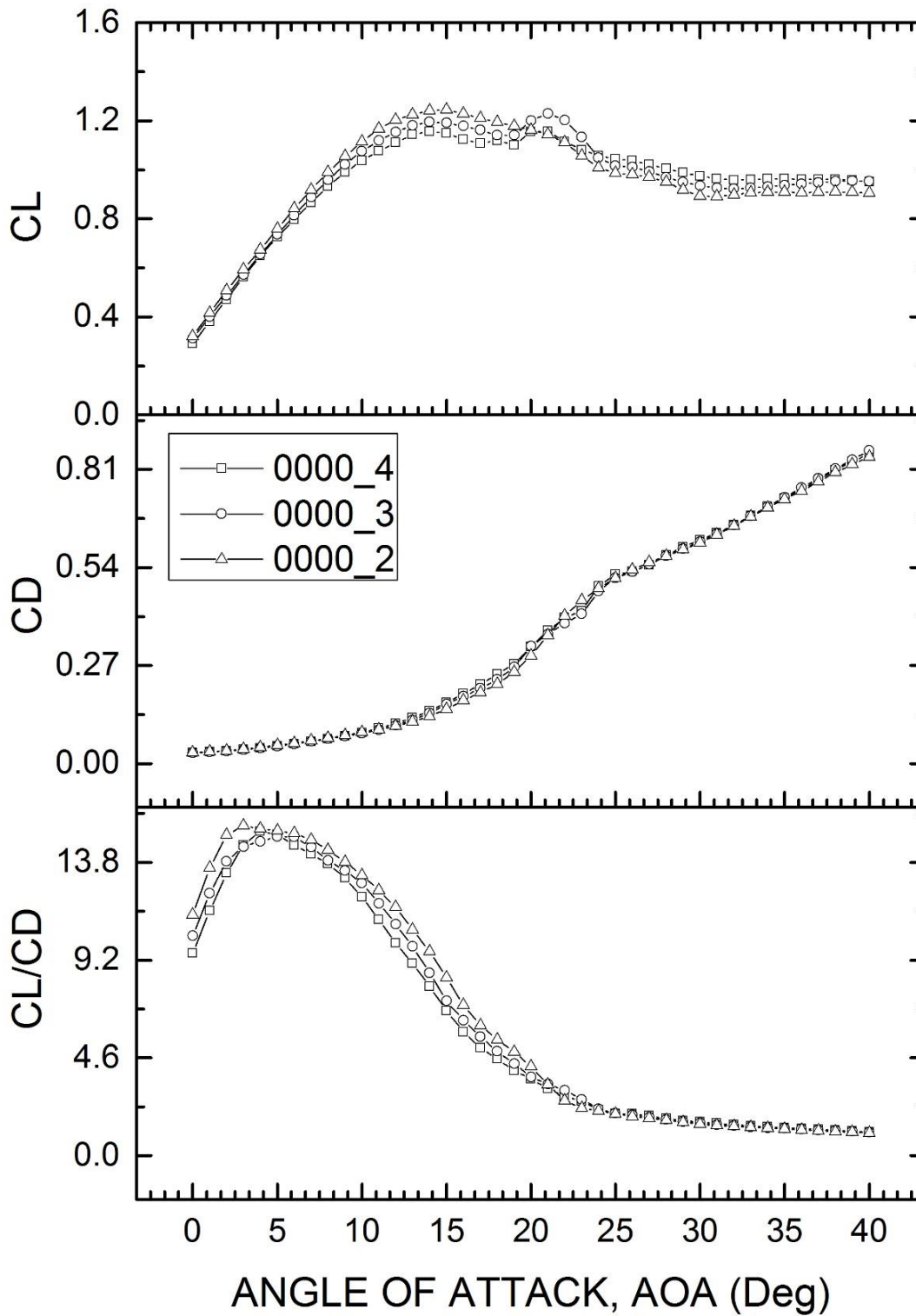


Figure 4-6 Experimental data for Foil "0000" with smooth leading edge at different incoming velocities

Reynolds number effect on "1111"

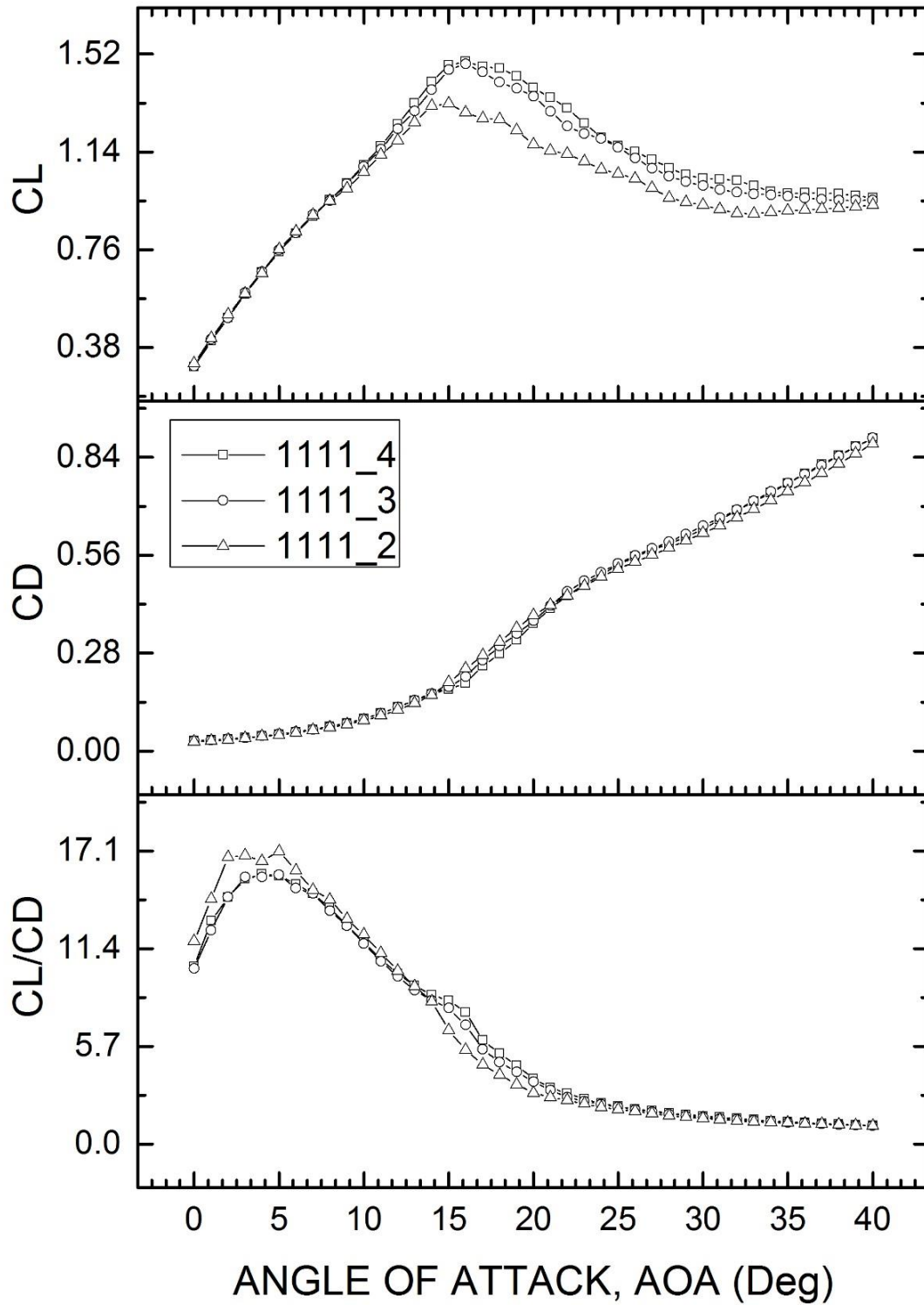


Figure 4-7 Experimental data for Foil "1111" with leading-edge tubercles at different incoming velocities

4.3.2.2 Performance Comparison between the Foils with and without Tubercles

From Figure 4-8 to Figure 4-10, it shows the comparison of the lift and drag performances for the reference foil (Foil “0000”) and its counterpart (Foil “1111”) with a full set of leading-edge tubercles, as inflow velocity varying from 2m/s to 4m/s. Reynolds number poses a significant impact on the tubercle effect. With the increasing Reynolds number, the tubercle effect is more obvious than itself under 2m/s, $Re=0.3 \times 10^6$. However as observed in Figure 4-6 and Figure 4-7, the opposite trend against the changing Re can be noticed. Therefore with the increasing velocity, the tubercle effect is getting more significant.

Therefore, Figure 4-10 clearly shows the beneficial effect of the tubercles on the lift coefficients and hence on the lift-to-drag ratios. It is interesting to note in Figure 4-10 that the lift coefficients of both foils are almost identical up to an AOA of 10-11° after which Foil “1111” can maintain a linear growth until 16° AOA while Foil “0000” cannot.

Figure 4-11 has demonstrated the comparison of lift-to-drag ratios under these three different velocities and hence Re numbers. From AOA=0° to AOA=8° while both models were performing linear increase in the lift coefficients, leading-edge tubercle demonstrates enhanced lift-to-drag ratio with generally 5-10% increment. The peak lift-to-drag ratio of Foil “1111” also shows a higher value. After the reference foil stalled after 9° AOA, tubercle operating at a higher Re number can improve lift-to-drag ratio for the foil and eventually results in a 32% increase at 4m/s at 16°. But the one at lower Re number, i.e. at 2m/s can’t improve the lift-to-drag ratio, as the increase in lift coefficients cannot surpass the increase in drag coefficients. As it was observed in Figure 4-7, there is a step change between the performances at 2m/s and 3m/s, which might be caused by the variation of flow transition point from laminar flow to turbulent flow. This recalls the use of turbulence trips in the future to directly trip the flow to be fully turbulent.

Comparison between "1111" and "0000"

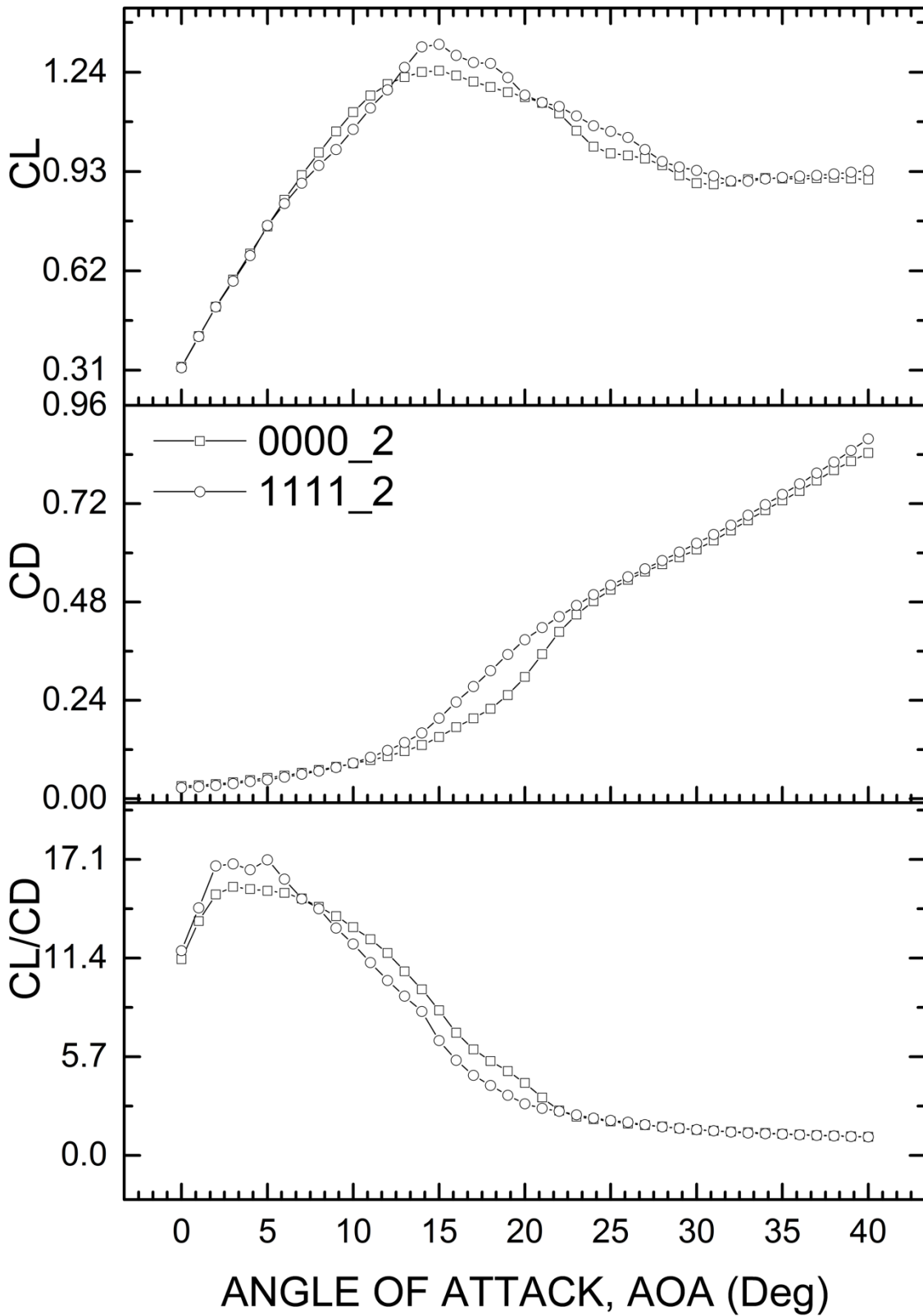


Figure 4-8 Comparison of experimental data for Foil "0000" and Foil "1111" at 2m/s

Comparison between "1111" and "0000"

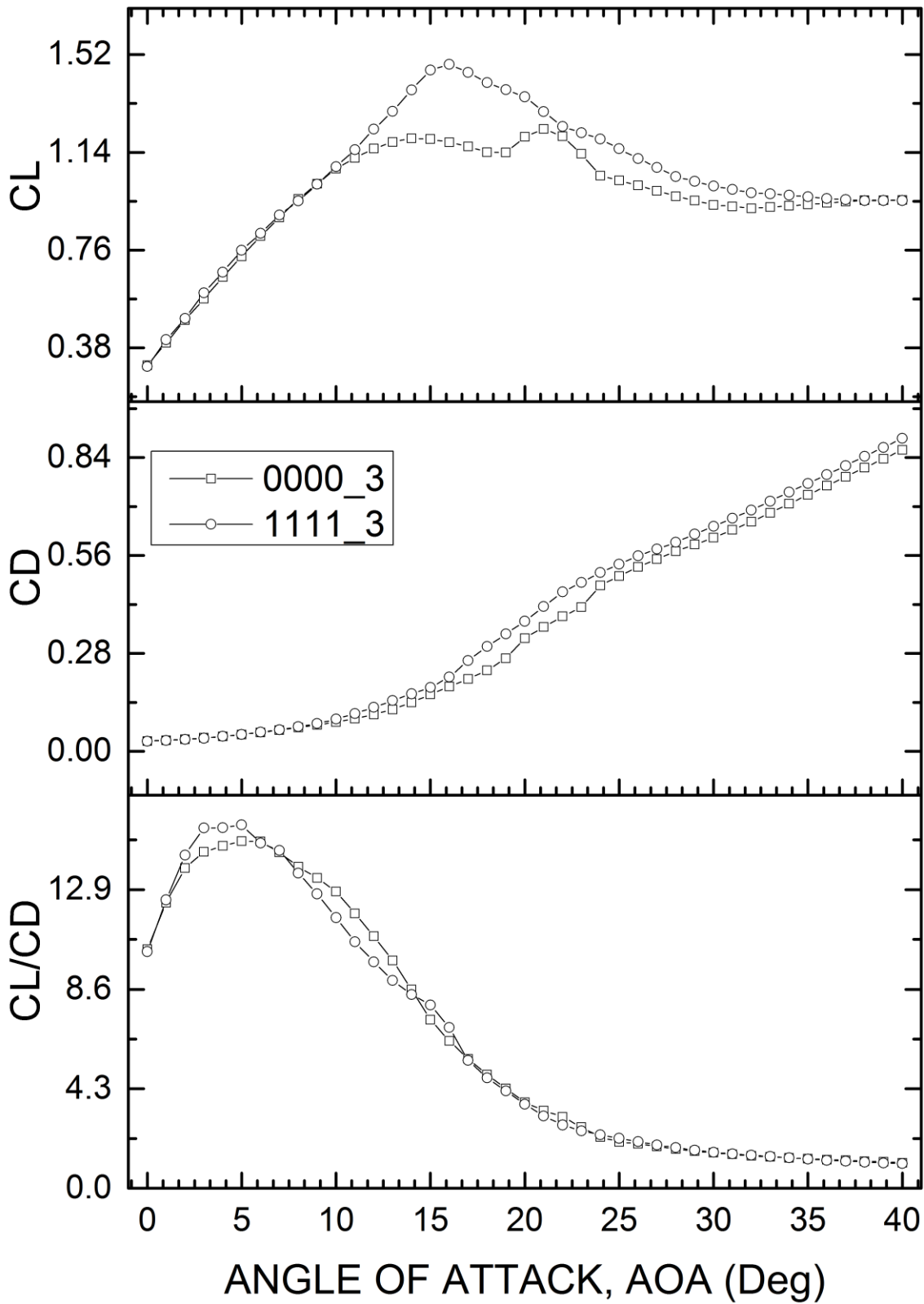


Figure 4-9 Comparison of experimental data for Foil "0000" and Foil "1111" at 3m/s

Comparison between "1111" and "0000"

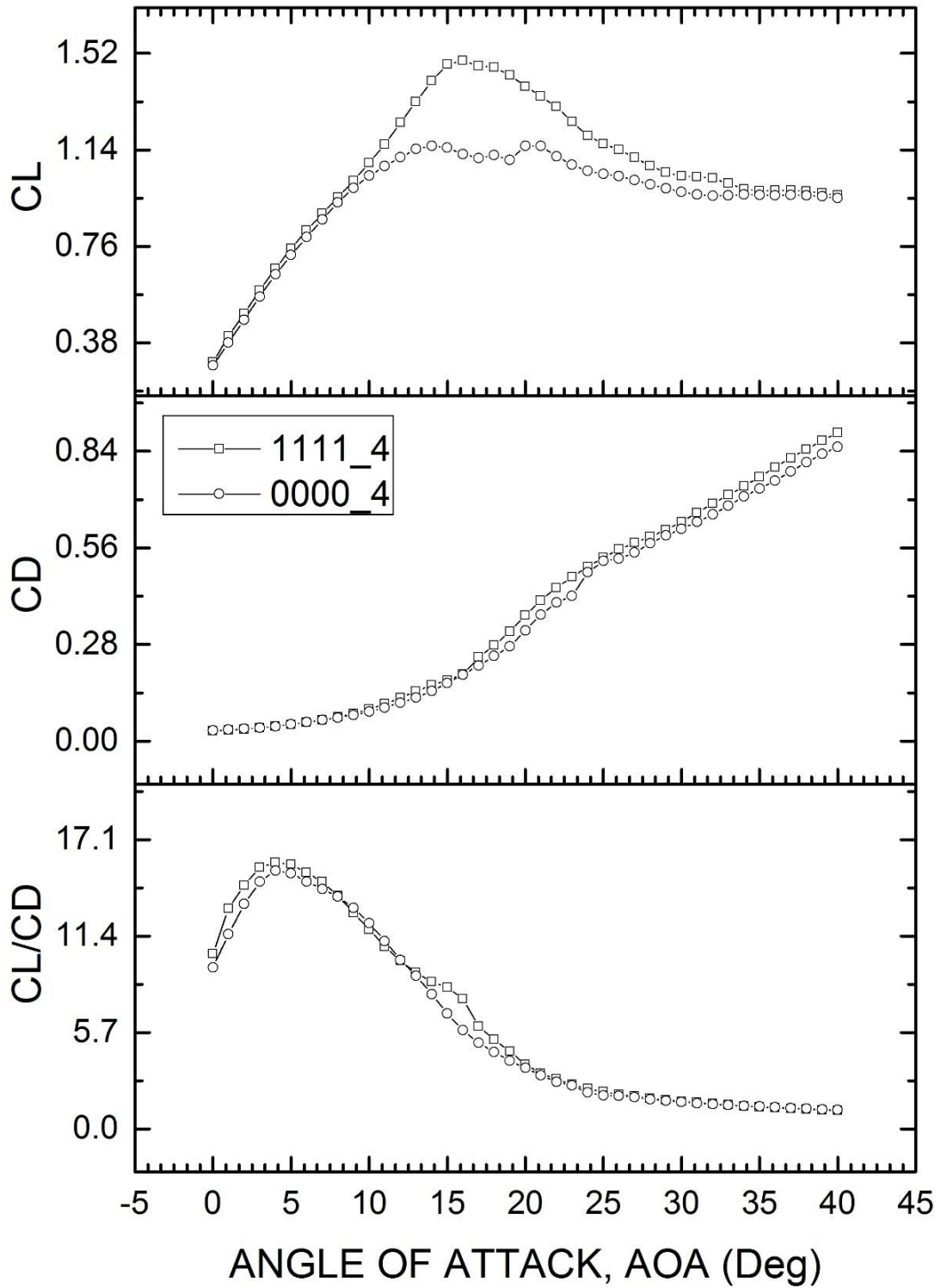


Figure 4-10 Comparison of experimental data for Foil "0000" and Foil "1111" at 4m/s

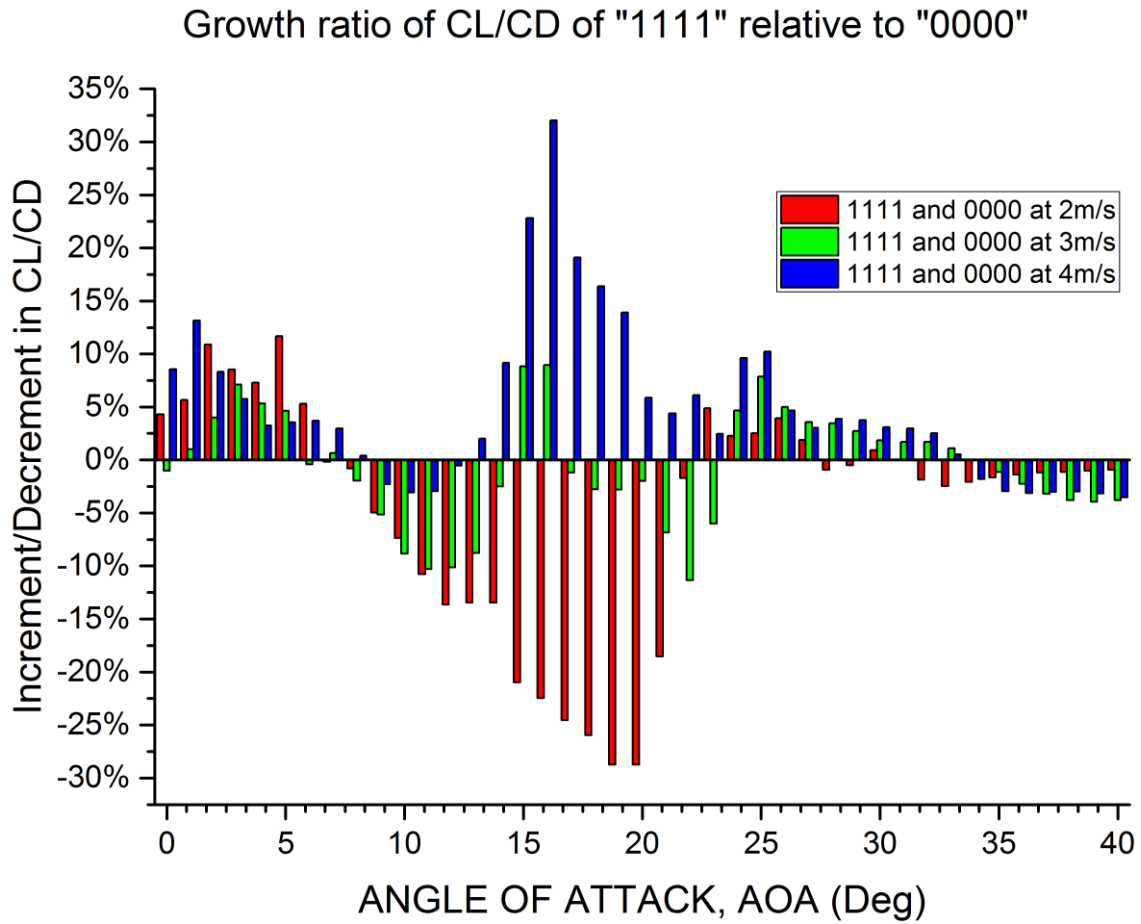


Figure 4-11 Growth ratio of C_L/C_D for Foil "1111" (with leading-edge tubercles) relative to Foil "0000" (with smooth leading edge)

4.3.2.3 Performance Tests with Different Tubercle Coverage Arrangements

Although the beneficial effect of leading-edge tubercles covering the whole span of the foil has been confirmed in the previous section, it has been reported in other research that this effect may vary depending on the position and extent of the tubercle coverage relative to the foil span (Gruber *et al.*, 2011). Therefore 3 different tubercle coverage arrangements, which were Foil “0001”, “0011”, “0111”, were tested to identify the optimum arrangement. Five sets of tests, which also included the reference foil (“0000”) and the foil with full coverage of tubercles (“1111”), were conducted at 3m/s and the results were compared, as shown in Figure 4-12 to Figure 4-14.

From the plots of the lift coefficients, it can be seen that the peak lift coefficient tends to increase with the extent of the tubercles. As shown in Figure 4-12, Foil “1111”, demonstrates the highest lift with a value of 1.48 at 16° AOA. Nevertheless this arrangement also displays the highest drag at the corresponding conditions.

Based on the comparisons of the lift-to-drag ratios of the tested arrangements, it appears that Foil “0001”, which had 1/4 of its leading-edge covered with tubercles, displayed an overall better performance. This can be clearly seen in Figure 4-13 and Figure 4-14 where Foil “0001” shows a positive impact from 0° to 26° AOA with more than 10% enhancement in the maximum lift-to-drag ratio at 5° AOA, compared to the reference (Foil “0000”). With Foil “1111” at 4m/s displayed the highest growth rate at 16° AOA, Foil “0001” may also offer the potential in improving the performance of a tidal turbine operating over a wider range of tip speed ratios. Therefore, these two designs were chosen for the following application on the tidal turbine blades.

Comparison of different configurations

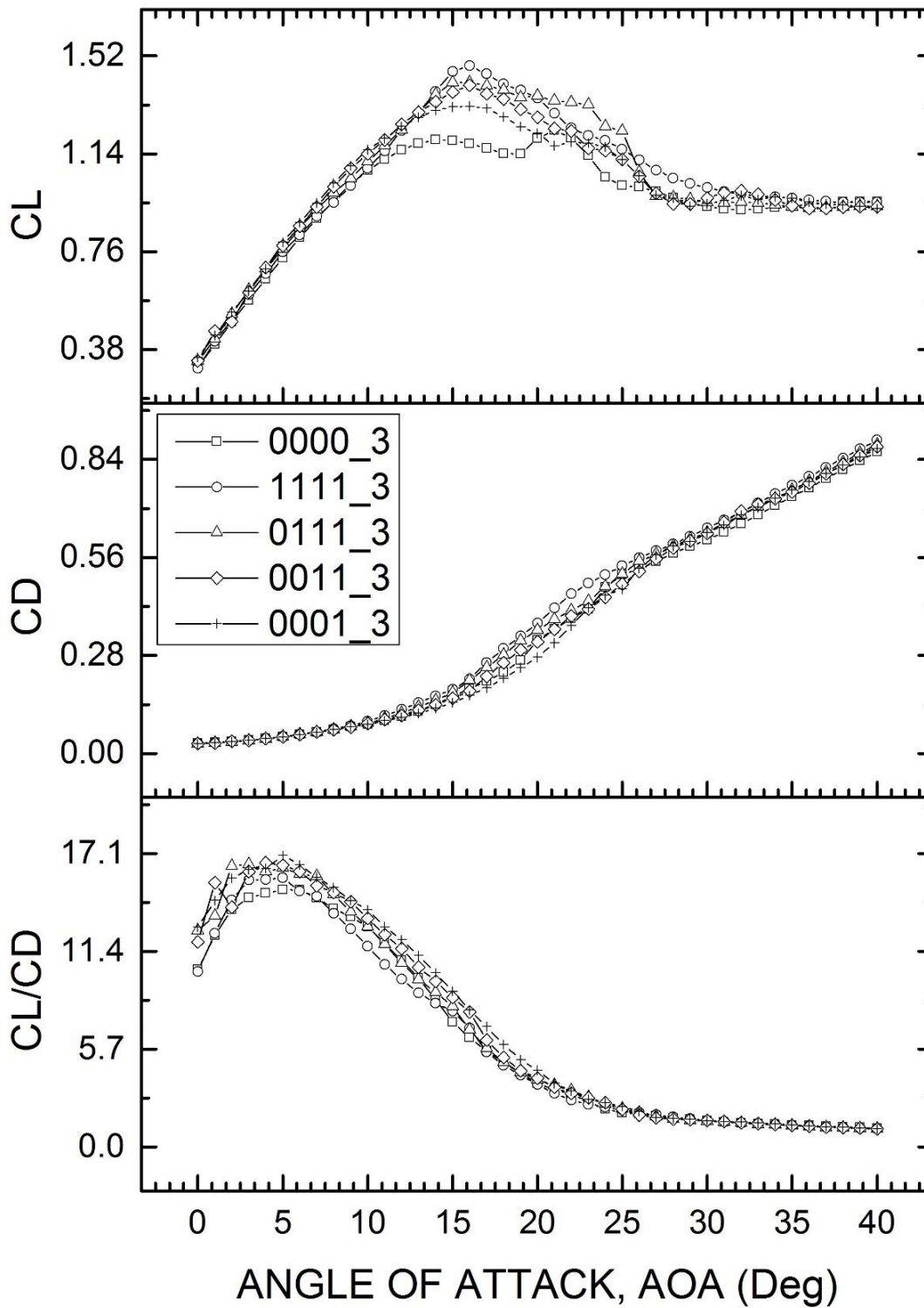


Figure 4-12 Comparison of experimental data for different leading-edge tubercle coverage arrangements

Comparison of "0000" and "0001"

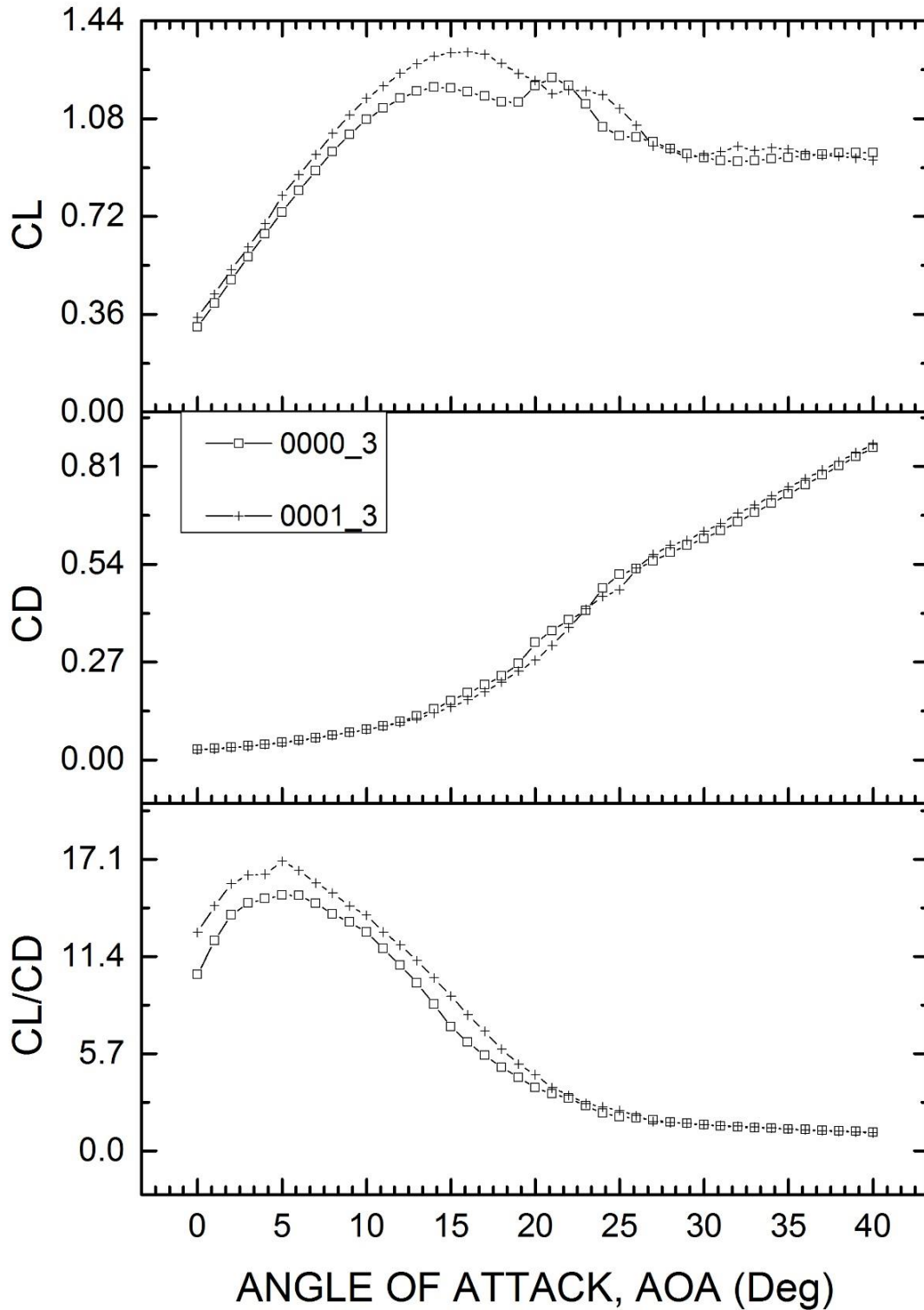


Figure 4-13 Comparison of experimental data for foil with minimum leading-edge tubercle coverage ("0001") and for the reference foil ("0000") at 3m/s.

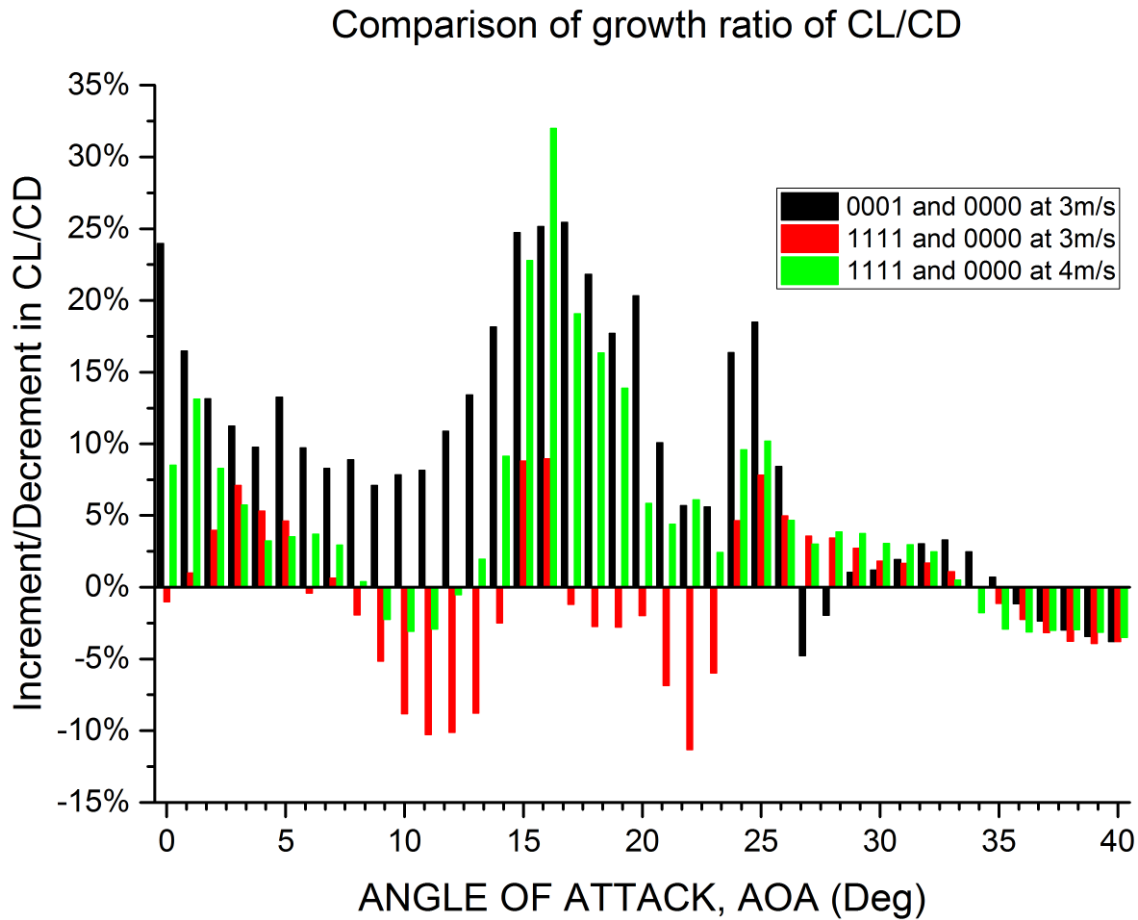


Figure 4-14 Comparison of relative growth ratios for C_L/C_D for Foil “1111” (with leading-edge tubercles applied on whole span) and Foil “0001” (with minimum leading-edge tubercles applied around the tip)

4.3.3 Flow visualisation results and discussion

4.3.3.1 Mapping the Flow Separation Region

Flow visualisation tests with Foil “0000” and Foil “1111” were performed at a 3 m/s tunnel inflow speed and at AOAs of 16° and 24°. With 16° angle of attack, the most significant performance difference has been observed in the force measurement; meanwhile when the AOA reached to 24°, the influence has almost disappeared. Therefore, for these conditions, the flow fields across three selected sections along the foil span were visualised using the PIV device. Limited by the setup, the locations of the selected sections are focusing on one tubercles shown in Figure 4-15 for Foil “1111” and these positions were repeated for Foil “0000”. For each test condition, 100 pairs of PIV images were analysed and averaged to achieve the time-averaged data. The images of the flow fields and associated velocity vectors at the three selected sections are shown in Table 4-3 and Table 4-4 for the AOA of 16° and 24°, respectively.

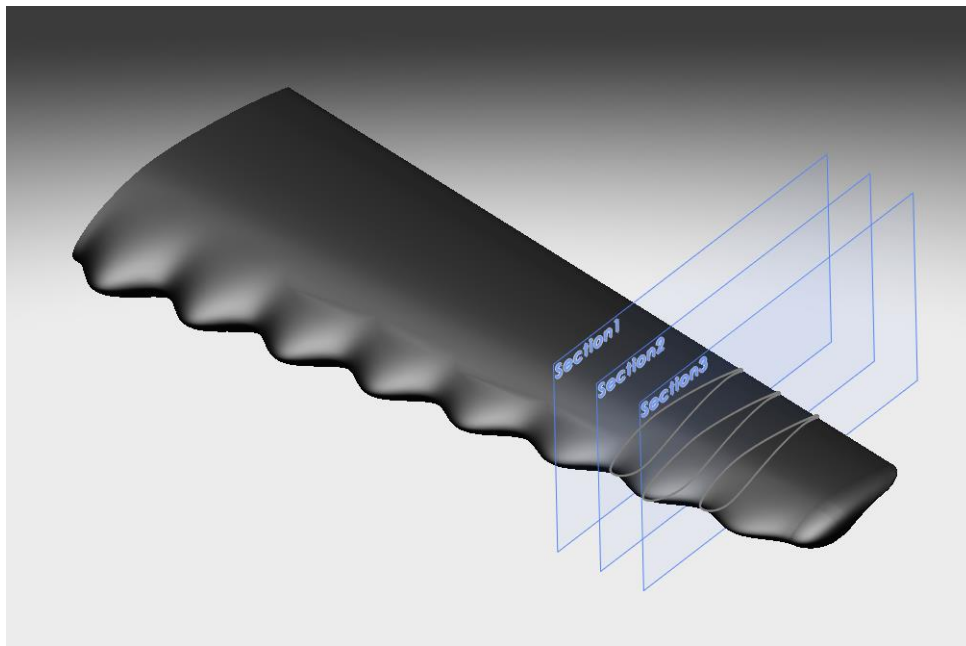


Figure 4-15 Sectional positions selected along Foil “1111” for flow visualisation using PIV. Firstly, concentrating on the 16° AOA results in Table 4-3, as shown in the first column (Section1), the flow separation (the blue region) observed at the back of Foil “1111” is much stronger than the separation observed at the back of Foil “0000”. Section 1 as shown in Figure 4-15 is a trough section located after the second tubercle from the tip. As the visualisation sections are getting closer to the foil tip, the flow separation gradually vanishes, as shown in the flow field results for “Section2” (the crest) and “Section3” (the trough).

As the measurement section is very close to the tip, the flow separation is dominated by mainly two factors, angle of attack and 3 dimensional flow. For a normal foil, like the reference foil “0000”, the foil will stall after critical angle of attack where flow separation should occur on the back of the foil starting from the trailing edge. However as the flow is trying to escape from the pressure side to the suction side at the tip, a spanwise flow can be generated which is called 3 dimensional flow for any finite length foil, as illustrated in Figure 4-16. This strong roll-up flow at the tip can form a tip vortex meanwhile recover the flow separation at the tip region. Nevertheless, this phenomenon will degrade the lift greatly since no lift can be produced in the tip region, also namely “tip loss”. Consequently, hardly any flow separation could be observed from the results of “Section2” and “Section3” with Foil “0000” while very small trailing-edge flow separation can be observed in “Section1”.

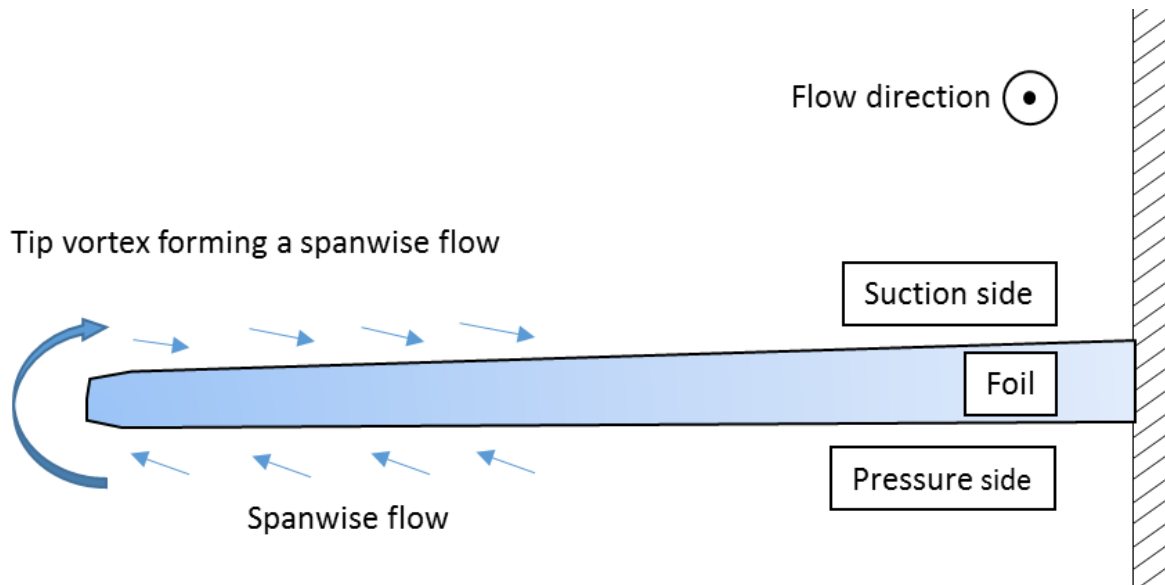


Figure 4-16 3 dimensional effect of typical 3D foil

Whereas, Foil “1111” has stronger flow separation than Foil “0000”, which indicated that foil with tubercles can limit this spanwise flow and maintain the flow around the foil to be 2 dimensional so that the tip loss can be greatly lowered. This phenomenon demonstrates tubercles have similar function with winglet to stop the spanwise flow. As a result, 33% higher lift can be achieved at 16° AOA at 4m/s, where the most significant performance difference were observed.

On the other hand, as shown in Table 4-4, even though the results indicate severe flow separation for both foils, the separation experienced by Foil “1111” was still more severe than that experienced by Foil “0000”. And in Section2, the flow separation for Foil “0000” started from the mid chord while the flow separation for foil started from the leading edge.

During the flow visualization test, another phenomenon has been observed that is the strong tip vortex cavitation generated by Foil “0000” while no visible cavitation for Foil “1111” can be seen. It can also prove the weakened 3 dimensional effect, as discussed in the following section.

Table 4-3 Comparative experimental flow patterns at 3 selected sections for Foil “0000” and Foil “1111” observed at 16° of angle of attack

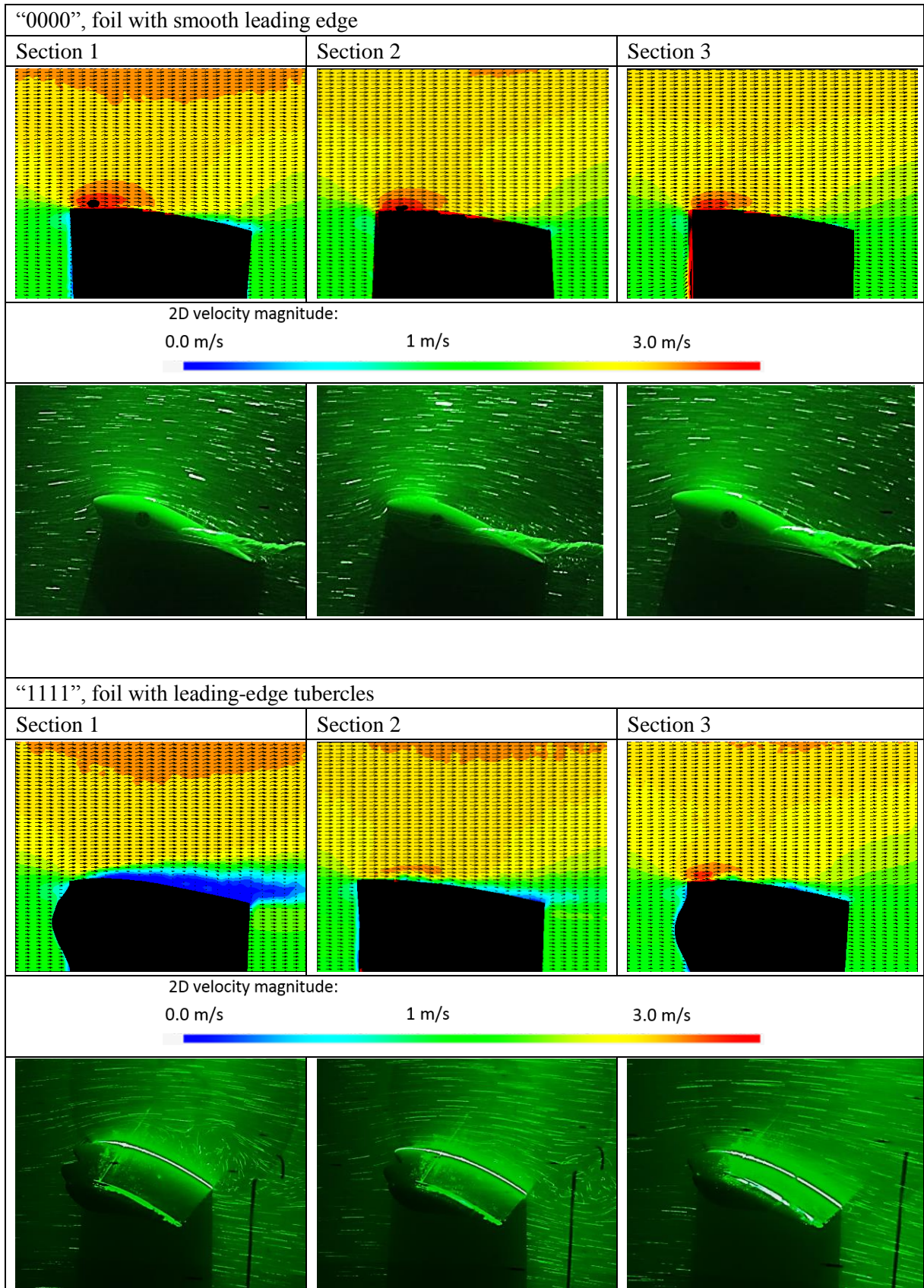
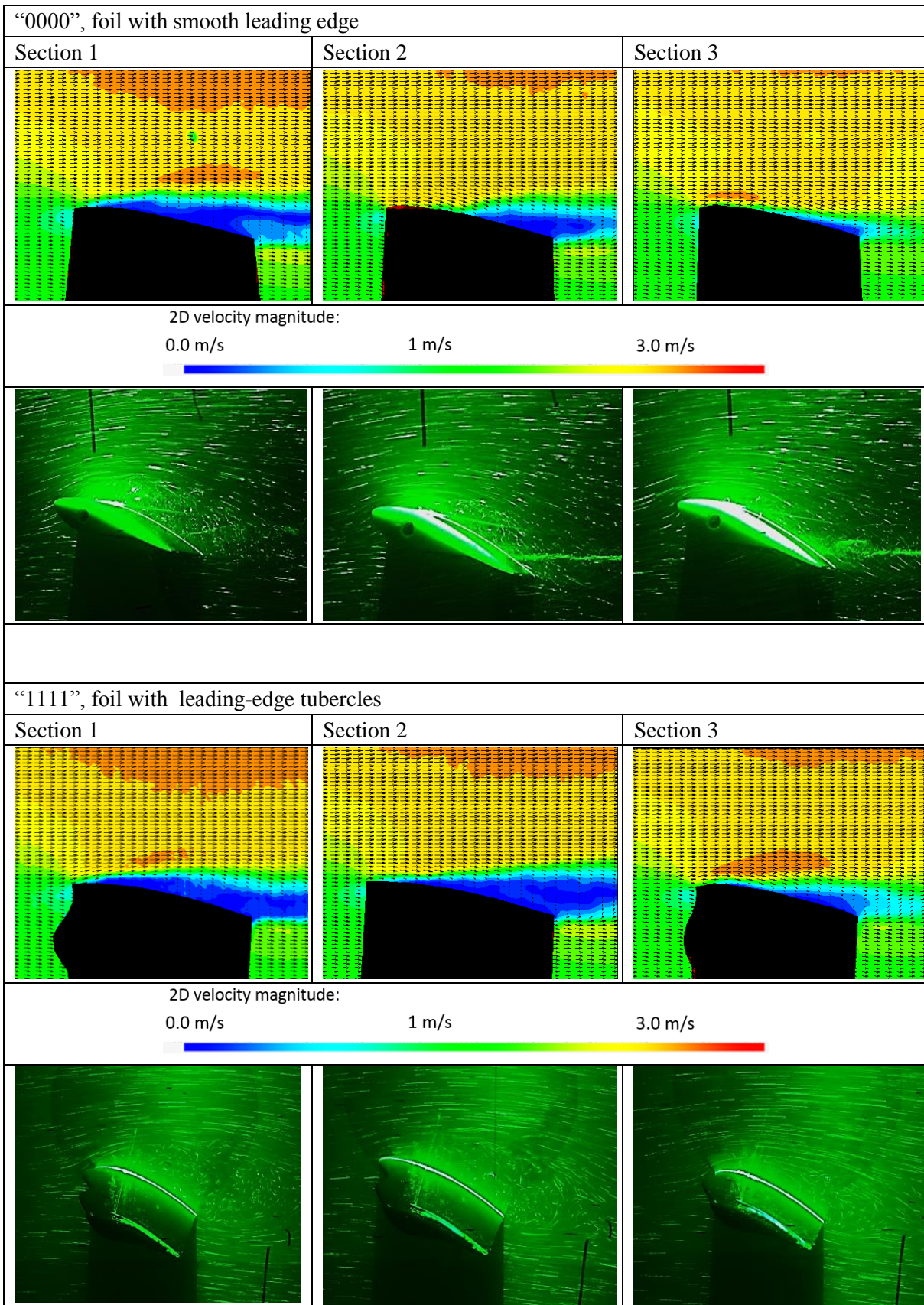


Table 4-4 Comparative experimental flow patterns at 3 selected sections for Foil “0000” and Foil “1111” observed at 24° of angle of attack



4.3.3.2 Development of Tip Vortex Cavitation

Perhaps the most striking difference between the flow pattern around Foil “0000” and Foil “1111”, was the development of a very strong tip vortex cavitation generated by Foil “0000” as opposed to almost no such cavitation generated by Foil “1111” due to the effect of the leading-edge tubercles. This can be clearly seen in the results given in Table 4-3 for the test condition with a 3m/s incoming velocity and 16° AOA. A close-up of this cavitating vortex, which emanated from the tip of the reference foil with about a 10mm diameter, is shown in Figure 4-17.

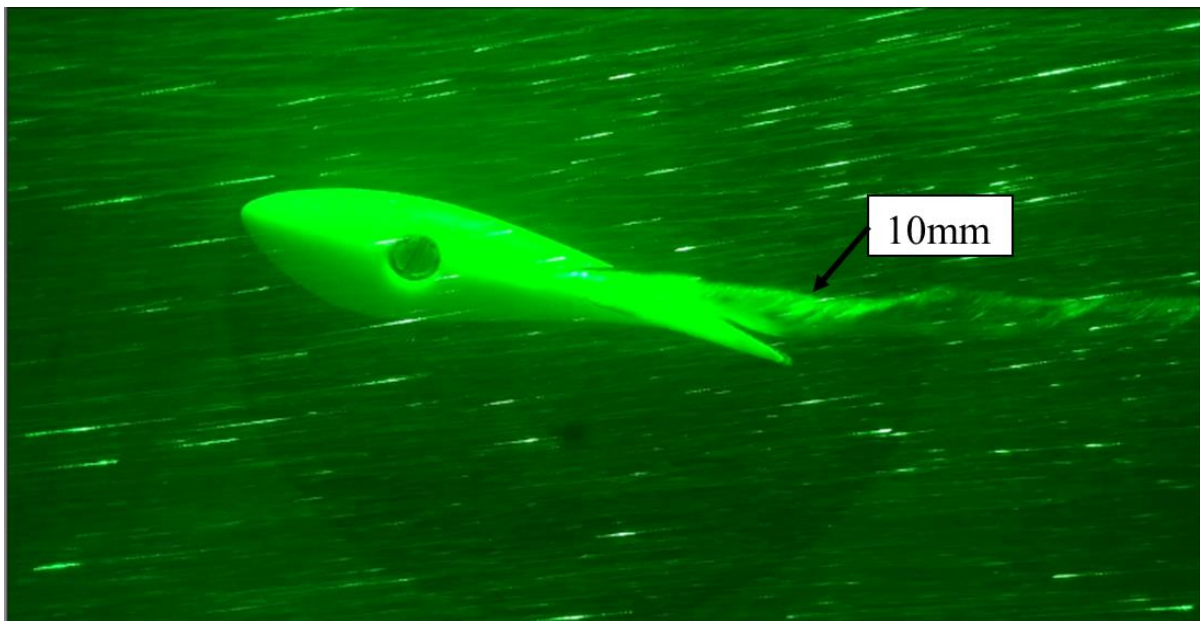


Figure 4-17 Cavitating tip vortex observation on reference foil with smooth leading edge
(Note a 10mm diameter tip vortex cavitation was generated)

Using a typical cavitating Rankine vortex expression, the relationship between the diameter of the cavitating tip vortex, a_c , and its circulation, Γ , can be given by Equation 4-3 (McCormick, 1962).

$$p_\infty - p_v = \frac{0.5\rho\Gamma^2}{4\pi^2 a_c^2} \quad \text{Equation 4-3}$$

where p_∞ is the pressure in far field and p_v is the saturated vapour pressure of the water.

According to Equation 4-3, the larger the diameter, the stronger the vorticity. Since both foils were tested under the same conditions, the larger tip vortex cavitation experienced by the reference foil would be responsible for the stronger “end effect” and hence greater loss of lift. Its counterpart (Foil “1111”), with the leading-edge tubercles, would maintain the 2D flow by lowering the end effect and therefore experience more favourable lift characteristics for the same condition.

4.3.4 Further remarks on the combined results of force measurements and flow visualisations

Comparative model tests of the 3D foil with a smooth leading edge (no tubercles) and with the leading-edge tubercles, which covered the whole span of the foil, confirmed the significant benefits of the tubercles on the lift and lift-to-drag ratio of the foil despite a slight increase in the drag characteristics. At 4m/s, 33% enhancement in C_L at a cost of 1% drag penalty results in a maximum improvement of 32% in C_L/C_D in the post stall region at a 16° of angle of attack due to the linear increase of the lift coefficient maintained with the increase of the angle of attack.

By optimising the application length of the leading-edge tubercles along the foil span, it was found that the maximum lift coefficient was reduced with the reduced tubercle application length. However, due to the enhanced lift coefficients before stall and lowered increase in the drag coefficient, the foil with the shortest tubercle application length, which was equal to 1/4 of the span, at the tip region displayed the best overall performance amongst the different combinations tested. This was based on the increased lift-to-drag coefficient ratio over the wider range of angles of attack and more than 10% increase in the peak lift-to-drag ratio.

Based on the observations and analyses so far, by combining the understandings from the flow analysis with regard to the effect of different grades of flow separation and that of tip cavitation generation with and without leading-edge tubercles, it can be concluded that the leading-edge tubercles can effectively weaken the 3 dimensional effect of the foil.

This hypothesis has been firstly supported by the evidence of much weaker separations observed on the back of the reference foil with the smooth leading edge compared to the much more severe separations observed on the counterpart foil with the leading-edge tubercles. Since the measuring sections are very close to the tip, the 3D effect generates the rolling up flow

which can reduce the flow separation close to the tip region. Therefore the more severe the flow separation at the tip region is, the weaker the 3D effect is.

On the other hand the hypothesis was also supported by the evidence of suppressed tip vortex cavitation and hence much reduced vortex strength resulting from the leading-edge tubercles. This also confirmed that the 3D effect was weakened by the leading-edge tubercles.

4.4 Numerical simulation of 3D blade with the optimised tubercles

In this section CFD simulations were conducted to complement the experimental investigation. The main objectives of the simulations are: (1) To provide further details of the flow field around the 3D blade with smooth leading edge and with different tubercle arrangements, and hence to understand the effect of tubercles further when applied to a turbine blade; (2) To validate the experimental results.

4.4.1 Methodology of CFD simulation

The simulations were conducted by using a commercial CFD software package Star-CCM+ to solve the incompressible Navier–Stokes equations with different turbulence models which were all acknowledged models for a better prediction of flow separations including: Shear Stress Transport (SST), Detached Eddy Simulation (DES) and Large Eddy Simulation (LES).

4.4.1.1 Computational domain and boundary conditions

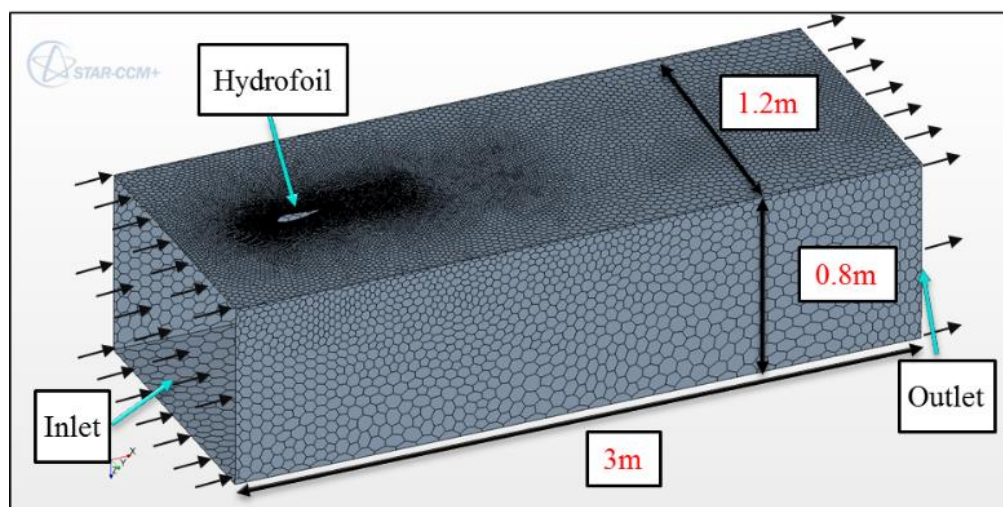


Figure 4-18 Computation domain and boundary conditions

The CFD simulation domain was described and dimensioned according to the experimental environment, i.e. the measuring section of the ECT, which is 3m long, 1.2m wide and 0.8m high, as shown in Figure 4-18. Similar to the experimental setup, the hydrofoil (3D blade section) was located 0.5m downstream of the inlet and connected to the top of the computational domain.

No-slip wall was chosen as the boundary condition of the hydrofoil, while free-slip wall was used for the tunnel wall to save the massive prism layer of the tunnel wall. Velocity-inlet with uniform flow of 3m/s was used as the boundary condition for the inlet. Meanwhile pressure-outlet condition was applied as the outlet condition.

4.4.1.2 Mesh generation

The automatic polyhedral mesher in Star-CCM+ was used as it has been designed to have four times fewer number of cells, half the memory required and a tenth to a fifth of computing time compared to tetrahedral meshes to reach solutions of the same accuracy for the mesh that this computational domain presented. Volumetric mesh control was used to control the growth of the mesh. As shown in Figure 4-19, three blocks were used to refine the mesh near the hydrofoil: Refine 1, Refine 2 and Refine 3. The generated mesh with volumetric control can be seen in Figure 4-20.

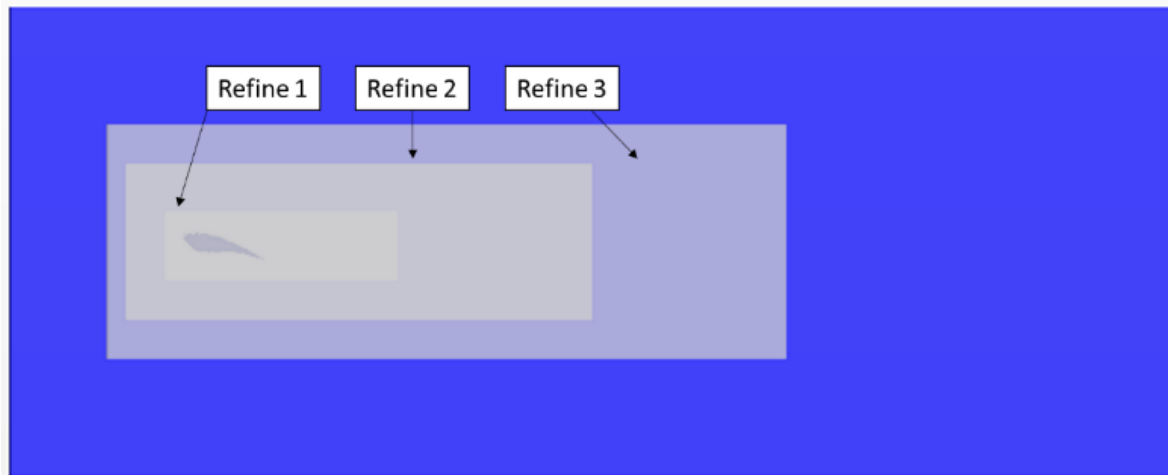


Figure 4-19 Volumetric mesh control

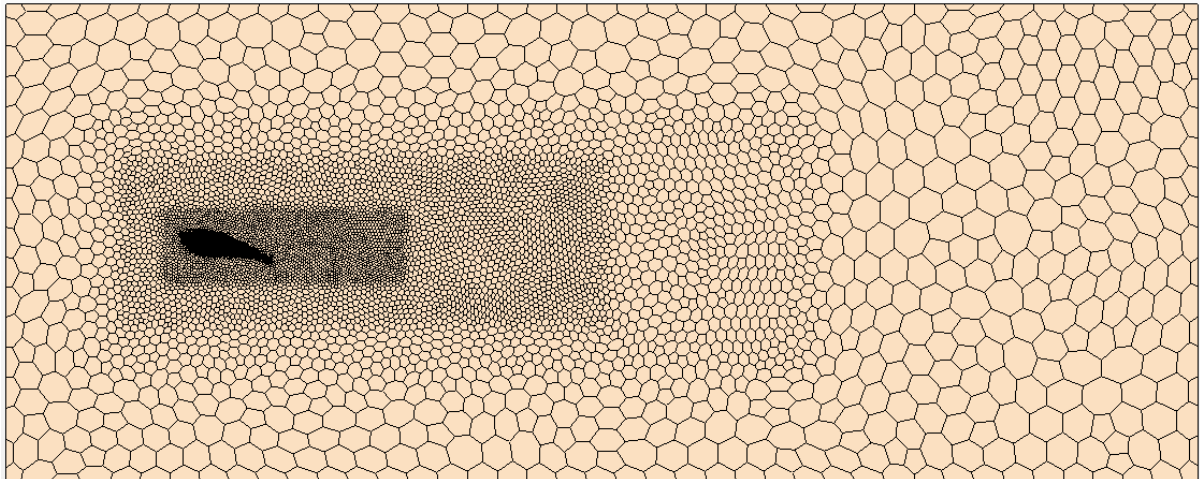


Figure 4-20 Generated mesh with volumetric control

To control the mesh resolution in the boundary layer, prism layer mesh was used to guarantee the near wall mesh quality. Ten layers of prism mesh were generated and the first layer thickness was set to be 1E-5m, as shown in Figure 4-21.

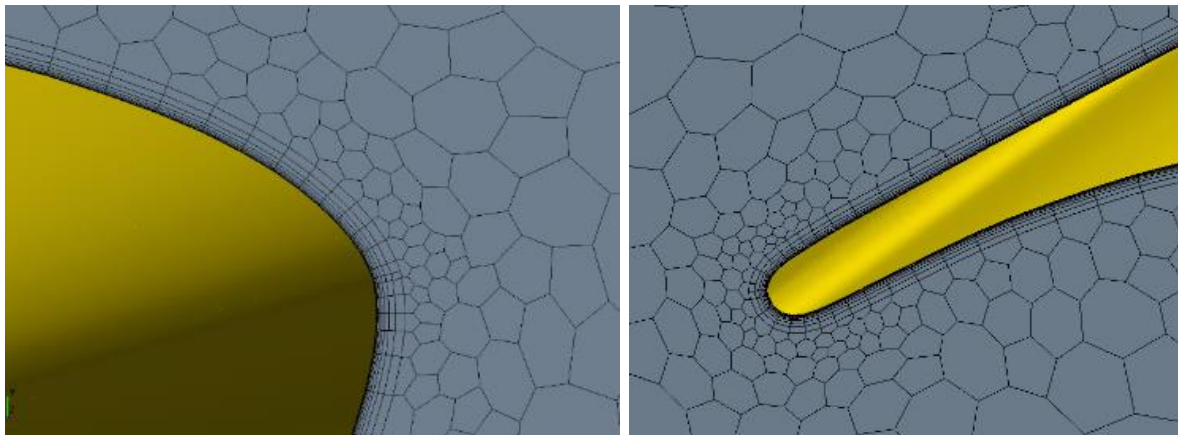


Figure 4-21 Prism layer mesh

A mesh convergence study was performed by gradually decreasing the base size of the mesh and increasing the mesh number, so that the resolution of the mesh would be improved until it reached sufficient accuracy. The mesh convergence study has been conducted under 8° angle of attack and evaluated with the manner of relative difference δ of C_L which is calculated with the following equation:

$$\delta = \frac{|C_{L1} - C_{L2}|}{C_{L1}} \quad \text{Equation 4-4}$$

The result has been presented in Table 4-5, with the mesh number ranging from 2 million to 21 million, the relative difference is below 1%, which indicates the mesh independence at the condition. More thorough validation combined with the turbulence model selection is demonstrated in the following section.

Table 4-5 Mesh convergence study under 8° angle of attack

Mesh number	C_L	δ
2M	0.9755	
5M	0.9820	0.66%
10M	0.9867	0.49%
21M	0.9958	0.92%

4.4.1.3 Turbulence model selection

Based on the previous experimental study it was noted that there were differences in the performance of the foils with different leading-edge profiles in the stall condition: while the reference hydrofoil suffered from flow separation and hence loss of lift; the hydrofoil with the leading-edge tubercles would delay the stall and maintain the lift. Therefore three acknowledged turbulence models for better modelling of flow separation were used and validated with the experimental results. These were namely Shear Stress Transport (SST), Detached Eddy Simulation (DES) and Large Eddy Simulation (LES).

Single phase incompressible flow was modelled during the simulation. Implicit unsteady analysis was used to model the flow separation in DES and LES simulations with 0.001s as the time step, while a time independent steady analysis was used in the SST turbulence model.

4.4.2 *Results and discussions*

4.4.2.1 Convergence and validation study

During the simulation, the C_L and C_D coefficients were monitored to check the convergence. One example of the convergence histogram against the iteration steps is shown in Figure 4-22, which shows a well converged simulation.

The mesh sensitivity was conducted based on the reference hydrofoil via using 4 different meshes by gradually increasing the mesh number from 2 million until 21 million cells. And turbulence model verification study was also conducted by combining the three different turbulence models: SST, DES and LES. Four different AOAs were simulated. According to the simulated lift coefficient, as shown in Figure 4-23, the DES model with a 21 million cell mesh

showed the best agreement with the experimental data (C_L), even at the stall conditions, which was very important for this simulation.

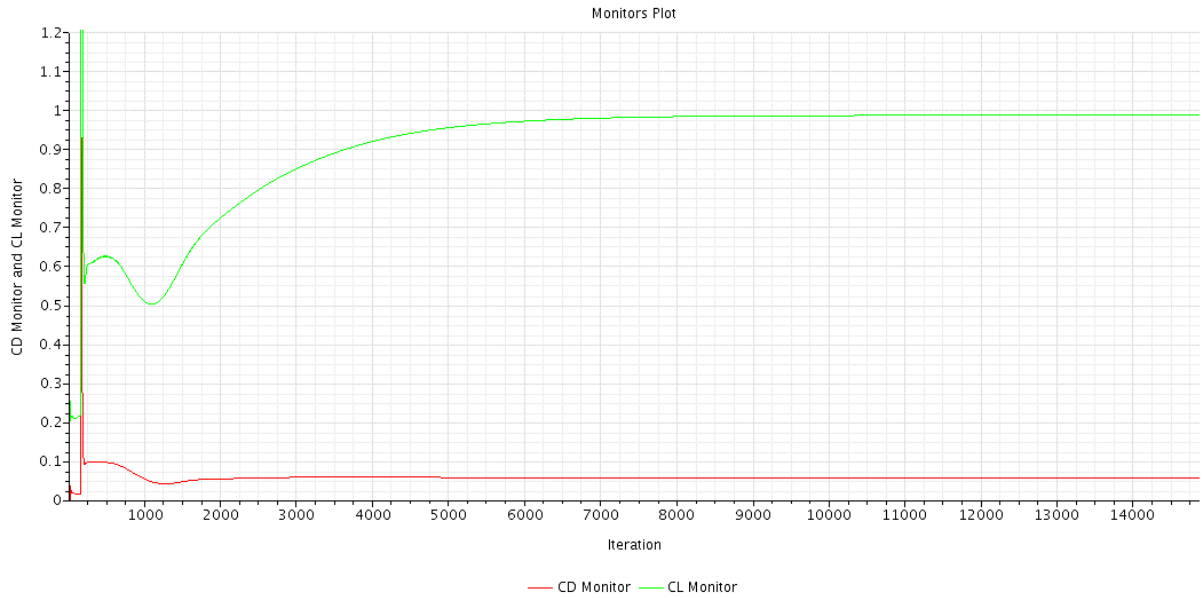


Figure 4-22 Example of convergence histogram of C_L and C_D

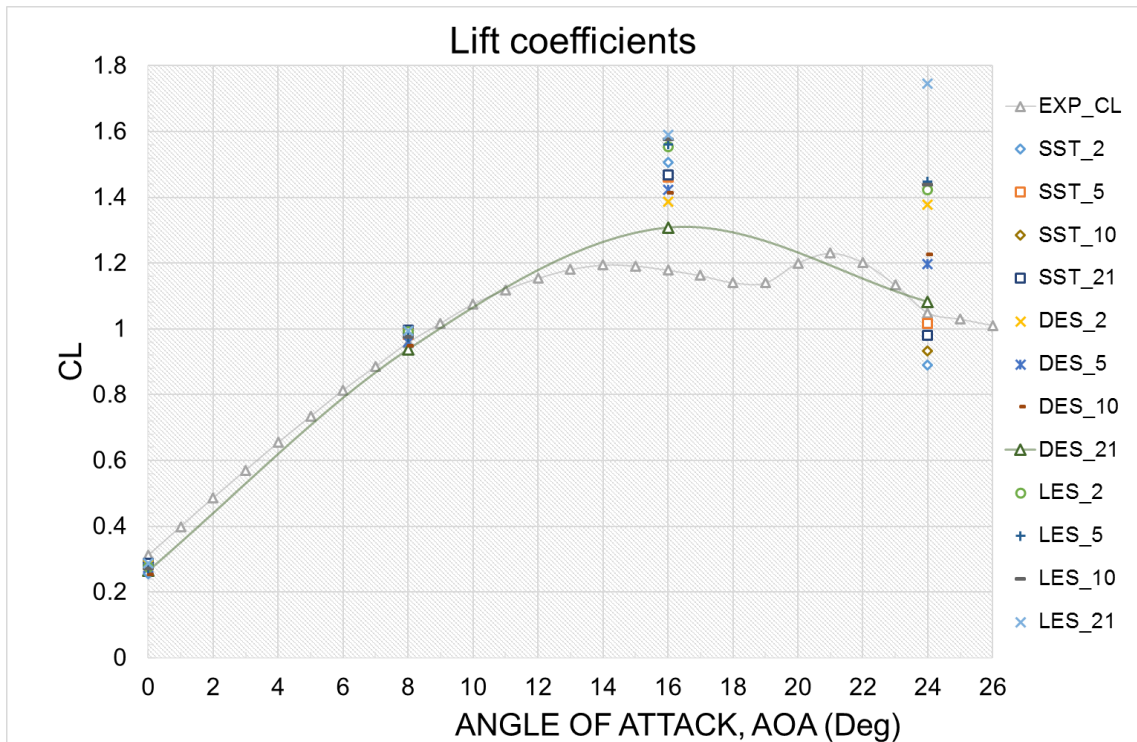


Figure 4-23 Mesh sensitivity and turbulence model verification

4.4.2.2 Force characteristics

According to the experimental study, the following analysis was focused on the condition when the most significant performance difference was observed, i.e. when the AOA was equal to 16° .

The details of the results for this condition are presented in Table 4-6. It can be seen that the numerical model can distinguish the difference between the two different leading-edge designs and shows a good agreement with the experimental data.

Table 4-6 Experimental and numerical results of the hydrofoil with and without tubercles at AOA=16°

Name	C _L	C _D
Ref_EXP	1.17858	0.18526
Ref_DES	1.25	0.1515
Sin8_EXP	1.48132	0.21297
Sin8_DES	1.45	0.1900

4.4.2.3 Flow patterns

The comparison of the CFD predicted flow separation patterns at AOA=16° for the reference hydrofoil and the one with the tubercles are shown in Figure 4-24 by the iso-surface representations for the axial velocity (V_x) equal to 0m/s. It can be clearly seen that the iso-surface of the reference hydrofoil was all connected together and formed into a huge cloud while the one for the tubercle hydrofoil was separated and containerised by the effect of the leading edge tubercles. In addition, the separated volume was much smaller than that observed for the reference blade. This was despite the fact that the flow separations of the foil with the tubercles were developing slightly earlier at the trough areas of the tubercles rather than at the tip region of the reference foil.

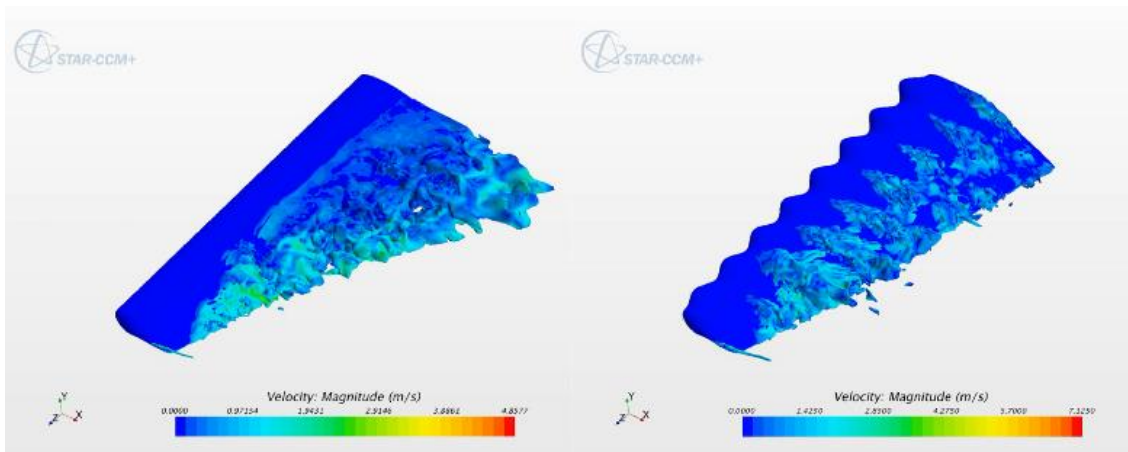


Figure 4-24 Comparative flow separation patterns of two hydrofoils (Iso-surface: V_x=0m/s; AOA=16°)

4.4.2.4 Vorticity distribution

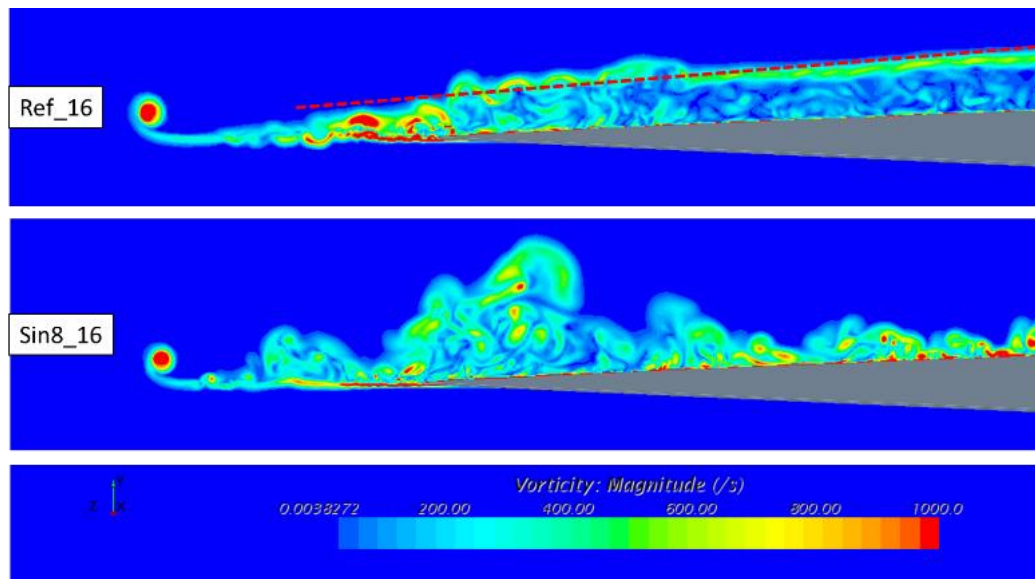


Figure 4-25 Comparative vorticity of tip vortex and flow separation from two hydrofoil sections, at section X=0.2m

Following the analysis of the flow separation patterns, a section cut was extracted from the flow field to see the magnitude of the tip vortices and the vorticity distribution along the span. Such a section cut was taken at $X=0.2\text{m}$, as shown in Figure 4-25, to illustrate the comparative vorticity development from the reference foil and the one with the tubercles. A strong tip vortex was generated by both hydrofoils. By comparing the vorticity distribution along the span direction, as shown Figure 4-25 (top), the reference hydrofoil displayed a rather uniform shear layer (marked with red dash line) with low vorticity flow inside. In contrast, the hydrofoil with tubercles displayed a highly disturbed and energetic flow with higher vorticity which was more attached to the foil surface, as shown in Figure 4-25 (bottom).

Further demonstrating the vortex activity on the foil surfaces Figure 4-26 is added for the separation pattern and the vorticity distribution on the suction and pressure sides of the two foils. One can see the more energetic flow pattern on the foil with tubercles. It is also clear to observe that the vorticity [i] distribution on the suction side, which is the vorticity pattern perpendicular to the main flow, indicates a pair of contra-rotating vortices generated from the tubercles along the span of the hydrofoil. The effects of the contra-rotating vortices can be seen even more clearly in Figure 4-27.

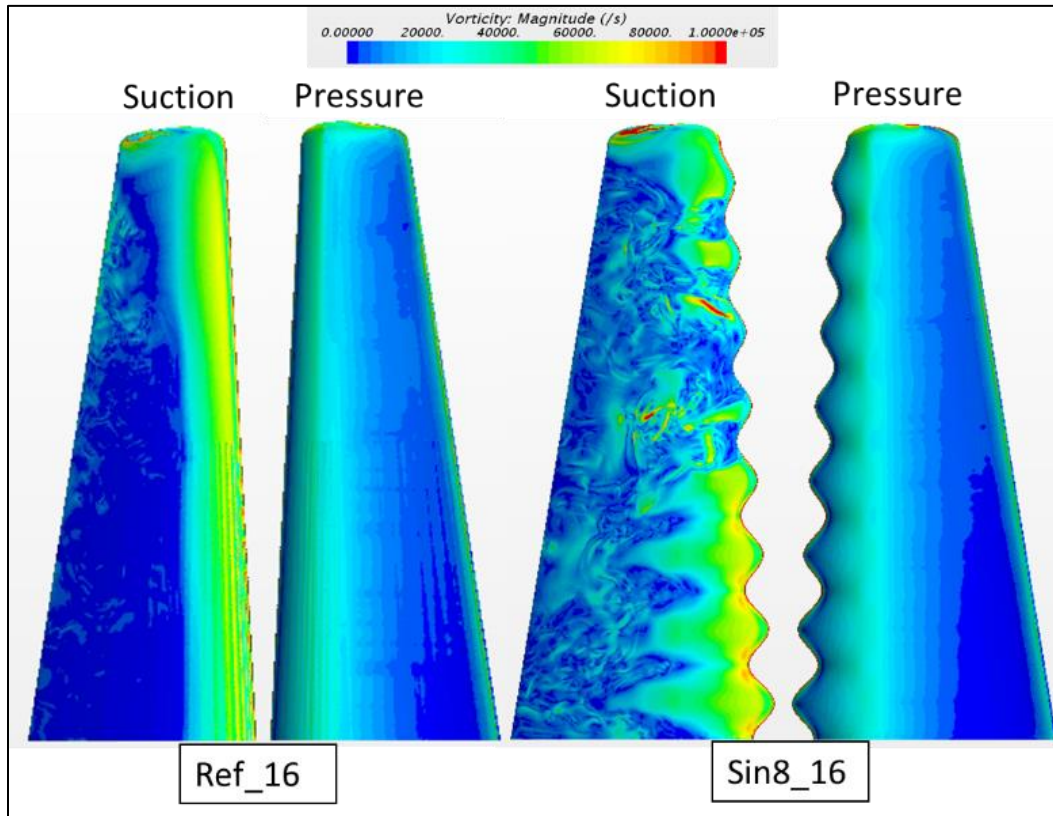


Figure 4-26 Comparative vorticity magnitude distributions along two hydrofoils

The above observations and findings with the 3D turbine blade appeared to be in line with the findings of the numerical and experimental research conducted with 3D tapered foils by (Miklosovic *et al.*, 2004; Miklosovic *et al.*, 2007; van Nierop *et al.*, 2008; Fish *et al.*, 2011; Rostamzadeh *et al.*, 2013; Rostamzadeh *et al.*, 2014; Shi *et al.*, 2015). It can be confirmed that the leading-edge tubercles can improve the lift-to-drag ratio for tapered 3D foils while they can only avoid the suddenly developing stall phenomenon for 2D infinite foils with a penalty that they would increase the drag and hence reduce the maximum lift capability.

By scrutinizing the details of the vorticity [i] distribution at the tip of the hydrofoil, the secret of why the leading-edge tubercles always perform better for a 3D foil than for a 2D foil was revealed. The contra rotating vortices generated by these tubercles were interacting with the tip vortex stopping it from spreading on the surface of the hydrofoil. As shown in Figure 4-28, a vortex generated by the tubercle next to the tip, which shows a positive vorticity [i] along a span position of $Z=0.525$ to 0.56 cancelled the strong negative tip vortex. As a result, the detrimental effect of the tip vortex that would be responsible for the performance loss was greatly weakened.

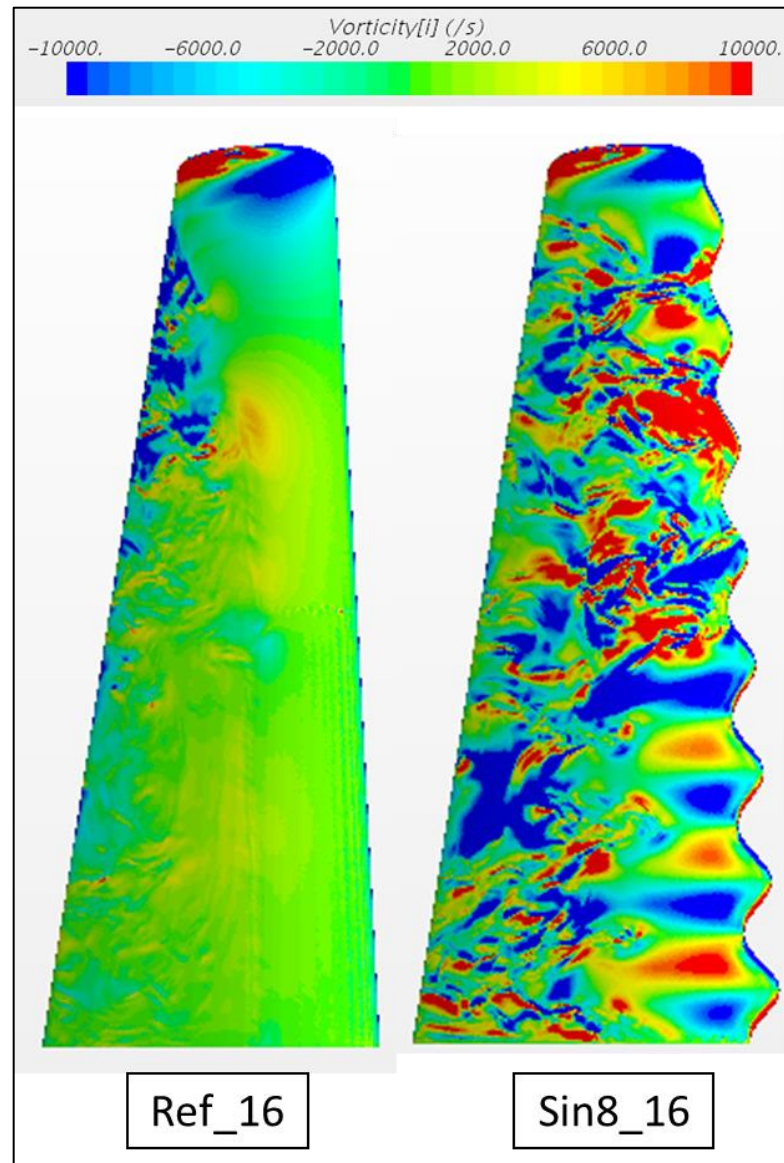


Figure 4-27 Comparative vorticity [i] distributions along two hydrofoils on the suction side

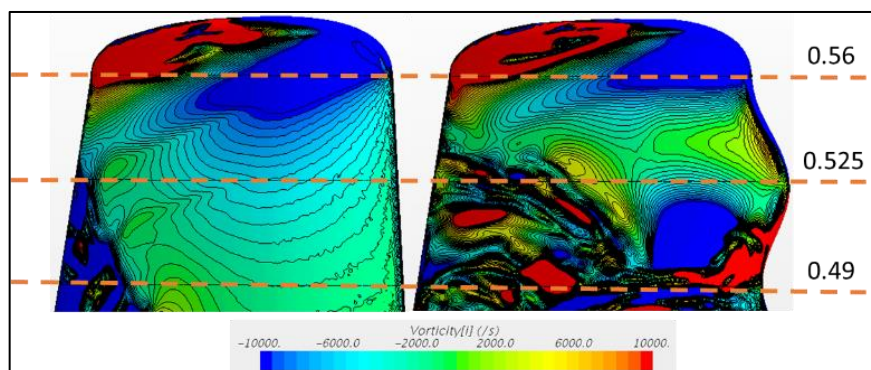


Figure 4-28 Comparative details of vorticity [i] distribution at the suction side and tip of two hydrofoils

4.4.2.5 Pressure distributions

The pressure coefficients (C_P) predicted by the CFD simulations were used to investigate the pressure distribution on the surface of the hydrofoil. As shown in Figure 4-29, the pressure distributions taken at nine sections of the troughs and crests of three tubercles were compared: one at the tip, one in the middle and the last one at the root. As noticed in Figure 4-29, the pressure distribution on the suction side of the foil with tubercles is rather unsteady and energetic compared to the rather steady trend of the reference foil with the smooth leading edge.

For the position at the crest of the tubercles, a better suction effect with negative C_P can be seen in the mid-chord regions of the sections taken at mid-span and root. This is because of the more attached flow as it can be seen in Figure 4-24. Closer to the root region, at the trough positions (plots at 0 and 0.07), the minimum value of the negative C_P is much lower than that for the reference turbine, which indicates higher velocity in the trough.

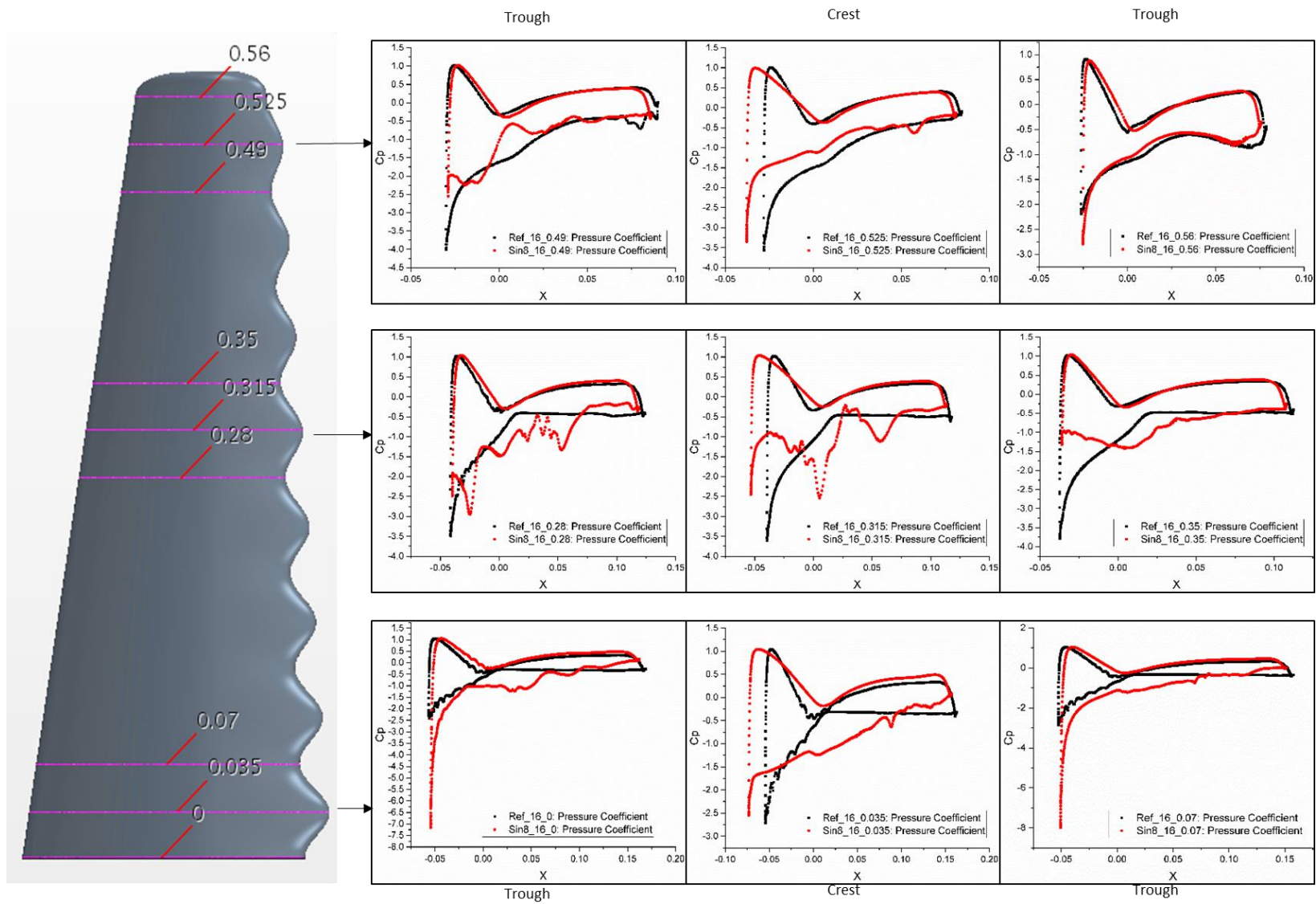


Figure 4-29 Comparison of pressure coefficient distributions in trough and crest area ($AOA=16^\circ$) for two foil sections

4.5 Summary

The main objective of this chapter was to provide further understanding of the tubercle concept, as applied to a representative 3D turbine blade, by conducting fundamental experimental and numerical investigations. The Chapter therefore presented the details and results of the experimental and numerical investigations on a representative 3D hydrofoil which was designed based on the reference turbine blade and optimised tubercle geometry described in Chapter 3.

The experimental work involved tests with the model hydrofoil to measure the lift and drag characteristics in a cavitation tunnel as well as to visualise the flow using a PIV system. The numerical investigations included CFD simulations of the detailed flow around the 3D blade by using the commercial CFD code, Star-CCM+, to predict the flow, force and pressure characteristics of the foil to support and validate the results of the model tests. Based on these investigations the following can be concluded:

1. The model tests with a 3D representative turbine blade without and with the leading tubercles confirmed the significant benefits of the tubercle application on the lift and lift-to-drag ratio of this blade despite a slight increase in its drag characteristics.
2. By optimising the application length of the leading-edge tubercles along the blade span, it was found that the blade with the shortest tubercle application (extension) length at the tip region, which was equal to a 1/4 of the span, displayed the best overall performance amongst the application lengths tested.
3. A striking difference was observed in the tip vortex cavitation generated by the foil with and without the leading-edge tubercles. Combined with the understanding from the visualisation of the separated flows by using a PIV system, the leading-edge tubercles can effectively weaken the 3D effect of the blade.
4. The numerical simulations demonstrated a good agreement with the experimental data and hence further proved the beneficial effect caused by the leading-edge tubercles.
5. Based on the post CFD analysis, the generation of the contra rotating vortices by the tubercles was further confirmed on the 3D blade, as claimed by other researchers on other applications. These kind of vortices energised the flow over the blade surface and

it helped to be more attached to the surface. Meanwhile it also consumed a certain amount of energy that led to the drag increment.

6. The above mentioned contra-rotating vortex mechanism in the tip region formed a vortex fence to stop the tip vortex inducing a detrimental spanwise cross flow over the turbine blade as well as weakening the tip vortex which confirmed the findings in the experimental campaign.

Chapter 5 Experimental Investigations of Leading-edge Tubercles as applied on Tidal Turbine

5.1 Introduction

With the confidence built through the results of the leading edge tubercles applied to the foil section and the simplified turbine blade (in Chapter 3 & 4), the next step was to investigate whether this biomimetic concept could be effective for improving the hydrodynamic performance of a state-of-the-art tidal turbine with actual blades. By going through a comprehensive set of experimental investigations for a turbine model with and without leading edge tubercles, the comparative hydrodynamic efficiencies were investigated including the cavitation and underwater noise performances. These investigations were supported with comprehensive flow analyses using state-of-the-art experimental tools for further exploration and understanding of the effects of tubercles on tidal turbines as well as generating bench mark data for future research and developments.

In order to satisfy the above objectives, within this chapter, the optimum tubercle design achieved in Chapter 4, was applied to a scaled turbine model with different levels of tubercle coverage, as described in Section 5.2. This was followed by a set of model tests conducted in a cavitation tunnel for different purposes. The most critical efficiency performance tests for the turbines with different blades, in steady current, were conducted in the Emerson Cavitation Tunnel (ECT) and are presented in Section 5.3. The efficiency performance tests were complemented further with investigations of the undesirable cavitation and noise phenomena in the same facility and details are presented in Section 5.4 and 5.5, respectively. Following the cavitation and noise tests, taking advantage of the state-of-the-art Stereo PIV equipment in the ECT, a campaign of comprehensive flow visualization and measurement around the turbines with different blades was also conducted and presented in Section 5.6. Finally, the main findings from the all investigations are summarized in the concluding remarks of this Chapter in Section 5.7.

5.2 Description of the tidal turbine models

The horizontal axis tidal turbine (HATT) was chosen as the reference turbine to which the leading-edge tubercles would be applied. A 400mm diameter (D) model turbine was built and tested in the previous EPSRC project by Wang et al (2007) and was again used for this work. The main particulars for the blades are shown in Table 5-1. The foil section used is the S814 airfoil section, as described in Chapters 3 and 4.

Table 5-1 Main particulars of the tidal stream turbine model

r/R	0.2	0.3	0.4	0.5	0.6	0.7	0.8	0.9	1
Chord length(mm)	64.35	60.06	55.76	51.47	47.18	42.88	38.59	34.29	30
Pitch angle (deg)	27	15	7.5	4	2	0.5	-0.4	-1.3	-2

Based on the tubercle design and results of the blade tests in Chapter 4, three pitch-adjustable turbine models with different leading-edge profiles were manufactured by Centrum Techniki Okrętowej S.A. (CTO, Gdansk), as shown Figure 5-1. The reference turbine model with smooth leading edges (i.e. without tubercles) was named “Ref” and used as the baseline. The one with two leading-edge tubercles at the tip, as shown in the middle of Figure 5-1, was named “Sin_2”; this performed most efficiently in the hydrofoil tests presented in Chapter 4. Finally the one with eight leading-edge tubercles was named “Sin_8” and this presented the maximum lift coefficient as well as the most sustained linear increase of the lift during the simplified blade tests in Chapter 4.



Figure 5-1 Tested turbine models

The sinusoidal leading-edge profile was developed as shown in Figure 5-2. The Height (H) of the sinusoidal tubercles was equal to 10% of the local chord length (C) while the eight tubercles were evenly distributed along the radius with a wavelength (W) which was equal to 20mm. The profile of the leading tubercles was represented by Equation 5-1.

$$h = \frac{H}{2} \cos \left[\frac{2\pi}{W} (r - 40) - \pi \right] + \frac{H}{2} \quad \text{Equation 5-1}$$

where h is the height of the leading-edge profile relative to the reference one which is the smooth leading-edge profile.

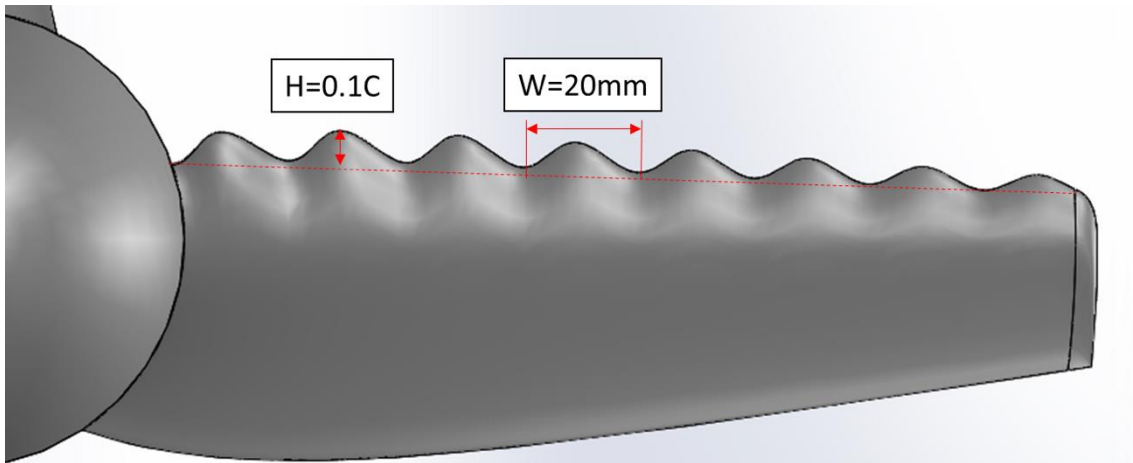


Figure 5-2 3D design of the turbine with leading-edge tubercles

Based on the above design methodology, the Sin8 turbine has 5% larger expanded blade area ratio (EAR) compared to the Ref turbine (EAR = 0.18), while the Sin2 turbine has only 0.9% larger EAR.

5.3 Open water hydrodynamic performance tests

Efficiency performance of a tidal turbine in an open and steady tidal current, which is also known as open water hydrodynamic performance, is the most critical performance data as it will define the power generation capability of the turbine. As briefly summarized in the Chapter 2, horizontal axis tidal turbines differ from each other in terms of control mechanisms, either variable/fixed speed control or variable/fixed blade pitch control. But turbines typically operate at following operational states:

- 1: Stand-by, when the turbine is available to run if external conditions permit.
- 2: Start-up, when the current speed reached the cut-in speed. A pitch controllable turbine will pitch its blades to the starting position to generate higher torque to start the turbine, whereas a fixed pitch turbine can only rely on the current to overcome the resistance to start the turbine.
- 3: Power production, after cut-in speed before cut-out speed. The turbine operate differently depends on its control mechanisms. For example, a variable speed control turbine can adjust the turbine's rotational speed such that the tip speed ratio remains constant to achieve the maximum C_p .
- 4: Shutdown and stopped with fault, when the turbine has to be stopped with its brake.

From the above conditions, two key parameters, the blade pitch angle and the tip speed ratio (TSR), can be used to represent the turbine's performance. Therefore in this test, the turbines would be evaluated by measuring the torque and the thrust of the turbine with different pitch angles over a range of TSRs. The following section describes the experimental setup in the ECT to conduct the open water performance tests with the models.

5.3.1 Experimental setup

The three tidal turbine models were tested in the ECT at Newcastle University. The turbine was mounted on a vertically driven dynamometer, K&R H33, designed to measure the thrust and torque of a propeller or turbine. The main technical data of H33 is given in Table 5-2. A 64kW DC motor is mounted on top of the dynamometer to control the rotational speed of the turbine.

Table 5-2 Technical data of propeller dynamometer H33

Type of dynamometer	Kempf & Rammers H33
Rated maximum thrust (N)	±3000
Rated maximum torque (Nm)	±150
Maximum rotation speed (RPM)	4000

During the model test the torque and thrust of the turbine were measured and from these measurements the power coefficient (C_p) and the thrust coefficient ($C_T/10$) can be derived by using Equation 5-2 and Equation 5-3, respectively. The torque data was corrected for the shaft frictional torque which was measured by replacing the turbine model with a shaft fairing (dummy mass) which had the same mass as the turbine blades, as shown in Figure 5-3.

$$C_p = \frac{Q\omega}{\frac{1}{2}\rho A_T V^3} \quad \text{Equation 5-2}$$

$$C_T/10 = \frac{T}{\frac{1}{2}\rho A_T V^2} / 10 \quad \text{Equation 5-3}$$

where Q is the torque of the turbine, Nm; T is the thrust, N; ω is the rotational speed, rad/s; A_T is the swept area of the turbine and equal $\pi D^2/4$, m²; ρ is the tunnel water density, kg/m³; V is the incoming velocity, m/s, D is the turbine diameter, m.

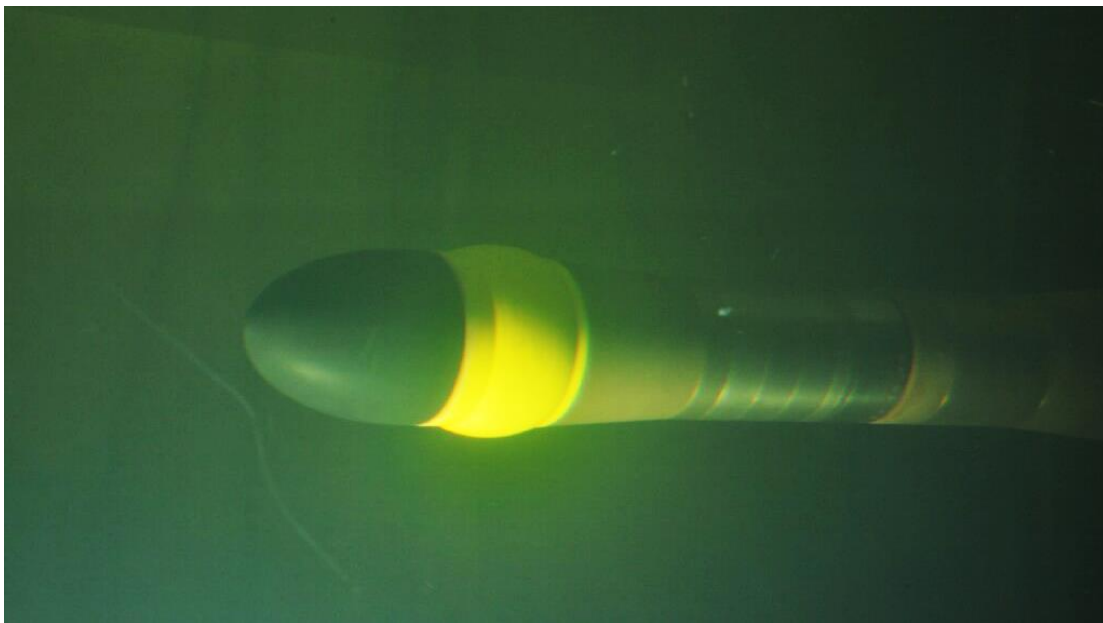


Figure 5-3 Frictional torque measurement with the dummy mass (the yellow coloured shaft fairing) fitted on the dynamometer inside the ECT

The rotational speed of the turbine was controlled by the motor to achieve the desired tip speed ratio (TSR) which can be calculated by Equation 5-4. As the performance of the turbine is strongly dependent on the Reynolds number and the cavitation number, these two non-dimensional numbers at 0.7 radius of the turbine blade, $Re_{0.7r}$ and $Cav_{0.7r}$ were monitored and can be derived from Equation 5-5 and Equation 5-6 respectively.

$$TSR = \frac{\omega r}{V} \quad \text{Equation 5-4}$$

$$Re_{0.7r} = \frac{C_{0.7r} \sqrt{(V^2 + (0.7\omega r)^2)}}{\nu} \quad \text{Equation 5-5}$$

$$Cav_{0.7r} = \frac{P_{0.7r} - P_v}{\frac{1}{2} \rho \sqrt{(V^2 + (0.7\omega r)^2)}} \quad \text{Equation 5-6}$$

where $C_{0.7r}$ is the chord length of the turbine at 0.7 radius, m; ν is the kinematic viscosity of the water, m^2/s ; $P_{0.7r}$ is the static pressure at the upper 0.7 radius of the turbine, Pa; P_v is the vapour pressure of the water, Pa.

Test matrix

During the tests, the incoming flow velocity of the tunnel was fixed and the rotational speed of the turbine was varied to achieve the required TSR. The tests were conducted according to the test matrix shown in Table 5-3. The test conditions are also shown in graphical format in Figure 5-4. At high Reynolds numbers, due to the increased incoming velocity, cavitation number was reduced and hence cavitation might occur at the turbine blades. Taking advantage of the pitch adjustable design, three different pitch angles of the turbine blades were tested.

Table 5-3 Test matrix

V	TSR	RPM	Pitch angle	Tunnel pressure	Cav	Re
(m/s)			(°)	(mmhg)	(0.7r)	(0.7r)
2	0.5 ~ 8	47 ~ 763	0	850	48.534 ~ 1.684	0.07E+06 ~ 0.22E+06
2	0.5 ~ 8	47 ~ 763	+4	850	48.534 ~ 1.684	0.07E+06 ~ 0.22E+06
2	0.5 ~ 8	47 ~ 763	+8	850	48.534 ~ 1.684	0.07E+06 ~ 0.22E+06
3	0.5 ~ 8	71 ~ 1145	0	850	21.571 ~ 0.748	0.12E+06 ~ 0.34E+06

3	0.5 ~ 8	71 ~ 1145	+4	850	21.571 ~ 0.748	0.12E+06 ~ 0.34E+06
3	0.5 ~ 8	71 ~ 1145	+8	850	21.571 ~ 0.748	0.12E+06 ~ 0.34E+06
4	0.5 ~ 8	95 ~ 1527	0	850	12.134 ~ 0.421	0.15E+06 ~ 0.45E+06
4	0.5 ~ 8	95 ~ 1527	+4	850	12.134 ~ 0.421	0.15E+06 ~ 0.45E+06
4	0.5 ~ 8	95 ~ 1527	+8	850	12.134 ~ 0.421	0.15E+06 ~ 0.45E+06

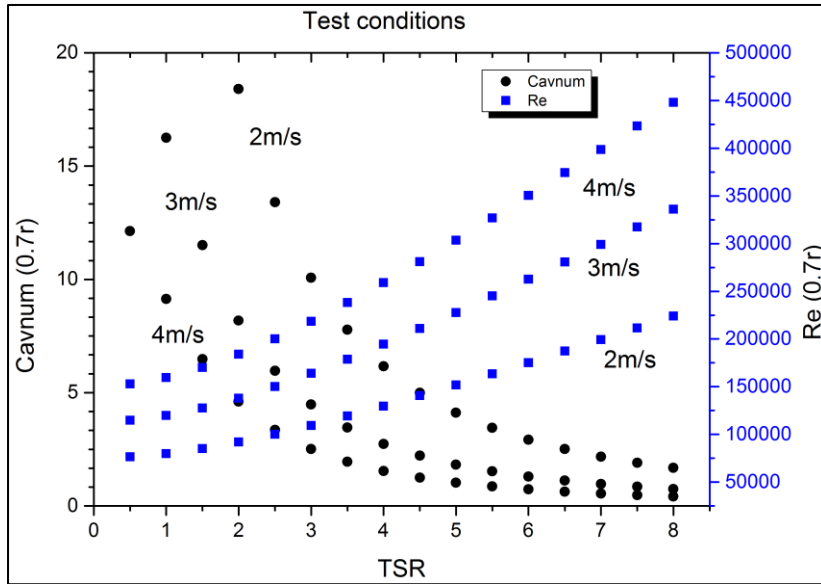


Figure 5-4 Test conditions

With this method, each condition was repeated three times for uncertainty analysis. The average results were then plotted and compared. The average standard deviation for C_p was around 2.9% and 0.7% for $C_t/10$. A sample of the uncertainty analysis is shown in Figure 5-5. As shown in the figure, the tests were quite repeatable.

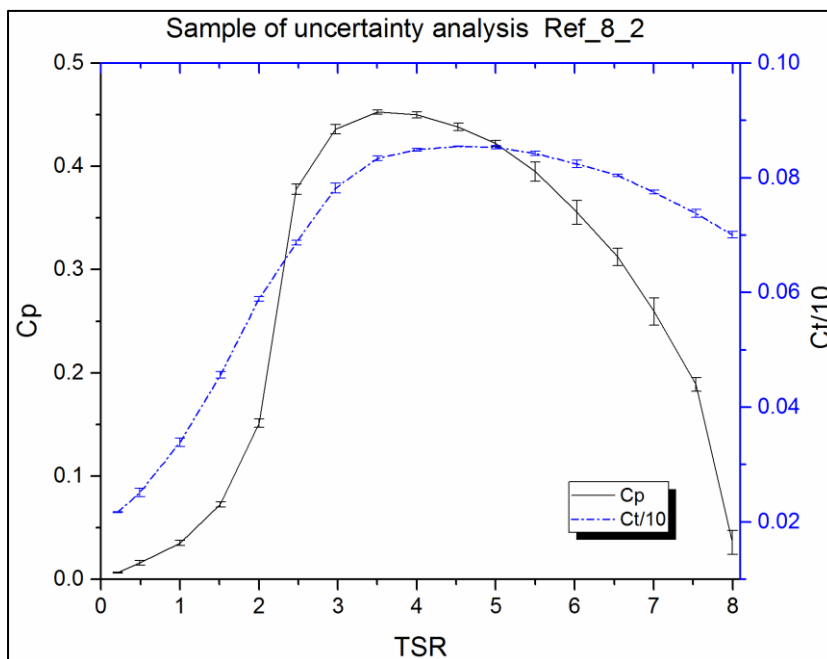


Figure 5-5 Sample of uncertainty analysis

5.3.2 Results and discussions

In order to analyse the effect of the leading-edge tubercles independently, each turbine model was tested by using the test matrix shown in Table 5-3. The performance was then compared at each test condition, for the reference turbine and the other two turbines with the tubercles. All of the cases were coded as “Model Name_Pitch Angle_Test Velocity”, for example “Ref_0_2” indicated the test results for the reference turbine model with 0° pitch angle setting tested at 2m/s incoming velocity.

5.3.2.1 Effect of Reynolds number and blade cavitation

As shown in Table 5-3 and Figure 5-4, the Reynolds number and cavitation number are cross-related to each other at constant tunnel pressure and are determined by the incoming velocity and TSR. In order to study the influence of the Reynolds number and the cavitation number, the reference turbine model with the smooth leading edge was first tested under different incoming velocities, i.e. 2, 3 and 4 m/s while the blade pitch angle was set to 0°.

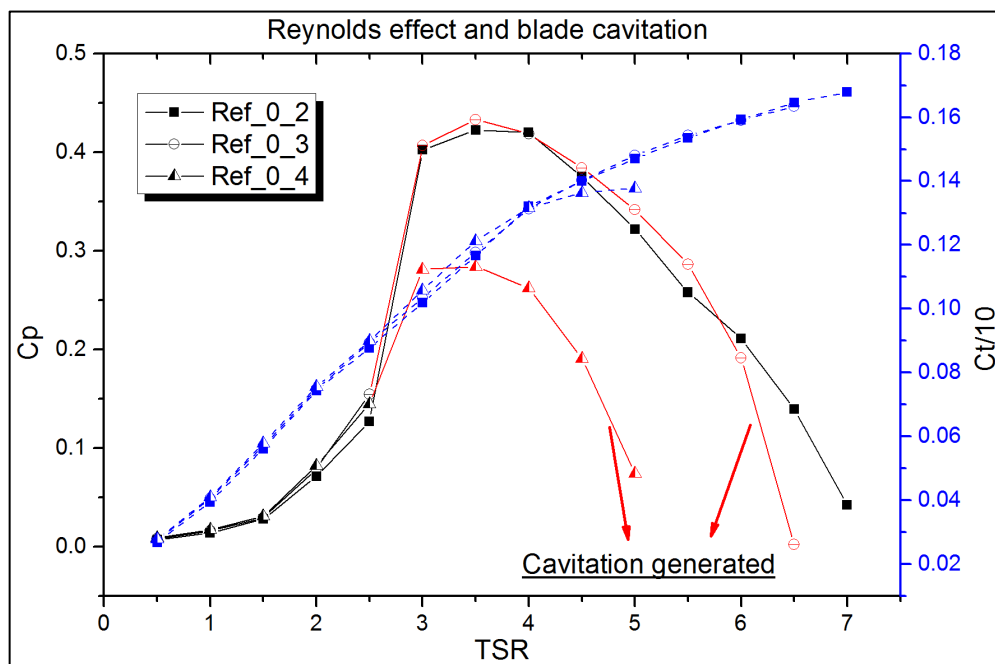


Figure 5-6 Influence on turbine performance caused by Reynolds number effect and blade cavitation

Based on the test results, the power coefficient, C_p , and thrust coefficient, $C_t/10$ were calculated and are presented in Figure 5-6. In this figure, the C_p curves marked in red are the data where cavitation inception occurred. The test results indicated that while the C_p curve would be greatly influenced by the blade cavitation, increasing the Reynolds number would only lead to

a slight enhancement in the performance. However, this was also based on the types of cavitation developed.

During the tests, various types of cavitation were observed including tip vortex cavitation and cloud cavitation at the back-side and face-side of the blade, as shown in Figure 5-7, which depends on the TSR. The development sequence of these cavitation types on the blades was usually that the tip vortex cavitation first appeared and then gradually transformed to a more severe and unsteady cloud cavitation on either side of the turbine blade depending on the TSR. While the cloud cavitation would greatly reduce the turbine efficiency, it could also cause erosion on the blades.

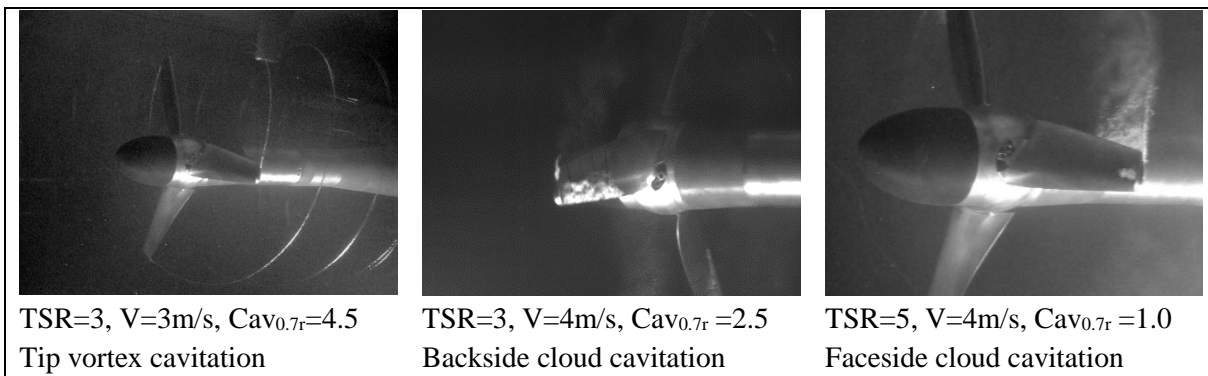


Figure 5-7 Types of blade cavitation

Based on the test results it was noticed that Reynolds number and tip vortex cavitation had a limited influence on the turbine performance in comparison to the effect of the cloud cavitation which would not only cause efficiency loss but also was expected to cause erosion damage on the blades.

5.3.2.2 Effect of blade pitch angle

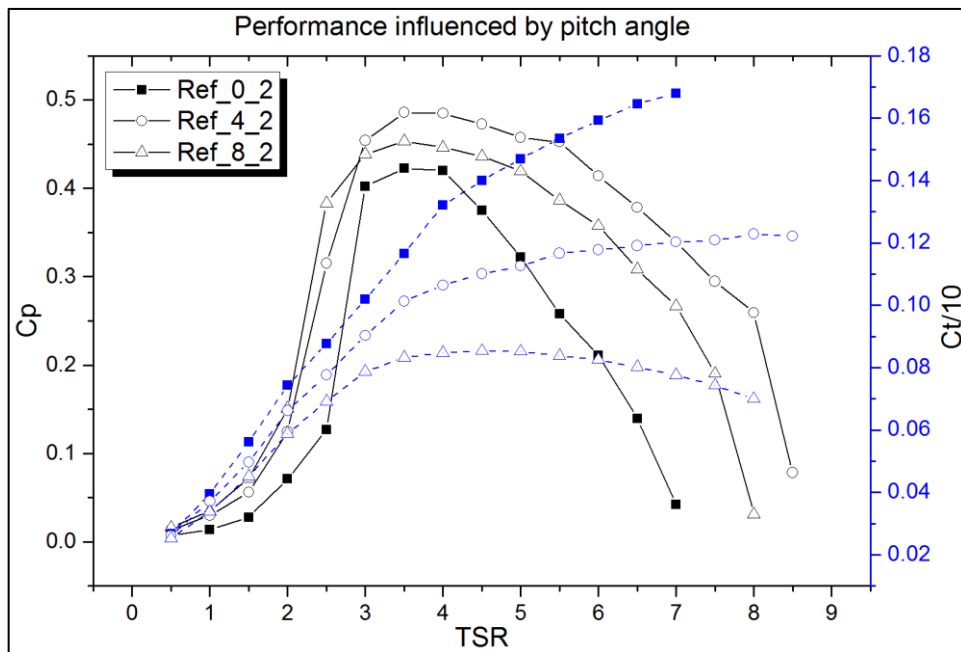


Figure 5-8 Performance influenced by pitch angle

Another important factor that influences the turbine performance is the blade pitch angle. During the tests three different pitch angles, 0°, +4° and +8° were set on the turbine blades. From the test results of the reference turbine, as shown, the Ct/10 was significantly reduced by increasing the pitch angle. On the other hand, the Cp reached its maximum value (0.49), with +4° pitch angle, while +8° pitch angle provided the turbine with a better performance over the lower range of TSRs up to TSR=2.5.

Based on the test results, the reference turbine had the best efficiency over the widest TSR when the blade pitch angle was set to +4°. When the blade pitch angle was set to 0° the force on the blade contributed more to the thrust, while for +8°, the increased pitch angle resulted in a reduced angle of attack and hence lower thrust force on the turbine.

Another phenomenon can be observed in the Figure 5-8, which is that the Ct/10 coefficient at 0° pitch angle setting is significantly higher than that of the HATTs in an open channel. One thing should be bear in mind: no blockage correction has been applied to fair these testing result. As the blockage ratio of the cavitation tunnel is around 13% based on the turbine swept disc area, lower power coefficients and thrust coefficients are expected if in open channel. By applying the wake expansion model based on actuator disk theory presented in Bahaj et. Al,

2007, it shows 14% lower power coefficient and 9% lower thrust coefficient for the reference turbine with +8° pitch angle at TSR=4.

However, this method is strongly related to thrust coefficient. Since the uncertainty associated with this will be further increased by the interaction of C_p and $C_t/10$ values and hence the effect will be more ambiguous to distinguish. Therefore in this thesis, the raw data is presented for better comparison as the turbines were all tested with the same experimental environment.

The test results of different pitch angle settings under other incoming velocities, i.e. 3m/s and 4m/s were all presented in Appendix A. Under different incoming velocities and hence Re numbers even with the influence of cavitation development, the results show similar trend with the result presented in Figure 5-8.

5.3.2.3 Effect of different leading-edge tubercle profiles

Following the tests with the reference turbine, the two counterpart turbines with the different leading-edge profiles were tested using the test matrix given in Table 5-3 but at a constant incoming velocity of 2 m/s. The reason for selecting 2 m/s incoming velocity was due to the negligible effect of the Reynolds number on the turbine efficiency as opposed to the considerable effect of the cavitation as discussed in Section 4.1 and 4.2. Therefore, in order to investigate the effect of leading-edge tubercles on the blade performance independent from the cavitation and blade pitch angle, the result of the tests at 2m/s was used for comparisons with the results of the reference turbine. Each set of tests was repeated three times and averaged to achieve the final result. Other test results which may be associated with the cavitation effect are also provided in Appendix A.

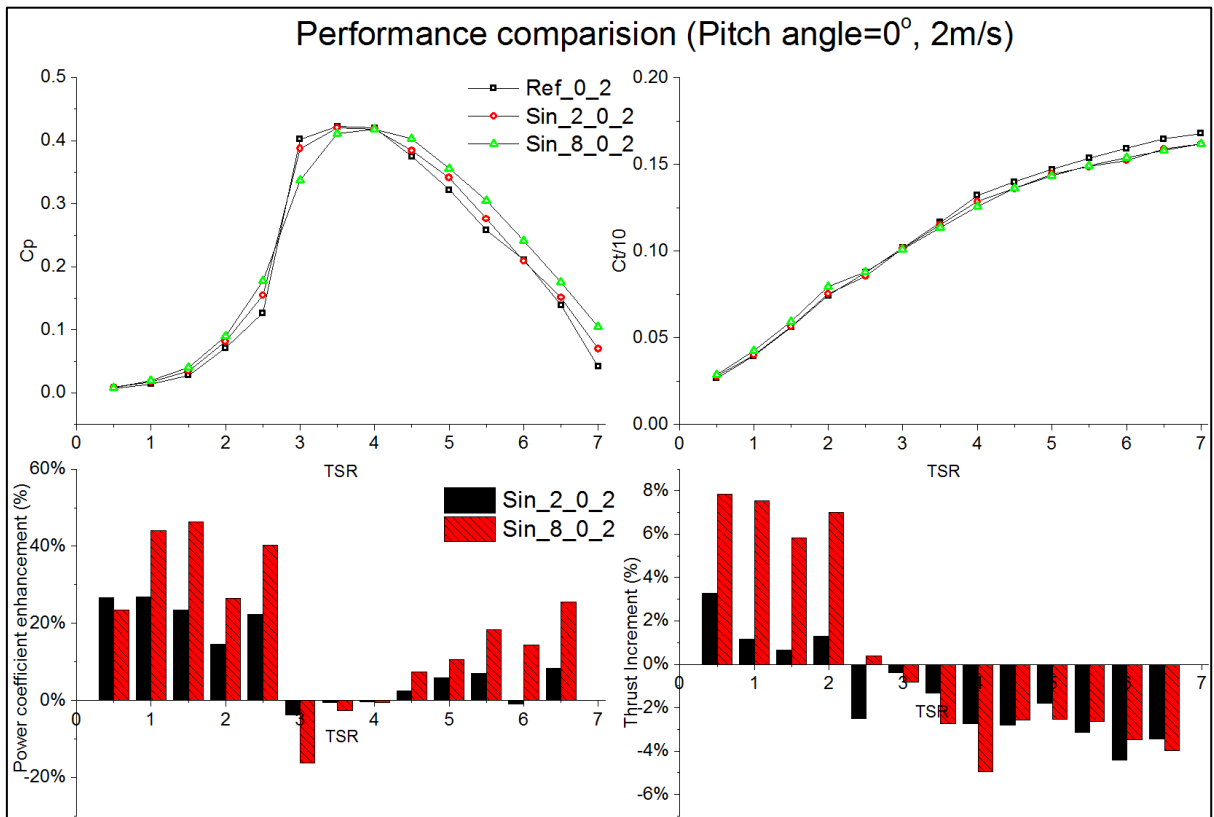


Figure 5-9 Performance comparison (Pitch=0°, 2m/s)

First of all the turbine models with 0° pitch angle were tested and the results are presented in Figure 5-9. The top two plots show the power coefficients (C_p) and the thrust coefficients ($C_t/10$) and the bottom two plots show the comparison of different leading-edge tubercle profiles against the reference turbine. It can be seen that the leading-edge tubercles can improve the performance of the turbine in the lower range of TSRs (0.5 to 2.5), where the turbine is suffering from stall. Under these conditions, a turbine with leading-edge tubercles can generate more force, which can be observed in both C_p and $C_t/10$. Around 40% more torque can be achieved due to the leading-edge tubercles. However, with the increase in TSR, the C_p values of the Ref turbine and Sin_2 turbine reach a maximum value of 0.43, at $TSR=3.5$, while the turbine Sin_8 reached its maximum at $TSR=4$. At the higher end of TSRs, turbines Sin_2 and Sin_8 can generate around 15 to 20% more torque and around 4% less thrust with the influence caused by Sin_8 more obvious than that of Sin_2.

Following the 0° pitch angle tests, the pitch angle setting was increased to +4°, which was the most efficient pitch angle setting for the reference turbine, and the tests were repeated. As shown in Figure 5-10, similar to the results with the 0° pitch angle, the leading-edge tubercles can contribute more torque at the lower end of the TSR range, as well as thrust. A maximum of

30% more torque can be produced at TSR=1.5. Compared with Sin_2, the impact caused by Sin_8 is more obvious in both C_p and $C_t/10$. On the other hand, the effect of the leading-edge tubercles was smaller relative to that at 0° pitch angle. As noted, the leading-edge tubercles did not have any effect on the maximum C_p apart from shifting its TSR from 3.5 to 4.0.

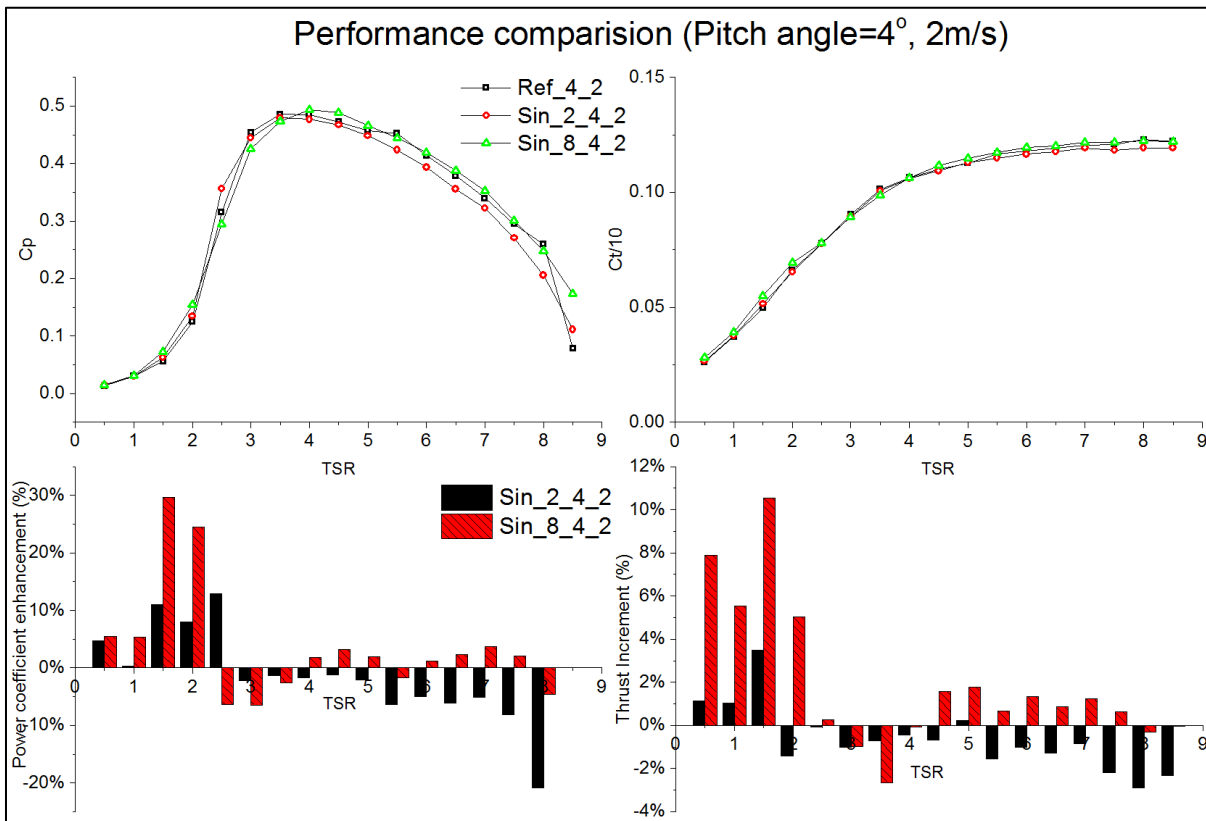


Figure 5-10 Performance comparison (Pitch= 4° , 2m/s)

Following the same procedure, the turbine models with 8° pitch angle were tested and results evaluated. According to Figure 5-11, as expected and in-line with the results of the previous test cases, the tubercles improved the performance over the lower TSR range and did not have any obvious impact on the maximum C_p . However, the leading edge tubercles significantly increased the thrust coefficient, $C_t/10$, with around a 10% increment caused by Sin_8. This indicated that the blades are generating higher force however this force contributes more to the thrust than the torque.

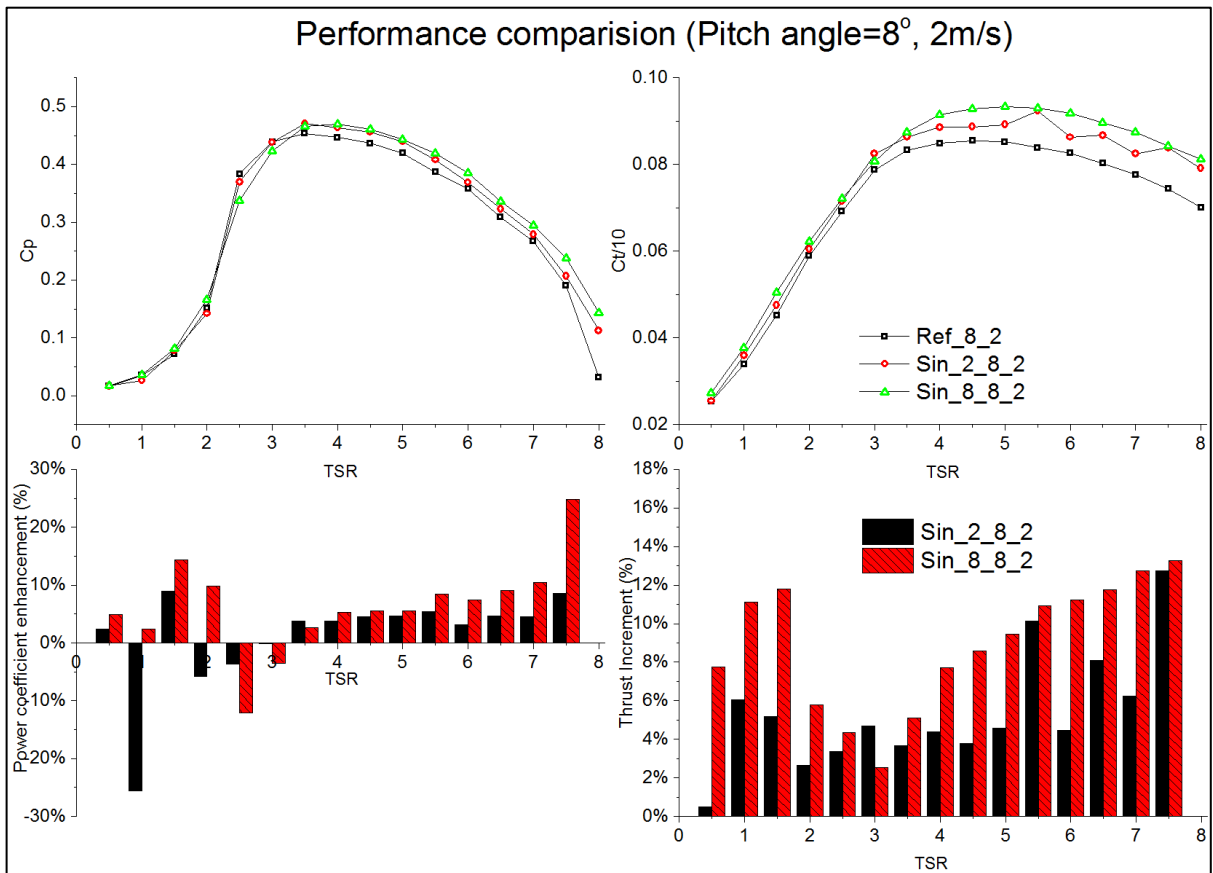


Figure 5-11 Performance comparison (Pitch=8°, 2m/s)

5.3.3 Key findings on the effects of tubercles on open water hydrodynamic performance

Based on the above open water tests of the reference turbine and the turbines with the biomimetic blades the following further remarks can be made on the effects of the tubercles:

- The impact of the leading-edge tubercles is mainly in the lower range of TSRs (up to 2.5), while the blade is operating under stall conditions. Leading-edge tubercles can greatly enhance the force generated by the turbine blade, which can both result in a higher torque and a higher thrust.
- For the lower pitch angles, the improvement caused by the leading-edge tubercles is higher than the case for higher pitch angle. It was also demonstrated that the biomimetic concept can help to improve the performance while the turbine is working under stall conditions. Turbines with leading edge tubercles will start at a lower current velocity.
- The application of the leading edge tubercle concept does not compromise the maximum power coefficient value of the turbine but slightly shifts the distribution of this coefficient over the tip speed ratios tested, towards the higher range.

5.4 Cavitation observation tests

As observed in the open water hydrodynamic performance test, various forms of blade cavitation have been observed, which may pose significant detrimental effect on the power generation, blade erosion and noise generation. Therefore how the leading-edge tubercles would affect the blade cavitation had to be investigated.

5.4.1 Experimental setup

The cavitation tests were also conducted in the ECT by using a similar set up to the open water tests described earlier. The turbine was mounted on the dynamometer, K&R H33. The DC motor was mounted on top of the dynamometer to drive the turbine and control its rotational speed for the purpose of achieving the desired TSR and cavitation number ($Ca_{V0.7r}$).

Two high-speed cameras (NanoSense MK III, as shown in Figure 5-12) and a still DSLR camera (Nikon D90) were used to capture the moving and still images of the cavitation patterns, respectively. During the tests the strobe lights and high-speed cameras were triggered by the encoder on the dynamometer, in phase-lock mode, in order to freeze the image recordings to be always in the same blade position.

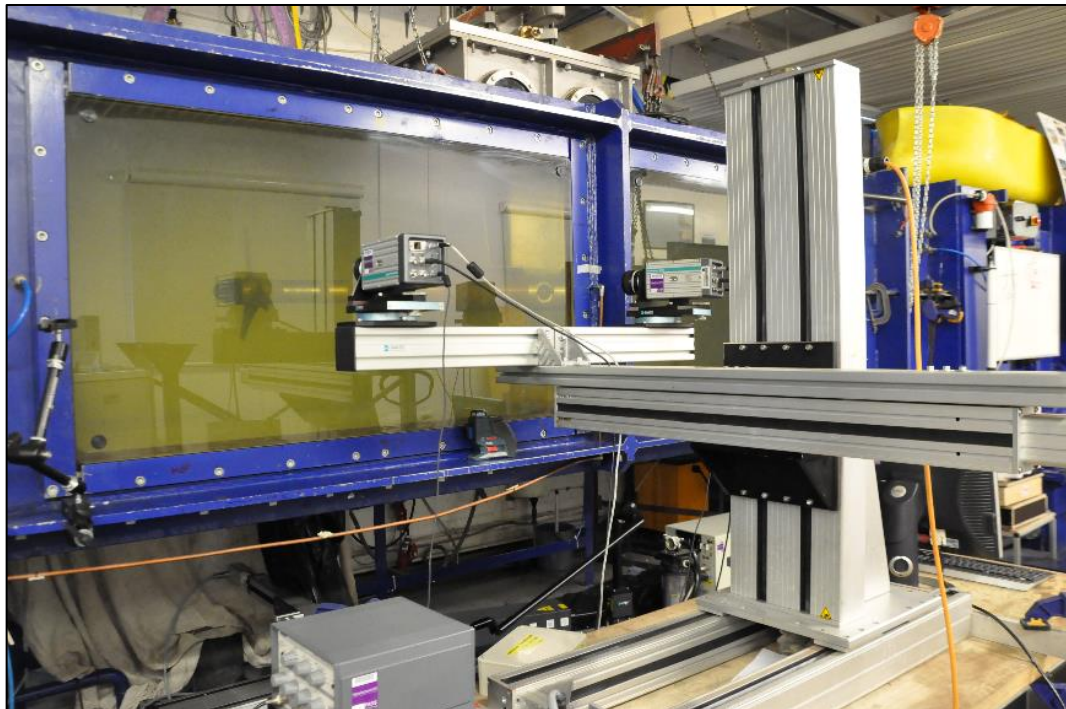


Figure 5-12 High-speed cameras to observe any cavitation.

Test matrix

Before conducting any cavitation experiments, understanding of the full-scale operating conditions is necessary in order to set the conditions during the test. As reviewed in Chapter 2, tidal energy researchers have developed various HATT devices to extract energy from the tidal current. These devices have different control systems to control either the blade pitch angle or the rotational speed to suit the changing incoming velocity in order to maintain the maximum power generating efficiency. They also have different designs of supporting structure, such as floating platforms, fixed foundations and so on.

Because of these differences, the operating conditions of HATTs are quite different. The blade radius, the blade pitch angle, the shaft emersion depth and also the rotational speed will all contribute in defining the operating conditions. The non-dimensional cavitation number, which assures the hydrodynamic similarity for cavitation between two geometrically similar turbines, is therefore dependent upon these parameters. The cavitation number, $Cav_{0.7r}$, which was described based on the radius at 0.7R, for different designs of tidal turbines was studied and calculated to determine the test conditions for the model tests.

Full-scale operating matrix of selected tidal turbine

According to the understanding in the literature review in Chapter 2, a 1.5MW tidal turbine is proposed here with around a 20m blade diameter subject to an assumed design tide (incoming flow) velocity of 3m/s with the assumption, $C_p=0.4$, the efficiency of gearbox=0.96 and the efficiency of generator=0.97. The main parameters of the notional full-scale design are given in Table 5-4. Depending on the supporting structure, the shaft immersion may change with the tide height and the wave height.

Table 5-4 Full-scale design

Diameter(m)	20	Rotation rate (RPM)	12
Number of blades	3	Current speed (m/s)	3
Immersion of shaft (m)	20	Max. wave height (m)	9

Considering the different working conditions, operating conditions matrices for a pitch control turbine and for a variable speed turbine combined with different shaft immersion depths and different incoming flow speeds were generated and are given in Table 5-5 and Table 5-6, respectively. By taking ebb tide and wave height into consideration, the shaft immersion varies

from 20m to 11m (only 1m blade tip clearance from the free surface). The incoming velocity (V_{in}) varies from 2m/s to 4.5m/s.

Based on the above assumptions, full-scale tidal turbine operating conditions were used to arrange the model tests. Because of the large number of test conditions, a systematic test regime was arranged to plot a cavitation diagram in order to cover a reasonable range of cavitation numbers.

Design of the test matrix

A systematic test matrix was arranged for the model experiments to consider the various parameters discussed earlier, as shown in Table 5-3. Three different incoming flow velocities were used and the rotational speed was varied accordingly to achieve the desired TSRs. By applying constant pressure on the tunnel the range of the cavitation numbers, which was applied in the test programme, covered the full-scale operating conditions, as shown in Figure 5-13. Three different pitch angles were also applied to understand the effect of pitch on the cavitation performance.

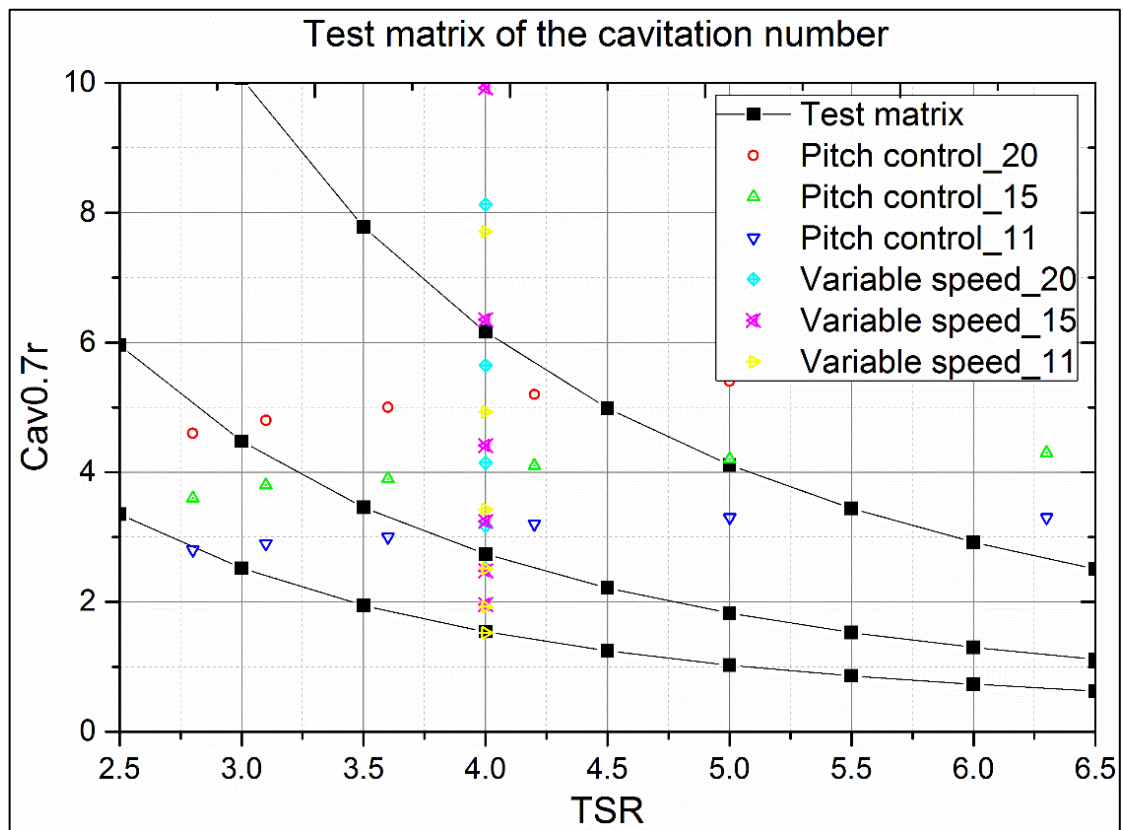


Figure 5-13 Test matrix against the full-scale conditions

Table 5-5 Full-scale operating conditions for pitch control turbine

Pitch control turbine with constant rotational speed					
Shaft immersion	Diameter	Vin	RPM	TSR	Cav
(m)	(m)	(m/s)			(0.7R)
20	20	4.5	12.0	2.8	4.6
20	20	4.0	12.0	3.1	4.8
20	20	3.5	12.0	3.6	5.0
20	20	3.0	12.0	4.2	5.2
20	20	2.5	12.0	5.0	5.4
20	20	2.0	12.0	6.3	5.5
15	20	4.5	12.0	2.8	3.6
15	20	4.0	12.0	3.1	3.8
15	20	3.5	12.0	3.6	3.9
15	20	3.0	12.0	4.2	4.1
15	20	2.5	12.0	5.0	4.2
15	20	2.0	12.0	6.3	4.3
11	20	4.5	12.0	2.8	2.8
11	20	4.0	12.0	3.1	2.9
11	20	3.5	12.0	3.6	3.0
11	20	3.0	12.0	4.2	3.2
11	20	2.5	12.0	5.0	3.3
11	20	2.0	12.0	6.3	3.3

Table 5-6 Full-scale operating conditions for variable speed control turbine

Variable speed control turbine with a constant TSR					
Shaft immersion	Diameter	Vin	RPM	TSR	Cav
(m)	(m)	(m/s)			(0.7R)
20	20	4.5	17.189	4.0	2.5
20	20	4.0	15.279	4.0	3.2
20	20	3.5	13.369	4.0	4.1
20	20	3.0	11.459	4.0	5.6
20	20	2.5	9.549	4.0	8.1
20	20	2.0	7.639	4.0	12.7
15	20	4.5	17.189	4.0	2.0
15	20	4.0	15.279	4.0	2.5
15	20	3.5	13.369	4.0	3.2
15	20	3.0	11.459	4.0	4.4
15	20	2.5	9.549	4.0	6.4
15	20	2.0	7.639	4.0	9.9
11	20	4.5	17.189	4.0	1.5
11	20	4.0	15.279	4.0	1.9
11	20	3.5	13.369	4.0	2.5
11	20	3.0	11.459	4.0	3.4
11	20	2.5	9.549	4.0	4.9
11	20	2.0	7.639	4.0	7.7

5.4.2 Result and discussion

In this section, the results of the cavitation observation are presented. First the comparison is made between the three different turbine models in order to find out the difference in the cavitation patterns caused by the leading-edge tubercles. Then, based on the experimental observations, a cavitation diagram is presented to provide a prediction for the full-scale operations. All of the cavitation observation pictures are also provided as a database in Appendix B.

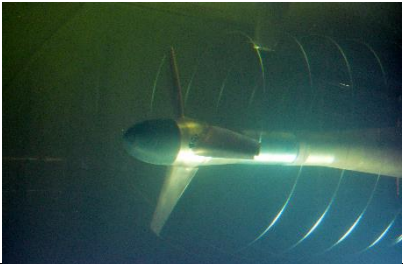
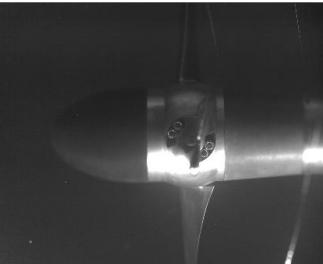

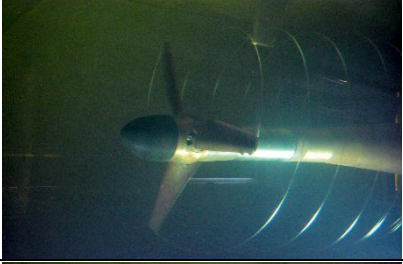
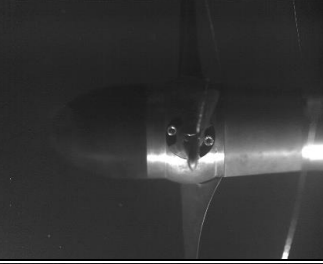

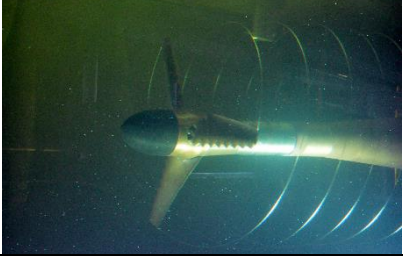
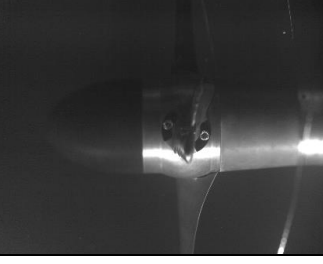

5.4.2.1 Typical cavitation patterns

During the tests, two main types of cavitation pattern were noted once the cavitation was observed. These were tip vortex cavitation and cloud cavitation with a misty appearance at the back or face side of the blade depending on the TSR. The development sequence of these cavitation types on the blades was such that first the tip vortex cavitation appeared due to the higher resultant velocity at the tip in a steady manner. Then the tip vortex cavitation was gradually accompanied by a rather misty appearance of unsteady cloud cavitation on either side of the turbine blade depending on the TSR. While the cloud cavitation would affect the turbine efficiency, the tip vortex cavitation did not have much impact on it.

Tip vortex cavitation

As presented in Table 5-7 (Pitch angle=+4°; V=3m/s; TSR=4; $C_{av0.75r}=3.5$) the tip vortex cavitation was the first and most common type of cavitation observed during the tests. This type of cavitation is also quite commonly observed in full-scale operation. Either a higher incoming velocity or ebb tide can trigger the tip vortex cavitation as well as extreme wave actions. During the tests it was noted that this cavitation was incepted downstream of the blades and then rapidly attached to all blade tips with increased loading in a rather steady and persistent manner. Once the vortices were attached and established at the tips it was noted that the nature (cavity dynamics) and size (diameter) of the vortices for the three different leading-edge profiles tested were quite similar in appearance.

Table 5-7 Tip vortex cavitation

Pitch angle=+4°; V=3m/s; TSR=4; Cav _{0.75r} =3.5			
Ref			
Sin_2			
Sin_8			

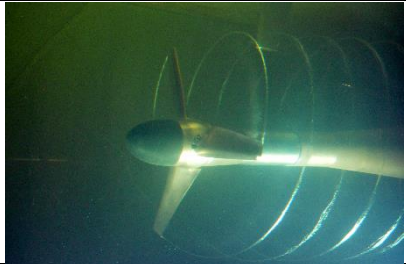
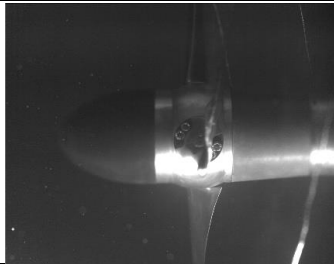

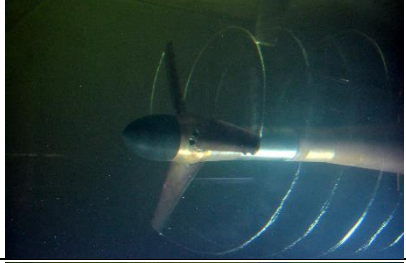
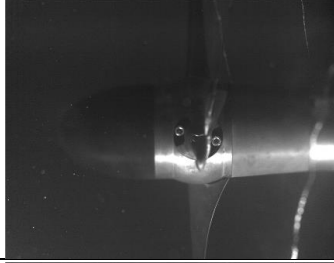
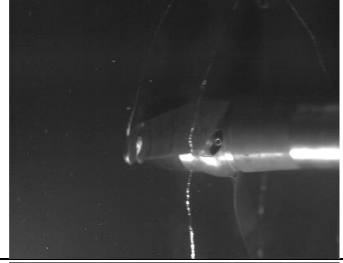
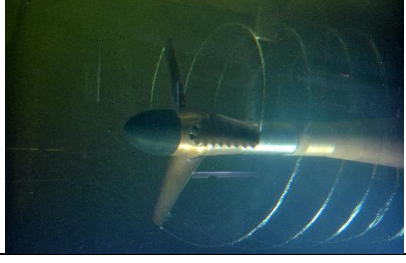
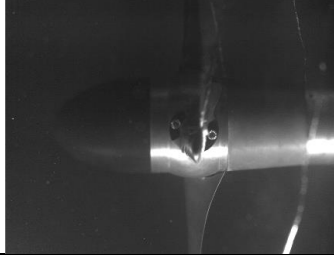
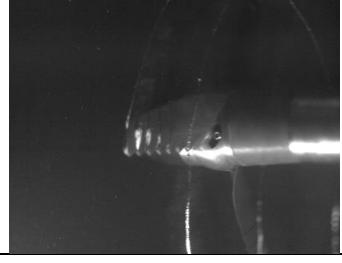
Back side cloud cavitation

As shown in Table 5-8, the tip vortex cavitation could be accompanied with a misty type cloud cavitation as the loading condition deteriorates (e.g. Pitch angle=+4°; V=4m/s; TSR=4; Cav_{0.75r}=1.5). This is the most severe condition that has been tested for the design TSR which corresponds to an extreme condition that a variable speed controlled turbine is working under 11m shaft immersion depth with only 1m tip clearance and 4.5m/s incoming velocity. This kind of cavitation is always observed at lower TSRs and lower pitch angle settings.

The observed cavitation was a cloud type cavitation but its nature was somehow different to classical cloud cavitation which has clear and relatively large bubbles. Instead it had a misty appearance composed of many micro-bubbles. The cavitation patterns of this type of cavitation were quite different for the different leading-edge designs. For the reference turbine, without leading-edge tubercles, the cavitation started from the leading edge and spread between 0.8r and 0.9r. Likewise for the turbines with the tubercles, the cavitation also started from the leading

edge. However, the tubercles helped the turbine to constrain the cavitation only to the trough areas. Because of the higher speed and lower pressure within the trough areas, Sin_8 produced more cavitation in the lower radius region (0.7R) compared to the other two turbines, i.e. the Ref and the Sin_2.

Table 5-8 Back side cloud cavitation

Pitch angle=+4°; V=4m/s; TSR=4; Cav _{0.75r} =1.5			
Ref			
Sin_2			
Sin_8			


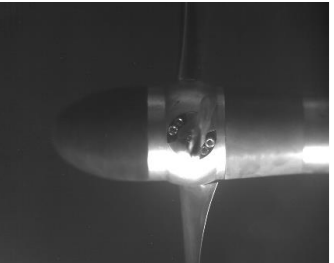

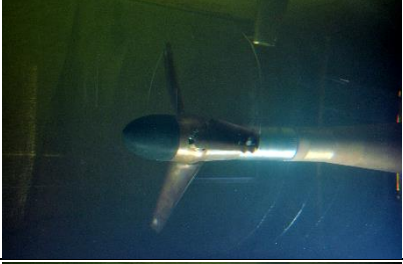
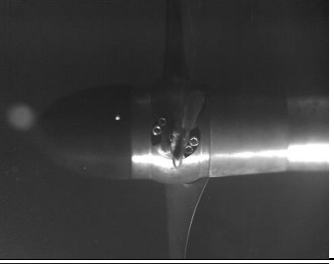
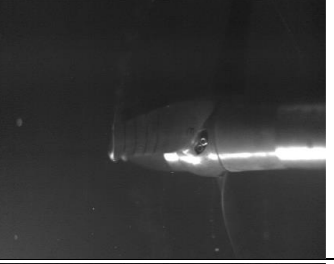
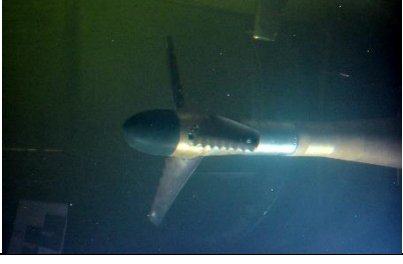
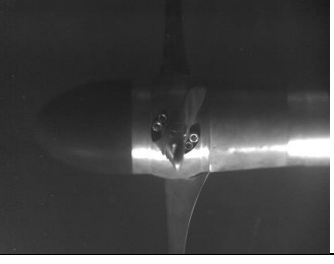

Face side cloud cavitation

The face side cloud cavitation, as presented in Table 5-9, was observed under the condition: Pitch angle=+8°; V=3m/s; TSR=6; Cav_{0.75r}=1.3. This kind of cavitation generally occurred at a higher TSR and a higher pitch angle setting. As shown in Figure 5-13, although this condition appeared to be more severe, it is not likely to be allowed to occur for a controlled turbine in full-scale. Nevertheless, if the turbine lost control and was freely spinning, this kind of cavitation might be experienced.

Regarding the cavitation pattern, this kind of cavitation started from the maximum thickness position along the blade section chord. The difference between the cavitation patterns

developed over the reference turbine and the turbines with tubercles was quite obvious and similar to the effect observed with the back side cloud cavitation. The tubercles helped the blades to constrain the cavitation development to the trough areas as it can be clearly seen in Figure 5-14.

Table 5-9 Face side cloud cavitation

Pitch angle=+8°; V=3m/s; TSR=6; Cav _{0.75r} =1.3			
Ref			
Sin_2			
Sin_8			

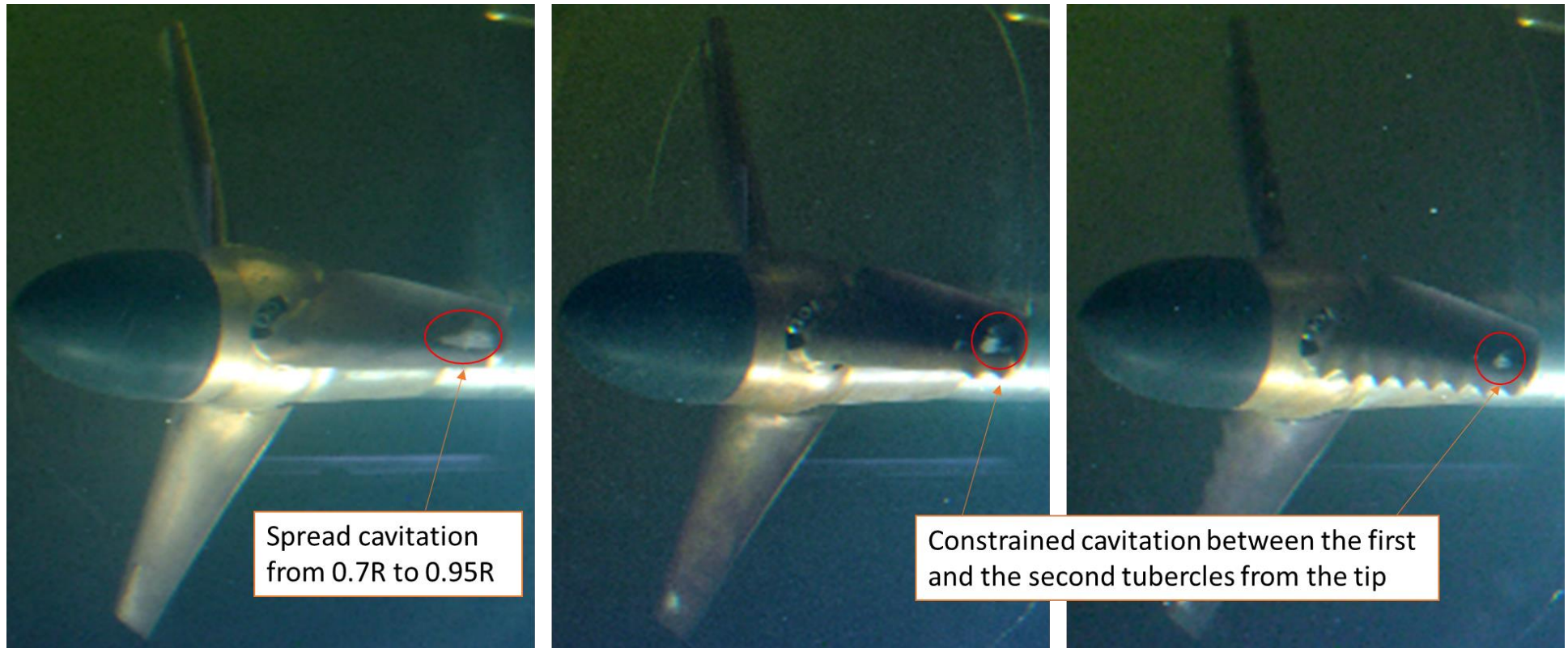


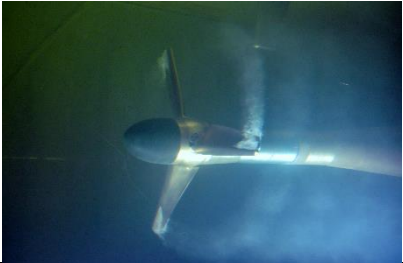
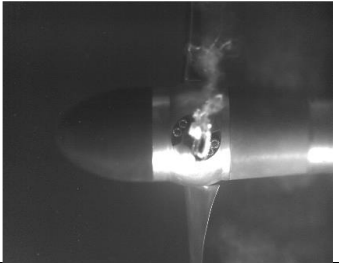
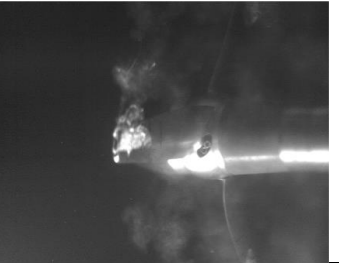

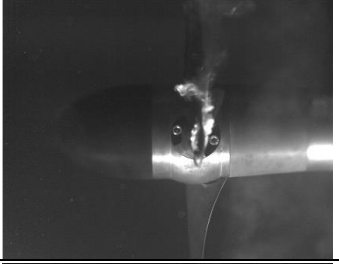

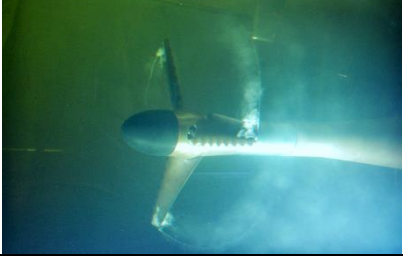
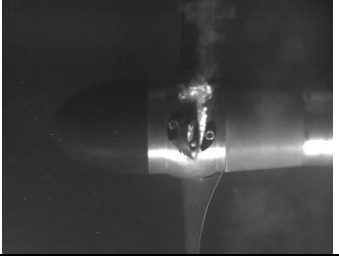

Figure 5-14 Detailed comparison of cavitation pattern (Pitch angle=+8°; V=3m/s; TSR=6; Cav_{0.75r}=1.3)

Double-side cloud cavitation

Imposing more severe conditions indicated that the turbines could develop cloud cavitation on both sides (back and face) of their blades in combination. This is shown in Table 5-10 for an operating condition of Pitch angle= $+4^\circ$; $V=4\text{m/s}$; $\text{TSR}=5.5$; $\text{Cav}_{0.75r}=0.86$. As for the face side cloud cavitation, this condition is not in the range of the full-scale operating conditions.

The influence caused by the leading-edge tubercles on this cavitation development was also very similar to that observed previously for the face side and back side cloud cavitation. Cavitation started from the maximum thickness position along the blade section chord. The tubercles helped the blades to constrain the cavitation to only to occur in the area after the trough of the leading edge and also to separate the cavitation into different regions.

Table 5-10 Double side cloud cavitation

Pitch angle= $+4^\circ$; $V=4\text{m/s}$; $\text{TSR}=5.5$; $\text{Cav}_{0.75r}=0.86$			
Ref			
Sin_2			
Sin_8			

5.4.2.2 Cavitation diagram

Following the observations and study of the cavitation patterns for the turbines, a cavitation inception diagram was devised for the different leading-edge designs and different pitch angles in order to provide a practical guideline for full-scale operation. The diagram is shown in Figure

5-15 where the different types of cavitation observed are labelled. In this diagram, the tip vortex cavitation inception was assumed when the vortex was attached to the blade tip.

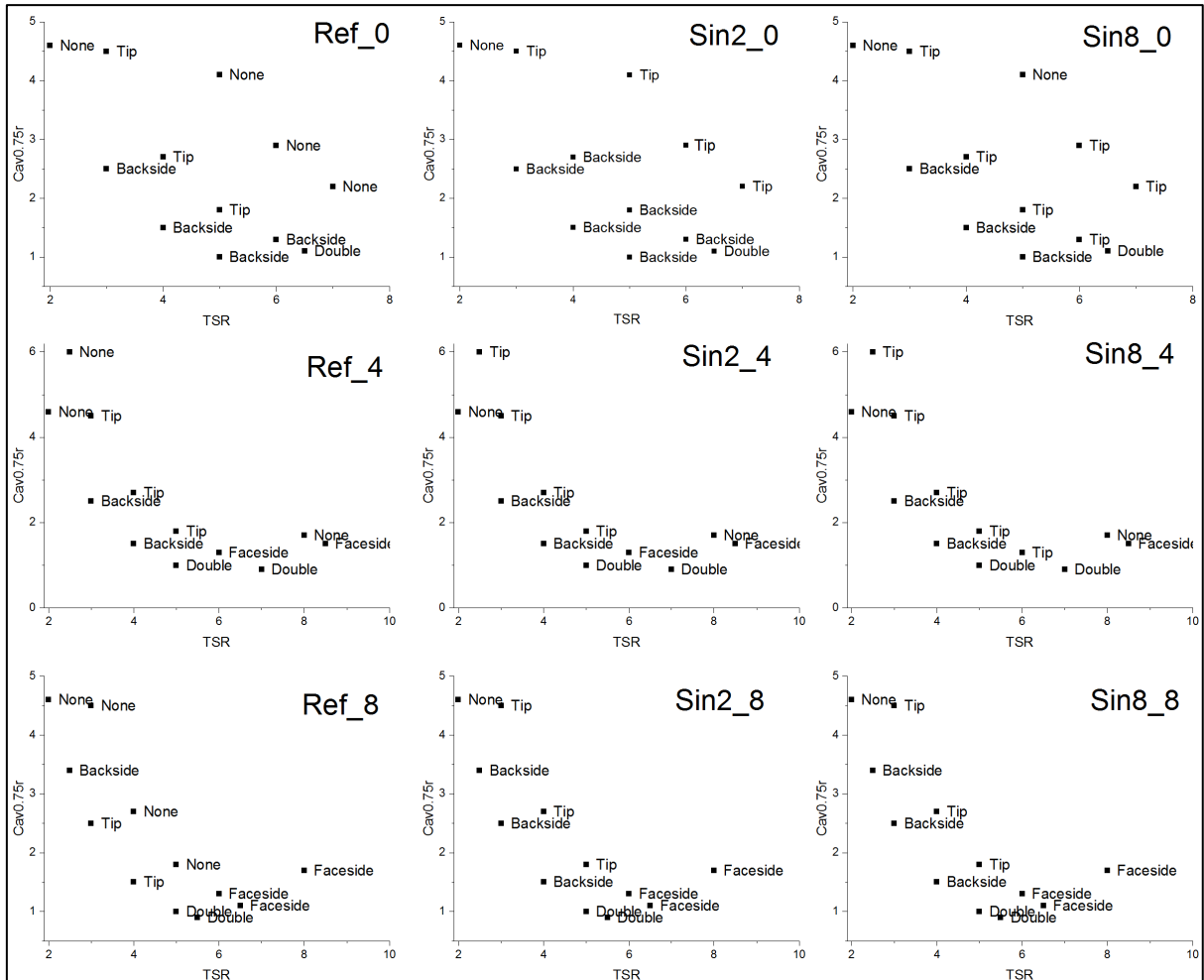


Figure 5-15 Cavitation inception diagram

As shown in Figure 5-14, the two main types of cavitation, which are the tip vortex and misty type cloud cavitation, can be observed with the turbines tested. The latter type can be erosive as well as potentially affecting the turbine efficiency while both types may contribute into the underwater noise level.

On the other hand, as remarked earlier, even though the leading-edge tubercles can limit the cavitation area to the trough parts of the profiles, they can also trigger the cavitation inception earlier than it would occur for the turbine without leading-edge tubercles depending on the pitch angle. This is because of the higher velocity and hence lower pressure in the trough area created by the tubercles.

5.4.3 Key findings on the effects of tubercles on cavitation performance

Based on the results and discussions of the cavitation observation tests the following concluding remarks can be made:

- Over the operating range tested the turbine models with three different leading edge profiles displayed mainly two types of cavitation pattern depending on the TSR, blade pitch and depth of the shaft submergence imposed. The observed cavitation types were restricted to the continuous tip vortex cavitation and gradually developing misty type cloud cavitation in combination with increasing blade loading. The latter type can develop on the back or face side of the blade as well as on both sides depending on the loading condition.
- The leading-edge tubercles may trigger earlier inception for the tip vortex cavitation compared to that for the reference turbine with the smooth leading edge. The strength of the tip vortex cavitation appeared to be similar for the different leading-edge profiles.
- However, the development of the misty type cloud cavitation over the leading-edge tubercles was restricted to the trough areas of the tubercles. This resulted in reduced cavitation extent and rather intermittent cavitation as opposed to the larger extent and continuous appearance of the cloud cavitation observed with the reference turbine.

5.5 Underwater radiated noise measurement tests

Alongside cavitation, underwater radiated noise (URN) is another undesirable physical phenomenon that may can be associated with turbines and might affect marine life. It is also a well-known fact that cavitation and noise are strongly related to each other and that the cavitation phenomenon is a major contributor to the URN levels, based on experience with marine propellers. Therefore alongside the cavitation observation tests, noise measurements were also conducted with the turbines with different blades, as described next.

5.5.1 Experimental setup

The noise measurements were captured by using a Bruel & Kjaer (B&K) data acquisition system and B&K Type 8103 hydrophone which was installed in a specially designed fin located in the tunnel with a straight-line distance 438mm to the centre of the model turbine, as shown in Figure 5-16.

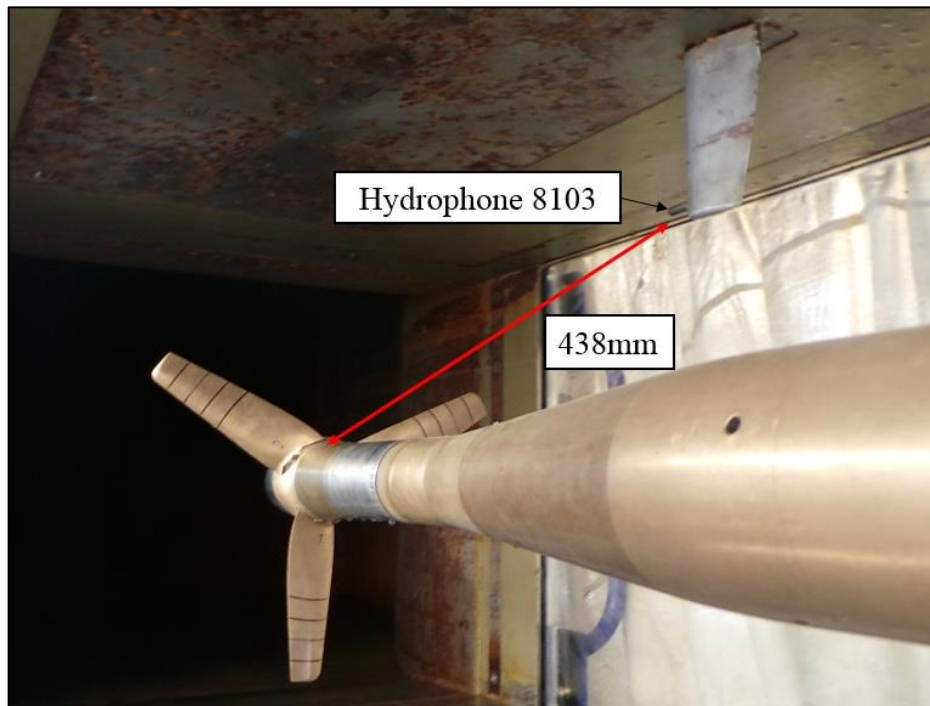


Figure 5-16 Arrangement of the test turbine and hydrophone

The noise signals were then processed using the PULSE lab-shop software CPB and FFT analysers. The captured signals, which are in 1Hz and 1/3 octave bands, were averaged over 50 seconds to eliminate the effect of any instantaneous noise sources. The settings in Table 5-11 were used with the 8103 hydrophone.

Table 5-11 Hydrophone data acquisition settings

Lower centre frequency	20 Hz
Upper centre frequency	20 kHz
Acoustic weighting	as signal
Reference Pressure	1 μ Pa
Overall bands - weighting	none

Figure 5-17 below shows various aspects related to the hydrophone. The top figure is the calibration configuration for the B&K 8103 with the Pistonphone Type 4228 and the couple UA-0548. Even though the hydrophone was factory calibrated, this system provided quick and accurate calibration and ensured that the factory calibration was still valid. The calibration frequency, nominally 250Hz, was 251.2Hz \pm 0.1% as defined by ISO 266. The sound level produced by the Pistonphone is nominally 156.8 \pm 0.2 dB re 1 μ Pa at the reference conditions. The middle figure shows the connection diagram. The hydrophone was submersible in water up to the BNC connection end. The connection end should be clear of the water at all times. The bottom figure in Figure 5-17 is the receiving frequency characteristics of the hydrophone, indicating accurate readings for the range of frequencies that were of interest for this study (up to 6 kHz).

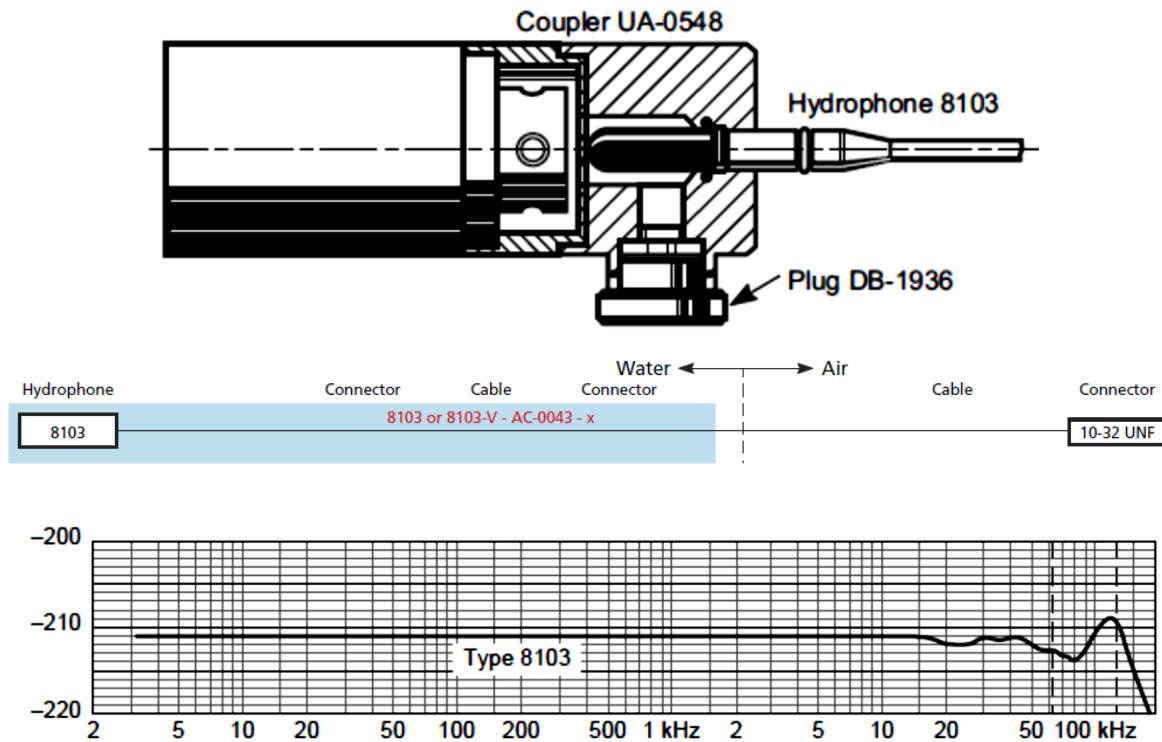


Figure 5-17 Calibration configuration of the Hydrophone (Top), The connection diagram of the hydrophone (Middle) Typical Receiving Frequency Characteristics of B&K 8103(Bottom).

Following the recommendations of the 15th ITTC Cavitation Committee, the measured Sound Pressure Levels (SPL) were corrected to an equivalent 1 Hz bandwidth and 1m source level using Equation 5-7 (ITTC, 1978).

$$SPL = SPL_m - 10\log\Delta f + 20\log(r) \quad \text{Equation 5-7}$$

where SPL is the Sound Pressure level in 1 Hz band in dB relative to 1 μPa at 1 m; SPL_m is the Sound Pressure level in 1/3 Octave band in dB relative to 1 μPa ; Δf is the frequency bandwidth for the 1/3 Octave band for each centre frequency; r is the distance of the location of the hydrophone from the turbine centreline.

In order to achieve the net noise sound pressure level (SPL_N) at each centre frequency, Equation 5-8 is used to subtract the background noise (SPL_B) from the total noise level (SPL_T) to interpret the contribution of the model turbine itself. The background noise level was measured by replacing tidal turbine model with a shaft fairing which has the same mass with the tidal turbine models as already shown in Figure 5-3. The background noise measurement was conducted in each corresponding conditions as per the test matrix in Table 5-3 with the same tunnel speed and the same shaft rotational speed.

$$SPL_N = 10\log[10^{(SPL_T/10)} - 10^{(SPL_B/10)}] \quad \text{Equation 5-8}$$

Test matrix

Alongside the cavitation observation tests, the underwater radiated noise (URN) levels of the subject turbines were also measured using the test matrix already shown in Table 5-3.

5.5.2 Results and discussions

The noise data generated within this experimental campaign was extremely large and hence to present all of the information was a challenge. Therefore, a comparison was first made between the different leading-edge designs to find out the effect of the leading-edge tubercles. These comparisons were made by using the total noise level data, which included the tunnel background noise due to the relative nature of the analysis. However, the measured sound pressure level of the reference model turbine was further analysed to subtract the tunnel

background noise and then the net noise levels were plotted to provide a bench mark database for a conventional HATT turbine model which is not readily available in open literature.

5.5.2.1 Effect of different leading-edge profiles on URN levels

A sampled dataset (Pitch angle= 8°) of this test campaign is shown in Figure 5-18, Figure 5-19 and Figure 5-20. Each figure presents the total URN noise level including the tunnel background noise, as raw data, that was collected by hydrophone 8103 in the 1Hz band with the incoming flow set to be 2, 3 and 4m/s respectively. Comparisons amongst the three different blade leading-edge profiles were made under the same operating conditions with respect to non-cavitating and cavitating conditions described in the following.

Non-cavitating conditions

As it can be seen in Figure 5-18, under the conditions starting from the lowest rotating speed of the motor (start) up to the highest condition (TSR=7), the noise levels of the three turbines with the different leading-edge profiles overlap each other. Similarly, from the top three plots of Figure 5-19, (for TSR=1 and TSR=2) and the first plot in Figure 5-20 (the starting condition), the noise levels of three different turbines overlap each other and are at a relatively low level under these cavitation free conditions.

Tip cavitation conditions

However, once the cavitation was incepted, the difference between the different leading-edge profiles was revealed. It can be seen in Figure 5-19 (for TSR=3 and TSR=4 at 3m/s) that the noise level of Sin2 and Sin8 in the frequency range from 1 KHz to 2 KHz is much higher than that for the reference turbine Ref. This was because, under these two conditions the turbines with the leading-edge tubercles can trigger the tip vortex cavitation earlier than for the reference turbine without the tubercles, as also shown in the cavitation diagram in Figure 5-15. This difference in noise results can also be seen in Figure 5-20 (for TSR=3 and TSR=4 at 4m/s) because of the additional cloud cavitation generated by Sin2 and Sin8 while only tip vortex cavitation was generated by the Reference turbine.

Cloud cavitation conditions

For the last condition in which all the three turbines were suffering from cloud cavitation, as shown in Figure 5-19 (for TSR=6), the noise level of the Reference turbine in the higher

frequency range from 3 KHz onwards was higher than that of the turbines with the leading-edge tubercles. This was because the face side cloud cavitation that was produced by the reference turbine had a larger extent and volume than that of the cavitation produced by the turbines Sin2 and Sin8, as shown in Table 5-9. In Figure 5-14 it can be easily seen that the face side cloud cavitation generated by the reference turbine has the largest extent while with the increase of the number of tubercles, the extent of cavitation is gradually reduced.

This phenomenon can also be seen under the condition $TSR=8$ and $V=2\text{m/s}$ as illustrated in Figure 5-18. It can be noticed that the noise level between the Reference turbine and the turbines with tubercles had a significant difference that ranges from 10-20dB. Comparing the detailed cavitation patterns shown Figure 5-21, while only a very small area of cavitation can be observed in the trough regions of the tubercles, the cloud cavitation generated by the reference turbine covered a much larger extent from around $0.8R$ to $0.95R$. Therefore, the tubercles can significantly change the noise signature via influencing the cavitation development pattern.

Based on the analysis of the noise measurements and the correlation with the cavitation observations, it is obvious that the underwater radiated noise level is highly dependent on the cavitation and its pattern. The leading-edge tubercles can influence the noise levels of the turbines through the particular cavitation patterned that they generate. However, when the turbine was working under a cavitation-free condition, the difference between the turbines with and without tubercles was negligible.

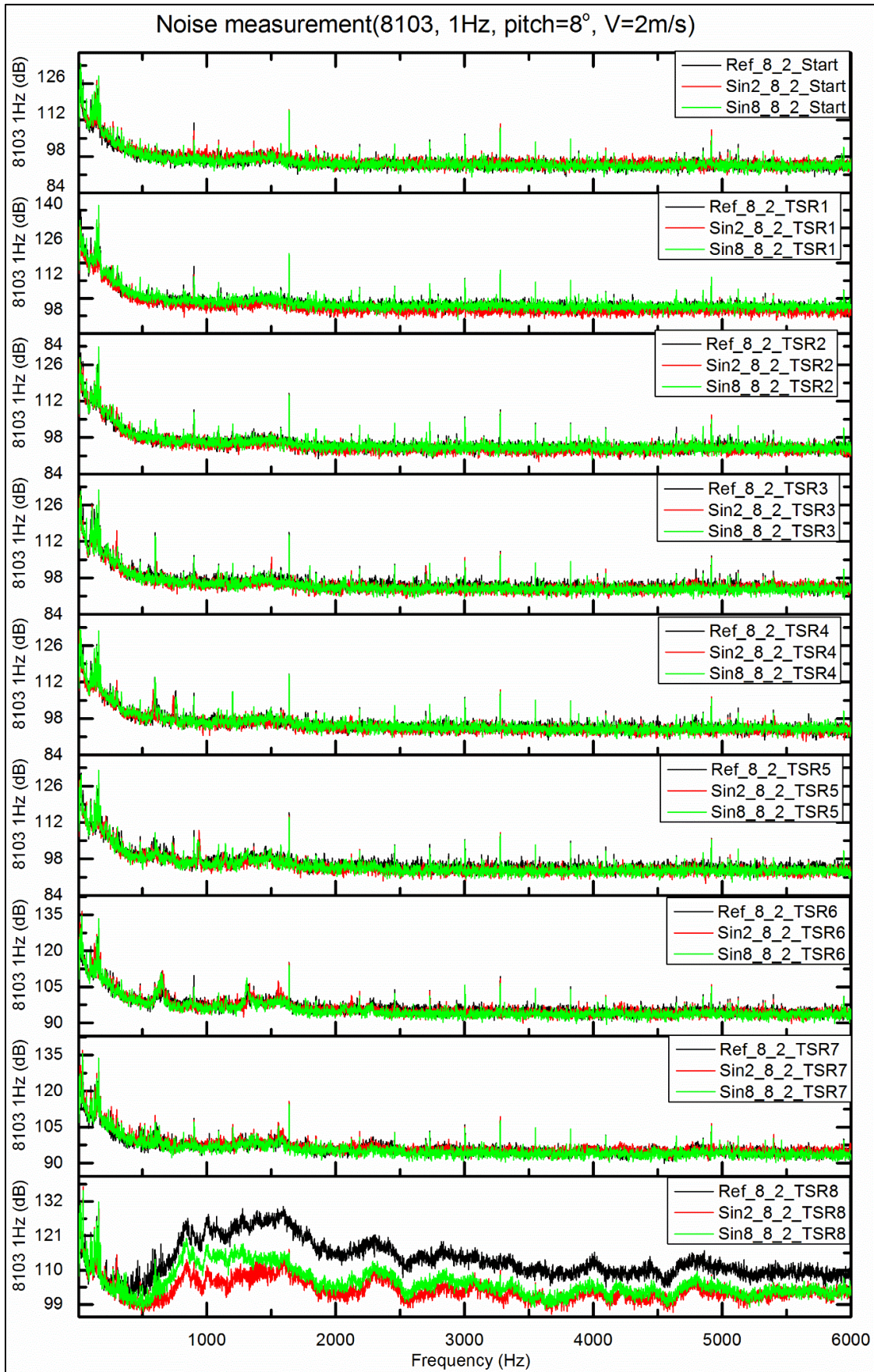


Figure 5-18 Comparative total noise levels measured in 1Hz band (Pitch angle=8°, V=2m/s)

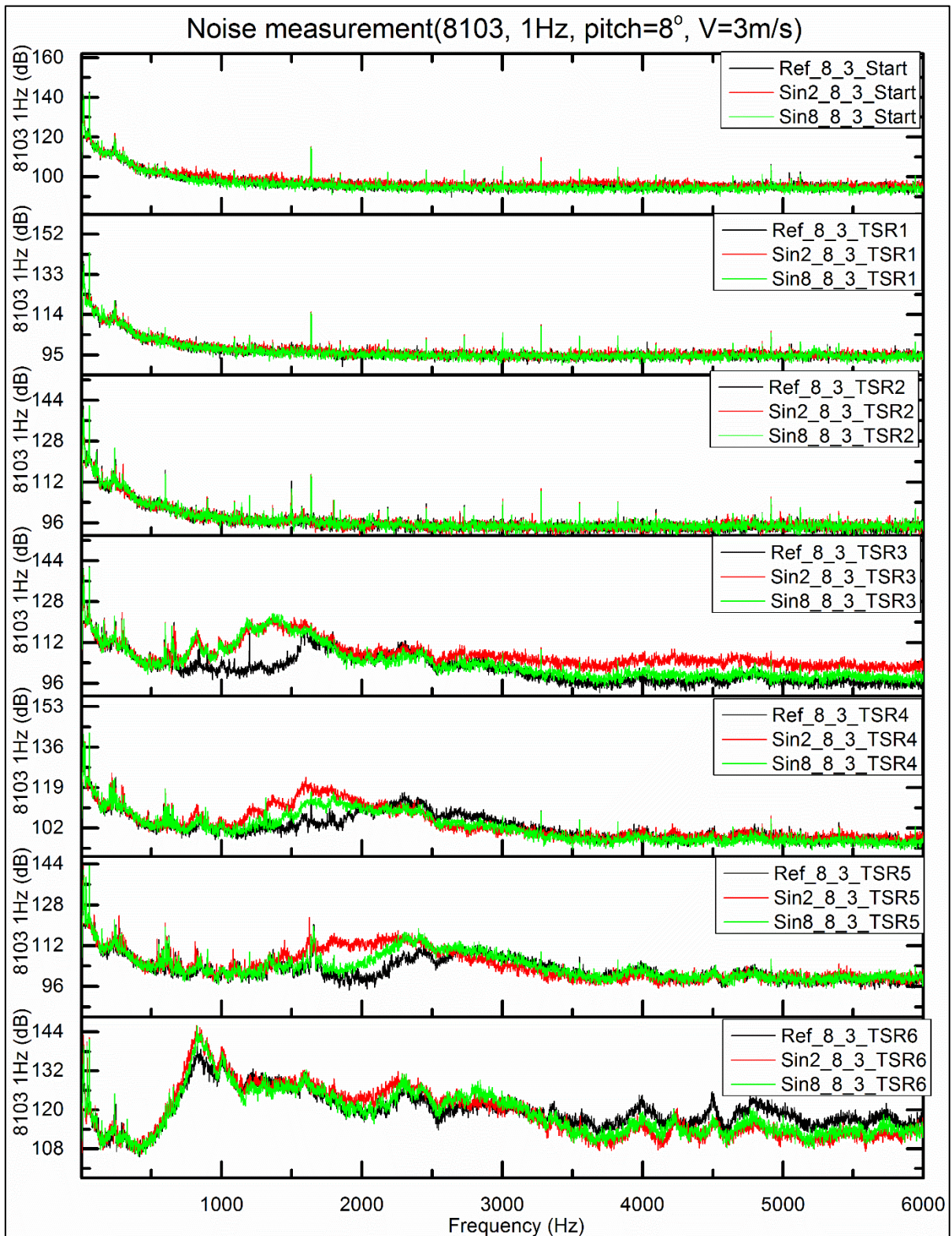


Figure 5-19 Comparative total noise levels measured in 1Hz band (Pitch angle=8°, V=3m/s)

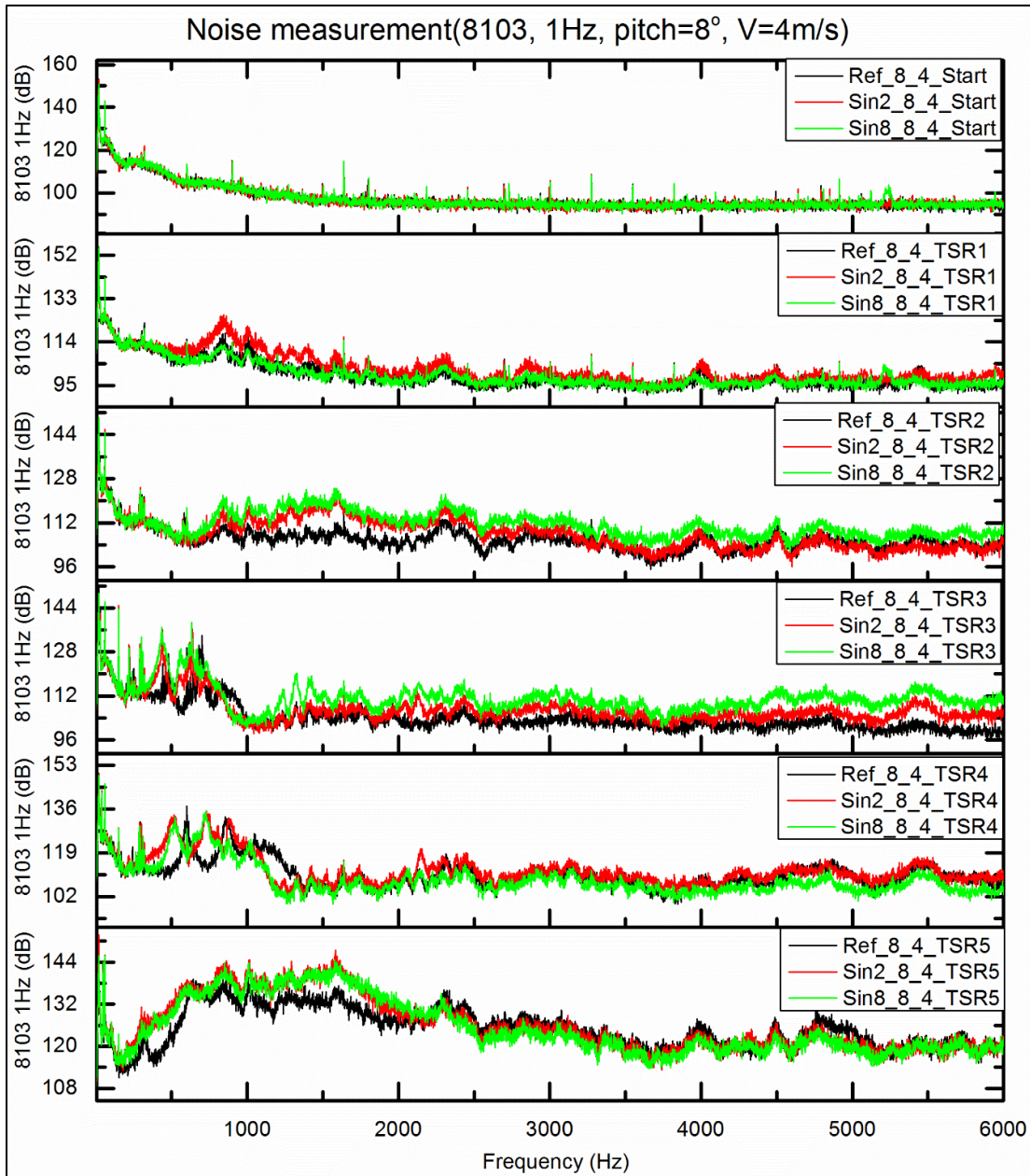


Figure 5-20 Comparative total noise levels measured in 1Hz band (Pitch angle= 8° , $V=4\text{m/s}$)

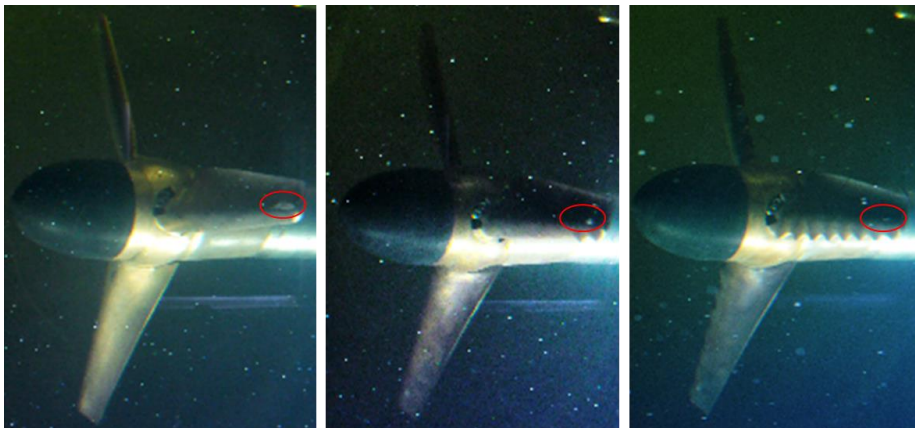


Figure 5-21 Detailed comparison of cavitation pattern (Pitch angle= $+8^{\circ}$; $V=2\text{m/s}$; $\text{TSR}=8$; $\text{Cav}_{0.75r}=1.7$)

5.5.2.2 Benchmark noise data for a typical HATT

Based on the relative noise analysis investigation, it was confirmed that the acoustic performance difference caused by the different leading-edge profiles is dominated by the cavitation patterns that are generated. In order to complement the earlier cavitation inception diagram, a noise map for the net noise levels of the reference turbine was also devised to provide benchmark data for a conventional HATT turbine model. This data together with the details of the turbine geometry presents an contribution to state-of-the-art tidal turbine hydrodynamic design studies as there is little if any data of this kind published other than limited resources such as Wang et al (2007).

As shown in Figure 5-22, Figure 5-23 and Figure 5-24, while the turbine was operating in a cavitation free condition, the total noise level was of a similar level to the background noise. Therefore, at certain frequencies, the noise data is apparently missing as the net noise level is less than 3dB. With the development of the blade cavitation the amplitude of the net noise SPL gradually increased. The cavitation contributed more in the higher frequency range as it can be observed in Figure 5-24 where from 500 Hz onwards the increase in the net noise SPLs was more obvious and gradually rose with the increased TSR and reduced cavitation number.

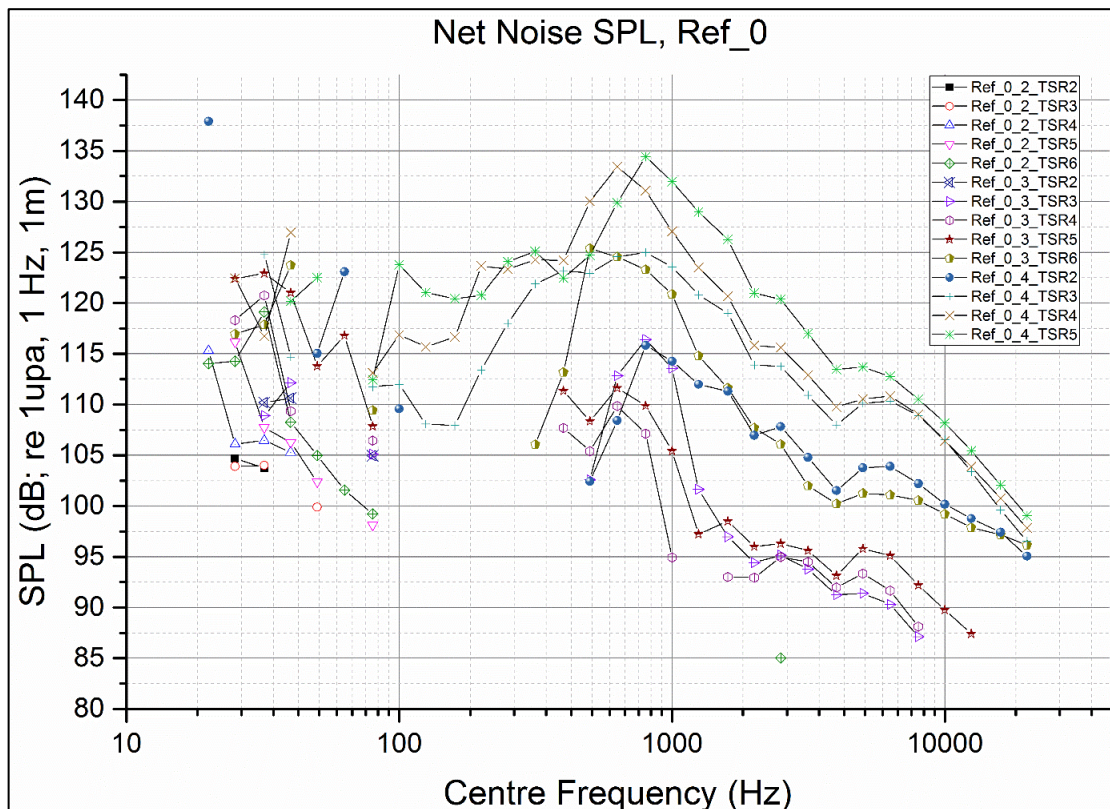


Figure 5-22 Net noise (sound pressure) level of Ref at pitch angle=0°

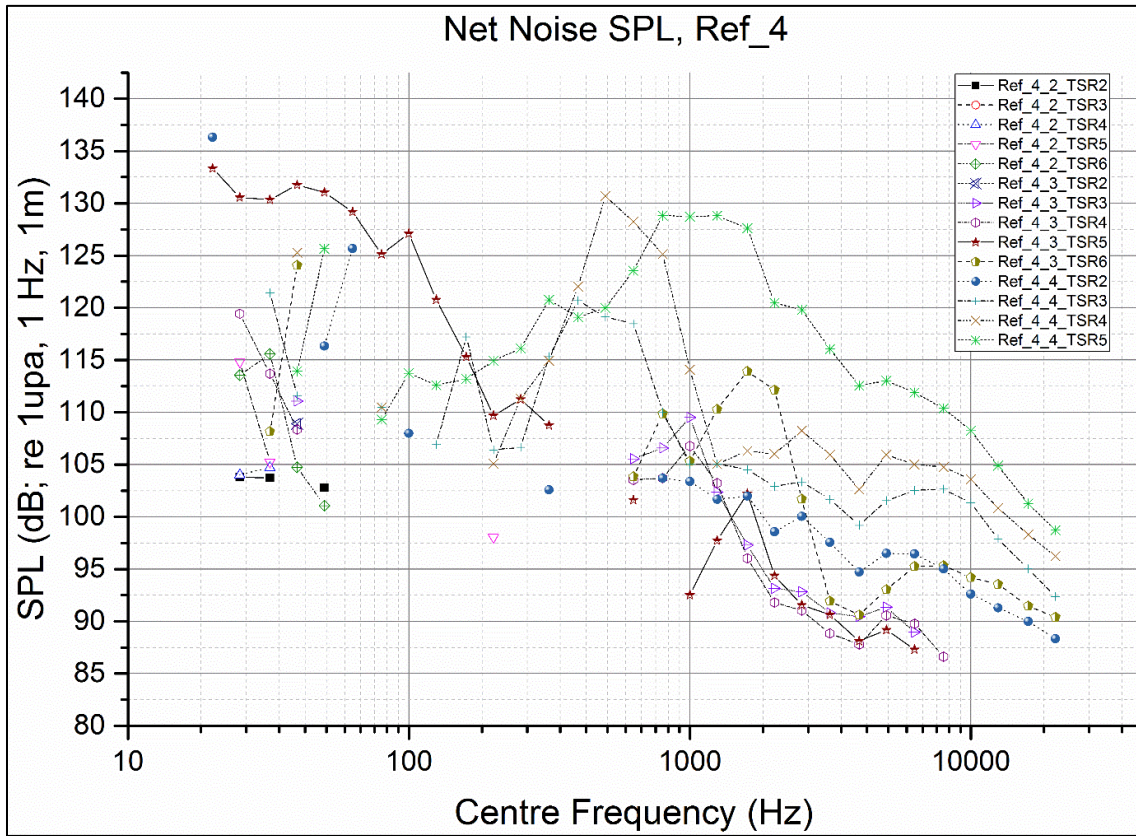


Figure 5-23 Net noise (sound pressure) level of Ref at pitch angle=4°

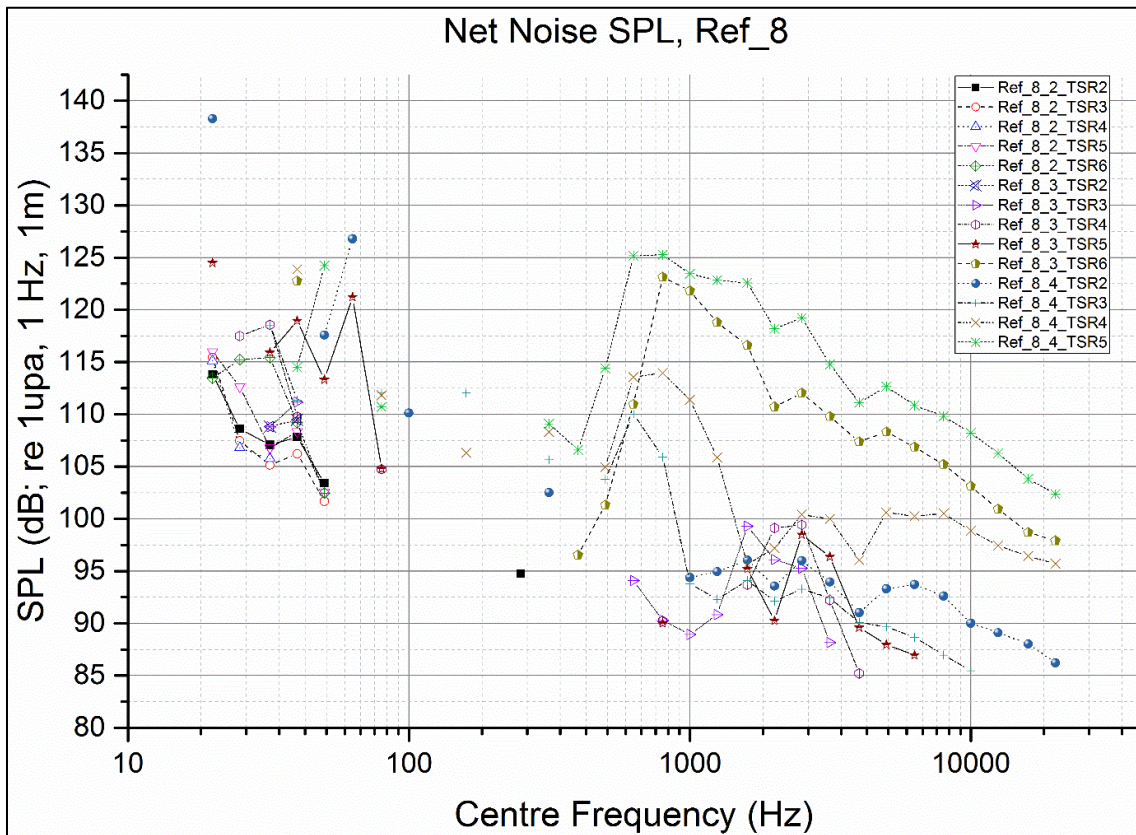


Figure 5-24 Net noise (sound pressure) level of Ref at pitch angle=8°

A cross plot given in Figure 5-25 is provided to demonstrate the effect of varying cavitation number on the Reference turbine SPLs by keeping the pitch angle and TSR (through by shaft speed) constant (at 0° and TSR4, respectively) while changing the tunnel inflow speed to 2, 3 and 4 m/s. Since the turbine was free of cavitation at 2m/s inflow speed (see Figure 5-15) there is no measurable SPL in Figure 5-25. However, with increasing inflow speed (at 3 and 4 m/s) the turbine first developed tip vortex cavitation at 3m/s which was further combined with cloud cavitation at 4m/s. This reflects as a 15-25dB increase in the measured SPLs for the broad range of frequencies after 300 Hz.

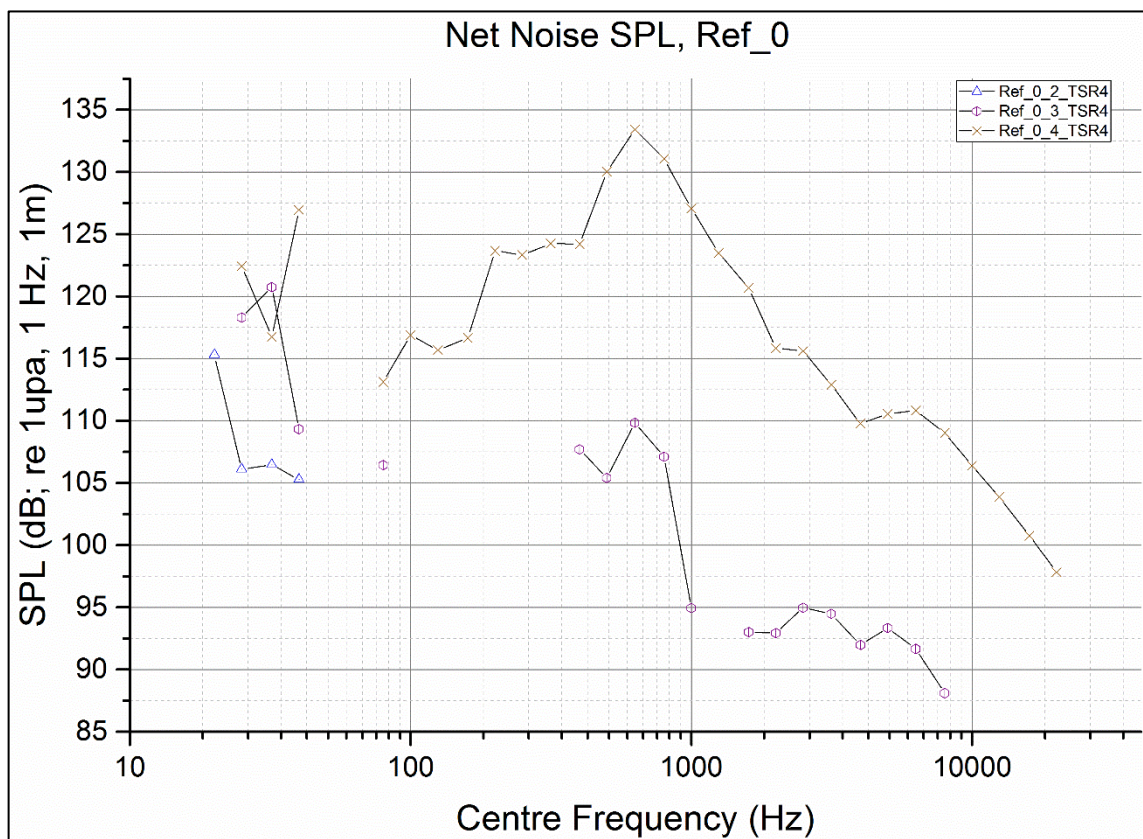


Figure 5-25 Net noise (sound pressure) level of Ref at pitch angle= 0° and TSR=4

Another cross plot of the measured SPLs with the Reference turbine is given in Figure 5-26 to demonstrate the effect of TSR (and hence cavitation number) for constant pitch and inflow speed (at 0° and 4m/s, respectively). As shown in this figure the trend is very clear as increasing the TSR (or reducing the cavitation number) via increasing the shaft speed resulted in increased SPLs.

The final cross plot for the Reference turbine is shown in Figure 5-27 to demonstrate the effect of blade pitch angle for constant TSR =4. As it is clearly shown, increasing blade pitch angle resulted in decreased blade loading and hence reduced SPLs.

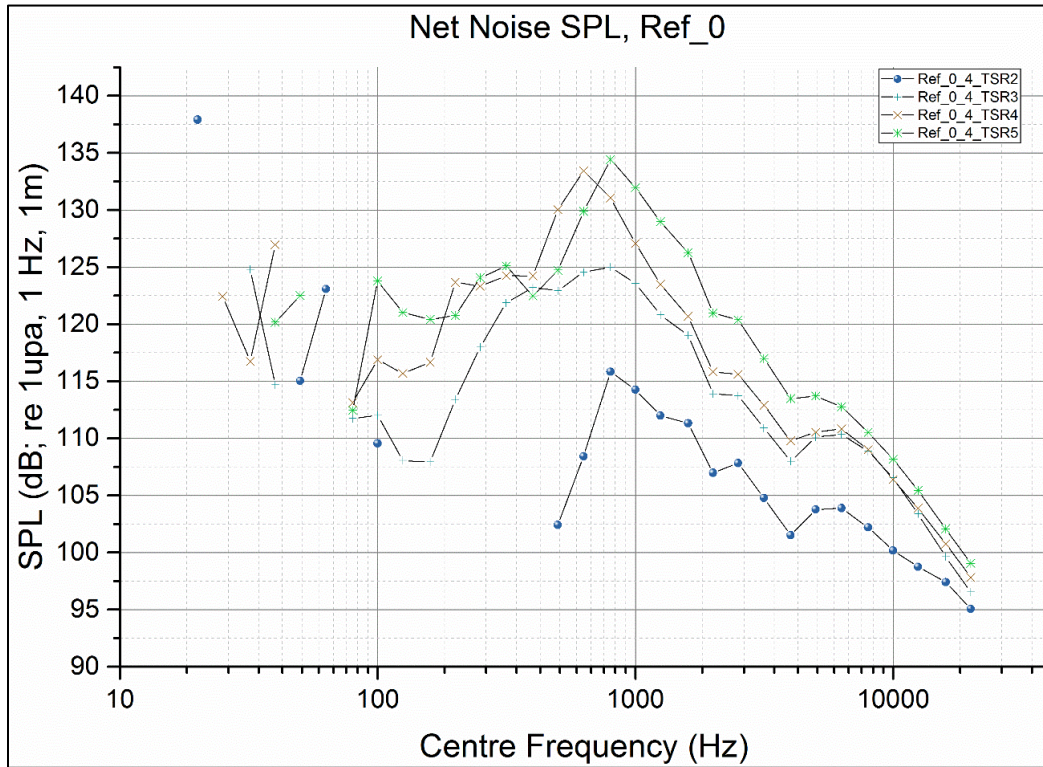


Figure 5-26 Net noise (sound pressure) level of Ref at pitch angle=0° and Vin=4m/s

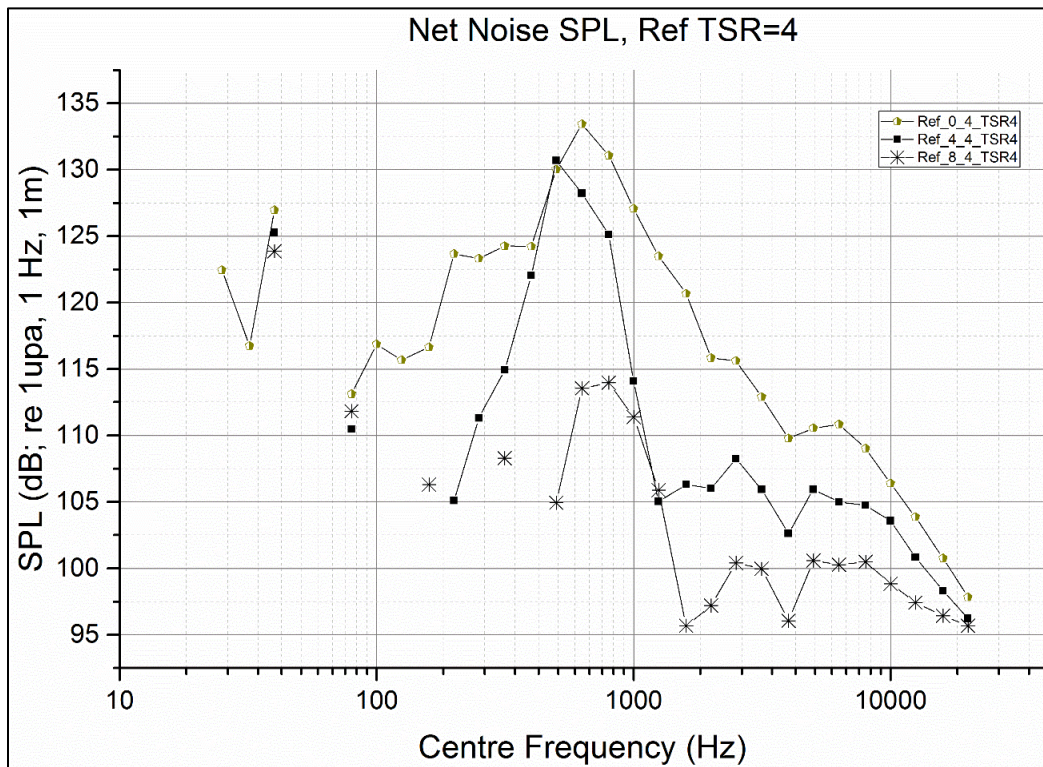


Figure 5-27 Net noise (sound pressure) level of Ref at TSR=4 and Vin=4m/s

5.5.3 Key findings on the effects of tubercles on underwater radiate noise

Based on the results and discussions of the underwater radiated noise tests, the following concluding remarks can be made:

- The three turbines displayed almost similar total noise levels until the cavitation was observed. Once the cavitation occurred, the noise levels of the turbines with tubercles are generally higher than those of the reference turbine because of the early inception of the tip cavitation. When cloud cavitation was generated, the noise levels of the turbines with the tubercles were lower than those of the Reference turbine due to the constrained development and the lesser extent of cloud cavitation.
- Net noise levels of a typical HATT turbine model indicated that the noise level was comparable to the background noise level while the turbine was not cavitating. Once the cavitation was incepted, the net noise level rose dramatically in the higher frequency (broad band) range due initially to the developing tip vortex and then gradually the combined contribution from the cloud cavitation.
- TSR and blade pitch angle are two important parameters affecting the noise levels of a typical HATT. While the increasing TSR increased the net SPL, the increased blade pitch angle reduced the net SPLs due to the reduced blade loading.

5.6 Detailed flow measurement tests with PIV

Having investigated the effect of the leading-edge tubercles on the various performance characteristics of the tidal turbine blades, significant differences were observed requiring further explanation. The most fundamental and perhaps effective explanations could be made by conducting a detailed flow investigation around the turbine blades and slipstream of the turbines, preferably, by using a state-of-the-art Stereo Particle Image Velocimetry (SPIV) system. In the following sections such experimental investigations were conducted in the ECT and the details of the tests are presented.

5.6.1 Experimental setup

2D/ Stereo PIV system and calibration

The PIV system used in these turbine tests was the same Dantec Dynamics Ltd system used for the simplified blade tests, presented in Chapter 4. However for the turbine tests, both 2D PIV (2D2V) and SPIV (2D3V) measurements were conducted. The 2D PIV measurement was carried out for the purpose of measuring the velocity distribution within the planar sections at different radii, as shown in Figure 5-28. The two dimensional velocity vectors in the turbine cross plane can be measured in this way. The flow separation area could be mapped and compared after the tests so that the differences of flow separation influenced by the leading-edge tubercles can be revealed. By following standard PIV practice the flow field was illuminated by a laser system and the highly seeded flow field was filmed using a high-speed CCD camera which was set perpendicular to the light sheet as shown in Figure 5-29 for a sample image.

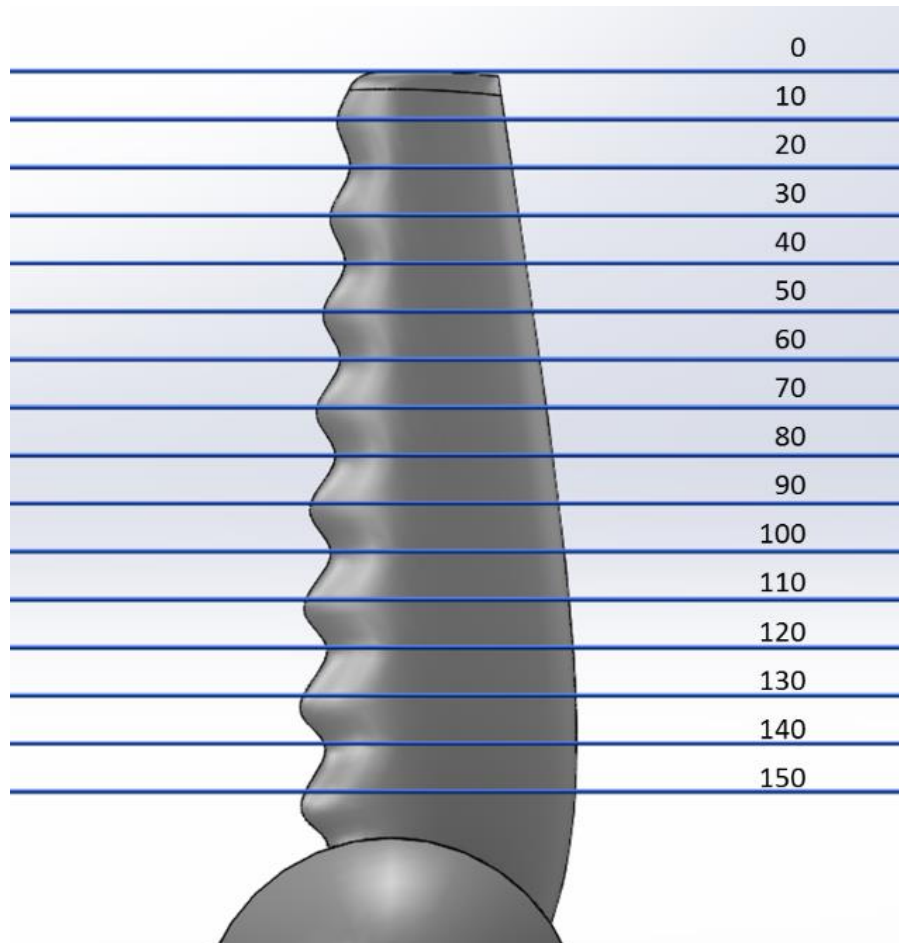


Figure 5-28. Radial positions of 2D PIV measurement planes

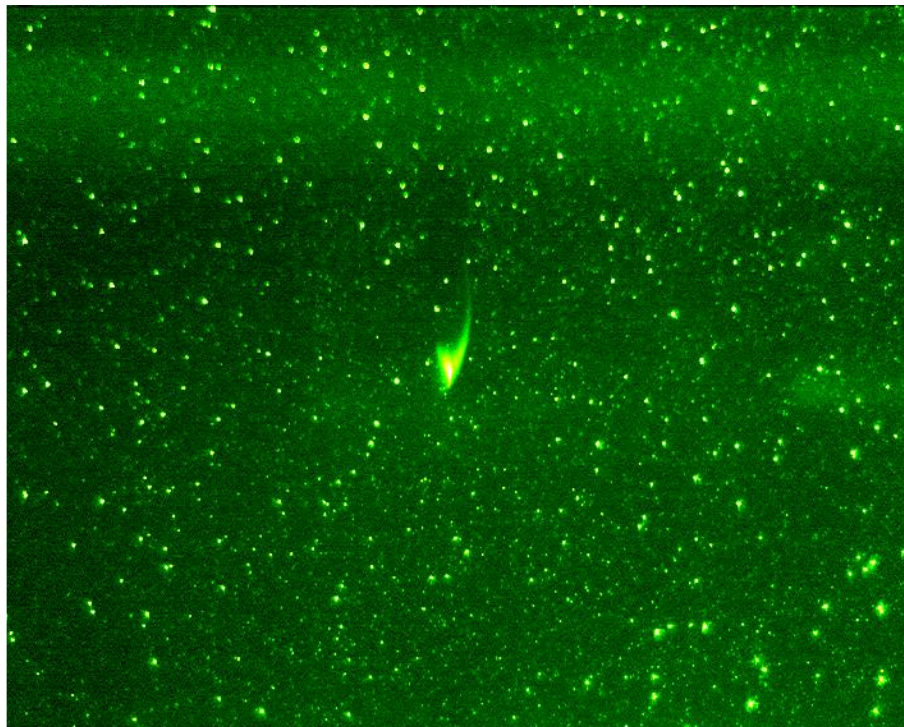


Figure 5-29. Sample image of 2D PIV

Following the 2D PIV measurement, a stereo PIV measurement was conducted to measure the three velocity components in a plane after the turbine. The measurement plane of the SPIV is shown in Figure 5-30. Stereo PIV also used the same laser system to illuminate the seeded flow field. However two high-speed cameras were used to capture the image from different angles. The setup of the Stereo PIV system in the ECT is shown in Figure 5-31. Typical images from the two cameras are shown in Figure 5-32.

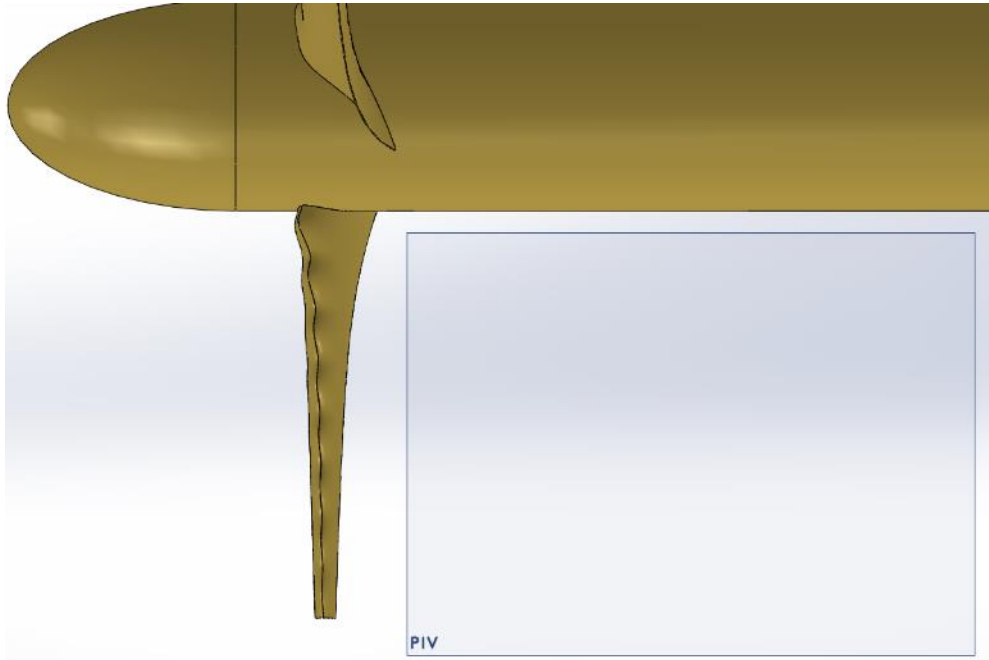


Figure 5-30. Stereo PIV measurement plane

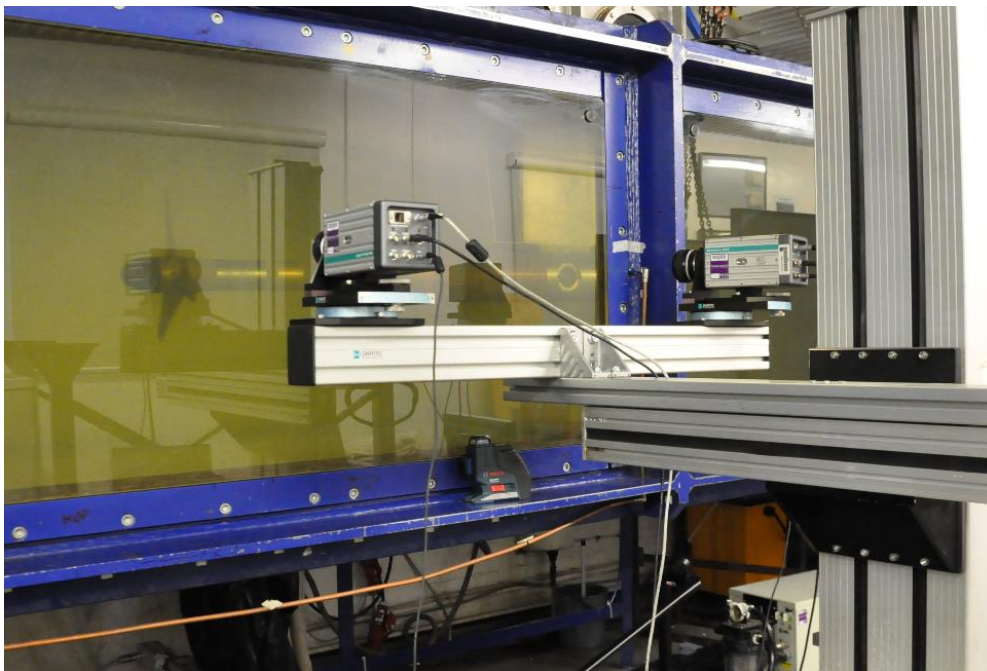


Figure 5-31. Setup of Stereo PIV alongside the test section of Emerson Cavitation Tunnel

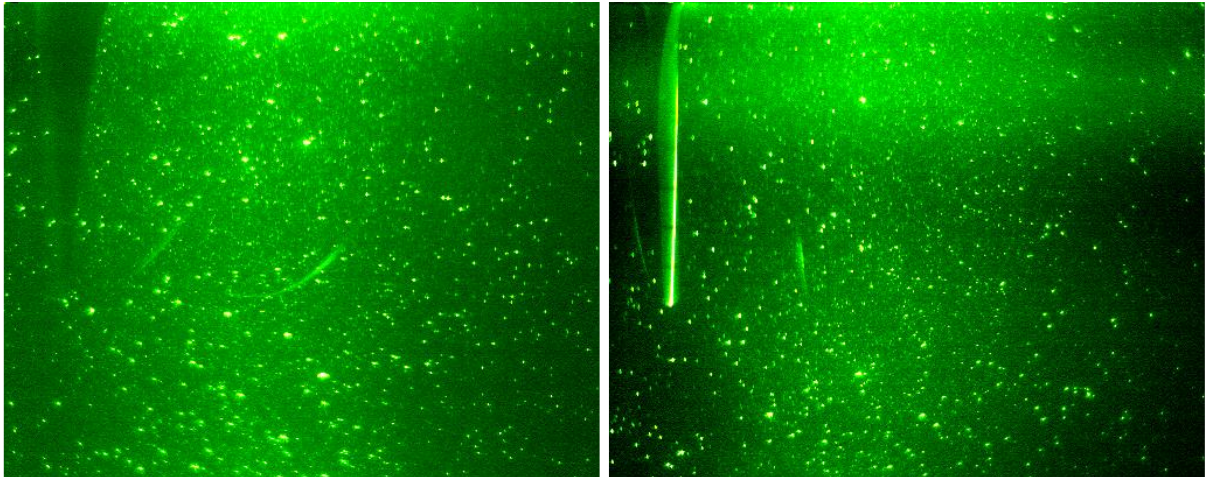


Figure 5-32. Typical stereo PIV Images from two different cameras shooting from different perspective angles

The use of the SPIV needs special calibration for the two cameras. Therefore a multi-level 270x190 mm calibration target was installed in the measurement plane, as shown in Figure 5-33. The two cameras viewed the calibration target from the same side but different angles. The calibration result is shown in Figure 5-34, which also shows the camera positions.

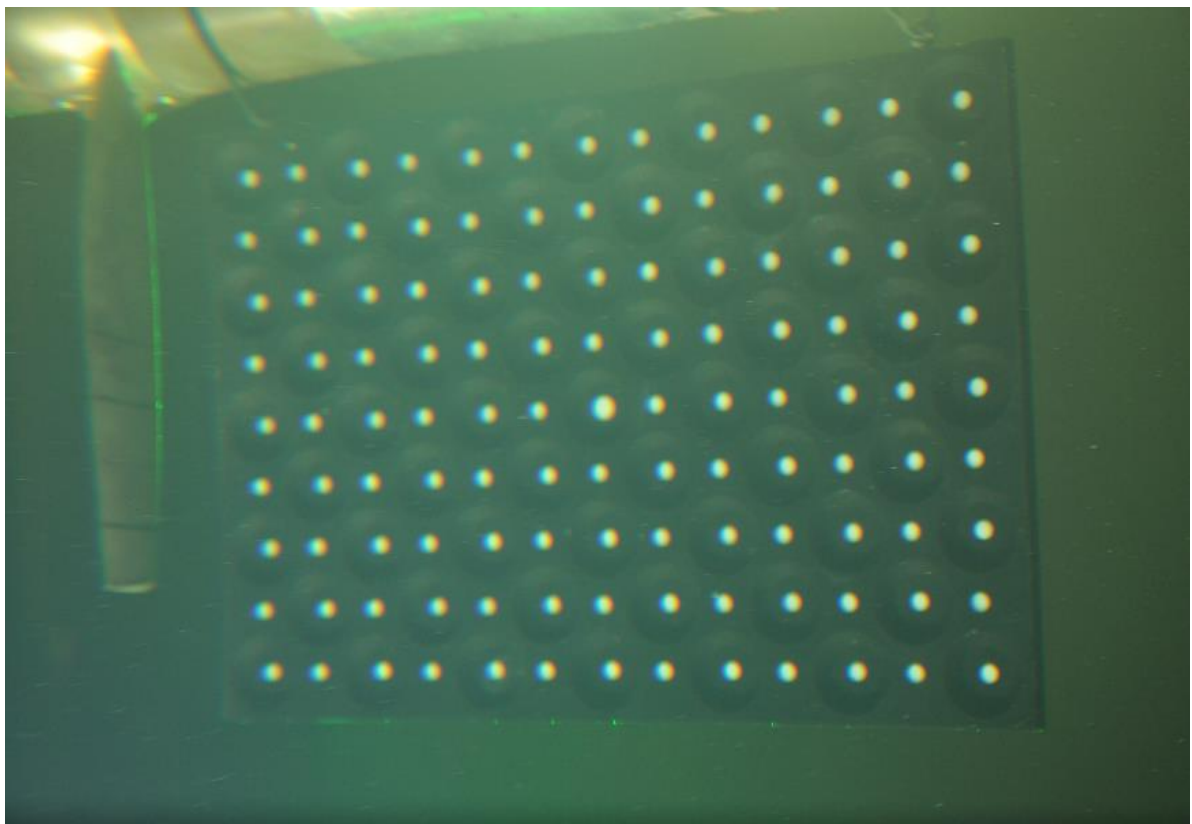


Figure 5-33. Calibration target for stereo PIV system located downstream of the model turbine

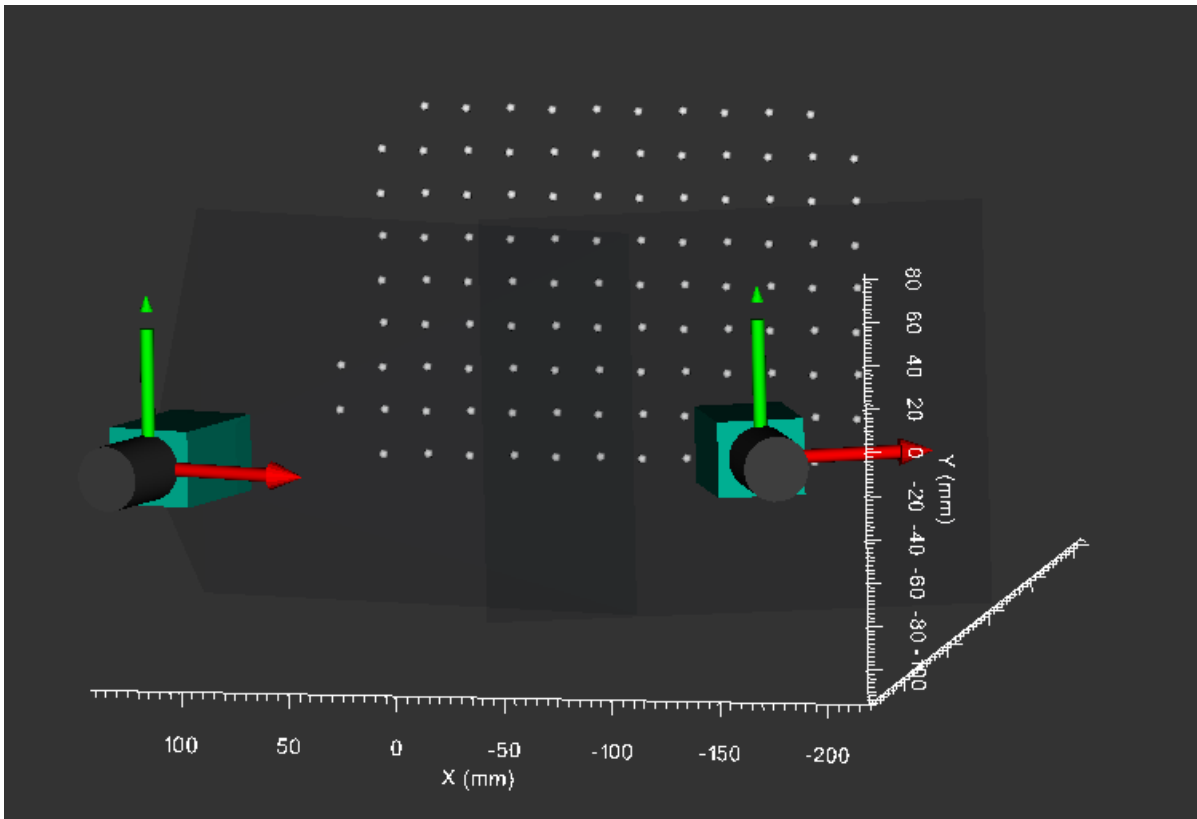


Figure 5-34 Calibration result of stereo PIV

Phase averaging and Image processing

Throughout the measurements of 2D PIV and SPIV, following the ECT's common practice in the use of PIV system for propeller measurement, 100 double-frame image pairs needed to be captured, analysed and averaged to achieve a high quality time-averaged velocity distribution with an economical cost of data handling and management. In order to capture these images always at the same azimuth position of the turbine, the camera and the laser were controlled and synchronized by a cyclic synchronizer. This cyclic synchronizer was based on an encoder on the motor and a CompactDAQ system from National Instruments coded in LabVIEW, which had the capability of triggering the camera at the desired angular positions. However, the rotational rate of the turbine needed to have a minimum value of 350rpm to enable the system.

In order to analyse the images and hence to determine the flow velocities, adaptive PIV analysis was used for the 2D images from each camera. Afterwards, the results of these 100 velocity samples were averaged to achieve a final 2D PIV measurement. By combining the calibration results and the 2D PIV data, finally the SPIV results with three component velocity could be achieved, as shown in Figure 5-35, and also the detailed structure of the tip vortex could be revealed.

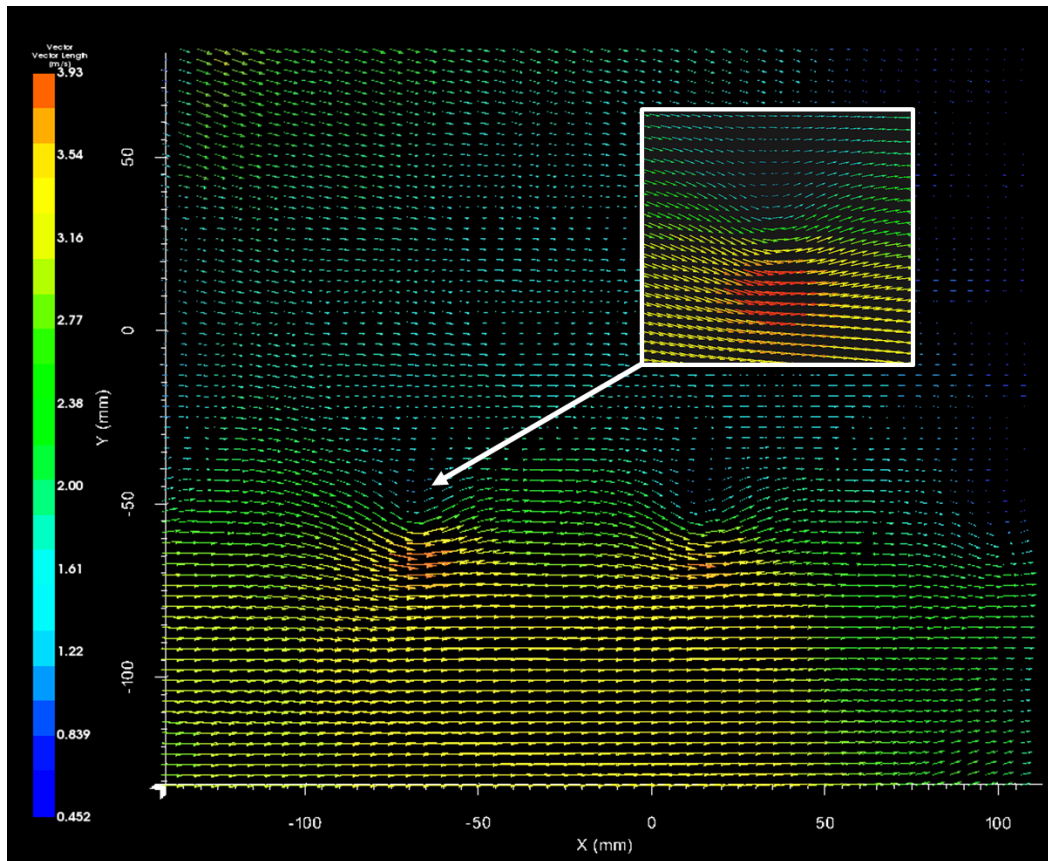


Figure 5-35 Stereo PIV result with a detailed tip vortex structure

Testing matrix

Based on the earlier open water hydrodynamic performance tests, the performance of the three turbines at three different pitch angles, 0° , $+4^\circ$ and $+8^\circ$, was evaluated in the first stage, which provided the guidelines for the PIV measurement. According to the test result at 2m/s, as already shown in Figure 5-8, even though the $+8^\circ$ pitch angle had a slightly lower peak power coefficient (C_p) compared to $+4^\circ$, it had much lower thrust ($C_t/10$) and also a higher C_p in the lower range of TSRs, which was critical for the starting performance of a fixed pitch turbine which couldn't operate its pitch angle to kick off spinning. Once the current speed reaches the turbine's cut-in speed, the turbine driven by the current starts spinning. With the increasing rotational speed, the TSR will increase from zero to the designed TSR (generally when C_p reached to its maximum value) and then the turbine will adjust its rotational speed to maintain the TSR to achieve the maximum power extraction. Therefore the lower end of TSR is critical for the turbine's starting performance.

Therefore the $+8^\circ$ pitch angle was selected with the following selected conditions to be investigated using PIV:

1. **Stall condition (TSR=2):** Tidal turbine will experience this condition while accelerating up to the optimum working condition (TSR=4). However under this stall condition, flow separation could occur. The most significant improvement resulting from the leading-edge tubercles has been found under this condition. During the test, an incoming velocity of 4m/s and a rotational speed of 382rpm were used. The performance comparison of C_p and $C_t/10$ is presented in Table 5-12.
2. **Optimum working condition (TSR=4):** This is the optimum condition under which the turbine would operate in order to maximise the power generation. This is also the turbine's design condition. Most turbines will maintain this TSR to achieve the maximum power coefficient. During the test, an incoming velocity of 3m/s and rotational speed of 573rpm were set.
3. **Overspeed condition (TSR=5):** This is the condition in which the turbine is working beyond the optimum TSR. This is often considered to be the overspeed condition that might be harmful for the generator and gearbox. However there are some turbines designed to operate under this condition since the higher rotational speed will result in better generator performance. More stable performance can be expected compared to the optimum working conditions under which the turbine might suffer from stall due to the natural flow fluctuation caused by waves or turbulence. During the test, an incoming velocity of 3m/s and rotational speed of 716rpm were set.

Comparisons of the measured C_p and $C_t/10$ for the different turbines at these conditions are presented in Table 5-12.

Table 5-12 Measured hydrodynamic performance data of model turbines in the selected PIV testing conditions

Power coefficient (C_p)					
Conditions	Ref	Sin2	(Increment ratio)	Sin8	(Increment ratio)
TSR2_4	17.1%	19.3%	12.4%	19.2%	12.1%
TSR4_3	46.4%	47.4%	2.2%	48.3%	4.3%
TSR5_3	44.4%	45.1%	1.6%	46.1%	4.0%
Thrust coefficient ($C_t/10$)					
Conditions	Ref	Sin2	(Increment ratio)	Sin8	(Increment ratio)
TSR2_4	6.0%	6.1%	1.4%	6.4%	6.4%
TSR4_3	8.6%	8.9%	4.6%	9.2%	7.7%
TSR5_3	8.6%	8.9%	4.0%	9.4%	9.2%

5.6.2 Results and discussions

5.6.2.1 Visualising the planar section using 2D PIV

For the purpose of mapping the flow separation region around the turbine blade, 2D PIV measurement was conducted for the above three turbines in the three typical conditions. All of the measurement results are presented as a database in Table 5-13 at TSR=2, Table 5-14 at TSR=4 and Table 5-15 at TSR=5. All of the cases are referred to in the form “Model_Velocity_TSR_Position”, i.e. “Ref_4_TSR2_10”. The velocity vector distribution is plotted with the actual image in the background.

Figure 5-36 illustrates the reference turbine being tested at 4m/s with TSR=2 and the measurement taken 10mm from the tip of the blade, 0.95R. The reference velocity vector, which is for the incoming velocity, has been subtracted from the total velocity measured in order to emphasise the flow separation. As it can be seen in Figure 5-36, the turbine is suffering from significant flow separation after the blade, as marked between the white dashed lines. With this methodology, the flow separation area can be clearly mapped and compared. However, under the conditions TSR4 (shown in Table 5-14) and TSR5 (shown in Table 5-15), as expected, there is no clear separation since the angles of attack are lower than the stall angle.

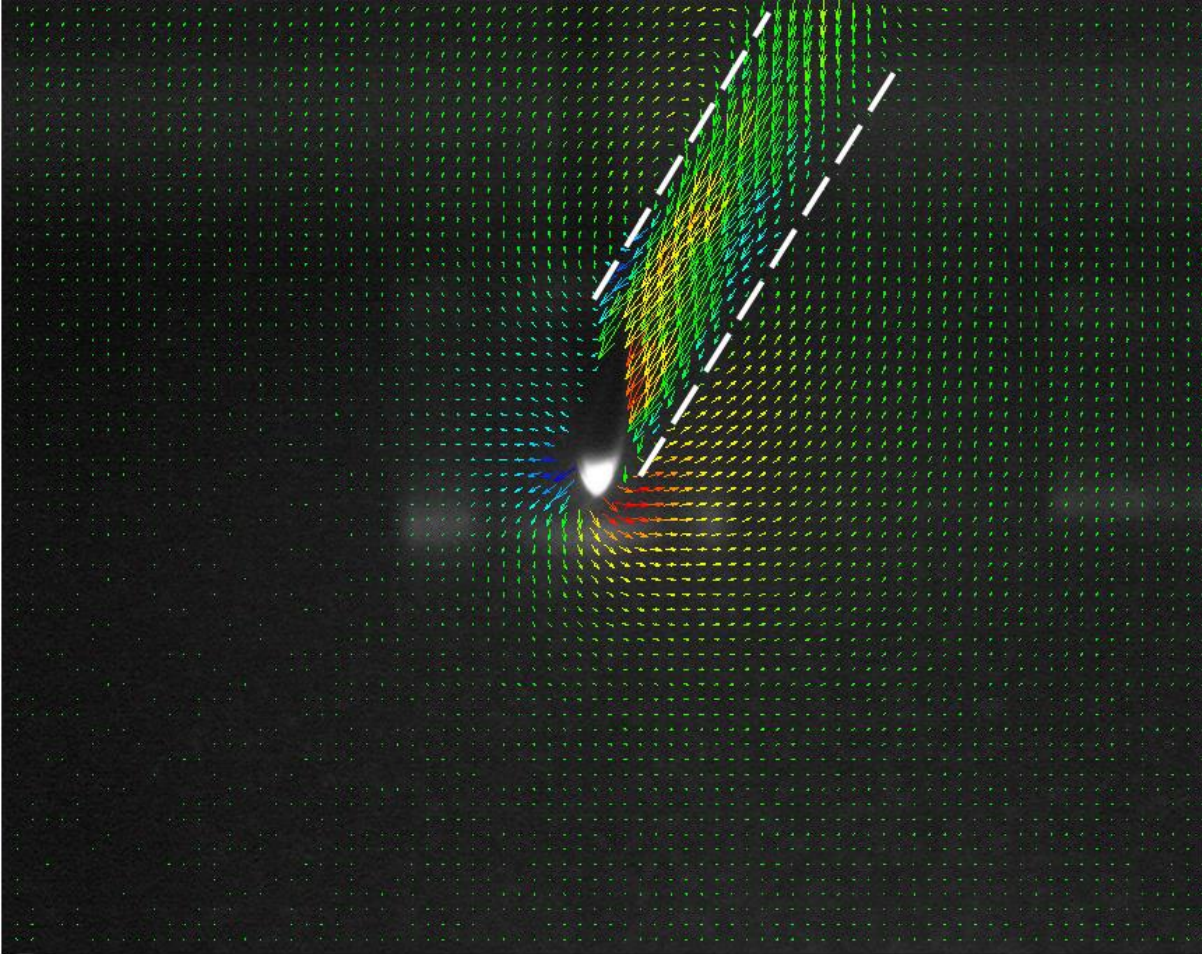
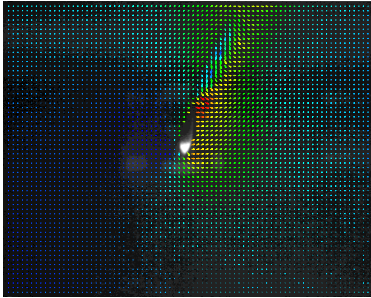
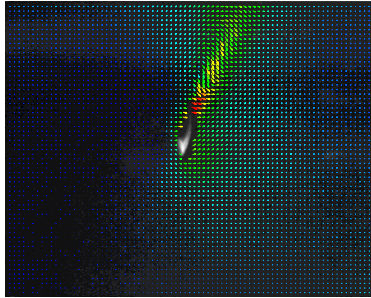
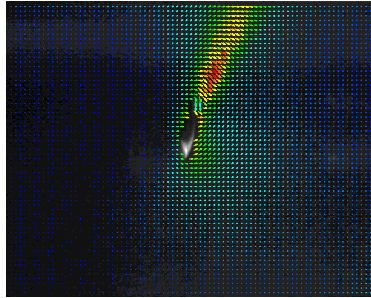
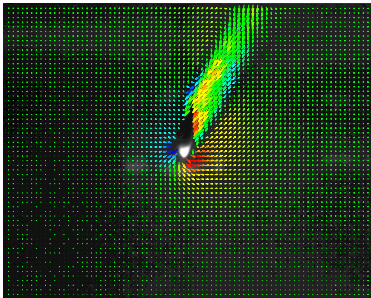
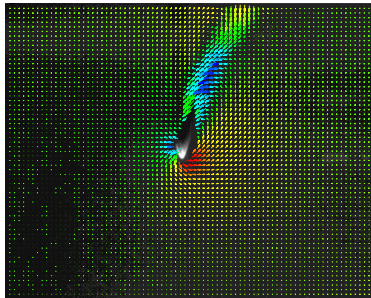
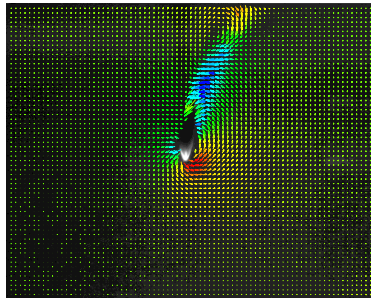
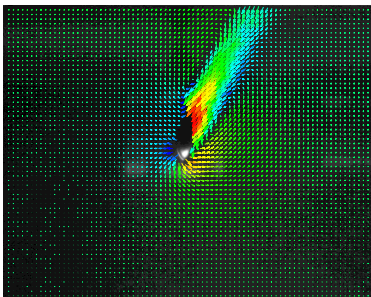
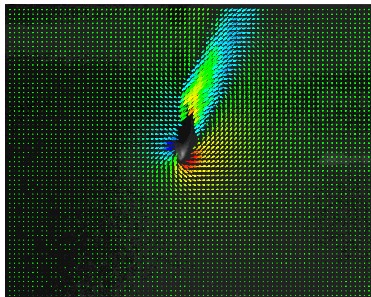
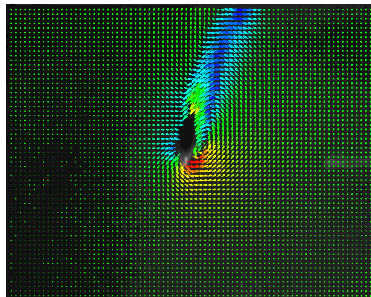
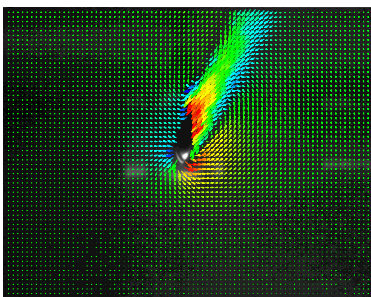
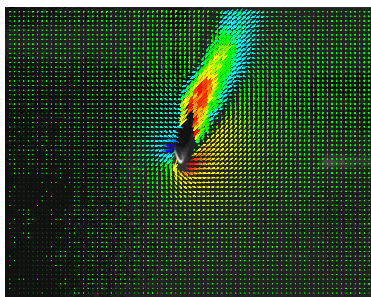
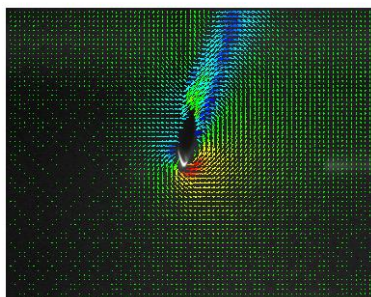
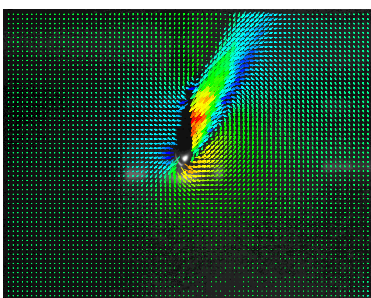
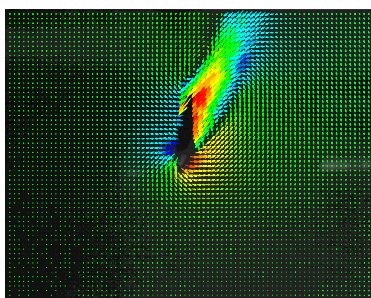
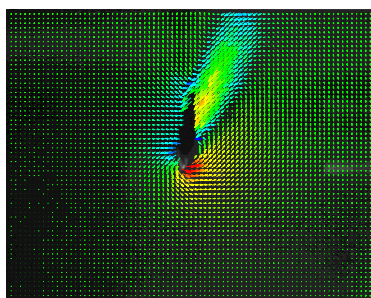
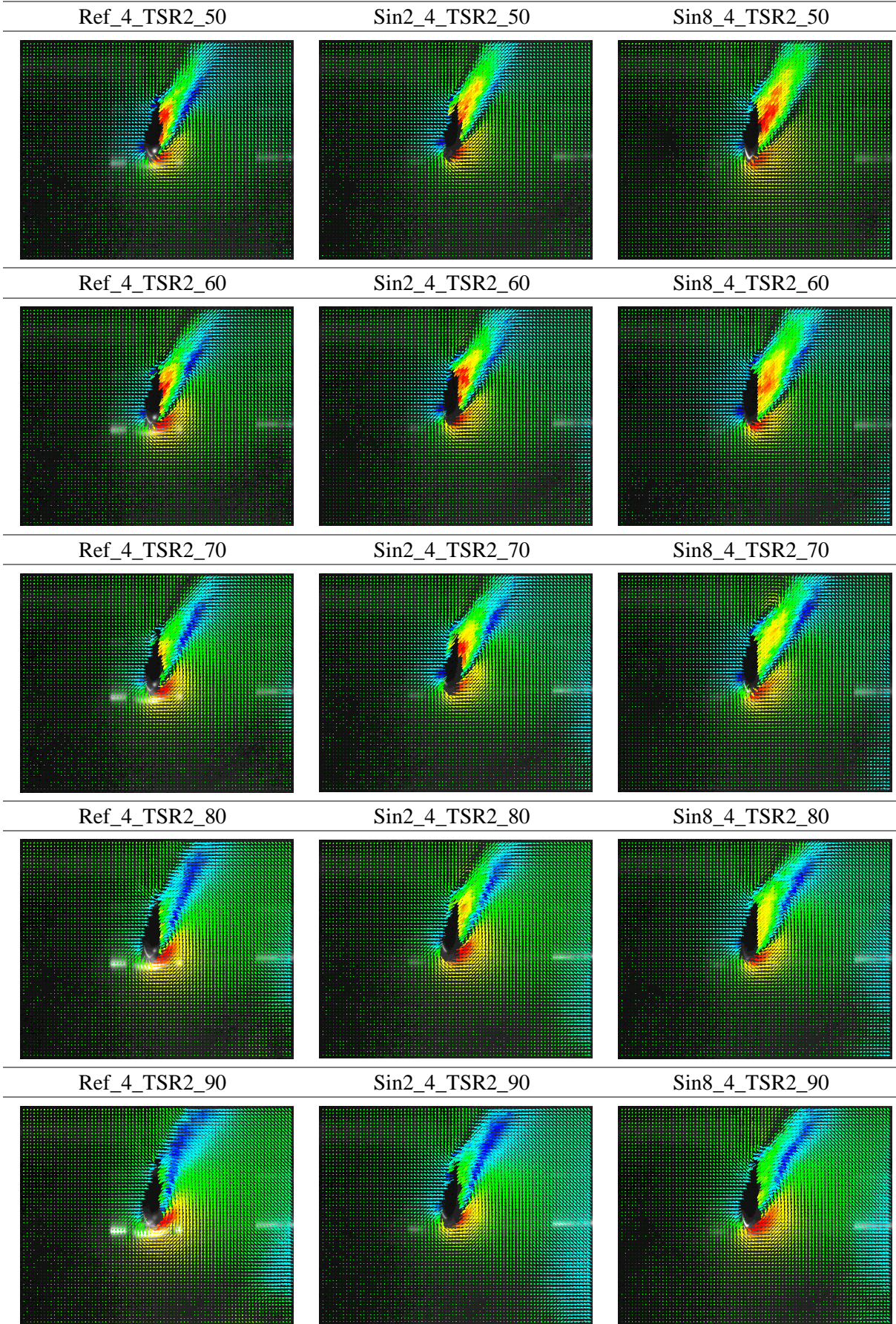


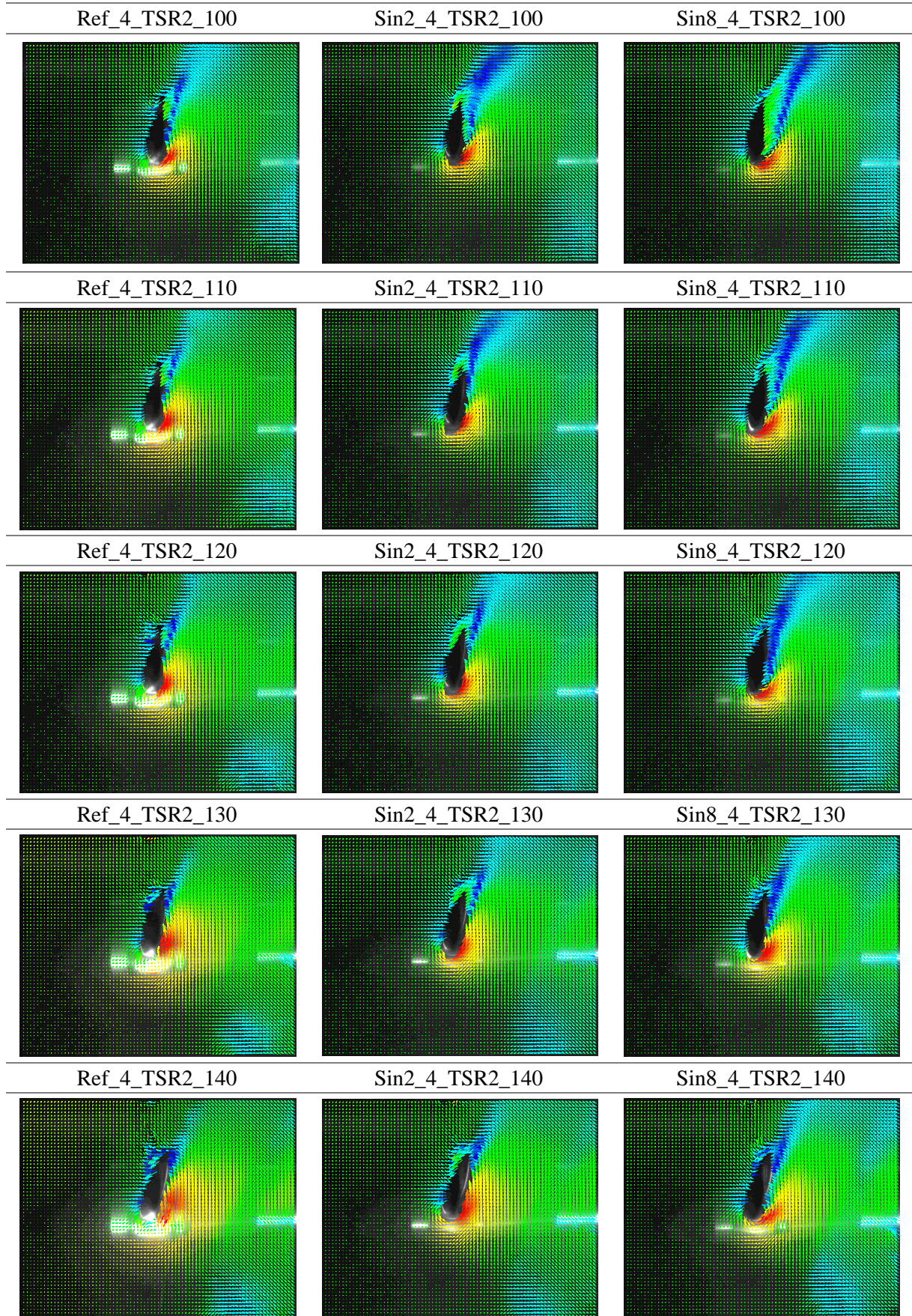
Figure 5-36 Mapping of flow separation area in downstream of turbine blade by using 2D PIV
(Case: Ref_4_TSR2_10)

In-depth analysis and a comparison between the performances of the three different turbines as shown in Table 5-13 can indicate the difference of flow field in the stall condition, under which the flow around the turbine would also be significantly changed by the tubercles. It can be clearly seen in Table 5-13 that the leading-edge tubercles help the flow to remain more attached to the turbine blade at various radial positions particularly from Position 10 to Position 40. This phenomenon has further proven the beneficial effect of the leading-edge tubercles for tidal turbines, especially under the stall condition, as a result of the more attached flow.

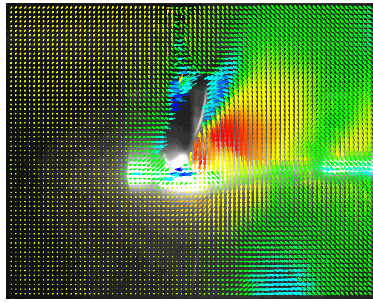
Table 5-13 2D PIV measurement results of turbines at different radial positions (at TSR=2)

Ref_4_TSR2_0	Sin2_4_TSR2_0	Sin8_4_TSR2_0
		
Ref_4_TSR2_10	Sin2_4_TSR2_10	Sin8_4_TSR2_10
		
Ref_4_TSR2_20	Sin2_4_TSR2_20	Sin8_4_TSR2_20
		
Ref_4_TSR2_30	Sin2_4_TSR2_30	Sin8_4_TSR2_30
		
Ref_4_TSR2_40	Sin2_4_TSR2_40	Sin8_4_TSR2_40
		

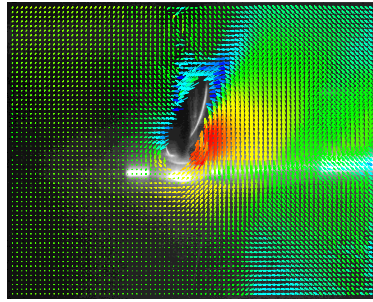




Ref_4_TSR2_150



Sin2_4_TSR2_150



Sin8_4_TSR2_150

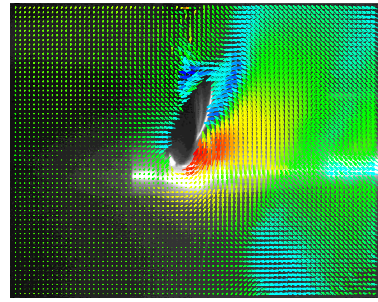
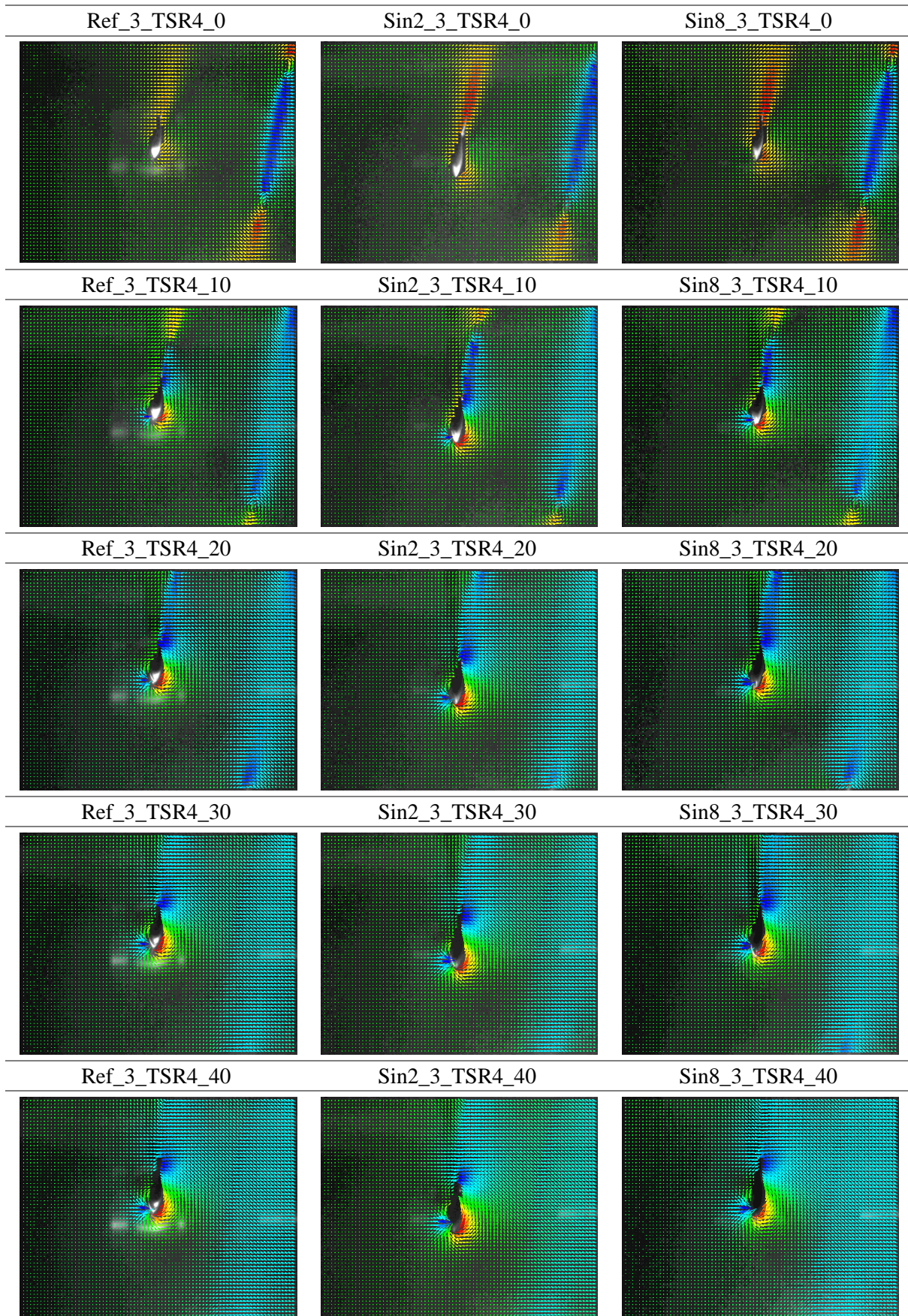
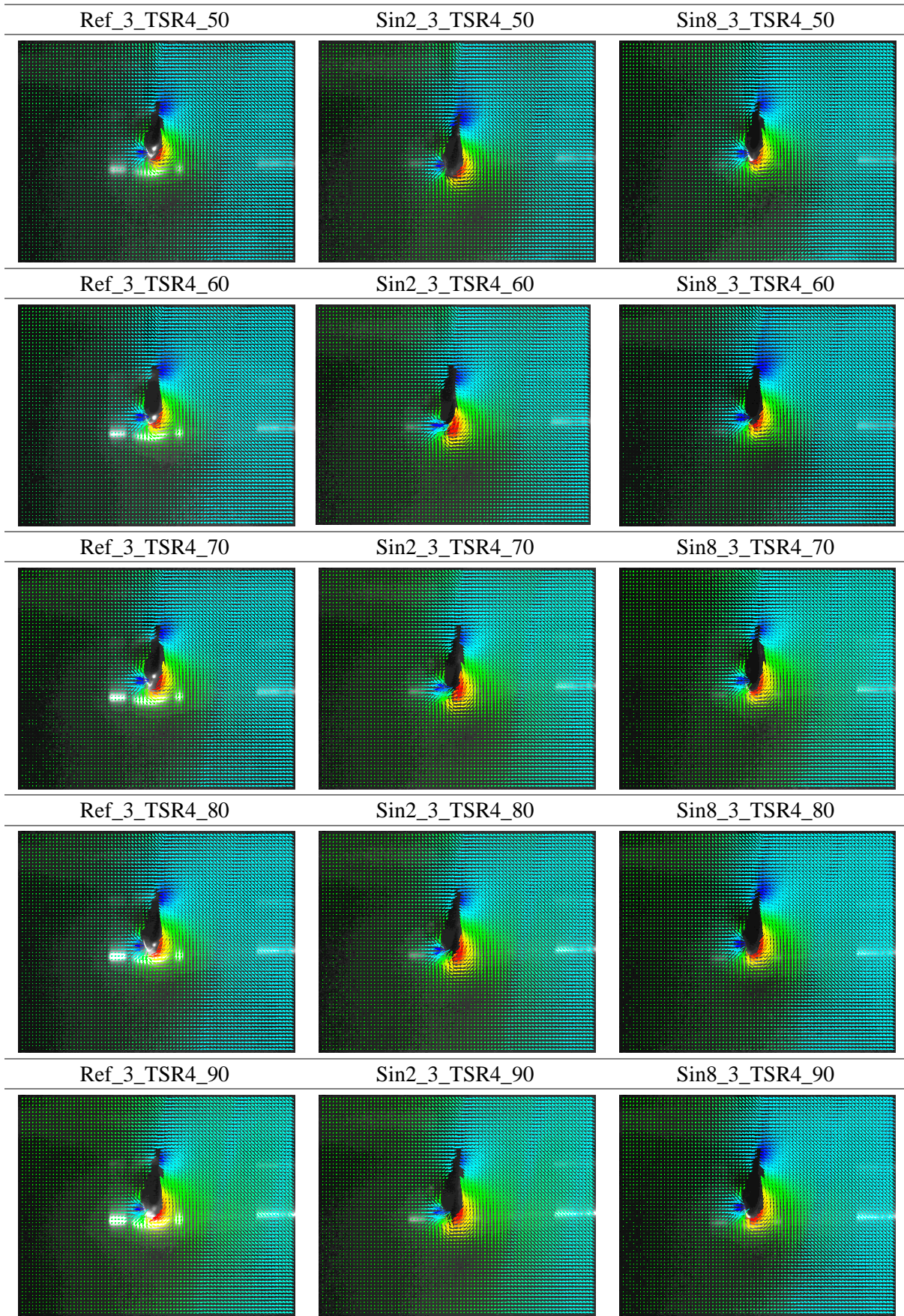
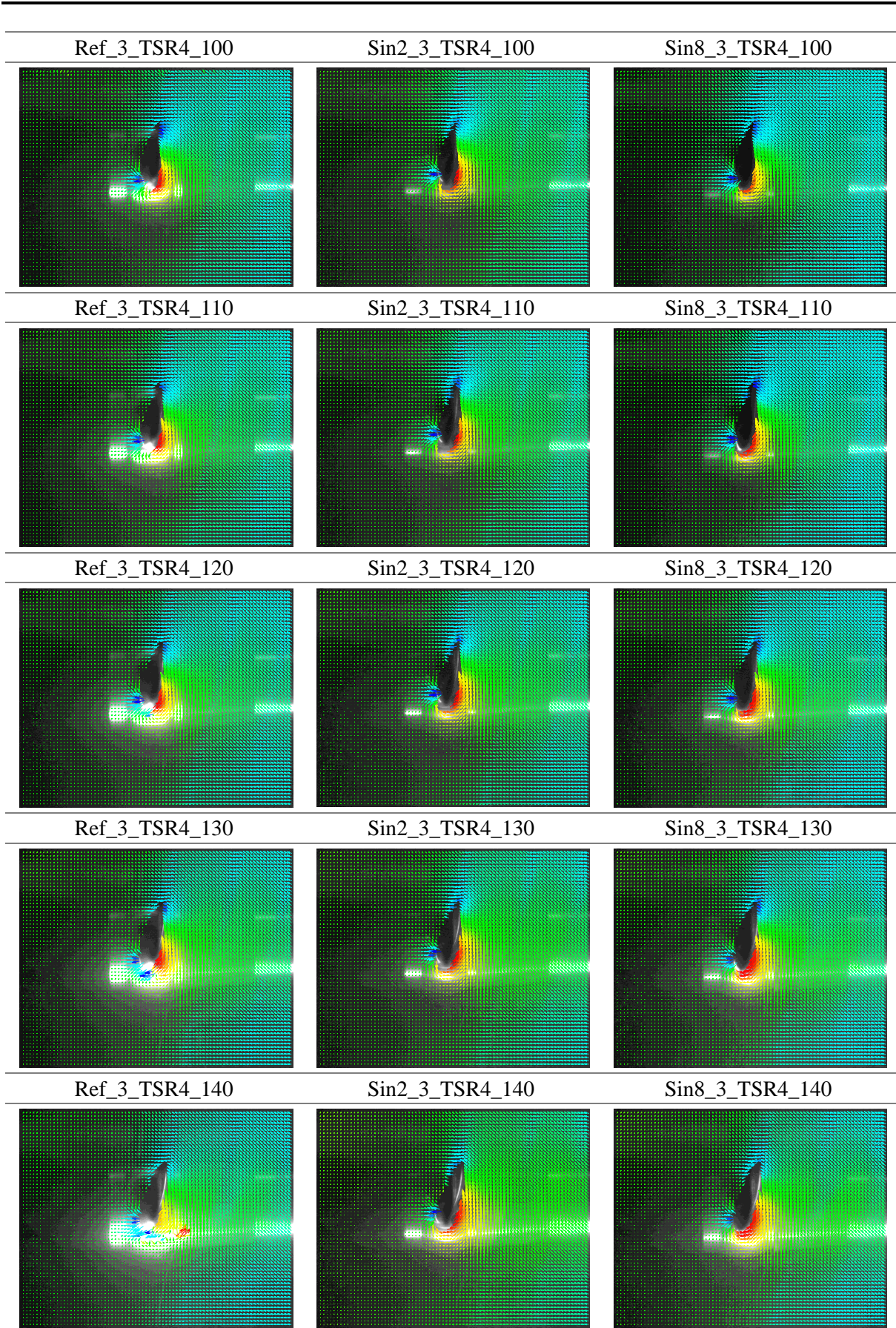


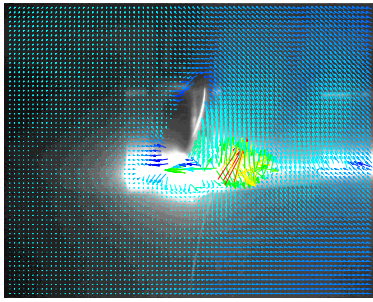
Table 5-14 2D PIV measurement results of turbines at different radial positions (at TSR=4)



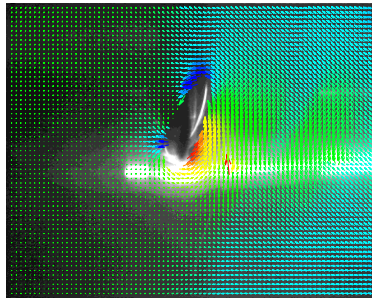




Ref_3_TSR4_150



Sin2_3_TSR4_150



Sin8_3_TSR4_150

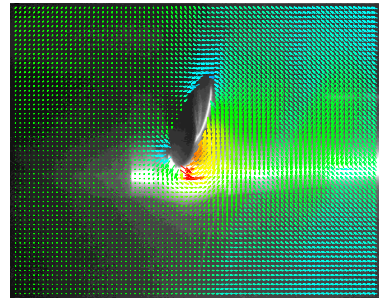
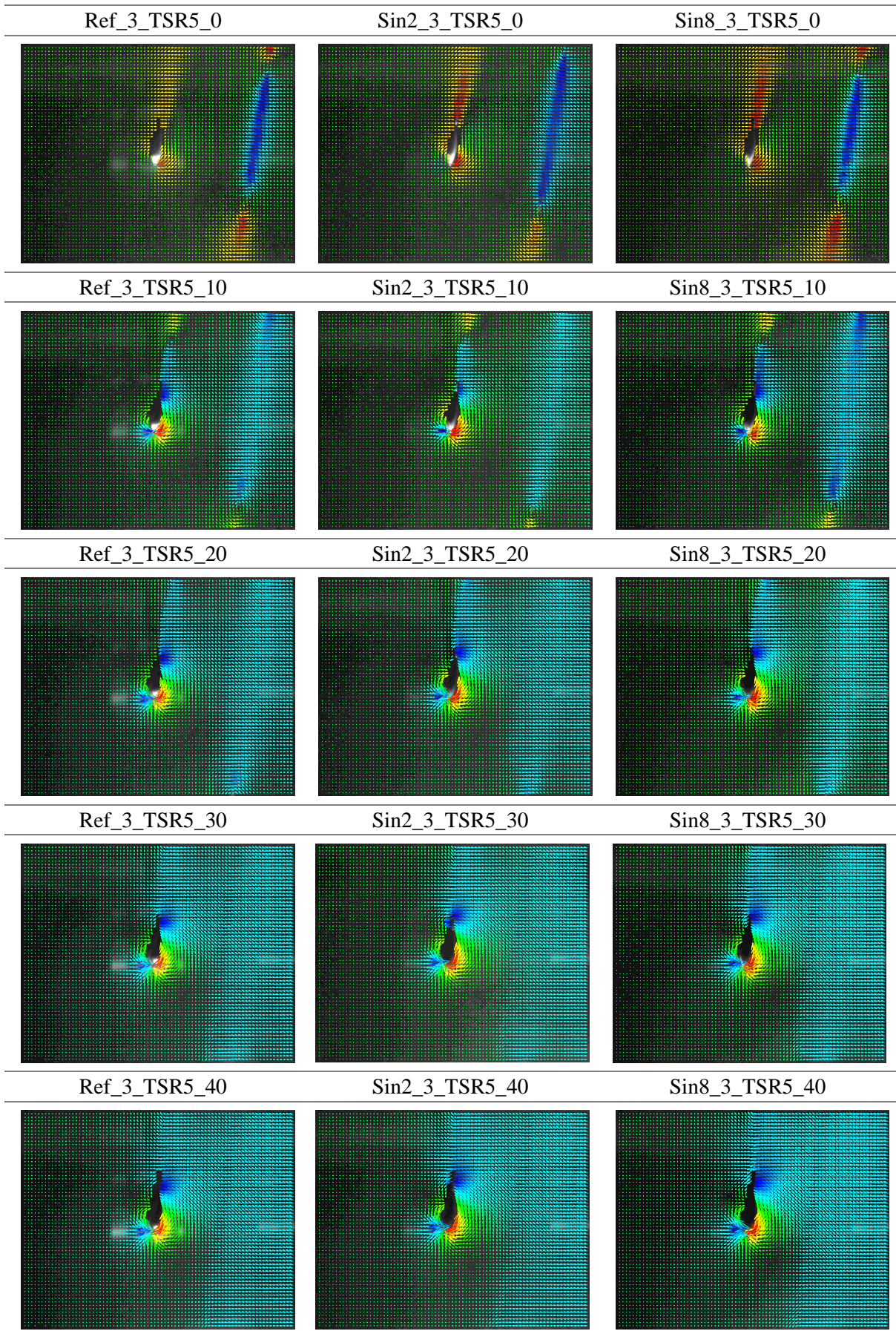
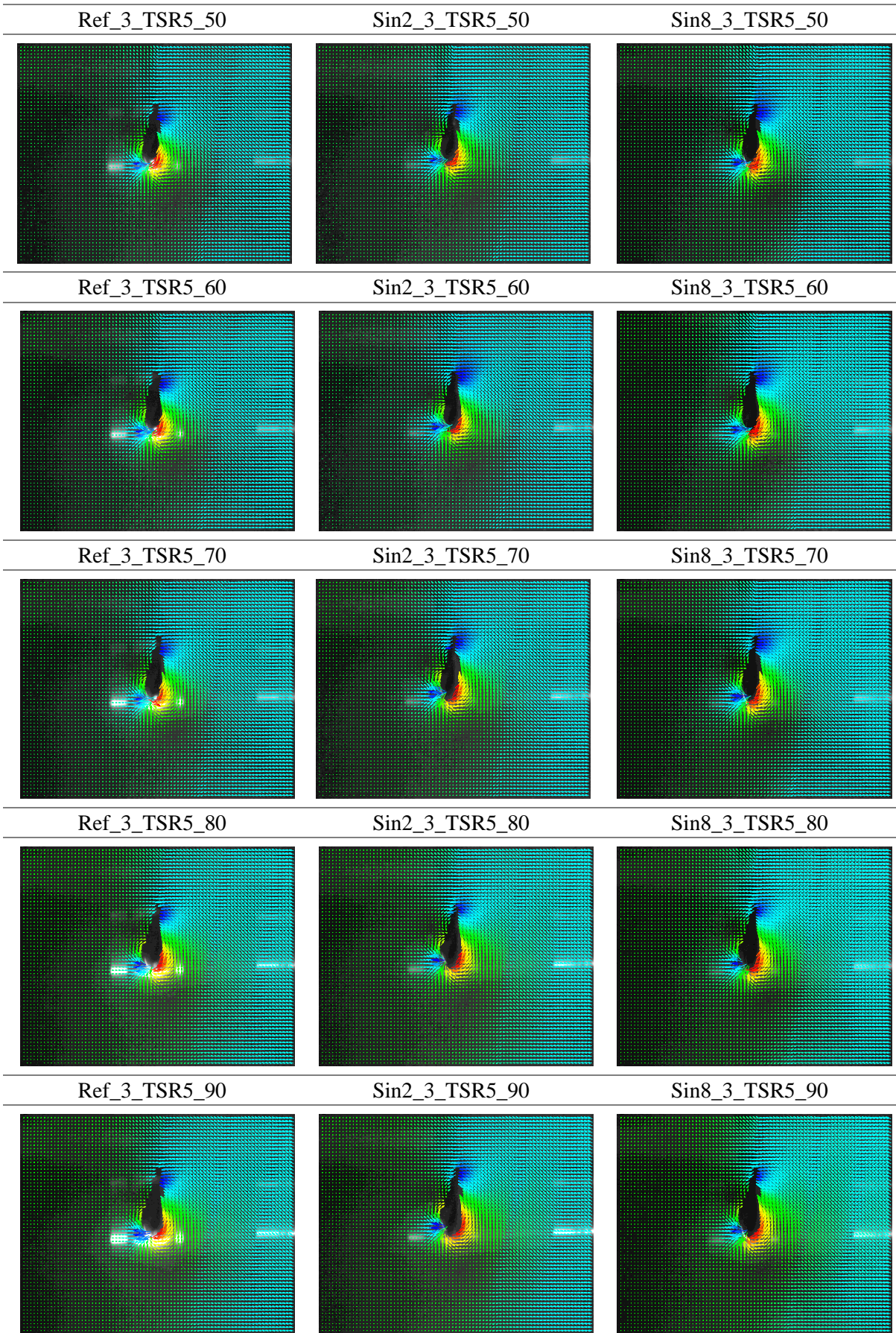
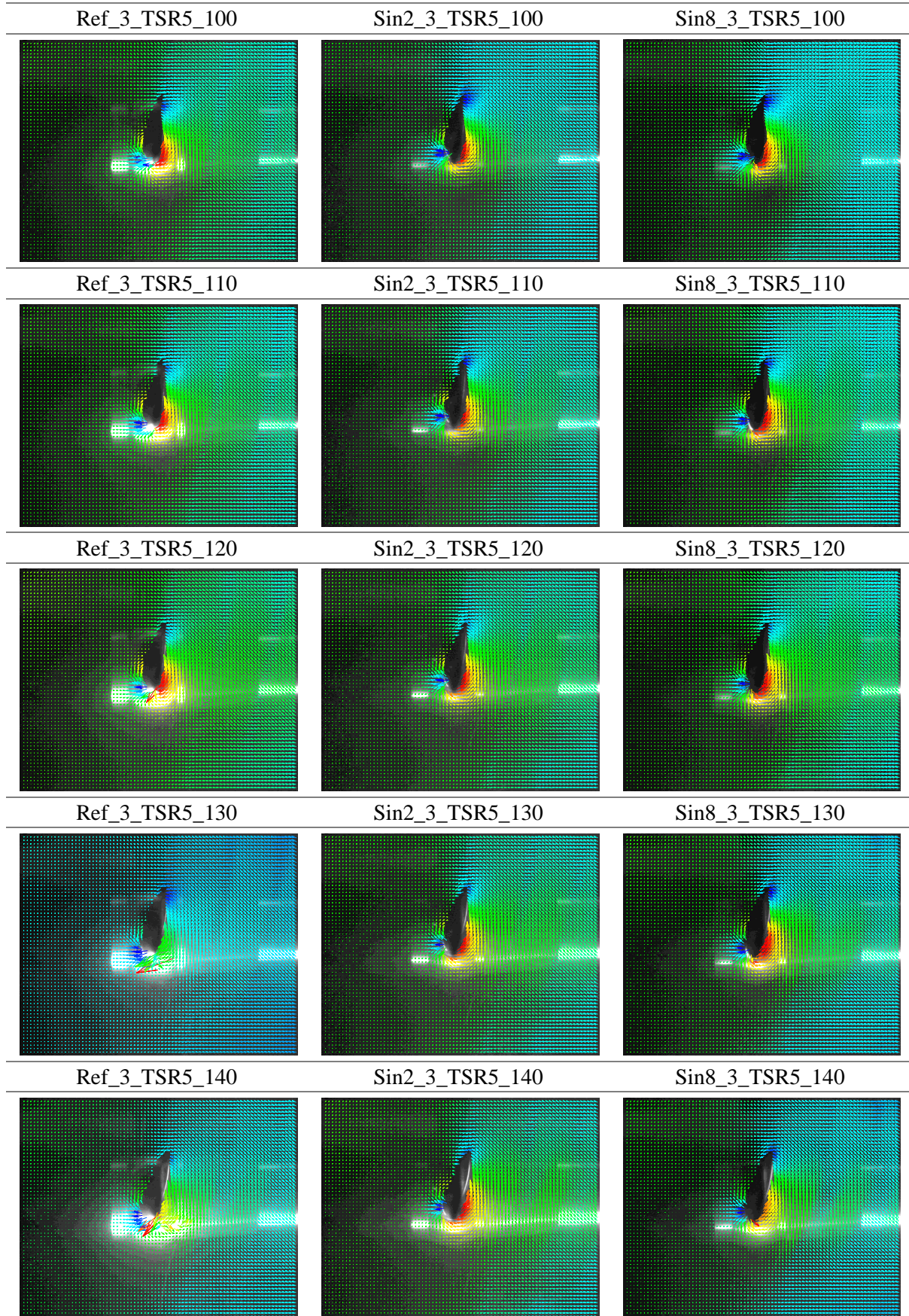
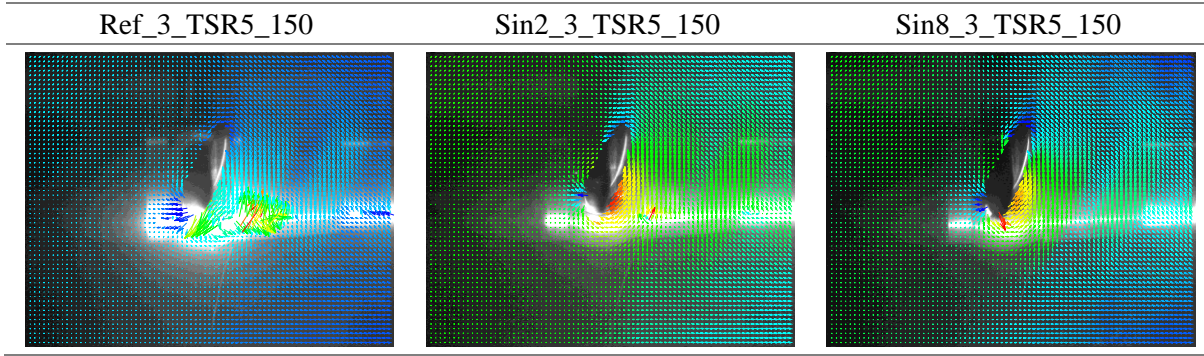


Table 5-15 2D PIV measurement results of turbines at different radial positions (at TSR=5)









5.6.2.2 Mapping the volumetric flow field using SPIV

By using SPIV, three velocity components: the axial velocity, the radial velocity and the tangential velocity, in a planar section can be measured in the measurement plane downstream the turbine blades; so as to the resultant vorticity distribution. With the aid of the phase locking and averaging technique discussed in the experimental setup, SPIV measurements were triggered when the turbine blades reached to different angular positions, in every 10° with extra $\pm 5^\circ$ next to the blades themselves. Finally, by summarizing all of the data in the measurement section at different angular positions, a volumetric flow field of a cylindrical volume can be achieved to map the turbine's wake field, as shown in Figure 5-37.

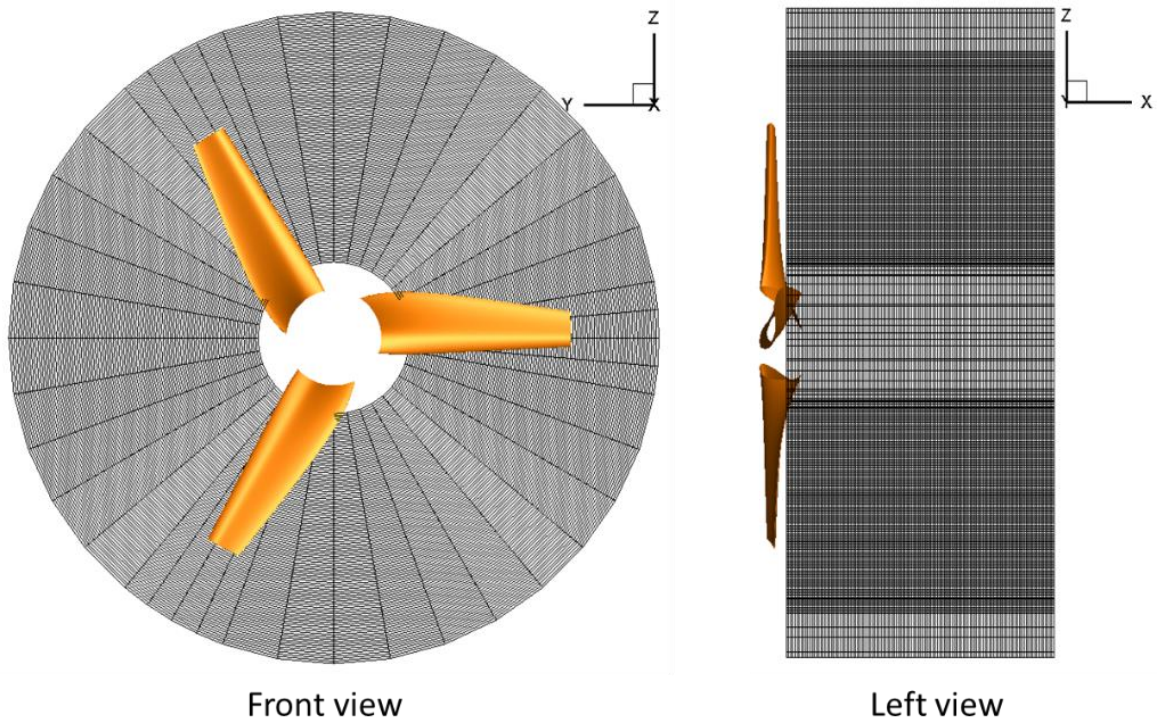


Figure 5-37 Volumetric flow field description for stereo PIV measurements

The velocity distributions in the wake field downstream these three different turbines, under the selected conditions, have been extracted. In the following sections, detailed analysis and discussion are presented with regard to each of the earlier specified test conditions. Three sections, which are consecutively 50mm, 150mm and 250mm downstream the turbine, were extracted and the velocity magnitudes plotted at those sections.

- Condition 1: Stall condition, TSR=2

In Figure 5-38 to Figure 5-40, the velocity distributions under the stall condition have been presented together with the iso-surface of axial velocity=1.5m/s. It needed to be bear in mind that during this condition the mass flux of the tunnel reached to $4016 \text{ kg s}^{-1} \text{ m}^{-2}$ and the blockage ratio based on the turbine swept area rated to 13%.

As it was discussed in Section 5.6.2.1, severe flow separation occurred under this condition. Because of the flow separation that the turbines suffered, in the wake field the flow is much more turbulent compared to the other conditions. Also, because of the low tip speed ratio, the tip vortex structure is not very clearly seen from the iso-surface. Therefore, a clear difference cannot be easily found from these plots.

However by extracting the iso-surface pair of radial velocity= +/-0.5m/s in Figure 5-41, the tip vortex can be revealed which is rolling from the pressure side to the suction side and disappearing in the wake. The iso-surface for the turbine Ref is wider and smoother than that for the other two turbines. For the case Sin8 especially, the iso-surface is quite narrow but extends for a longer distance. This trend can also be seen in Figure 5-42 which shows the iso-surface of the vorticity (tangential) = 100. This component of vorticity results from the axial velocity and the radial velocity and also reveals the tip vortex. As it can be seen, the iso-surface of the Sin8 case is longer but narrower. This indicates that the tip vortex of the turbines with tubercles under the stall condition is stronger but cannot influence as large an area of the blade because of the contra-rotating vortex fences created in-between the tubercles. This phenomenon was also reported in a previous paper which claimed that these contra-rotating vortices generated by the tubercles help to reduce the blade from suffering further lift loss caused by the tip vortex (Shi *et al.*, 2016).

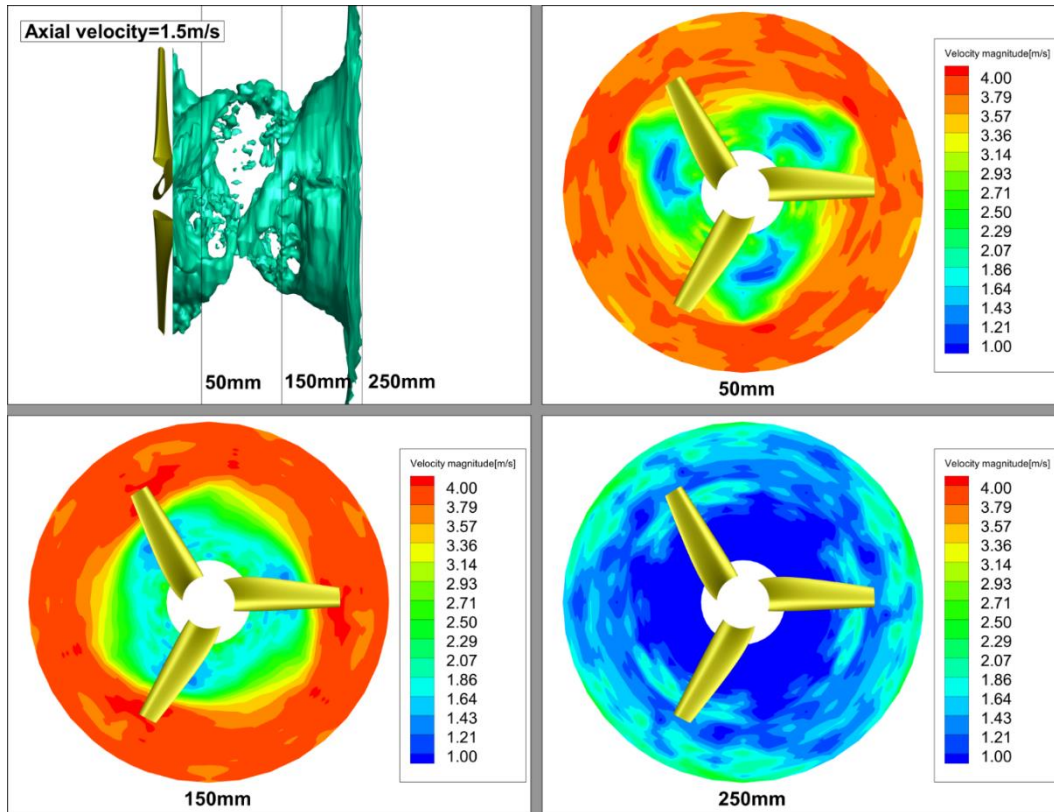


Figure 5-38 Velocity distribution for the reference turbine at varied sections, 50mm, 150mm and 250mm downstream of model turbine at TSR2 with the iso-surface of axial velocity = 1.5m/s

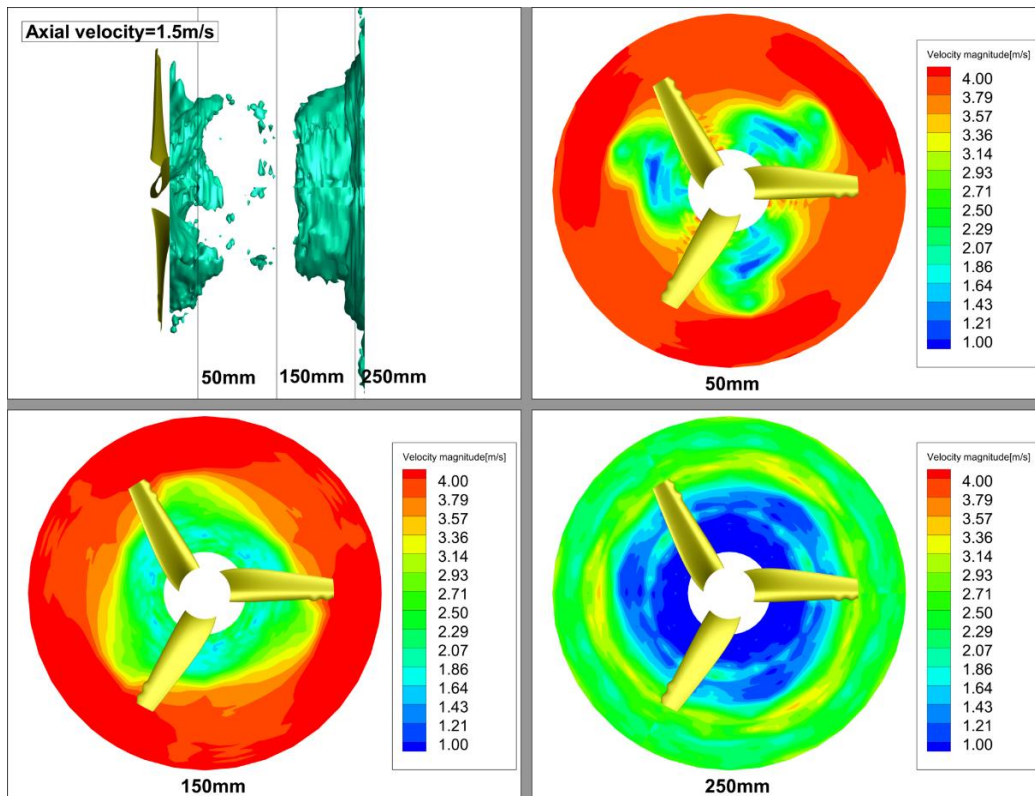


Figure 5-39 Velocity distribution for the Sin2 turbine at varied sections, 50mm, 150mm and 250mm downstream of model turbine at TSR2 with the iso-surface of axial velocity = 1.5m/s

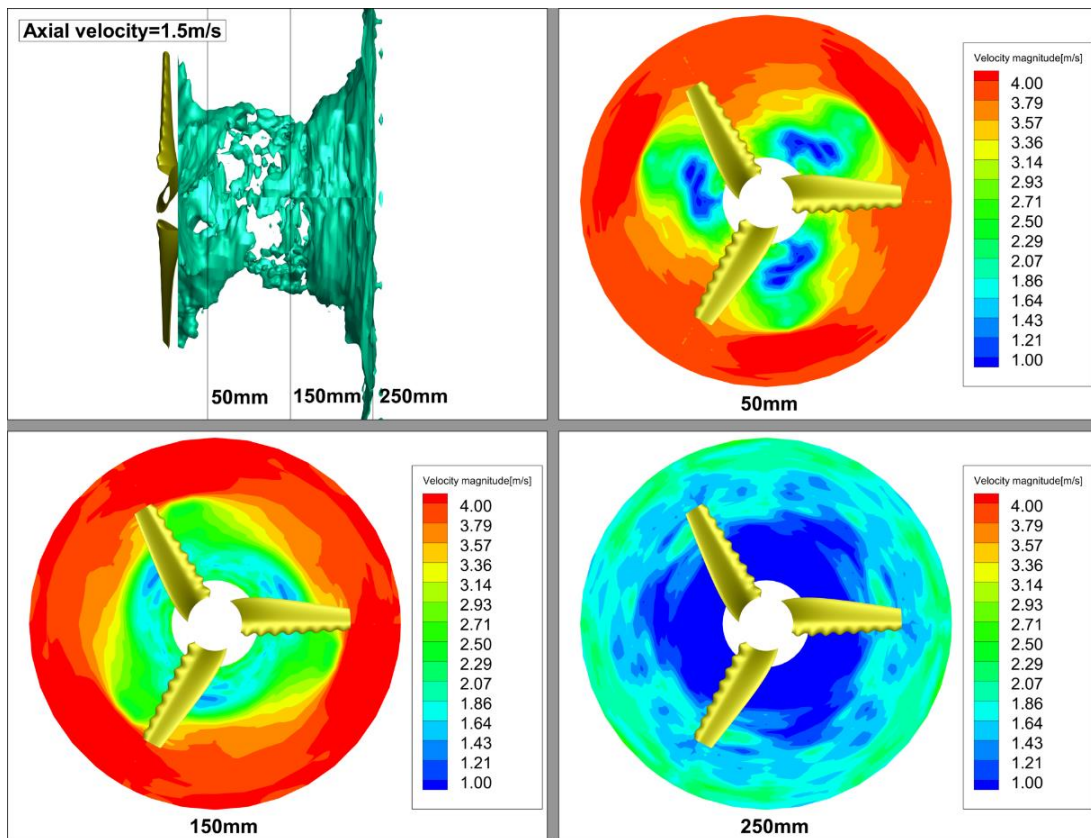


Figure 5-40 Velocity distribution for the Sin8 turbine at varied sections, 50mm, 150mm and 250mm downstream of model turbine at TSR2 with the iso-surface of axial velocity = 1.5m/s

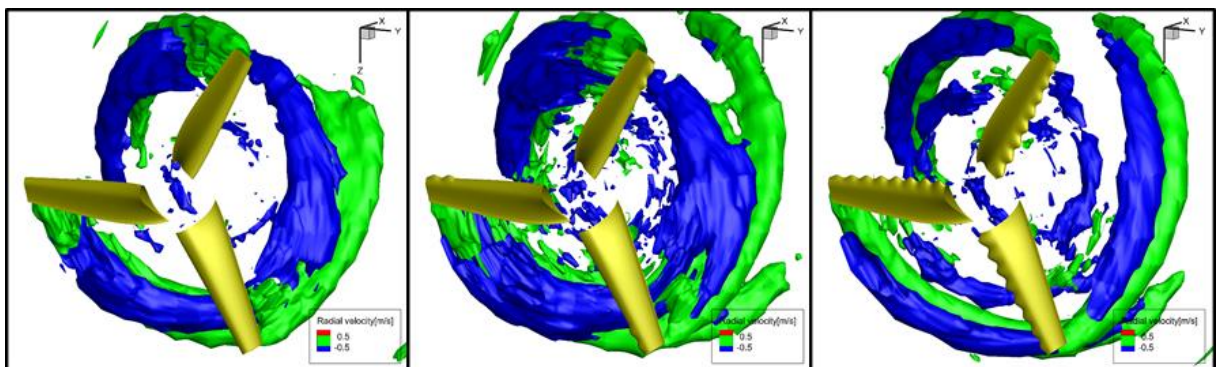


Figure 5-41 Iso-surface pair of radial velocity = +/-0.5m/s (Left: Ref; Middle: Sin2; Right: Sin8)

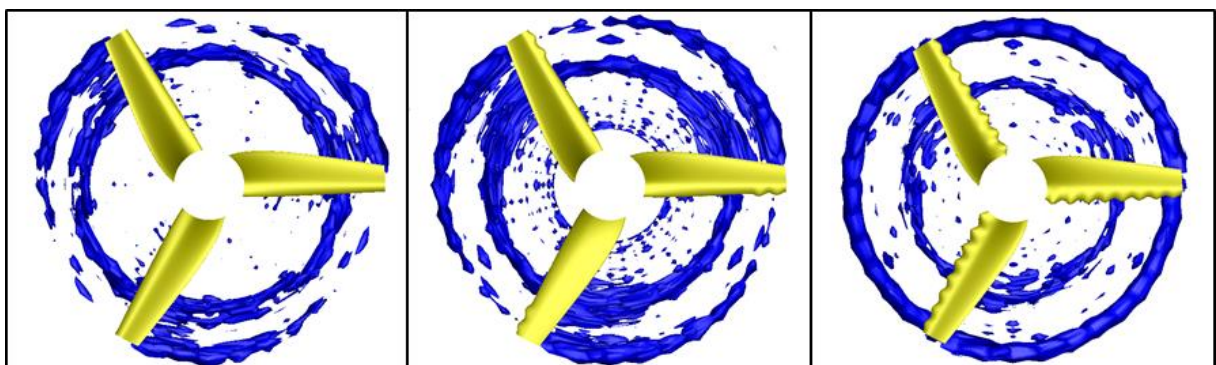


Figure 5-42 Iso-surface of vorticity (tangential) = 100 (Left: Ref; Middle: Sin2; Right: Sin8)

- Condition 2: Optimum working condition, TSR=4

In Figure 5-43 to Figure 5-45, the velocity distributions, while the turbines are operating at the optimum power coefficient condition, are presented together with the iso-surface of axial velocity=3.3m/s. The iso-surfaces in these plots reveal the classic structure of the tip vortex. By comparing these iso-surfaces, it can be seen that the strength of these tip vortices is gradually weakened by the tubercles as the iso-surface gradually gets shorter with the increase in the number of tubercles.

On the other hand, the velocity deficit behind the turbine increases with the numbers of tubercles, as it can be seen in the section plots. This is due to the higher induction factor that is generated by the turbine with tubercles. This can also be seen in Table 5-12 where the force measurement, represented by the thrust coefficient, is 4.6% and 7.7% higher for the Sin2 and Sin8 cases, respectively, relative to the reference turbine, and the power coefficient is similarly 2.2% and 4.3% higher.

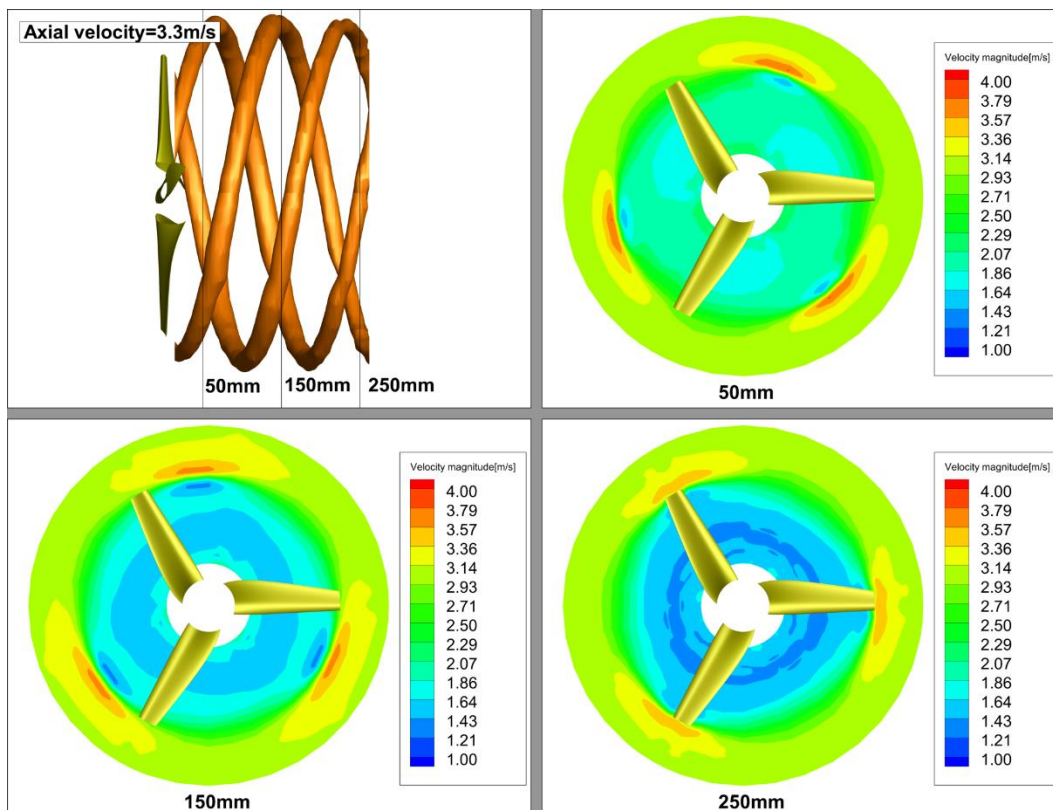


Figure 5-43. Velocity distribution for the reference turbine at varied sections, 50mm, 150mm and 250mm downstream of model turbine at TSR4 with the iso-surface of axial velocity = 3.3m/s

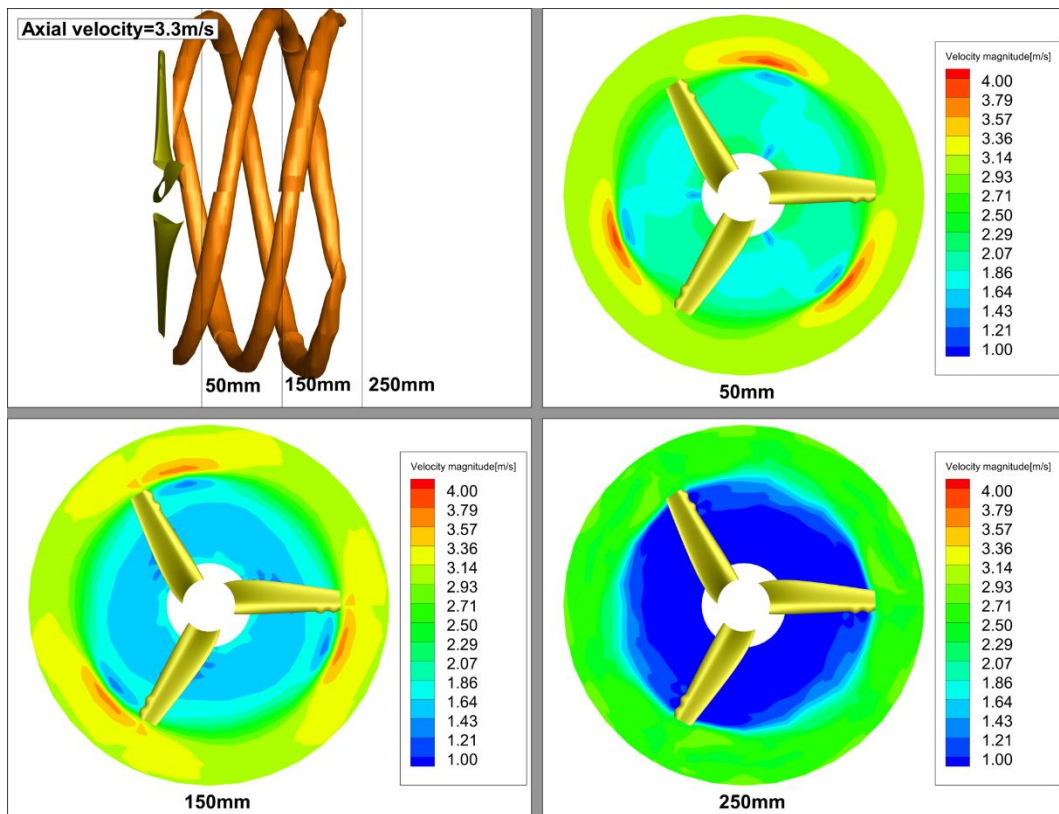


Figure 5-44. Velocity distribution for the Sin2 turbine at varied sections, 50mm, 150mm and 250mm downstream of model turbine at TSR4 with the iso-surface of axial velocity = 3.3m/s

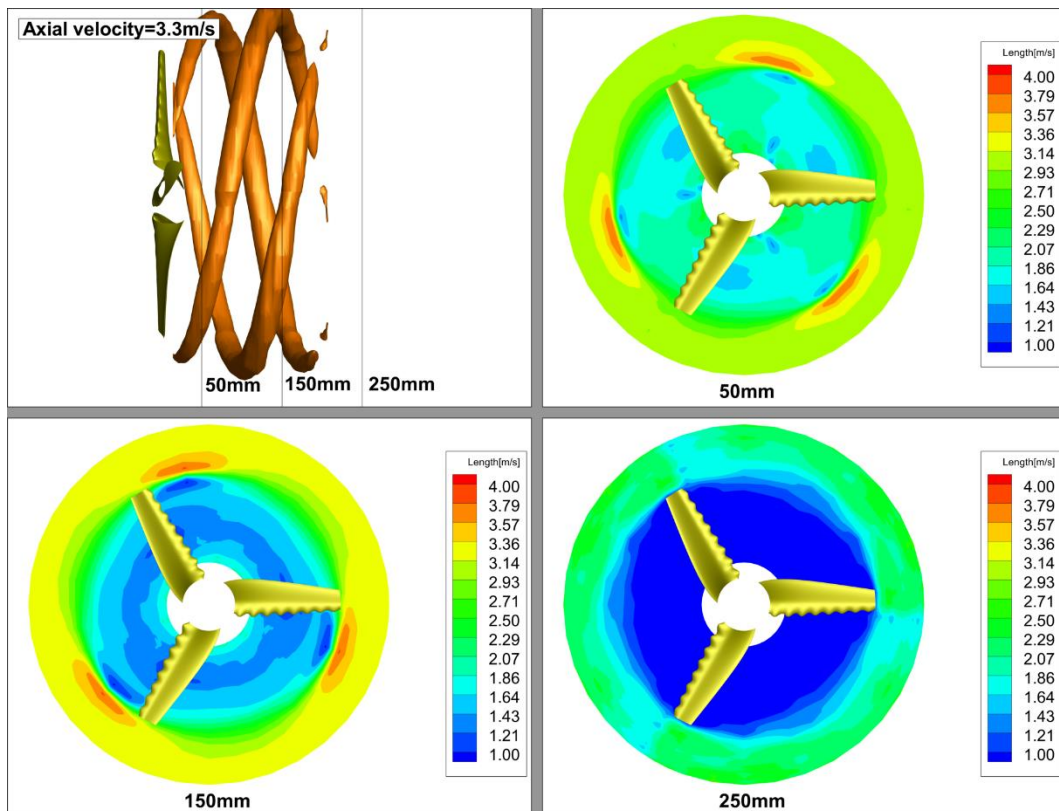


Figure 5-45. Velocity distribution for the Sin8 turbine at varied sections, 50mm, 150mm and 250mm downstream of model turbine at TSR4 with the iso-surface of axial velocity = 3.3m/s

- Condition 3: Overspeed condition, TSR=5

A similar trend to Condition 2 can also be observed in Condition 3 in Figure 5-46 to Figure 5-48, where the turbine is working under the overspeed condition. The iso-surface also gradually shortens with the increase in the number of tubercles, which shows the weakened tip vortex resulting from the tubercles. The same trend is also seen in terms of the increased velocity deficit from the tubercles and this is even more pronounced compared to Condition 2; the thrust coefficient being 4.0% and 9.2% higher and the power coefficient 1.6% and 4.0% higher for the Sin2 and Sin8 cases, respectively, compared to the reference turbine, as seen in Table 5-12.

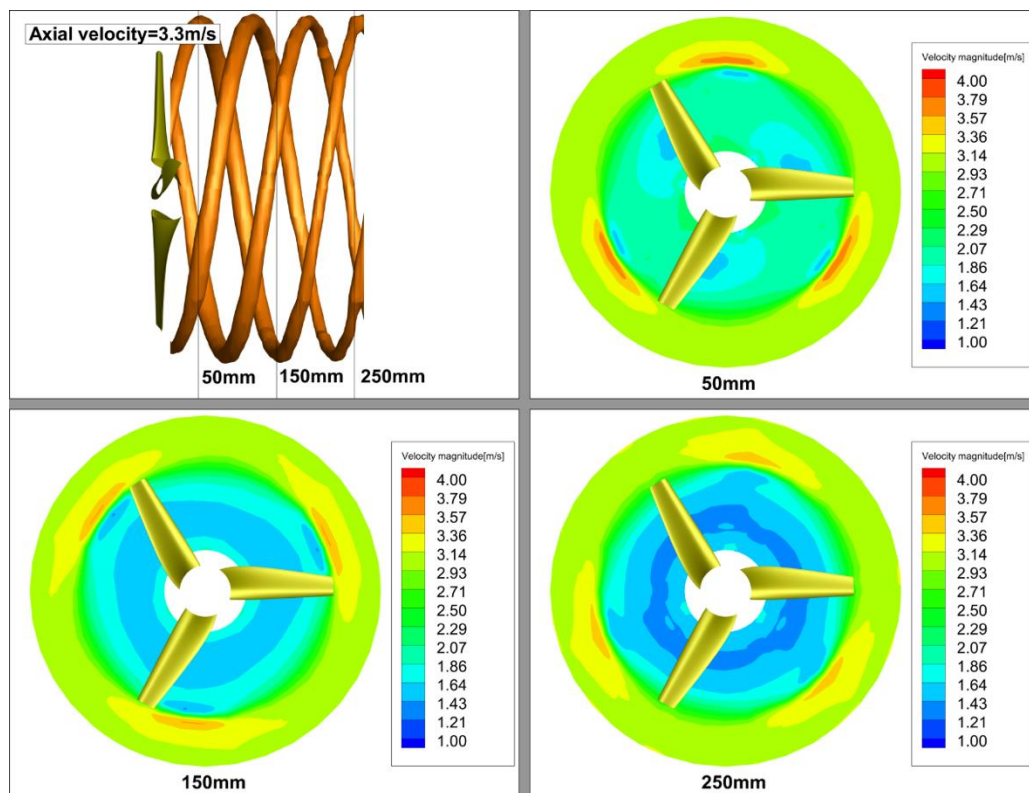


Figure 5-46. Velocity distribution for the reference turbine at varied sections, 50mm, 150mm and 250mm downstream of model turbine at TSR5 with the iso-surface of axial velocity = 3.3m/s

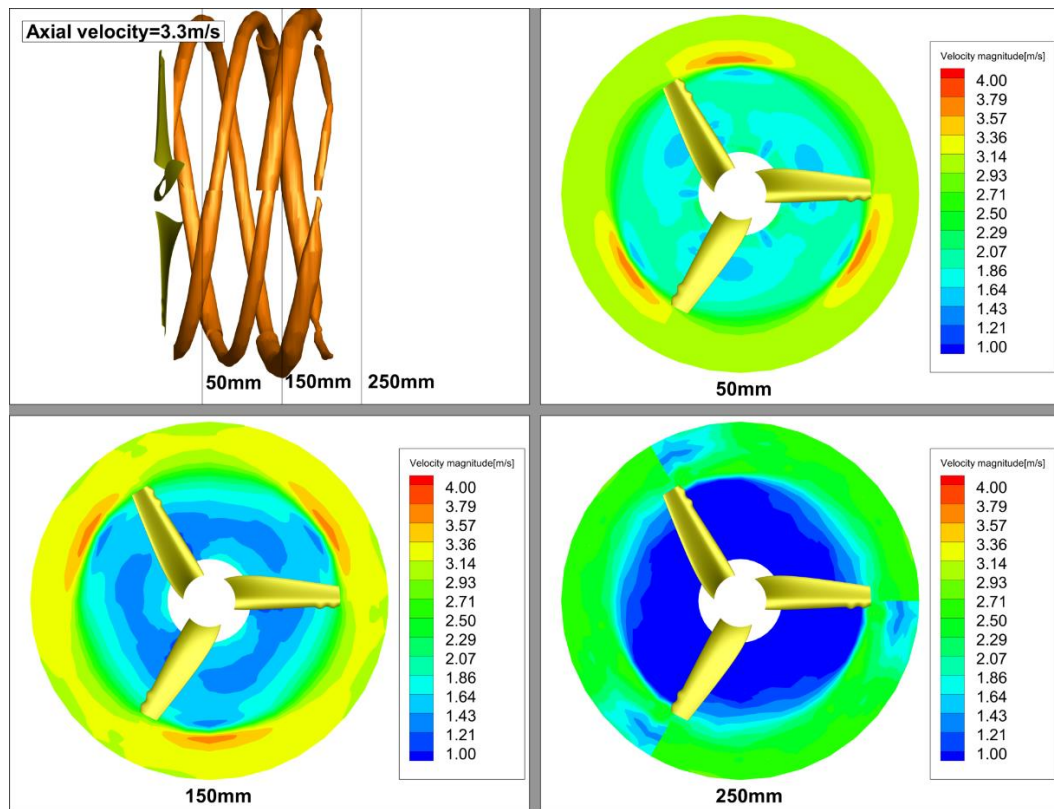


Figure 5-47. Velocity distribution for the Sin2 turbine at varied sections, 50mm, 150mm and 250mm downstream of model turbine at TSR5 with the iso-surface of axial velocity = 3.3m/s

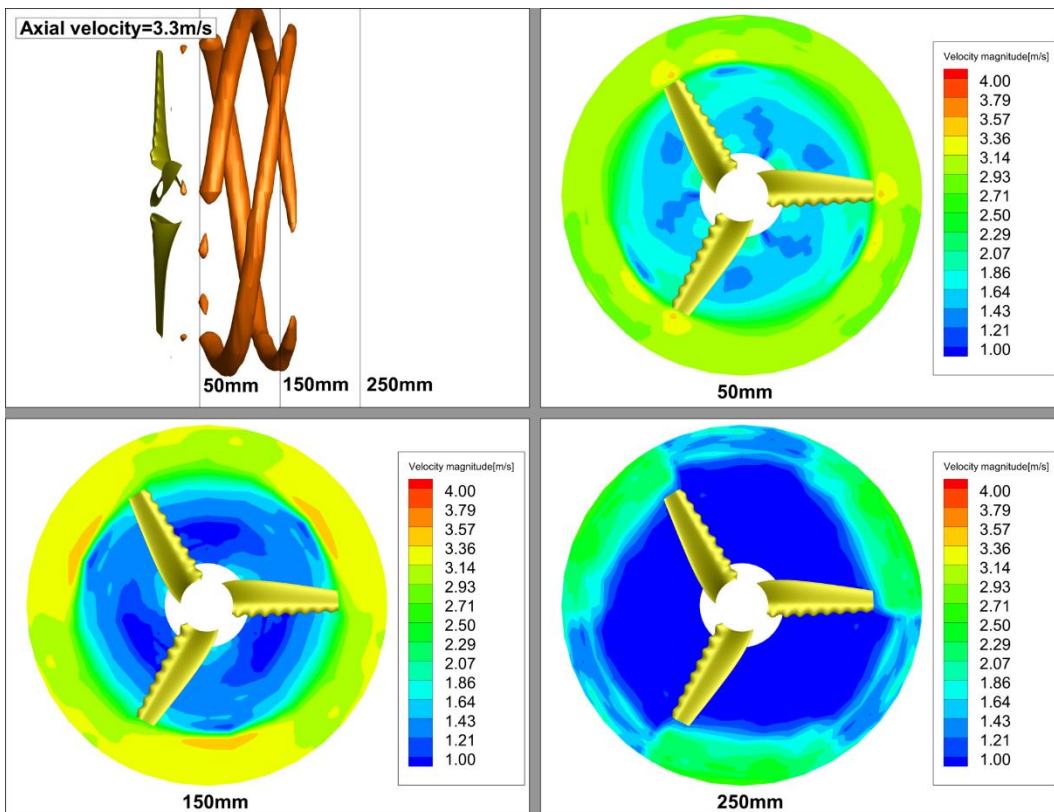


Figure 5-48. Velocity distribution for the Sin8 turbine at varied sections, 50mm, 150mm and 250mm the turbine at TSR5 with the iso-surface of axial velocity = 3.3m/s

5.6.3 Key findings on the effects of tubercles based on detailed flow investigations

Based on the results and discussions of the flow measurements made at the three typical operating conditions of the model turbines by using 2D PIV and SPIV, the following concluding remarks can be made:

- 2D PIV measurements under the “Stall condition” of the turbines indicated that while all the tested turbine blades suffered from severe flow separations, the turbine blades with the leading-edge tubercles were able to maintain the flow to be more attached to their surfaces at certain positions. This provided the turbine with additional torque for starting. In the other two conditions, since the flow did not separate, there were no clear differences in the torque values.
- By using SPIV, the flow structure measured downstream of the turbine revealed that the turbines with tubercles can induce a higher induction factor, which resulted in lower velocities in the wake field. This effect is positively related to the number of tubercles. With the improved performance for individual turbine devices, special care might be taken for the array development since the velocity recovery process might be slowed down, which might eventually affect the overall power generation performance for the turbine farm.
- SPIV measurements also revealed that the tip vortex was weakened and its axial trajectory was shortened by the tubercles in the “Optimum working condition” and the “Over speed condition”. This was further confirmation of the reduced 3D effects of the actual turbine blades by the tubercles. Under the stall condition, the tubercles helped the turbine to confine the vortex at the tip region and isolate it from influencing larger areas of the blades which weakened the 3D effects of the turbine blades further.

5.7 Summary

In this chapter, with the knowledge gained in previous chapters, a model test campaign was conducted, with the three tidal turbine models, to explore the effect of leading edge tubercles on the hydrodynamic performance of the turbines and results have been presented and discussed. The aim was to determine whether the leading-edge tubercles can really improve the performance through detailed model tests conducted in a cavitation tunnel in steady current. The major findings may be summarised as follow:

1. The open water performance tests conducted in the cavitation tunnel demonstrated that the application of the leading-edge tubercle concept does not compromise the maximum power coefficient value of the turbine but improves the performance while the turbine is working under stall conditions in the low TSR region and at lower pitch angles.
2. The cavitation observation tests showed that the development of the misty-type cloud cavitation over the leading-edge tubercles was restricted to the trough areas of the tubercles, which resulted in reduced cavitation extent. However, the leading-edge tubercles may trigger earlier inception for tip vortex cavitation compared to that for the reference turbine with smooth leading edges.
3. The radiated noise level measurements with the three tested turbines displayed similar total noise levels until the cavitation was incepted. The noise levels of the turbines with the tubercles were lower than those of the Reference turbine, a fact which may be accredited to the constrained development and the lesser extent of cloud cavitation.
4. With regard to the detailed flow measurements made with the SPIV system, the turbines with leading-edge tubercles can help to maintain the flow to be more attached to the blade surfaces. Turbines with tubercles can induce a higher induction factor, which results in lower velocity in the wake field and hence higher power and thrust coefficients. Meanwhile, the tip vortex can be weakened and its axial trajectory is shortened by the tubercles, thus the three-dimensional effect can be reduced by the tubercles.

Having finalized the tests in the ECT, in order to validate the efficiency performance of the tubercles under a bigger size of testing facility to rule out the concern of blockage ratio and also to explore the unsteady effects under regular and irregular waves, the turbines were also tested

in the Kelvin Hydrodynamics Laboratory (KHL) in Strathclyde University and details are presented in Appendix C.

Chapter 6 Conclusions & Recommendations for Future Research

6.1 Introduction

The main objective of Chapter 6 is to give an overall review of the research study presented in this thesis with an emphasis on the original contributions made to the state-of-the-art while achieving the aim and objectives of the research study which involved an investigation into the application of leading-edge tubercles on the blades of horizontal axis tidal turbines for hydrodynamic performance improvement. The chapter also summarises the main conclusions of the research as well as providing recommendations for the future research.

Following this introductory section (Section 6.1), next is an overall review of the thesis (Section 6.2) which is followed by a summary of the main conclusions given in Section 6.3. The recommendations for future research are then presented in Section 6.4.

6.2 Overall review of the thesis and contributions to the state-of-the-art

The process of learning from Mother Nature has never stopped. Originating from the research investigations started in the late 2000s, biomimetic application of the leading-edge tubercles of humpback whale flippers has shown great potential to improve the performance of foils. Since then, considerable research efforts have been spent on fundamental and theoretical studies to understand the mechanism of the performance improvements by tubercles in applying this interesting technology solution in air and water. However, few studies have been conducted in real technology applications, especially in the renewable energy field.

With the aim of exploring the feasibility of enhancing the hydrodynamic performance of tidal turbines, this PhD project has made original and useful contributions to the state-of-the-art research in applying the leading-edge tubercle concept to tidal turbine blade design and demonstrating its beneficial effects on the turbine performance. In order to meet its research aim, the project has presented for the first time a systematic and wide ranging set of experimental investigations, which have been also supported by numerical investigations, to exploit this biomimetic concept for performance improvement in tidal turbines. Within limitations, the experimental data and supporting findings not only provide further confidence in applying this biomimetic concept to tidal turbines in full-scale applications but also provide invaluable benchmark data for CFD and other research activities in the field of tubercle research in general, as well as for their specific application in tidal turbines.

The research study had four main objectives which have been stated in Chapter 1 and tackled within the six chapters of the thesis. Starting from Chapter 2, the state of the art has been reviewed regarding the development of the tidal energy industry, recent research about the leading-edge tubercle concept and the associated cutting-edge experimental and numerical methodologies. Chapter 2 indicated that an extremely limited amount of research is available on the application of leading-edge tubercles on tidal turbines; this being a major research gap that needed to be addressed and bridged. This would require further research, in particular experimental research, to help in understanding the physics of the leading-edge tubercles and whether they can improve the turbine performance as well as demonstrating the design and optimisation of this biomimetic concept. Chapter 2 also identified other research gaps and appropriate research methodologies used for the development work presented in the remaining chapters of the thesis while satisfying *#Objective 1*.

Chapter 3 tackled the first and also the primary question of how to design the tubercles to be applied on a tidal turbine blade. The chapter therefore focused on the design and optimisation of the tubercles for a specific blade section by using numerical methods. The application work was conducted within the ANSYS software packages, including 3D modelling, mesh generation and CFD simulation, where a reference foil with a smooth leading-edge section has been fitted with various sizes of leading-edge tubercle design and the effect of the tubercles on the performance of the lift and drag characteristics was evaluated. With the aid of this work, an “optimum” design for the foil section was proposed for the remaining part of the research study, satisfying *#Objective 2*. This is another contribution of this research study to the state-of-the-art as there has been no such detailed investigation reported in the literature concerning applications for tidal turbine blade sections.

By applying the above mentioned optimum design methodology to a representative 3D tidal turbine blade, that was designed based on an existing tidal turbine blade, Chapter 4 aimed to achieve some basic understandings of the tubercle concept in a turbine blade application as well as to validate the design methodology using experimental methods. Therefore, a 3D basis foil model, which could be fitted with a smooth edge and various leading-edge tubercle profiles, was designed, fabricated and tested in the Emerson Cavitation Tunnel to measure its lift and drag characteristics under various angle of attacks and flow speeds. These tests also involved detailed flow measurements and visualizations using the PIV technique. The test results demonstrated significant benefits from the use of tubercles in terms of improving the lift coefficient and lift-to-drag ratio of this representative turbine blade. The experimental

measurements were further validated and complimented by numerical simulations using the commercial CFD software Star-CCM+ for detailed flow analysis. The flow analysis showed that the contra-rotating vortices generated by the tubercles were forming vortex fences which prevented the tip vortex from inducing detrimental spanwise cross-flow and also helped the flow to remain more attached to the blade surface. The systematic experimental force and flow data provided for the representative turbine blade in this chapter is a unique contribution to the state-of-the art while #Objective 3 of the research study has been achieved in Chapter 4.

Based on the confidence gained with the representative blade performance in Chapter 4, whether the leading-edge tubercles can really improve the performance of a state-of-the-art tidal turbine with efficient blades had to be fully investigated in the Chapter 5 with #Objective 4 in mind. In Chapter 5, therefore, a series of model test campaigns were conducted in the cavitation tunnel. Various aspects of the hydrodynamic performance have been investigated with three model turbines with different leading-edge profiles (one with a smooth leading edge and another two with different extents of leading edge tubercles) including the following:

1. Systematic open water performance tests conducted both in the Emerson Cavitation Tunnel evaluated the performance differences of the turbines in terms of their power coefficients and thrust coefficients to investigate the effect of the tubercles.
2. Systematic cavitation observation tests covering the most probable full-scale operating conditions evaluated the differences in the cavitation performance of the turbines to identify the effect of tubercles.
3. Systematic noise measurement tests were conducted to evaluate the implementation of leading-edge tubercles on the underwater noise performance of the turbines.
4. Detailed flow measurements and analysis with a Stereo PIV system were carried out in order to study the complex hydrodynamic flow structure of the turbine system, including its slipstream; this would help to understand the beneficial/detrimental effect of the tubercles on the hydrodynamic performance of the turbines;

Considering the above research activities presented in Chapter 5, it can be claimed that the systematic experimental data presented for the three turbines, in terms of their torque and thrust data, cavitation performances and underwater radiated noise levels, are major contributions to the state-of-the-art in identifying the effect of tubercles on these hydrodynamic characteristics.

In addition to reporting the research in this thesis, during the PhD the Author has also published parts of this research in numerous respected journals and international conferences listed as follows:

Thesis related

1. Shi, W., M. Atlar, R. Norman, B. Aktas and S. Turkmen (2016). "Numerical optimization and experimental validation for a tidal turbine blade with leading-edge tubercles." *Renewable Energy* 96: 42-55.
2. Shi, W., M. Atlar, R. Rosli, B. Aktas and R. Norman (2016). "Cavitation observations and noise measurements of horizontal axis tidal turbines with biomimetic blade leading-edge designs." *Ocean Engineering* 121: 143-155.
3. Shi, W., R. Rosli, M. Atlar, R. Norman, D. Wang and W. Yang (2016). "Hydrodynamic performance evaluation of a tidal turbine with leading-edge tubercles." *Ocean Engineering* 117: 246-253.
4. Shi, W., M. Atlar, K. Seo, R. Norman and R. Rosli (2016). "Numerical simulation of a tidal turbine based hydrofoil with leading-edge tubercles." 35th International Conference on Ocean, Offshore and Arctic Engineering, OMAE2016. Busan, Korea, Proceedings of the ASME 2016.
5. Shi, W., M. Atlar, R. Norman, B. Aktas and S. Turkmen (2015). "Biomimetic improvement for a tidal turbine blade." EWTEC 2015. Nantes, France. 07B3-5: 01-05.
6. Shi, W., M. Atlar, R. Norman and K.-c. Seo (2014). "CFD investigations on leading-edge tubercles as applied on a tidal turbine blade." GRAND RENEWABLE ENERGY 2014. Tokyo, Japan. P-Oc-1-12.
7. Shi, W., R. Rosli, M. Atlar, R. Norman, D. Wang and W. Yang (2015). "Hydrodynamic performance of a biomimetically improved tidal turbine blade." AMT 15. Istanbul, Turkey.
8. Shi, W., D. Wang, M. Atlar and K.-c. Seo (2013). "Flow separation impacts on the hydrodynamic performance analysis of a marine current turbine using CFD." Proceedings of the Institution of Mechanical Engineers, Part A: Journal of Power and Energy 227(8): 833–846.

9. Shi, W., D. Wang, M. Atlar and D. Wang (2013). "Similarity laws and model test approaches to determine hydrodynamic performance of a marine turbine." *Advanced Materials Research* 694-697: 665-672.

Other publications during the PhD

1. Shi, W., D. Wang, M. Atlar, B. Guo and K.-C. Seo (2015). "Optimal design of a thin-wall diffuser for performance improvement of a tidal energy system for an AUV." *Ocean Engineering*.
2. Aktas, B., M. Atlar, S. Turkmen, W. Shi, R. Sampson, E. Korkut and P. Fitzsimmons (2015). "Propeller Cavitation Noise Investigations of a Research Vessel Using Medium Size Cavitation Tunnel Tests and Full-Scale Trials." *Ocean Engineering*.
3. Butterworth, J., M. Atlar and W. Shi (2015). "Experimental analysis of an air cavity concept applied on a ship hull to improve the hull resistance." *Ocean Engineering* 110, Part B: 2-10.
4. Carchen, A., W. Shi, N. Sasaki and M. Atlar (2006). "A prediction program of manoeuvrability for a ship with a Gate Rudder system." *A. Yücel Odabaşı Colloquium Series - 2nd International Meeting on Recent Advances in Prediction Techniques for Safe Manoeuvring of Ships and Submarines*. Istanbul, Turkey.
5. Rosli, R., Shi, W., Norman, R. and Atlar, M. (2015) "Cavitation tunnel investigation on the performance cavitation pressure pulses noise of the hydro-spinna turbine," *AMT2015*. Istanbul, Turkey.
6. Turkmen, S., B. Aktas, M. Atlar, N. Sasaki, R. Sampson and W. Shi (2017). "On-board measurement techniques to quantify underwater radiated noise level." *Ocean Engineering* 130: 166-175.
7. Turkmen, S., B. Aktas, M. Atlar, N. Sasaki, R. Sampson, W. Shi and P. Fitzsimmons (2015). "On-board measurement techniques to quantify underwater radiated noise level." *AMT 2015*. Istanbul.
8. Wang, D., Wang, D., Mei, L. and Shi, W. (2013) "The hydrodynamic analysis of propeller based on ANSYS-CFX." *Advanced Materials Research*, 694-697, pp. 673-677.

9. Zoet, P., S. Turkmen, P. Kellett, B. Aktas, R. Sampson, W. Shi, M. Atlar and O. Turan (2015). "On board structure borne noise measurements and underwater radiated noise." AMT 2015. Istanbul.
10. Sampson, R., Turkmen, S., Aktas, B., Shi, W., Fitzsimmons, P. and Atlar, M. (2015) "On the full scale and model scale cavitation comparisons of a Deep-V catamaran research vessel." Fourth International Symposium on Marine Propulsors, SMP 15. Austin, Texas, USA.
11. Aktas, B., Atlar, M., Fitzsimmons, P., Shi, W., Turkmen, S. and Sasaki, N. (2015) "Systematic cavitation tunnel tests for cavitation noise prediction of commercial ships using a standard series approach." AMT 2015. Istanbul, Turkey.
12. Guo, B., Wang, D. and Shi, W. (2015) "Power output performance characteristics of bidirectional tidal current turbine in a circulating water channel." AMT 2015. Istanbul, Turkey.

6.3 Main conclusions

Complementing the conclusion and summary of each chapter stated earlier, the following are the main conclusions of this thesis:

1. Investigations conducted in this thesis exploring the feasibility of enhancing the hydrodynamic performance of tidal turbines have made original and useful contributions to the state-of-the-art research in applying the leading-edge tubercle concept to tidal turbine blade design and demonstrating its beneficial effects on various hydrodynamic performances of these turbines.
2. The leading-edge tubercles can enhance the lift coefficients and lift-to-drag ratio of the 3D hydrofoil despite a slight increase in the drag characteristics, especially beyond the point at which the reference blade had already stalled. This effect was observed, later on, when the tubercles were applied on the turbine model, improving the performance in the low TSR region where the turbine blade stalled.
3. It was noticed that the tubercles constrained (boxed) the development of the blade sheet cavitation patterns within the troughs of the tubercles, as opposed to the continuous sheet/cloud cavitation development of the blades with the smooth leading edge. Since

the underwater noise levels were strongly related to the cavitation patterns, the associated noise levels of the biomimetic turbines were also reduced because of the constrained cavitation effect.

4. The tubercle effect observed both in the 3D hydrofoil case and the turbine case was mainly accredited to the contra rotating vortices. This energized the flow to trigger a turbulent flow to remain attached to the surface while forming a vortex fence to stop the spanwise cross-flow induced by the 3D effect/tip vortex; this was the reason for the performance difference of 2D foil and 3D foil.
5. By reducing the numbers of tubercles, the effect of improved performance was gradually reduced. The design with two tubercles at the tip, during the 3D hydrofoil test, displayed the best overall performance because of the increased lift-to-drag coefficient ratio over a wider range of angles of attack. During the tests with the turbine models, however, the Sin2 model showed a similar trend to the reference turbine but still maintained the beneficial effect at low TSR but not as significantly as the Sin8 model.
6. The finding stated in 5, was later investigated by the PIV measurements with the turbine models. The difference between the turbine model test and the 3D hydrofoil test was: when the turbine was operating under low TSR the blade sections at different radial positions were experiencing different angles of attack; while the sections of the hydrofoil always operated under the same angle of attack. Therefore, some tubercles on the blades did not play their role (i.e. operating in optimum condition) effectively.
7. During the optimisation process of the tubercle arrangement, by varying the size of tubercles on the blade section, it was shown that the application of tubercles could maintain high lift coefficients under post-stall conditions, at the price of lowering the maximum lift. Therefore, a balanced design needed to be found for the successful application of leading-edge tubercles.

6.4 Recommendations for the future research

While the Author is confident that he did his best to satisfy the aim and objectives of his thesis within the limitation of the time and resources of this project, he can recommend the following, which have stemmed from his study, for future research:

- 1. Development of a control scheme for the tubercle based biomimetic turbine:** Nowadays self-starting of a modern tidal/wind turbine is a difficult task to perform even with good pitch control. Turbine designers often choose a strategy to drive the turbine using the generator to kick start the rotation or even drive the turbine constantly instead of stopping the turbine when the current is not sufficient to generate power. This will consume enormous amounts of electrical power instead of generating. However, using the tubercle-based biomimetic blades with improved performance in low TSR, there is great scope to improve the starting performance. Therefore, the associated control development is urgently needed to get the maximum benefit from the tubercle-based turbines.
- 2. Direct optimisation study for leading-edge tubercles on tidal turbine:** In this thesis, the author employed a computation economical optimisation methodology via optimising the tubercle on a 2D foil section first and then apply the design onto the 3D foil and eventually to the tidal turbine blade. However, there is a future scope to employ advanced numerical methodologies to directly optimise the leading-edge tubercles as applied on tidal turbine blades, which requires further development of CFD simulation and support from extensive computer power.
- 3. Commercial viability study of retrofitting leading-edge tubercles to modern tidal/wind turbines:** Combined with the above described control scheme, a feasibility study of retrofitting the biomimetic leading-edges to existing turbines should be conducted including the life cycle cost evaluation.
- 4. Full-scale numerical study for the prototype turbine:** Even though the test in the cavitation tunnel was able to reach a Reynolds number independent status, considerable blockage effect, scale effect and Reynolds number effect still influence the test results. In the future the research should continue including full-scale numerical simulations.
- 5. Large-scale experimental tests for the wave-current interaction:** Because of the scale limitation, the current conclusion with regard to the wave tank tests is limited by the small scale and for the deeply submerged condition. Sufficiently large turbine models need to be built to perform the wave test, preferably conducting tests in a wave basin rather than a towing tank to include the flow directionality.

- 6. Applications to other devices:** with the accumulated knowledge, the application of this wavy leading-edge concept can also be pursued for other applications, e.g. on marine propellers especially for heavily cavitating propellers or highly loaded propellers while the propeller is operating under stall conditions. The PhD candidate is intending to continue this study in his Post-doctoral research.

Reference

- Alstom (2013) *Alstom produced electricity with its 1MW tidal turbine as a part of ETI ReDAPT project*. Available at: <http://www.eti.co.uk/alstom-produced-electricity-with-its-1mw-tidal-turbine-as-a-part-of-eti-redapt-project/>.
- ANSYS (2013) 'Release 14.5 Documentation', *Inc ANSYS*.
- Arai, H., Doi, Y., Nakashima, T. and Mutsuda, H. (2010) 'A Study on Stall Delay by Various Wavy Leading Edges', *Journal of Aero Aqua Bio-mechanisms*, 1(1), pp. 18-23.
- Atlantis (2015) *AR1000*. Available at: <http://atlantisresourcesltd.com/turbines/ar-series/ar1000.html>.
- Atlas, M. (2011) 'Recent upgrading of marine testing facilities at Newcastle University', *AMT'11*. Newcastle upon Tyne, UK, 4-5 April, 2011. pp. 4-6.
- Badcock-Broe, A., Flynn, R., George, S., Gruet, R. and Medic, N. (2013) *Ocean energy technology: gaps and barriers*. Strategic Initiative for Ocean Energy (SI Ocean). [Online]. Available at: <http://www.si-ocean.eu/en/upload/docs/WP3/Gaps> and Barriers Report FV.pdf.
- Badcock-Broe, A., Flynn, R., George, S., Gruet, R. and Medic, N. (2014) *Wave and Tidal Energy Market Deployment Strategy for Europe*. Strategic Initiative for Ocean Energy (SI Ocean). [Online]. Available at: <http://www.si-ocean.eu/en/Market-Deployment/Market-Deployment-Strategy/>.
- Bahaj, A.S., Batten, W.M.J. and McCann, G. (2007) 'Experimental verifications of numerical predictions for the hydrodynamic performance of horizontal axis marine current turbines', *Renewable Energy*, 32(15), pp. 2479-2490.
- Barltrop, N., Varyani, K.S., Grant, A., Clelland, D. and Pham, X. (2006) 'Wave-current interactions in marine current turbines', *Proceedings of the Institution of Mechanical Engineers, Part M: Journal of Engineering for the Maritime Environment*, 220(4), pp. 195-203.
- Bellequant, L. and Howle, L.E. (2009) 'Whalepower Wenvor Blade'.
- BlueTEC (2015) *BlueTEC Modular*. Available at: <http://www.bluewater.com/new-energy/bluetec-modular/>.

-
- Bolzon, M.D., Kelso, R.M. and Arjomandi, M. (2014) 'The Effects of Tubercles on Swept Wing Performance at Low Angles of Attack', *19th Australasian Fluid Mechanics Conference*. Melbourne, Australia.
- Bolzon, M.D., Kelso, R.M. and Arjomandi, M. (2016) 'Tubercles and Their Applications', *Journal of Aerospace Engineering*, 29(1), p. 04015013.
- Charlier, R.H. (2003) 'A "sleeper" awakes: tidal current power', *Renewable & Sustainable Energy Reviews*, 7(6), pp. 515-529.
- Chen, J.H., Li, S.S. and Nguyen, V.T. (2012) 'The effect of leading edge protuberances on the performance of small aspect ratio foils', *15th International Symposium on Flow Visualization*. Minsk, Belarus.
- Corsini, A., Delibra, G. and Sheard, A.G. (2013) 'On the Role of Leading-Edge Bumps in the Control of Stall Onset in Axial Fan Blades', *Journal of Fluids Engineering-Transactions of the Asme*, 135(8), pp. 081104-081104.
- Custodio, D. (2007) *The effect of humpback whale-like leading edge protuberances on hydrofoil performance*. WORCESTER POLYTECHNIC INSTITUTE.
- Day, A.H., Babarit, A., Fontaine, A., He, Y.P., Kraskowski, M., Murai, M., Penesis, I., Salvatore, F. and Shin, H.K. (2015) 'Hydrodynamic modelling of marine renewable energy devices: A state of the art review', *Ocean Engineering*, 108, pp. 46-69.
- de Jesus Henriques, T.A., Tedds, S.C., Botsari, A., Najafian, G., Hedges, T.S., Sutcliffe, C.J., Owen, I. and Poole, R.J. (2014) 'The effects of wave–current interaction on the performance of a model horizontal axis tidal turbine', *International Journal of Marine Energy*, 8, pp. 17-35.
- Douglas, C.A., Harrison, G.P. and Chick, J.P. (2008) 'Life cycle assessment of the Seagen marine current turbine', *Proceedings of the Institution of Mechanical Engineers Part M-Journal of Engineering for the Maritime Environment*, 222(M1), pp. 1-12.
- EMEC (2013) *Tidal devices*. Available at: <http://www.emec.org.uk/marine-energy/tidal-devices/>.
- Fish, F.E. and Battle, J.M. (1996) 'Hydrodynamic design of the humpback whale flipper', *Journal of Morphology*, 225:51-60.

Fish, F.E., Howle, L.E. and Murray, M.M. (2008) 'Hydrodynamic flow control in marine mammals', *Integr Comp Biol*, 48(6), pp. 788-800.

Fish, F.E., Weber, P.W., Murray, M.M. and Howle, L.E. (2011) 'The tubercles on humpback whales' flippers: application of bio-inspired technology', *Integr Comp Biol*, 51(1), pp. 203-13.

Gaurier, B., Germain, G., Facq, J.V., Johnstone, C.M., Grant, A.D., Day, A.H., Nixon, E., Di Felice, F. and Costanzo, M. (2015) 'Tidal energy “Round Robin” tests comparisons between towing tank and circulating tank results', *International Journal of Marine Energy*, 12, pp. 87-109.

Gruber, T., Murray, M.M. and Fredriksson, D.W. (2011) 'Effect of humpback whale inspired tubercles on marine tidal turbine blades', *ASME 2011 International Mechanical Engineering Congress and Exposition*. 11-17 November American Society of Mechanical Engineers, pp. 851-857.

Hain, J.H.W., Carter, G.R., Kraus, S.D., Mayo, C.A. and Winn, H.E. (1982) 'Feeding-Behavior of the Humpback Whale, Megaptera-Novaeangliae, in the Western North-Atlantic', *Fishery Bulletin*, 80(2), pp. 259-268.

Hammond, D.A., Amateau, M.F. and Queeney, R.A. (1993) 'Cavitation Erosion Performance of Fiber-Reinforced Composites', *Journal of Composite Materials*, 27(16), pp. 1522-1544.

Hansen, K., Kelso, R. and Doolan, C. (2012) 'Reduction of Flow Induced Airfoil Tonal Noise Using Leading Edge Sinusoidal Modifications', *Acoustics Australia*, 40(3), pp. 172-177.

Hansen, K.L., Kelso, R.M. and Dally, B.B. (2009) 'The effect of leading edge tubercle geometry on the performance of different airfoils', *ExHFT-7*. Krakow, Poland, 28 June, 2009.

Hansen, K.L., Kelso, R.M. and Dally, B.B. (2011) 'Performance Variations of Leading-Edge Tubercles for Distinct Airfoil Profiles', *Aiaa Journal*, 49(1), pp. 185-194.

Hansen, K.L., Rostamzadeh, N., Kelso, R.M. and Dally, B.B. (2016) 'Evolution of the streamwise vortices generated between leading edge tubercles', *Journal of Fluid Mechanics*, 788, pp. 730-766.

Harper, P.W. and Hallett, S.R. (2015) 'Advanced numerical modelling techniques for the structural design of composite tidal turbine blades', *Ocean Engineering*, 96, pp. 272-283.

-
- Harrison, M., Batten, W., Myers, L. and Bahaj, A. (2010) 'Comparison between CFD simulations and experiments for predicting the far wake of horizontal axis tidal turbines', *Renewable Power Generation, IET*, 4(6), pp. 613-627.
- Huang, G.Y., Shiah, Y.C., Bai, C.J. and Chong, W.T. (2015) 'Experimental study of the protuberance effect on the blade performance of a small horizontal axis wind turbine', *Journal of Wind Engineering and Industrial Aerodynamics*, 147, pp. 202-211.
- Ibrahim, I.H. and New, T.H. (2015) 'Tubercle modifications in marine propeller blades', *10th Pacific Symposium on Flow Visualization and Image Processing*. Naples, Italy.
- ITTC (1978) *Proceedings of the 15th International Towing Tank Conference (ITTC)*. Netherland: ITTC.
- Janiszewska, J.M., Ramsay, R.R., Hoffmann, M.J. and Gregorek, G.M. (1996) *Effects of grit roughness and pitch oscillations on the S814 airfoil*. National Renewable Energy Lab., Golden, CO (United States).
- Jo, C.H., Yim, J.Y., Lee, K.H. and Rho, Y.H. (2012) 'Performance of horizontal axis tidal current turbine by blade configuration', *Renewable Energy*, 42, pp. 195-206.
- Johari, H. (2015) 'Cavitation on hydrofoils with sinusoidal leading edge', *9th International Symposium on Cavitation (Cav2015)*, 656, p. 012155.
- Johari, H., Henoch, C., Custodio, D. and Levshin, A. (2007) 'Effects of leading-edge protuberances on airfoil performance', *Aiaa Journal*, 45(11), pp. 2634-2642.
- Khan, J. and Bhuyan, G.S. (2009) 'Ocean energy: global technology development status', *IEA-OES. Document*, (T0104).
- Khan, M.J., Bhuyan, G., Iqbal, M.T. and Quaiocoe, J.E. (2009) 'Hydrokinetic energy conversion systems and assessment of horizontal and vertical axis turbines for river and tidal applications: A technology status review', *Applied Energy*, 86(10), pp. 1823-1835.
- King, J. and Tryfonas, T. (2009) 'Tidal stream power technology-state of the art', *OCEANS 2009-EUROPE*. May. IEEE, pp. 1-8.

- Li, D., Wang, S.J. and Yuan, P. (2010) 'An overview of development of tidal current in China: Energy resource, conversion technology and opportunities', *Renewable & Sustainable Energy Reviews*, 14(9), pp. 2896-2905.
- Magagna, D. and Uihlein, A. (2015) 'Ocean energy development in Europe: Current status and future perspectives', *International Journal of Marine Energy*, 11, pp. 84-104.
- Malipeddi, A.K. (2011) *Numerical analysis of effects of leading-edge protuberances on aircraft wing performance*. Wichita State University.
- Mason-Jones, A., O'Doherty, D.M., Morris, C.E. and O'Doherty, T. (2013) 'Influence of a velocity profile & support structure on tidal stream turbine performance', *Renewable Energy*, 52, pp. 23-30.
- Mason-Jones, A., O'Doherty, D.M., Morris, C.E., O'Doherty, T., Byrne, C.B., Prickett, P.W., Grosvenor, R.I., Owen, I., Tedds, S. and Poole, R.J. (2012) 'Non-dimensional scaling of tidal stream turbines', *Energy*, 44(1), pp. 820-829.
- McCormick, J.B.W. (1962) 'On Cavitation Produced by a Vortex Trailing From a Lifting Surface', *Journal of Fluids Engineering*, 84(3), pp. 369-378.
- Menter, F., Kuntz, M. and Langtry, R. (2003) 'Ten years of industrial experience with the SST turbulence model', *Turbulence, heat and mass transfer*, 4, pp. 625-632.
- Miklosovic, D.S., Murray, M.M. and Howle, L.E. (2007) 'Experimental evaluation of sinusoidal leading edges', *Journal of Aircraft*, 44(4), pp. 1404-1408.
- Miklosovic, D.S., Murray, M.M., Howle, L.E. and Fish, F.E. (2004) 'Leading-edge tubercles delay stall on humpback whale (*Megaptera novaeangliae*) flippers', *Physics of Fluids*, 16(5), pp. L39-L42.
- Mitchell, C. and Connor, P. (2004) 'Renewable energy policy in the UK 1990–2003', *Energy Policy*, 32(17), pp. 1935-1947.
- O'Doherty, T., Mason-Jones, A., O'Doherty, D., Byrne, C., Owen, I. and Wang, Y. (2009) 'Experimental and computational analysis of a model horizontal axis tidal turbine', *8th European Wave and Tidal Energy Conference (EWTEC)*, Uppsala, Sweden. 7-10 September.
- Ocean Energy Systems (2016) *GIS map*. Available at: <https://www.ocean-energy-systems.org>.

-
- Pelc, R. and Fujita, R.M. (2002) 'Renewable energy from the ocean', *Marine Policy*, 26(6), pp. 471-479.
- Rostamzadeh, N., Hansen, K.L., Kelso, R.M. and Dally, B.B. (2014) 'The formation mechanism and impact of streamwise vortices on NACA 0021 airfoil's performance with undulating leading edge modification', *Physics of Fluids*, 26(10), pp. 1-22.
- Rostamzadeh, N., Kelso, R.M., Dally, B.B. and Hansen, K.L. (2013) 'The effect of undulating leading-edge modifications on NACA 0021 airfoil characteristics', *Physics of Fluids*, 25(11).
- Scotrenewables (2015) *SR2000*. Available at: <http://www.scotrenewables.com/sr2000>.
- Shi, W., Atlar, M., Seo, K., Norman, R. and Rosli, R. (2016) 'Numerical simulation of a tidal turbine based hydrofoil with leading-edge tubercles', *35th International Conference on Ocean, Offshore and Arctic Engineering, OMAE2016*. Busan, Korea. Proceedings of the ASME 2016.
- Shi, W., Rosli, R., Atlar, M., Norman, R., Wang, D. and Yang, W. (2015) 'Hydrodynamic performance of a biomimetically improved tidal turbine blade', *AMT 15*. Istanbul, Turkey.
- Shi, W.C., Wang, D.Z., Atlar, M. and Wang, D. (2013) 'Similarity Laws and Model Test Approaches to Determine Hydrodynamic Performance of A Marine Turbine', *Manufacturing Process and Equipment, Pts 1-4*, 694-697, pp. 665-672.
- Sisinni, G., Pietrogiacomini, D. and Romano, G.P. (2012) 'Biomimetic Wings', *Advances in Science and Technology*, 84, pp. 72-77.
- Somers, D.M. (2004) 'The S814 and S815 Airfoils'.
- Stanway, M.J. (2008) *Hydrodynamic effects of leading-edge tubercles on control surfaces and in flapping foil propulsion*. Massachusetts Institute of Technology.
- Stuart, R. (2014) *Spitfire*. Available at: <http://www.roystuart.biz/2014/11/surfboard-fins-explained.html?view=sidebar>.
- Swanson, T. and Isaac, K.M. (2011) 'Biologically Inspired Wing Leading Edge for Enhanced Wind Turbine and Aircraft Performance'. AIAA.

SwiftSwan, M. (2015) *Tale of Whales and Whistling for Dolphins*. Available at: <http://www.afterguard.net/single-post/2015/02/03/Tale-of-Whales-and-Whistling-for-Dolphins> (Accessed: 28/09).

Tatum, S.C., Frost, C.H., Allmark, M., O'Doherty, D.M., Mason-Jones, A., Prickett, P.W., Grosvenor, R.I., Byrne, C.B. and O'Doherty, T. (2016) 'Wave-current interaction effects on tidal stream turbine performance and loading characteristics', *International Journal of Marine Energy*, 14, pp. 161-179.

van Nierop, E.A., Alben, S. and Brenner, M.P. (2008) 'How bumps on whale flippers delay stall: an aerodynamic model', *Phys Rev Lett*, 100(5), p. 054502.

Wang, D., Atlar, M. and Sampson, R. (2007a) 'An experimental investigation on cavitation, noise, and slipstream characteristics of ocean stream turbines', *Proceedings of the Institution of Mechanical Engineers, Part A: Journal of Power and Energy*, 221(2), pp. 219-231.

Wang, D., Atlar, M. and Sampson, R. (2007b) 'An experimental investigation on cavitation, noise, and slipstream characteristics of ocean stream turbines', *Proceedings of the Institution of Mechanical Engineers Part a-Journal of Power and Energy*, 221(A2), pp. 219-231.

Weber, P.W., Howle, L.E. and Murray, M.M. (2010) 'Lift, Drag, and Cavitation Onset On Rudders With Leading-edge Tubercles', *Marine Technology and Sname News*, 47(1), pp. 27-36.

Wei, Z.Y., New, T.H. and Cui, Y.D. (2015) 'An experimental study on flow separation control of hydrofoils with leading-edge tubercles at low Reynolds number', *Ocean Engineering*, 108, pp. 336-349.

Whalepower (2016) *Fans*. Available at: <https://whalepowercorp.wordpress.com/fans/>.

Wikipedia (2016) *Humpback whale*. Available at: https://en.wikipedia.org/wiki/Humpback_whale.

Yoon, H.S., Hung, P.A., Jung, J.H. and Kim, M.C. (2011) 'Effect of the wavy leading edge on hydrodynamic characteristics for flow around low aspect ratio wing', *Computers & Fluids*, 49(1), pp. 276-289.

Zhang, R.K. and Wu, J.Z. (2012) 'Aerodynamic characteristics of wind turbine blades with a sinusoidal leading edge', *Wind Energy*, 15(3), pp. 407-424.

Zhang, Y.-l., Lin, Z. and Liu, Q.-l. (2014) 'Marine renewable energy in China: Current status and perspectives', *Water Science and Engineering*, 7(3), pp. 288-305.

Appendix A - Test results of open water hydrodynamic performance

As described in the Section 5.3, the rest results of the open water test under higher speed in the ECT have been presented in this Appendix A. The test results might be affected by the blade cavitation. But the results are also valuable to show the performance difference in the higher Reynolds numbers and under the cavitation conditions.

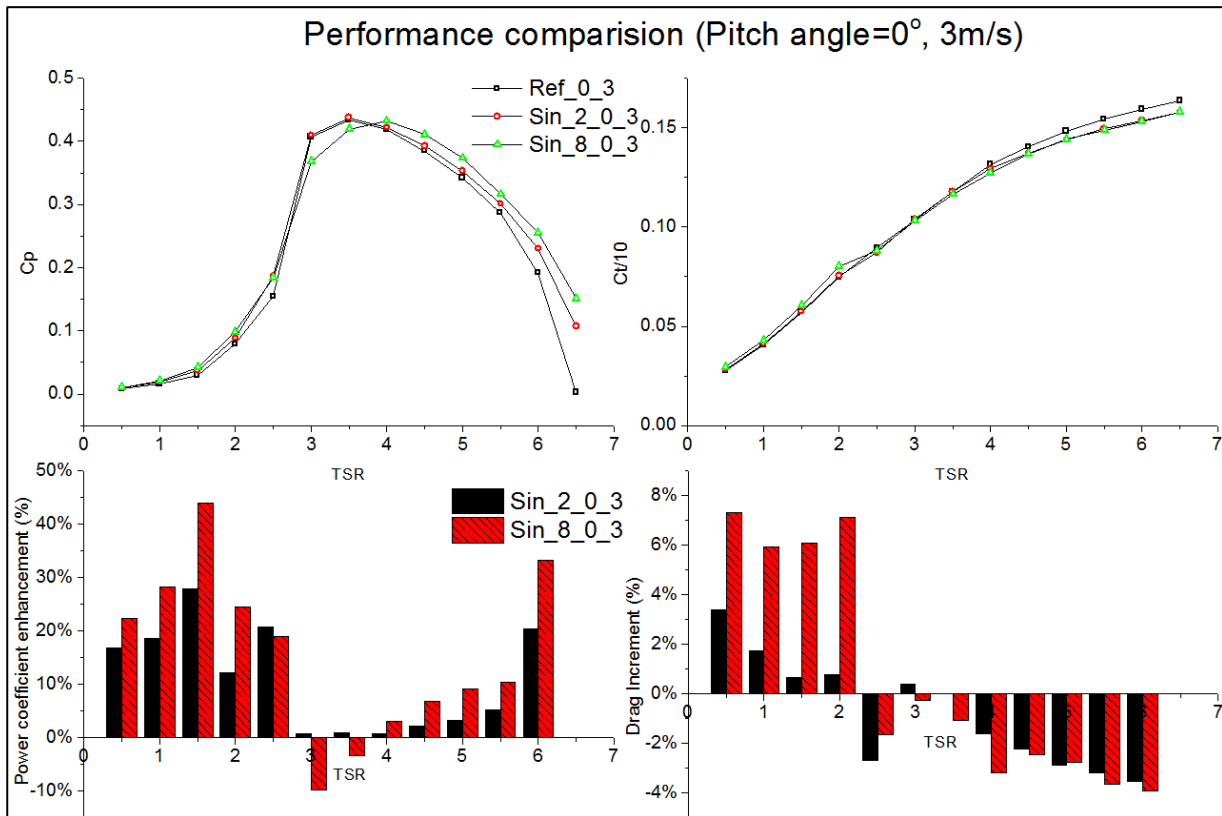


Figure A-1 Performance comparison (Pitch=0°, 3m/s)

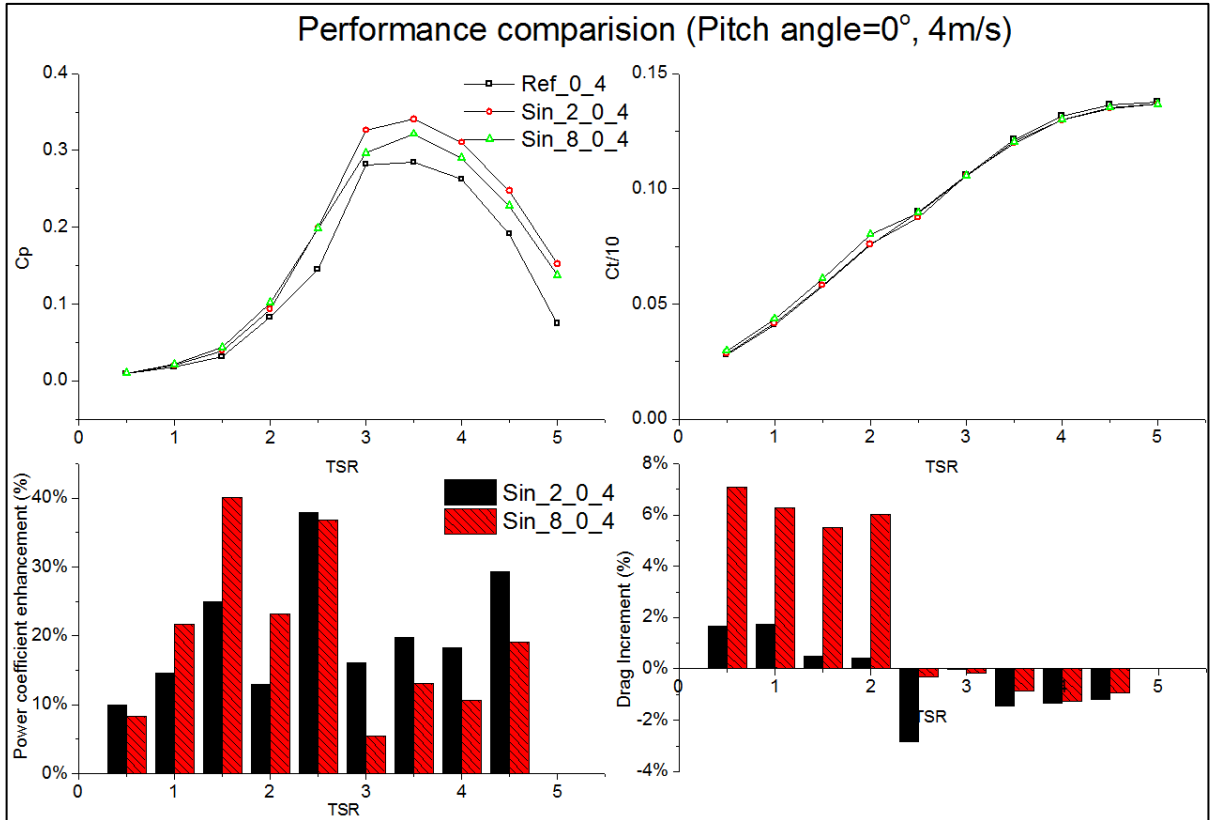


Figure A-2 Performance comparison (Pitch=0°, 4m/s)

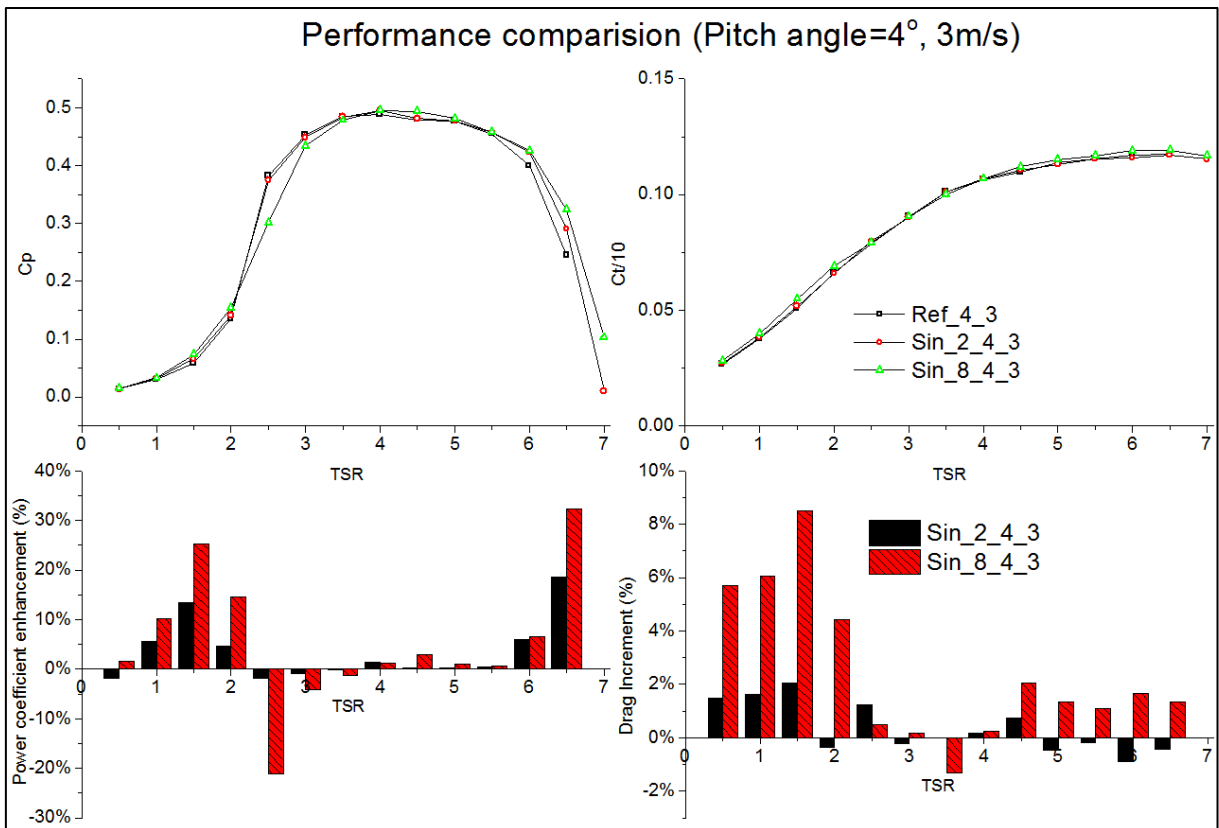


Figure A-3 Performance comparison (Pitch=4°, 3m/s)

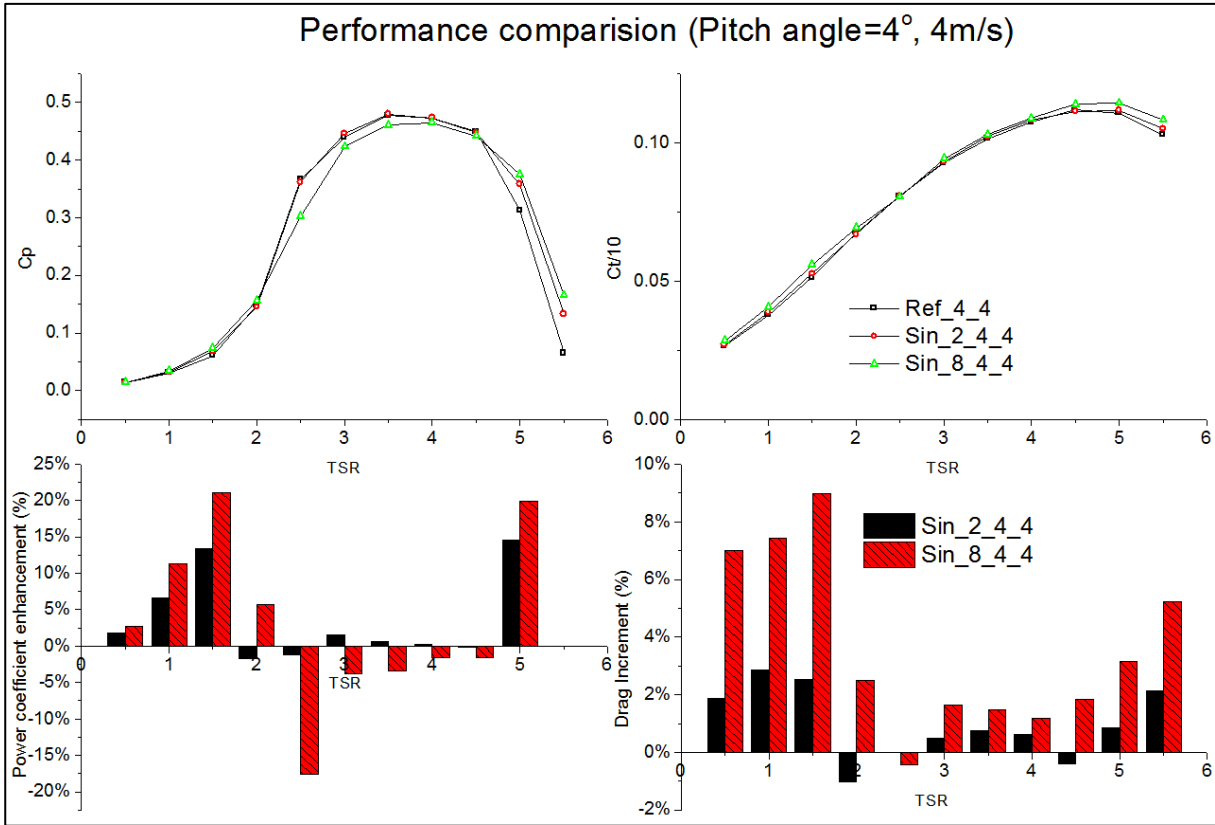


Figure A-4 Performance comparison (Pitch=4°, 4m/s)

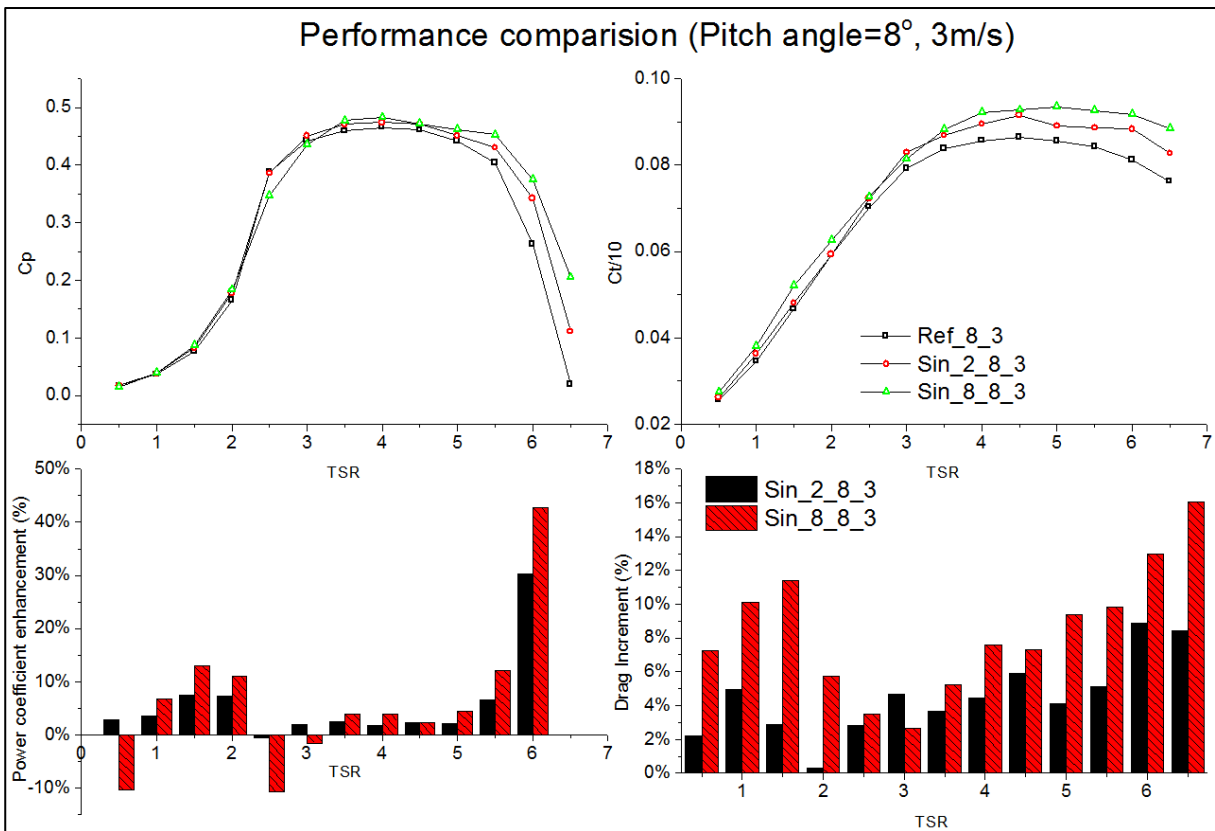


Figure A-5 Performance comparison (Pitch=8°, 3m/s)

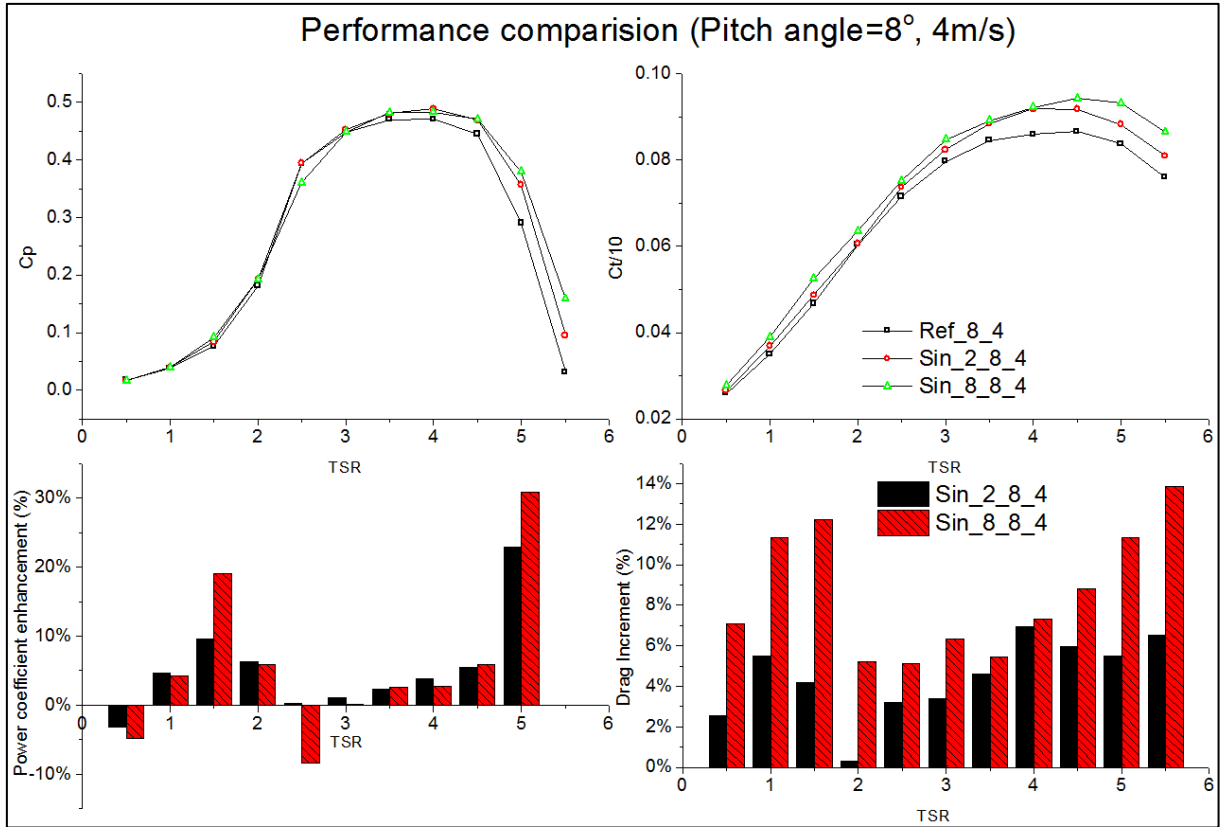

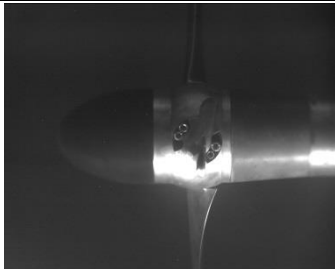
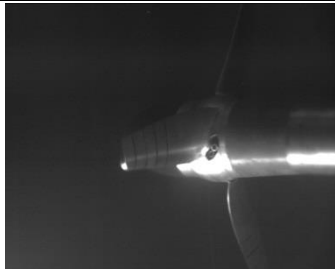
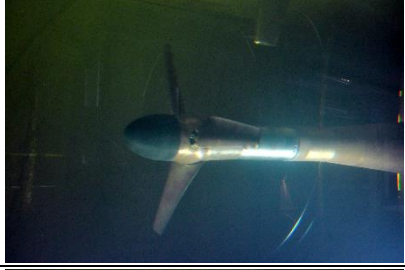
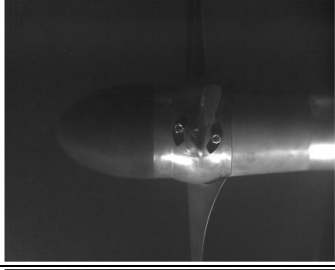


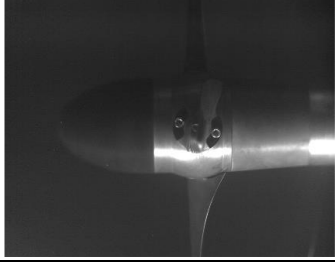
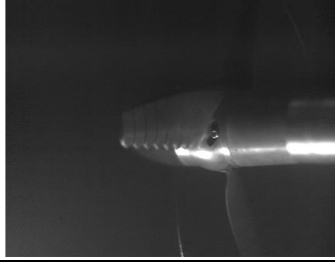

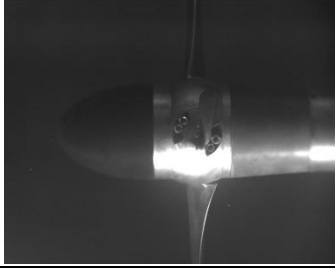


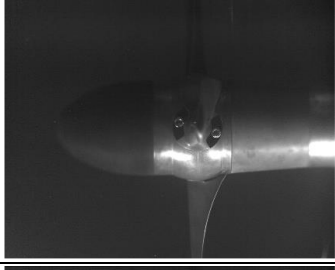
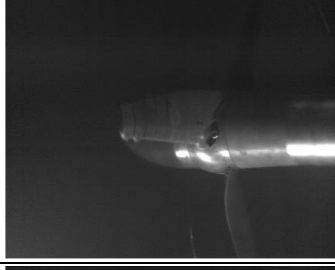

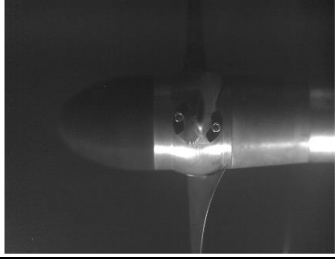



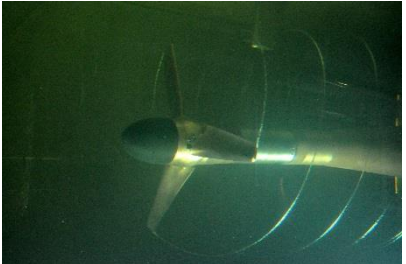
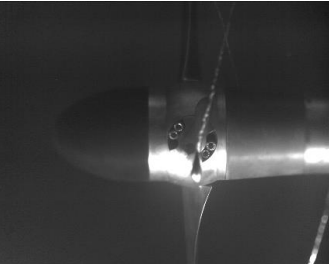
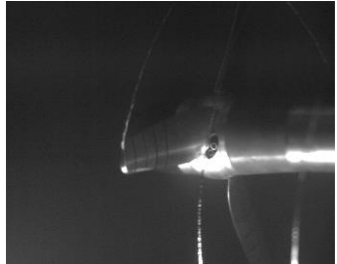
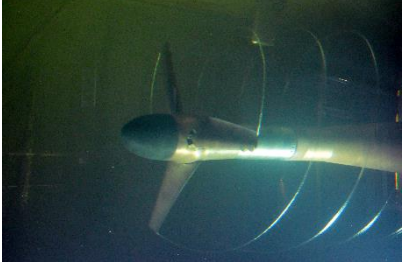
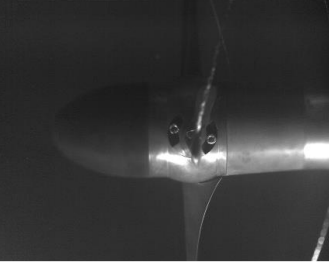
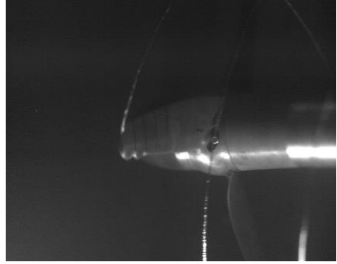
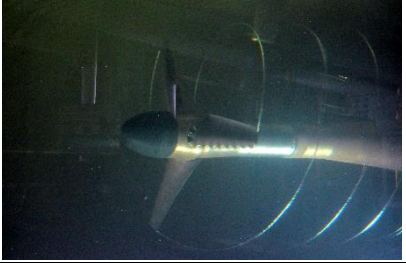
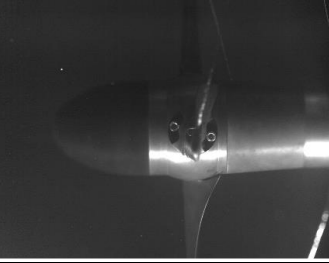
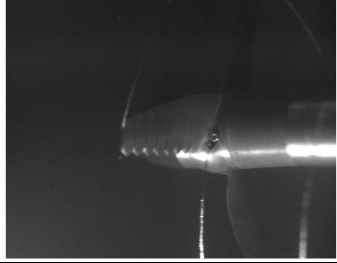
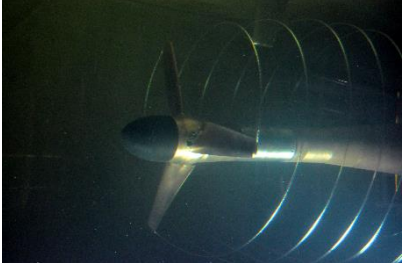
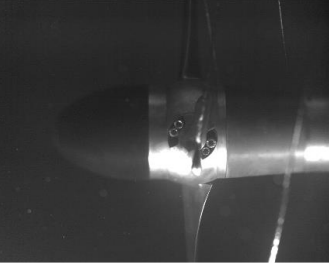
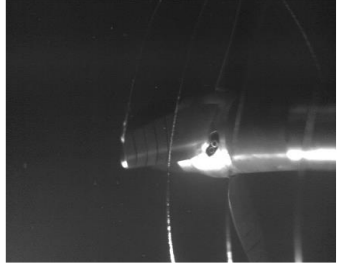
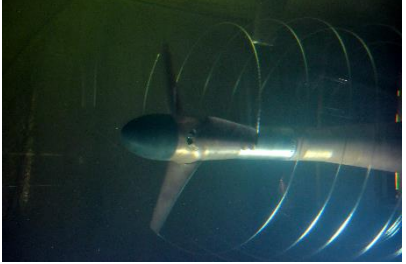
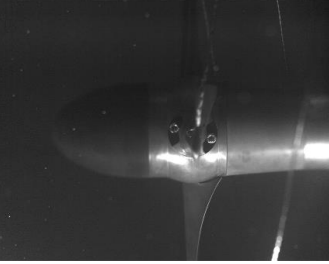
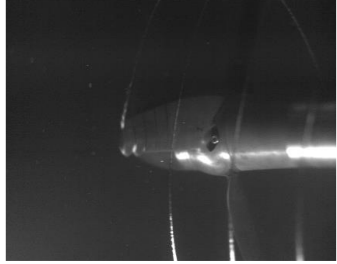
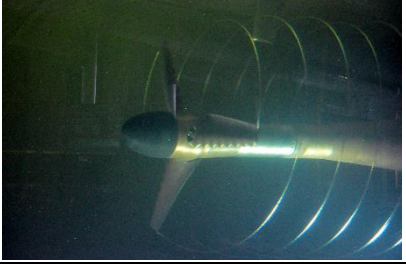
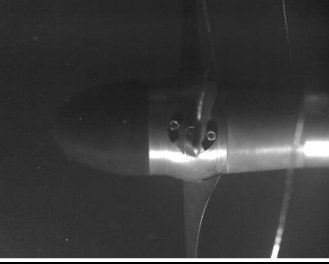
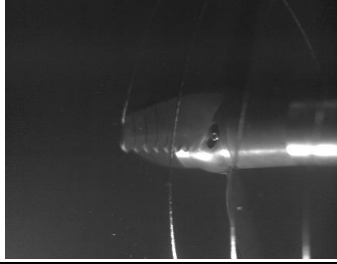
Figure A-6 Performance comparison (Pitch=8°, 4m/s)

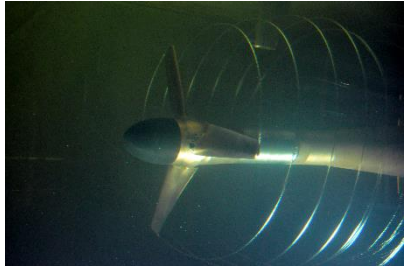
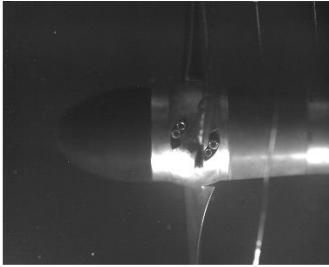
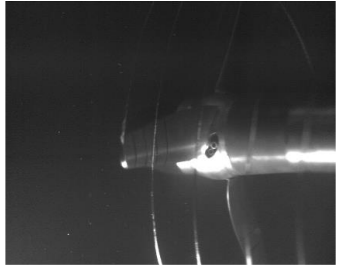
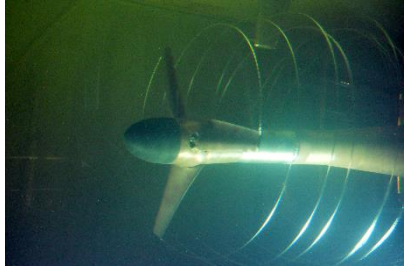
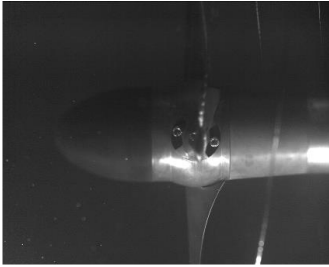
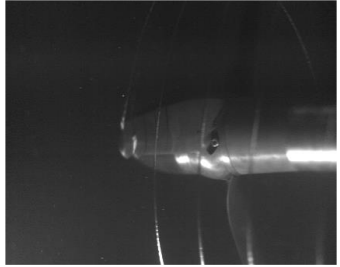
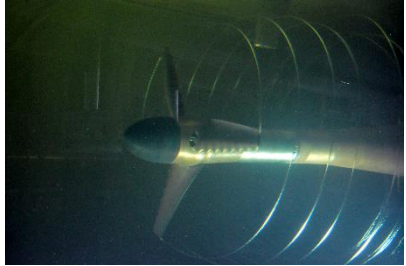
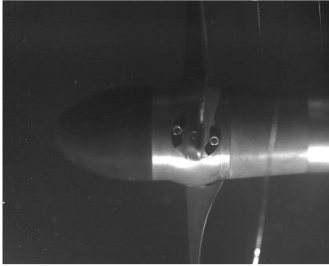
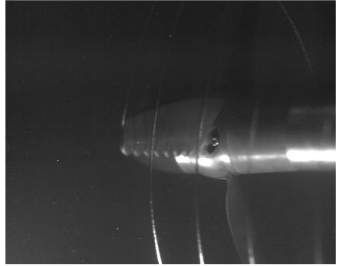
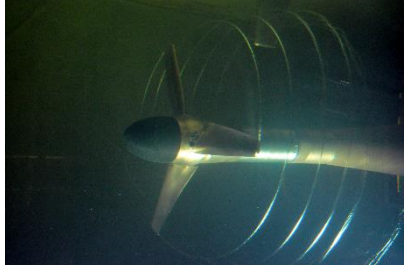
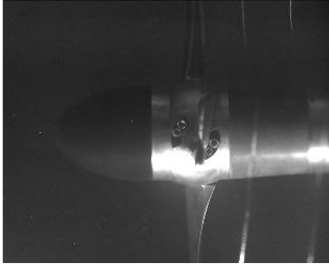
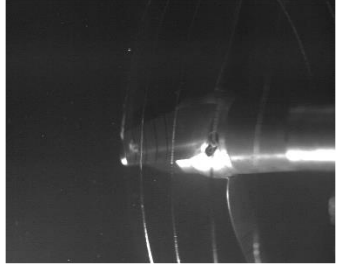
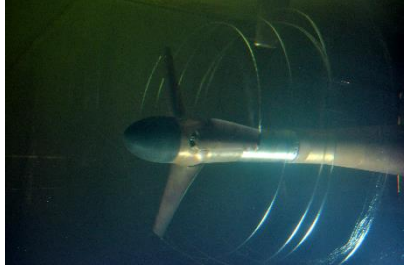
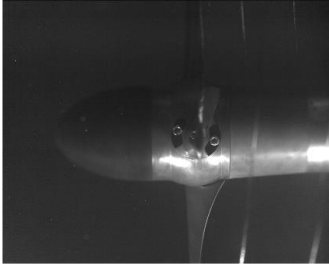
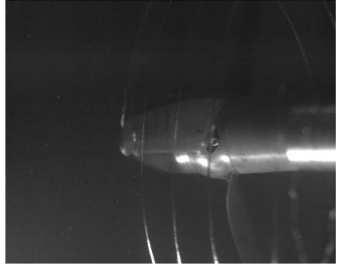
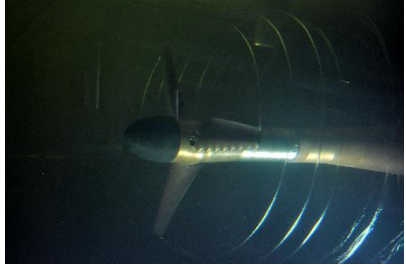
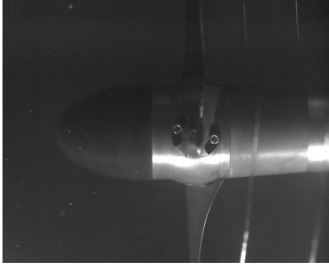
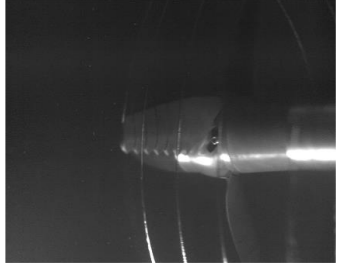
Appendix B - Pictures of cavitation observation

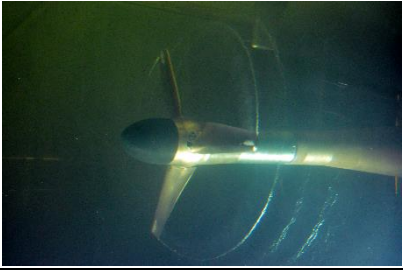
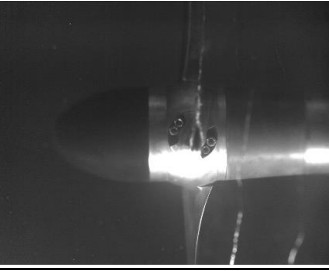
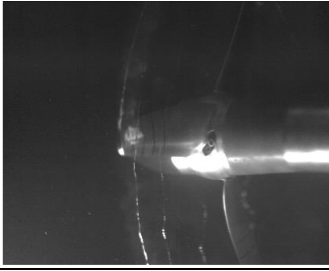
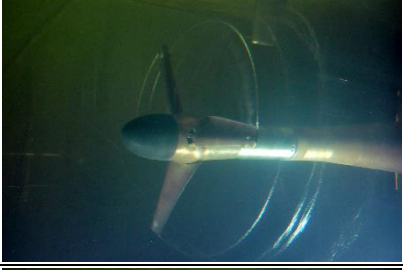
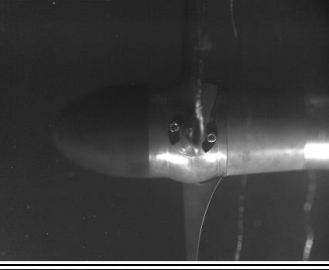
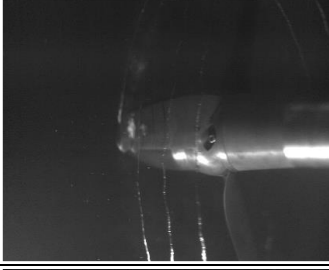
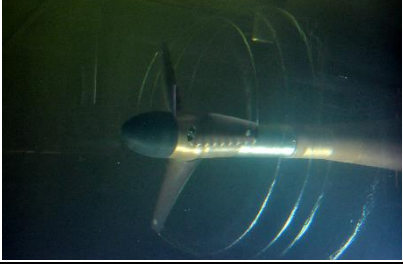
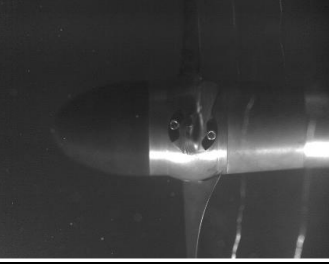
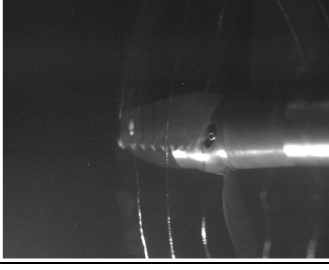

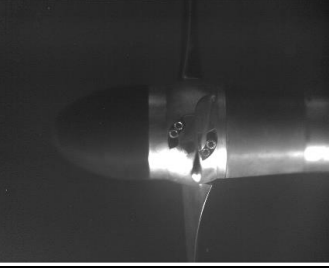


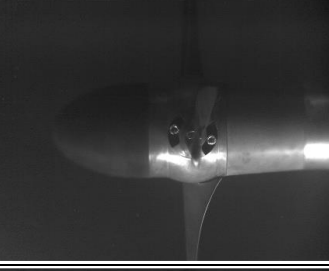


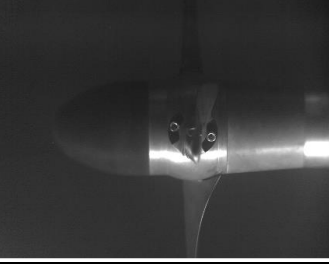
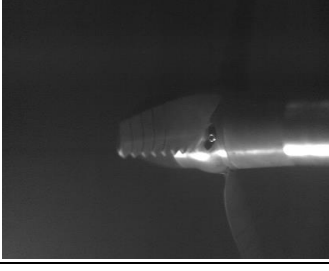
Apart from the typical cavitation pattern that was shown in Section 5.4, the image database of cavitation observation has been summarized and presented in Table B-1.

Table B-1 Cavitation observation results


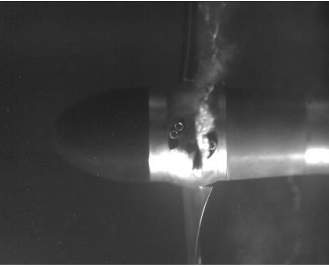
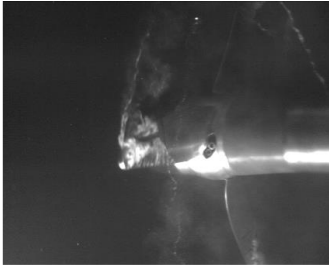
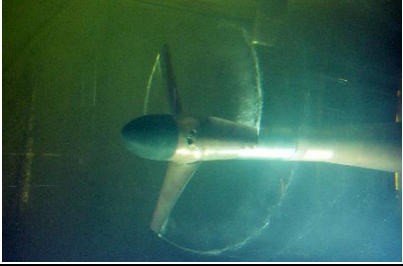
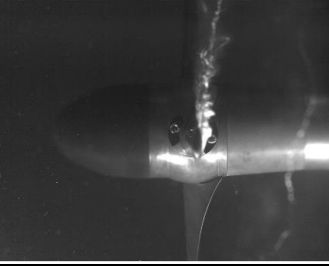


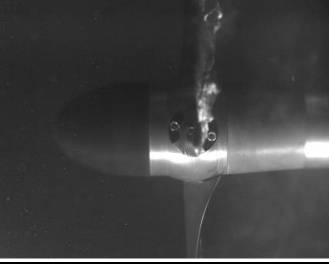
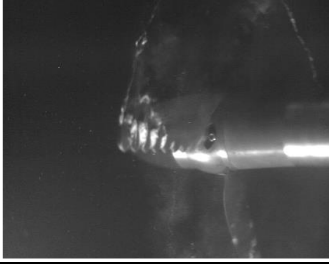
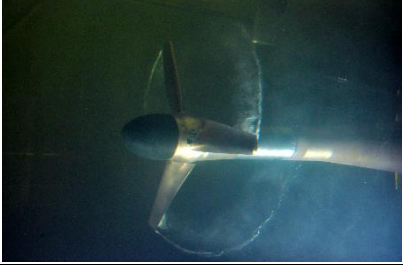
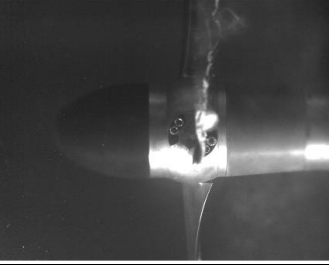
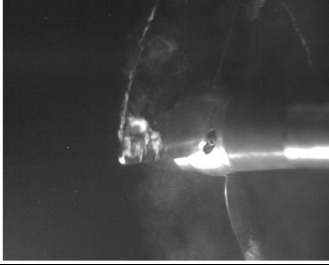
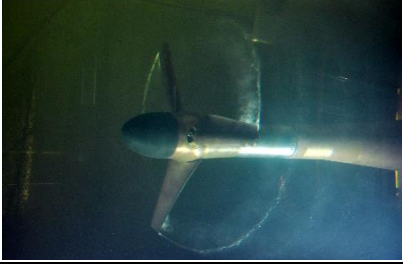
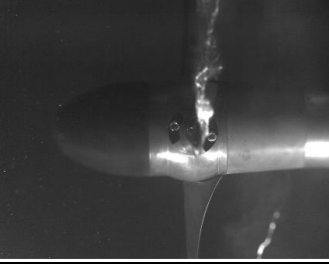
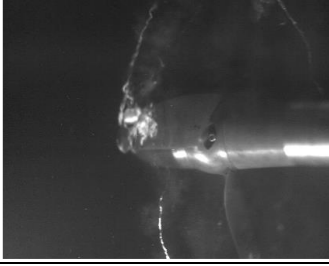

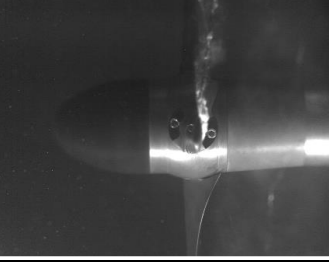

Pitch angle=0°; V=2m/s; TSR=6; Cav _{0.75r} =2.9; Re=0.18e+6			
Ref			
Sin_2			
Sin_8			
Pitch angle=0°; V=2m/s; TSR=7; Cav _{0.75r} =2.2; Re=0.20e+6			
Ref			
Sin_2			
Sin_8			


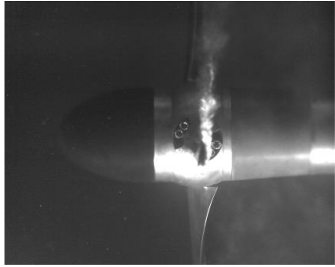
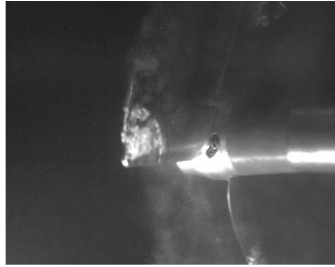
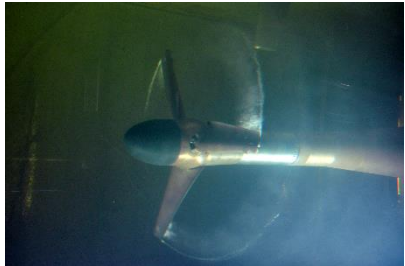
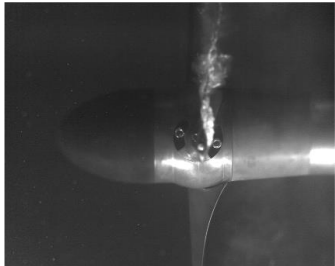
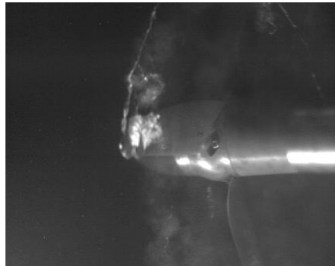

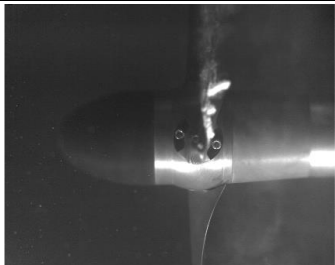
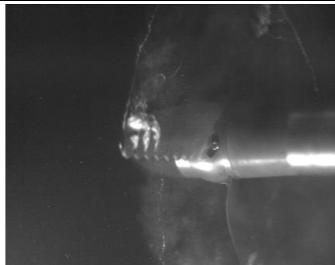

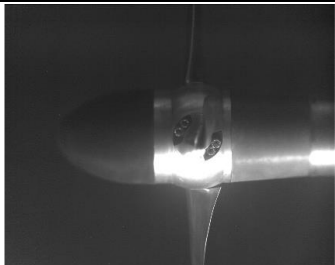


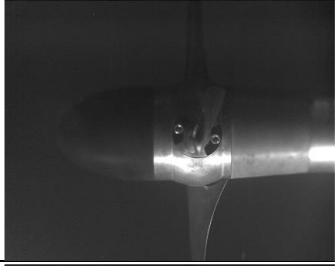


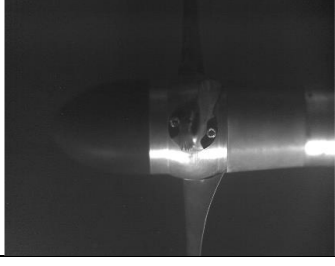
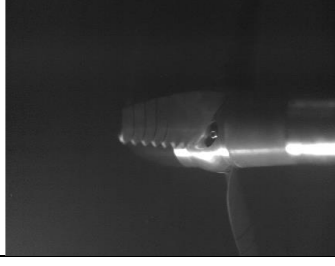
Pitch angle=0°; V=3m/s; TSR=3; Cav _{0.75r} =4.5; Re=0.16e+6			
Ref			
Sin_2			
Sin_8			
Pitch angle=0°; V=3m/s; TSR=4; Cav _{0.75r} =2.7; Re=0.19e+6			
Ref			
Sin_2			
Sin_8			

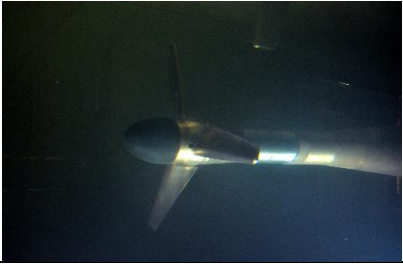
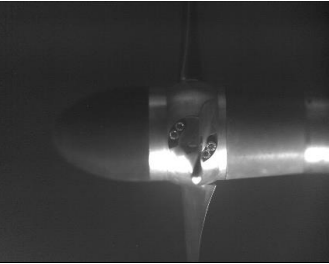
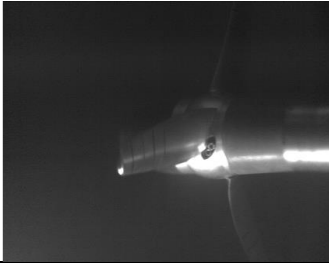

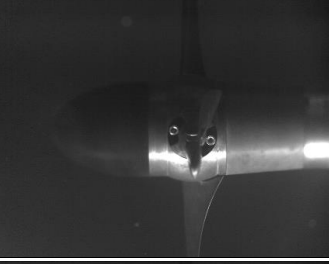


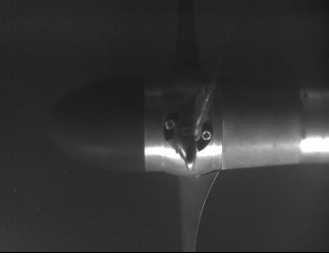
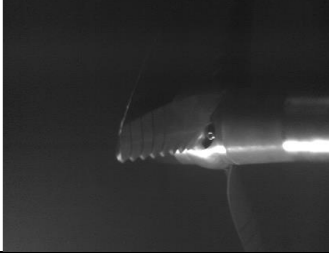

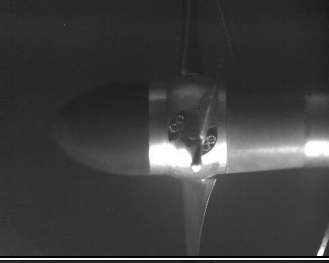


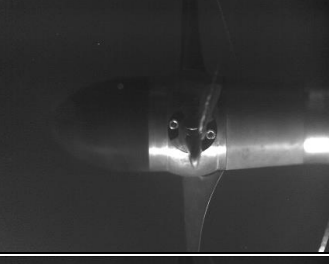

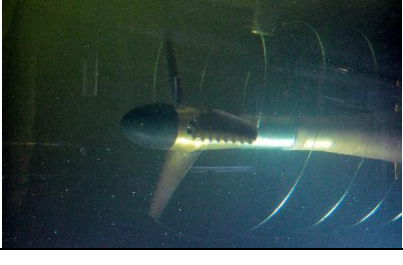
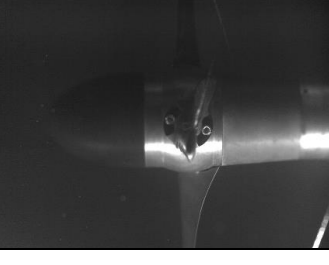

Pitch angle=0°; V=3m/s; TSR=5; Cav _{0.75r} =1.8; Re=0.23e+6			
Ref			
Sin_2			
Sin_8			
Pitch angle=0°; V=3m/s; TSR=6; Cav _{0.75r} =1.3; Re=0.26e+6			
Ref			
Sin_2			
Sin_8			

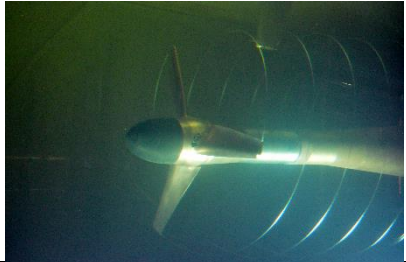
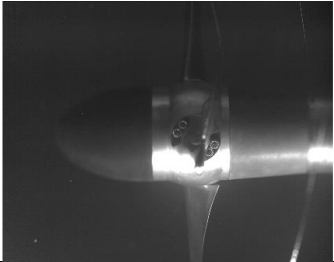

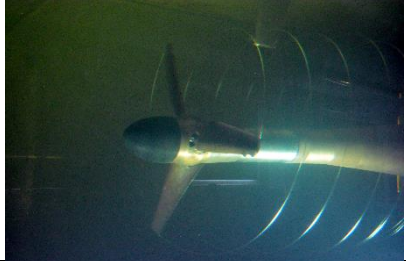
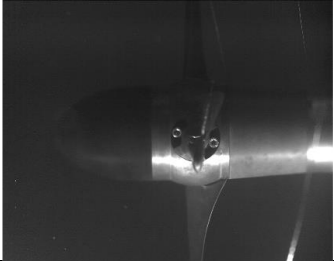

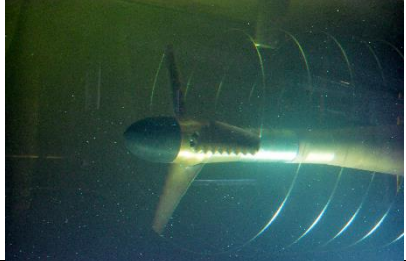
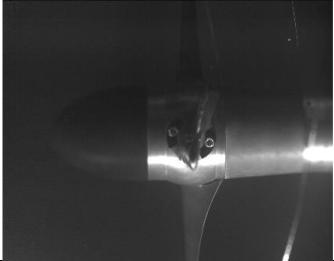


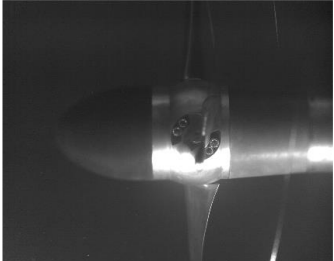
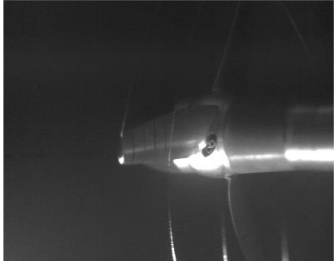
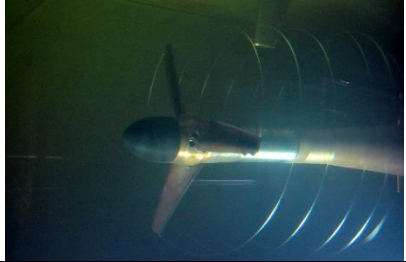
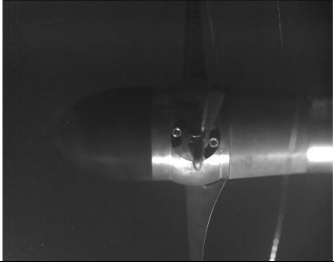
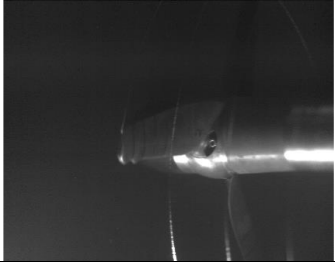

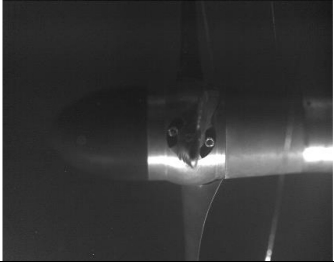
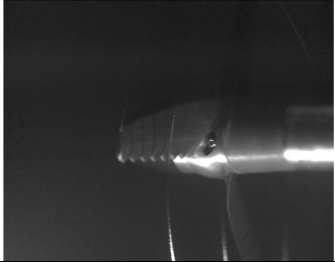
Pitch angle=0°; V=3m/s; TSR=6.5; Cav _{0.75r} =1.1; Re=0.28e+6			
Ref			
Sin_2			
Sin_8			
Pitch angle=0°; V=4m/s; TSR=2; Cav _{0.75r} =4.6; Re=0.18e+6			
Ref			
Sin_2			
Sin_8			


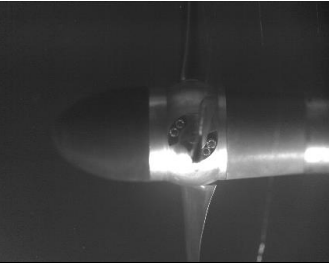
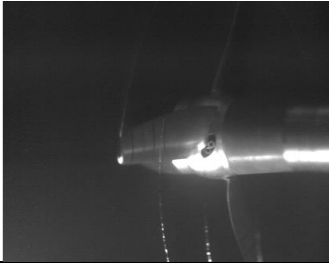
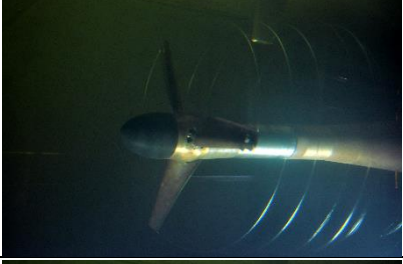
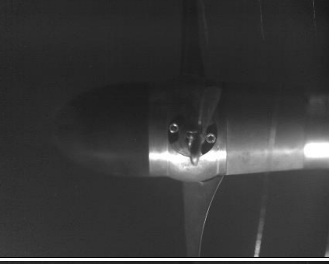

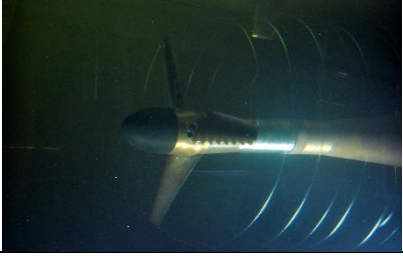
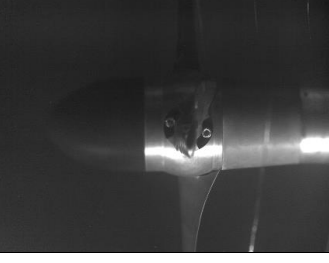
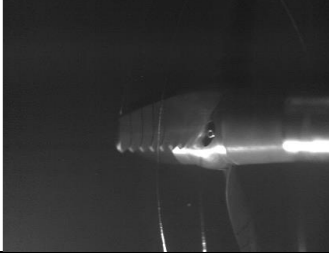

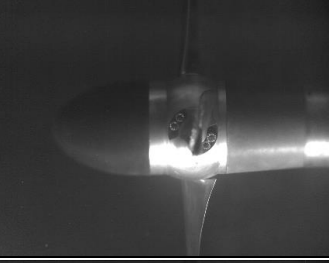


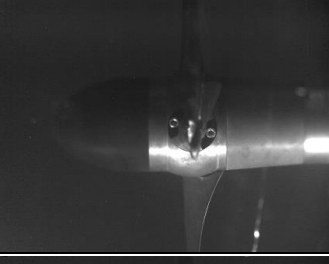

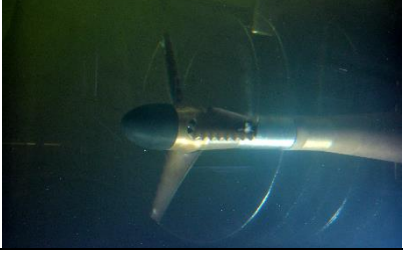
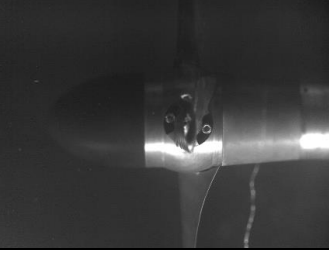

Pitch angle=0°; V=4m/s; TSR=3; Cav _{0.75r} =2.5; Re=0.22e+6			
Ref			
Sin_2			
Sin_8			
Pitch angle=0°; V=4m/s; TSR=3.5; Cav _{0.75r} =1.9; Re=0.24e+6			
Ref			
Sin_2			
Sin_8			

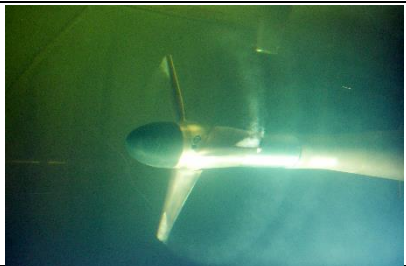
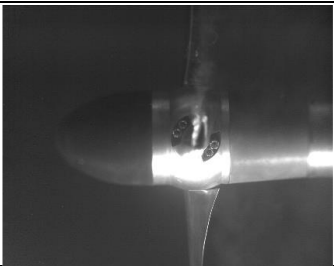


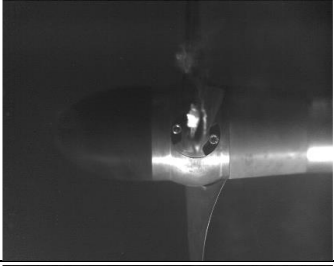


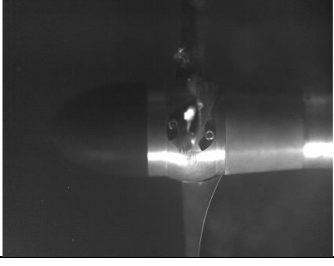

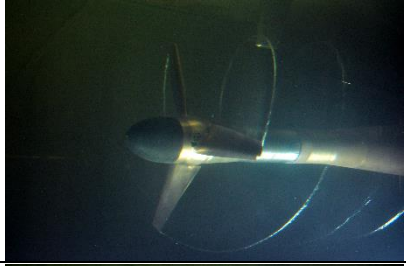
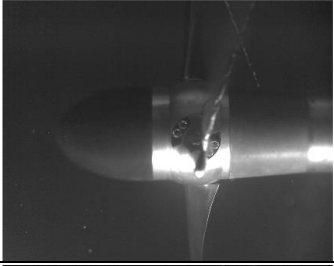

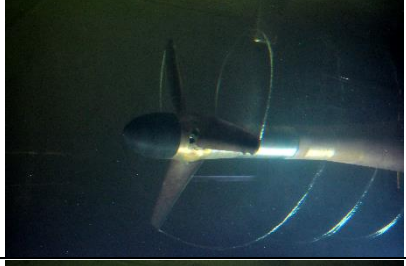
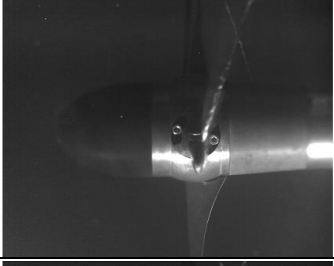
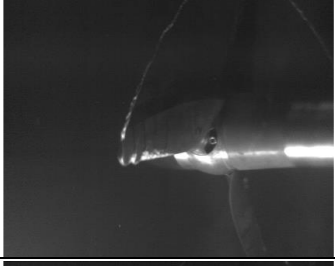
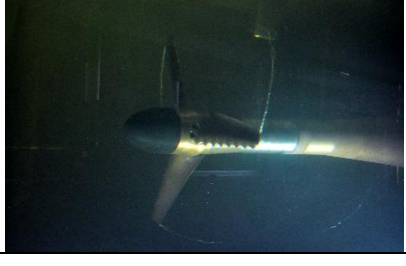
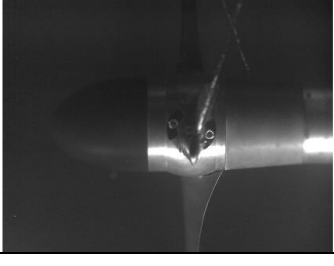
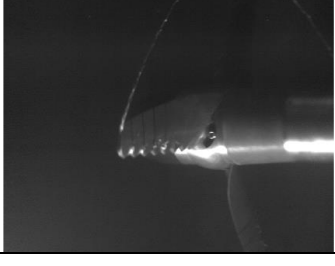
Pitch angle=0°; V=4m/s; TSR=4; Cav _{0.75r} =1.5; Re=0.26e+6			
Ref			
Sin_2			
Sin_8			
Pitch angle=0°; V=4m/s; TSR=4.5; Cav _{0.75r} =1.2; Re=0.28e+6			
Ref			
Sin_2			
Sin_8			

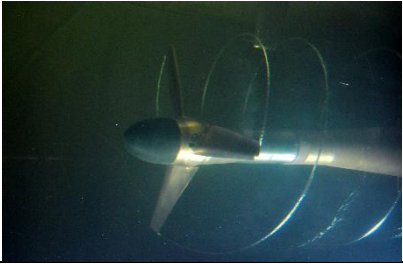
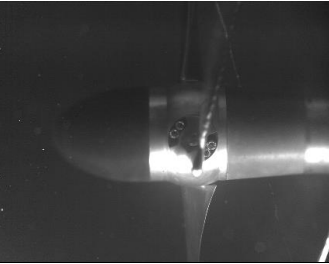
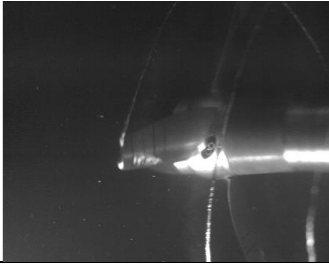
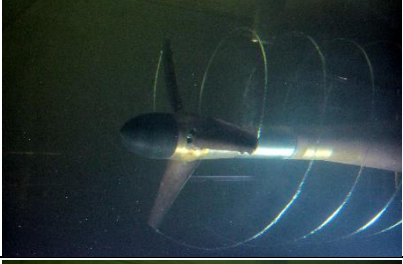
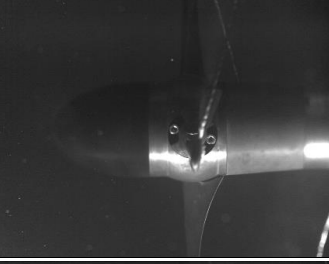

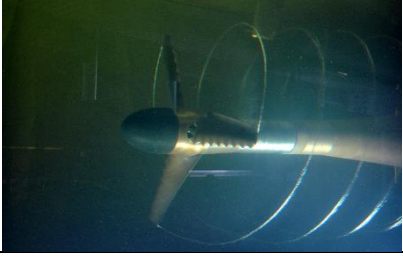
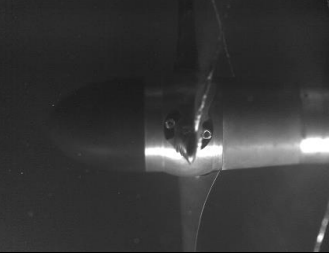
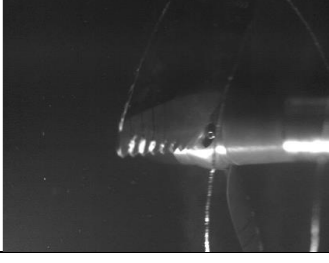
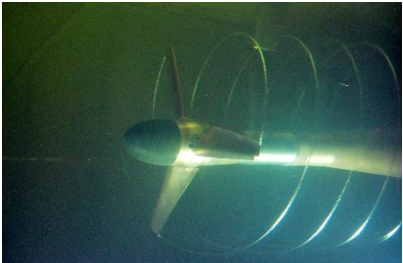
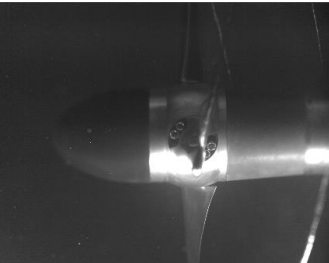
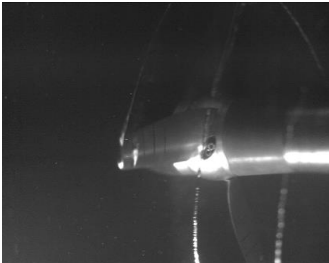
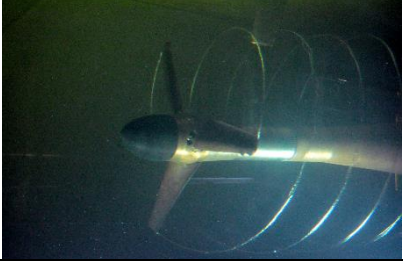
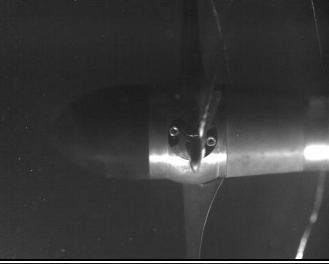
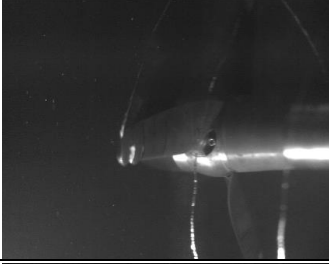
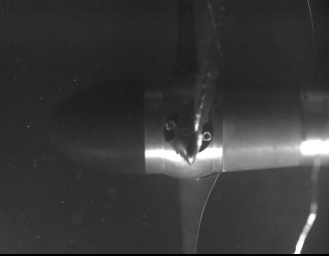
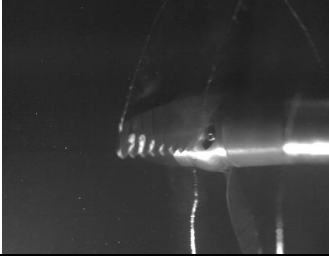
Pitch angle=0°; V=4m/s; TSR=5; Cav _{0.75r} =1.0; Re=0.3e+6			
Ref			
Sin_2			
Sin_8			
Pitch angle=+4°; V=2m/s; TSR=8.5; Cav _{0.75r} =2.134; Re=0.24e+6			
Ref			
Sin_2			
Sin_8			

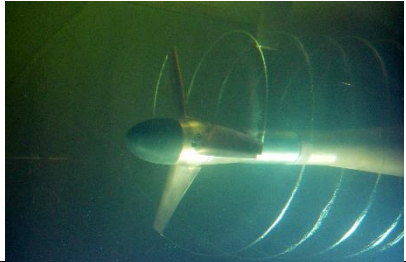
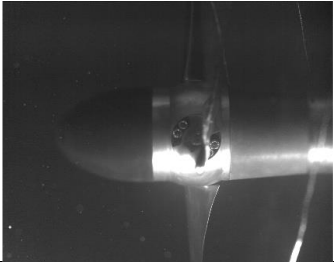

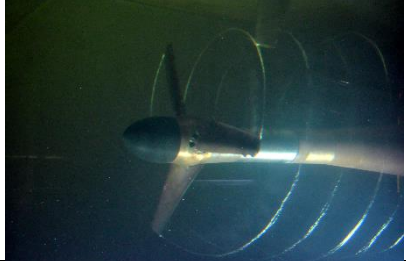
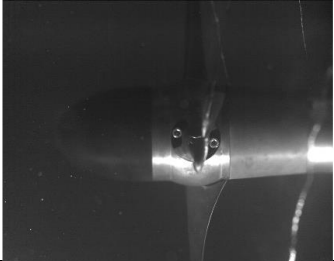
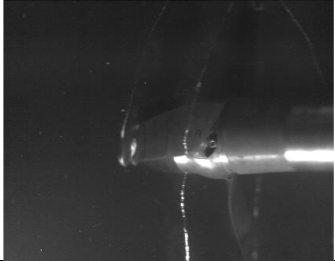
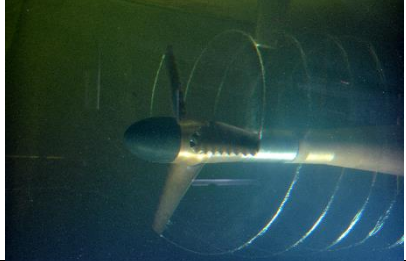
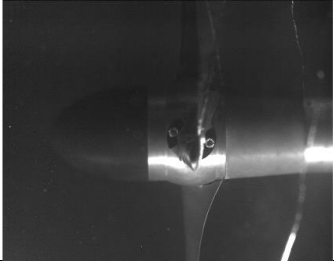
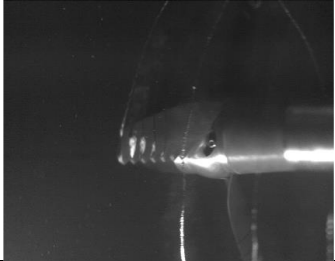
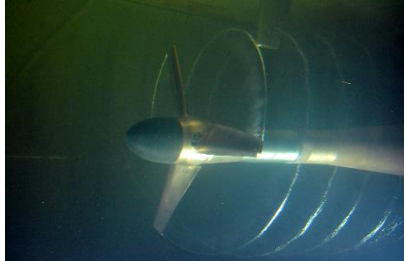
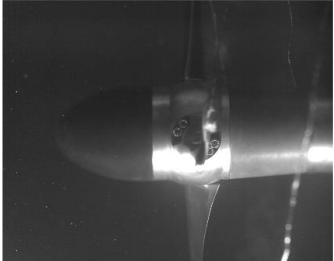
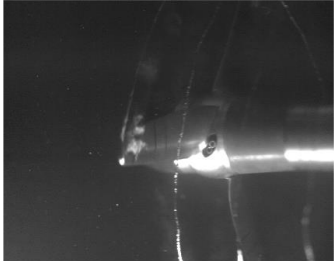
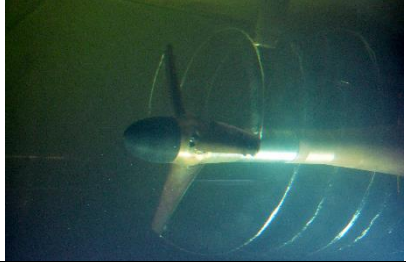
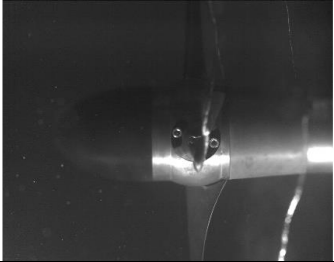
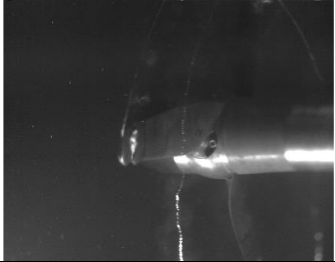
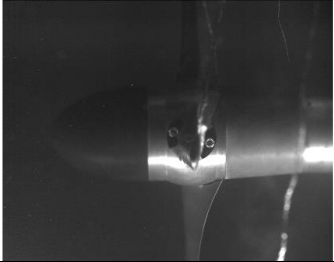
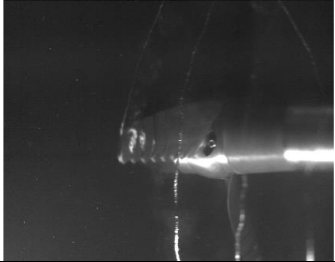
Pitch angle=+4°; V=3m/s; TSR=2.5; Cav _{0.75r} =6.0 ; Re=0.15e+6			
Ref			
Sin_2			
Sin_8			
Pitch angle=+4°; V=3m/s; TSR=3; Cav _{0.75r} =4.5; Re=0.16e+6			
Ref			
Sin_2			
Sin_8			


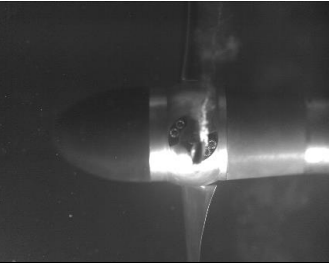
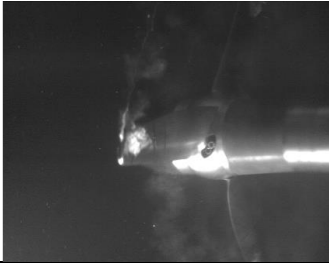
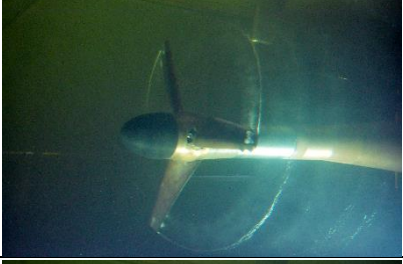
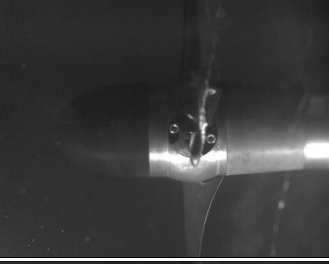

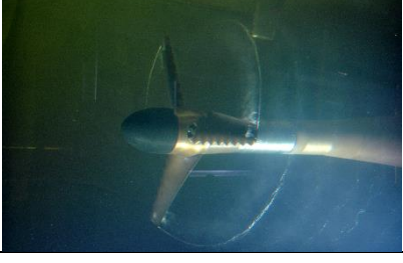
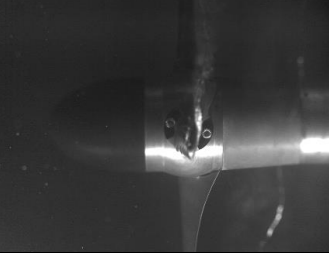
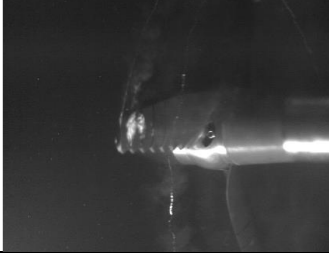

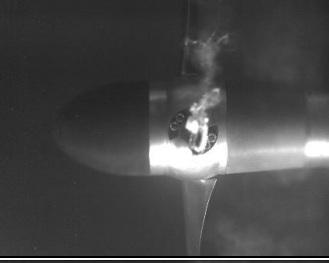
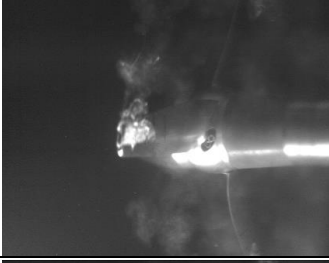

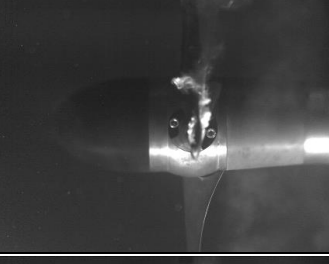

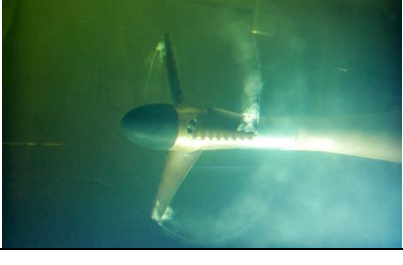
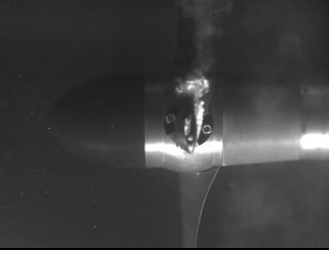
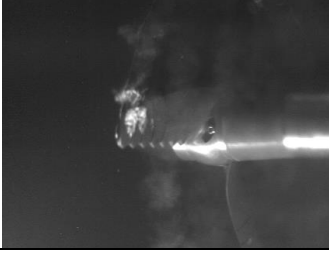
Pitch angle=+4°; V=3m/s; TSR=4; Cav _{0.75r} =2.7; Re=0.19e+6			
Ref			
Sin_2			
Sin_8			
Pitch angle=+4°; V=3m/s; TSR=5; Cav _{0.75r} =1.8; Re=0.23e+6			
Ref			
Sin_2			
Sin_8			

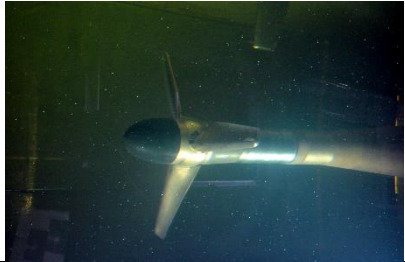
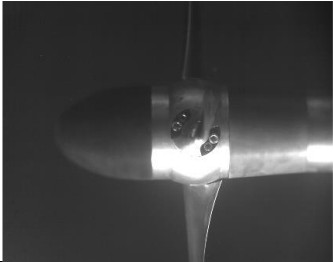
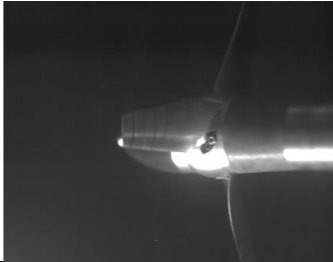

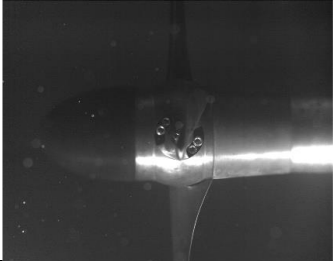
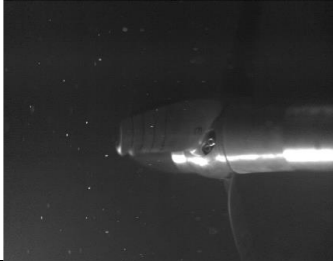

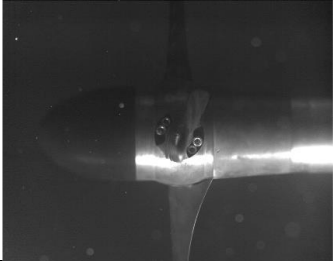

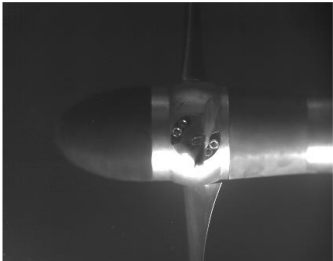
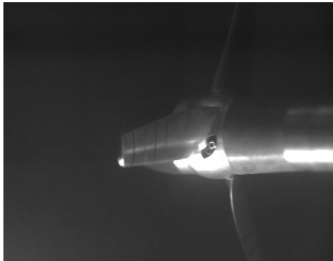
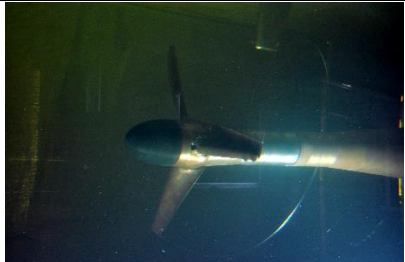
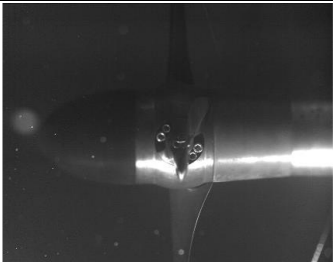

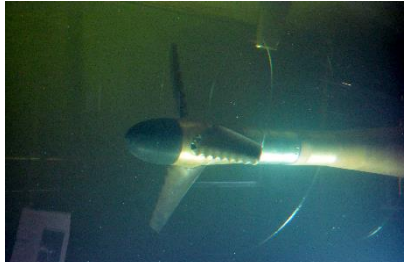
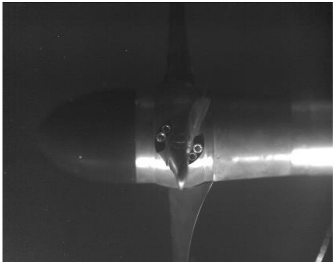

Pitch angle=+4°; V=3m/s; TSR=6; Cav _{0.75r} =1.3; Re=0.26e+6			
Ref			
Sin_2			
Sin_8			
Pitch angle=+4°; V=3m/s; TSR=6.5; Cav _{0.75r} =1.1; Re=0.28e+6			
Ref			
Sin_2			
Sin_8			

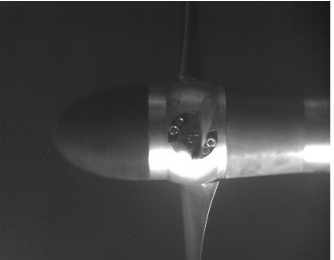

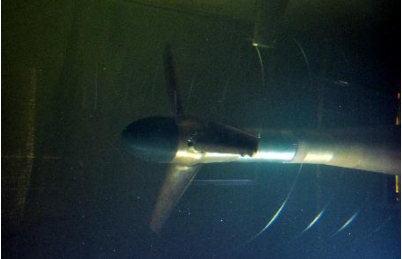
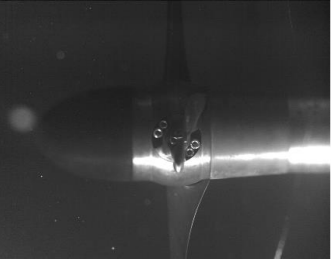

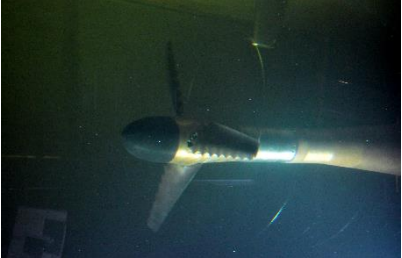
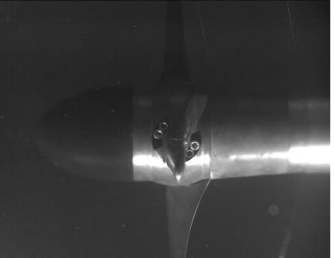

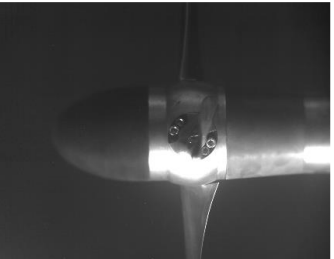

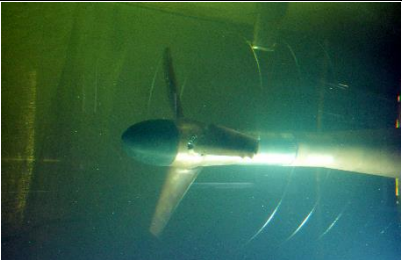
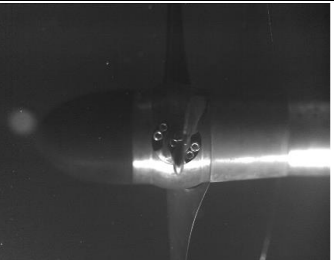


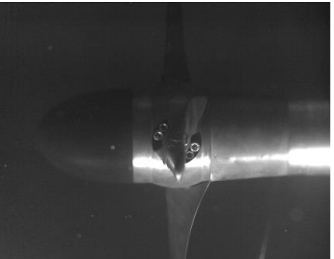
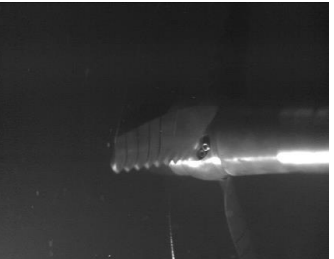
Pitch angle=+4°; V=3m/s; TSR=7; Cav _{0.75r} =0.9; Re=0.3e+6			
Ref			
Sin_2			
Sin_8			
Pitch angle=+4°; V=4m/s; TSR=2.5; Cav _{0.75r} =3.4; Re=0.2e+6			
Ref			
Sin_2			
Sin_8			

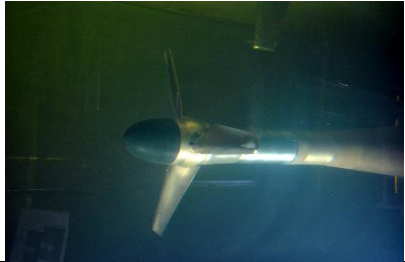
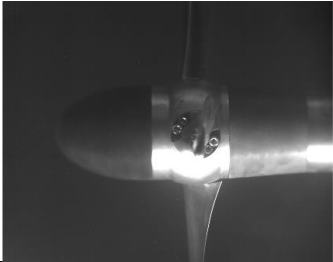


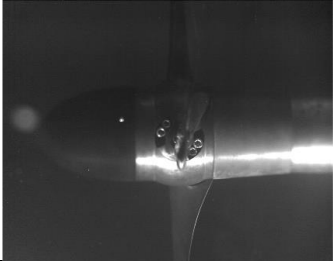
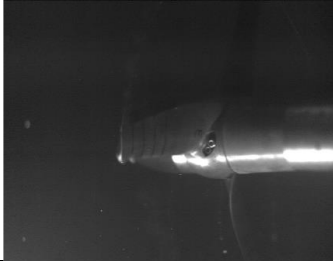

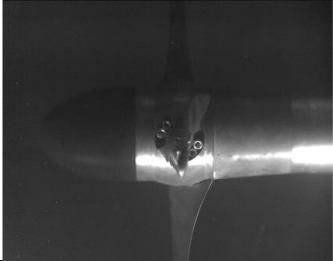

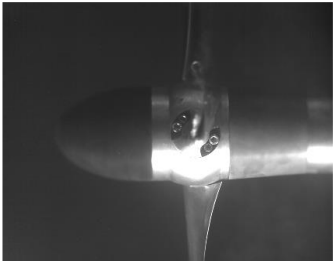


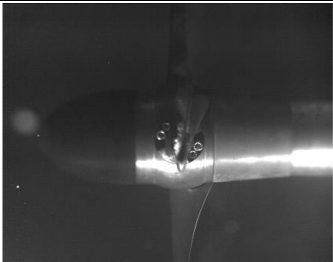


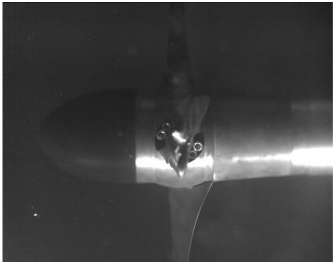

Pitch angle=+4°; V=4m/s; TSR=3; Cav _{0.75r} =2.5; Re=0.2e+6			
Ref			
Sin_2			
Sin_8			
Pitch angle=+4°; V=4m/s; TSR=3.5; Cav _{0.75r} =1.9; Re=0.2e+6			
Ref			
Sin_2			
Sin_8	None		

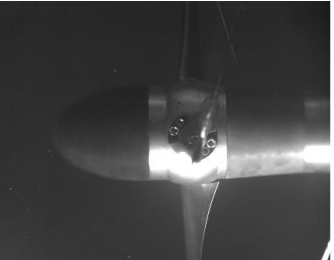
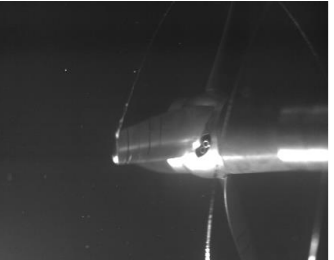
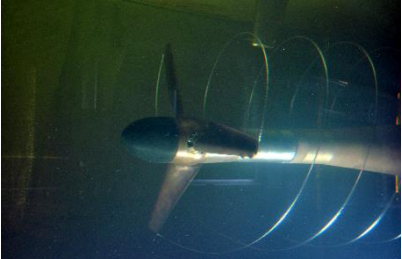
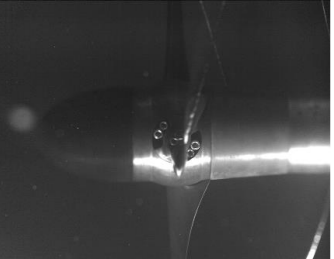
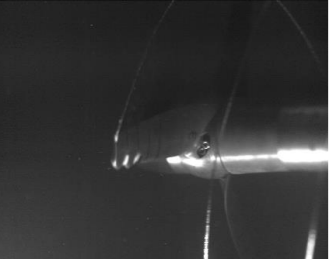
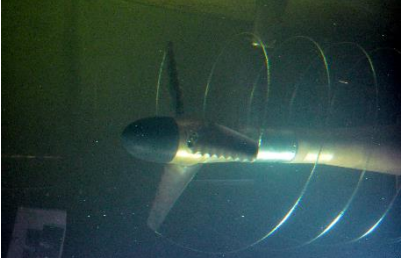
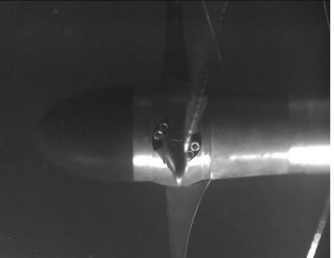
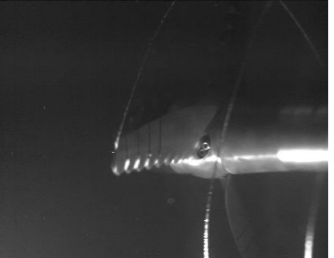
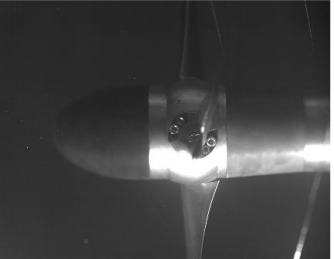
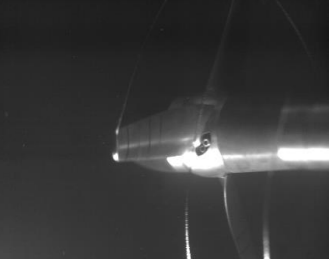
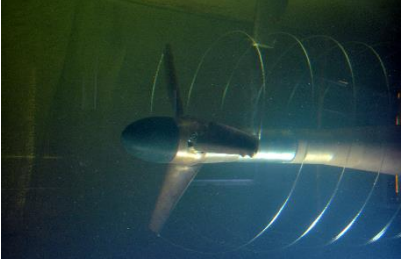
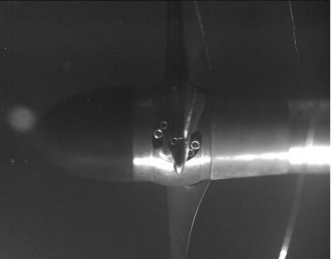
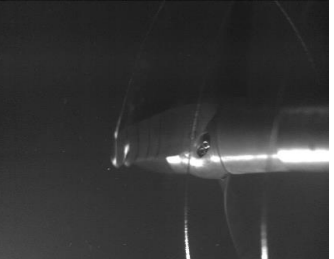
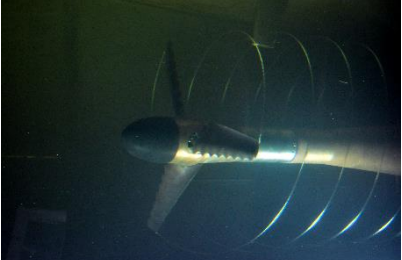
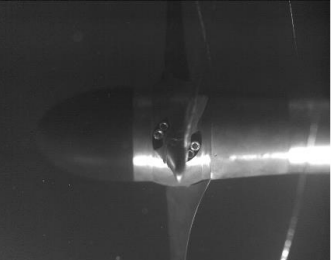
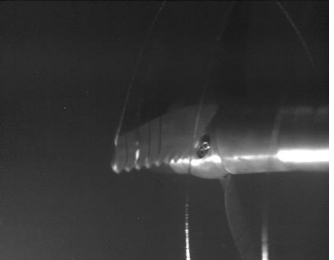
Pitch angle=+4°; V=4m/s; TSR=4; Cav _{0.75r} =1.5; Re=0.26e+6			
Ref			
Sin_2			
Sin_8			
Pitch angle=+4°; V=4m/s; TSR=4.5; Cav _{0.75r} =1.2; Re=0.28e+6			
Ref			
Sin_2			
Sin_8	None		


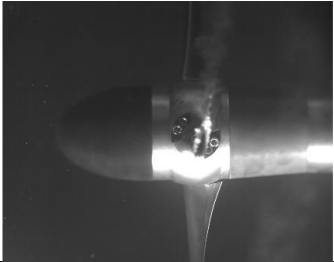


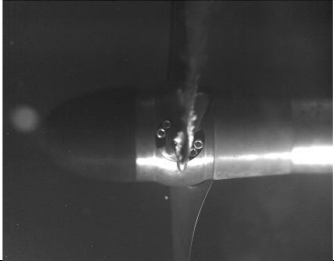

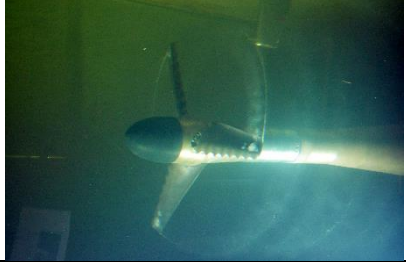
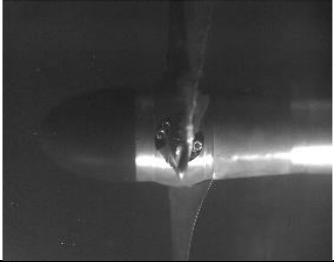

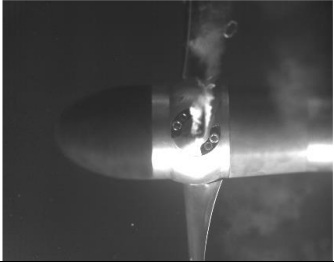

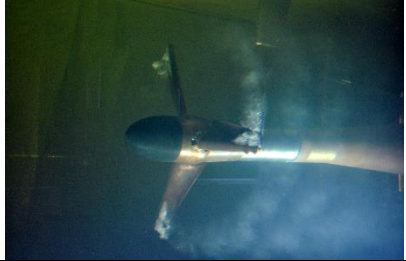
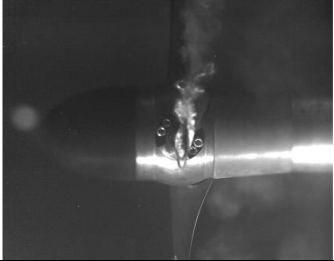


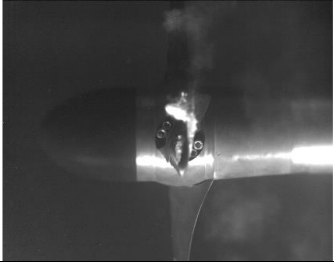

Pitch angle=+4°; V=4m/s; TSR=5; Cav _{0.75r} =1.0; Re=0.3e+6			
Ref			
Sin_2			
Sin_8			
Pitch angle=+4°; V=4m/s; TSR=5.5; Cav _{0.75r} =0.86; Re=0.32e+6			
Ref			
Sin_2			
Sin_8			

Pitch angle=+8°; V=2m/s; TSR=8; Cav _{0.75r} =1.7; Re=0.22e+6			
Ref			
Sin_2			
Sin_8			
Pitch angle=+8°; V=3m/s; TSR=3; Cav _{0.75r} =4.5; Re=0.16e+6			
Ref	None		
Sin_2			
Sin_8			

Pitch angle=+8°; V=3m/s; TSR=4; Cav _{0.75r} =2.7; Re=0.19e+6			
Ref	None		
Sin_2			
Sin_8			
Pitch angle=+8°; V=3m/s; TSR=5; Cav _{0.75r} =1.8; Re=0.23e+6			
Ref	None		
Sin_2			
Sin_8			

Pitch angle=+8°; V=3m/s; TSR=6; Cav _{0.75r} =1.3; Re=0.26e+6			
Ref			
Sin_2			
Sin_8			
Pitch angle=+8°; V=3m/s; TSR=6.5; Cav _{0.75r} =1.1; Re=0.28e+6			
Ref	None		
Sin_2			
Sin_8			

Pitch angle=+8°; V=4m/s; TSR=3; Cav _{0.75r} =2.5; Re=0.2e+6			
Ref	None		
Sin_2			
Sin_8			
Pitch angle=+8°; V=4m/s; TSR=4; Cav _{0.75r} =1.5; Re=0.26e+6			
Ref	None		
Sin_2			
Sin_8			

Pitch angle=+8°; V=4m/s; TSR=5; Cav _{0.75r} =1.0; Re=0.3e+6			
Ref			
Sin_2			
Sin_8			
Pitch angle=+8°; V=4m/s; TSR=5.5; Cav _{0.75r} =0.9; Re=0.33e+6			
Ref	None		
Sin_2			
Sin_8			

Appendix C - Performance evaluation under wave-current interaction

Having the concern from the cavitation tunnel about the relatively high blockage ratio, it is worthwhile to further validate the performance of turbine with tubercles under a different experimental environment which is ideal to be conducted in a larger size of facility. Therefore the test in a towing tank was initiated. Meanwhile as stated in Chapter 2, to the best of the Author's knowledge, there has been no study exploring the effect of waves on the performance of leading edge tubercles as applied to a tidal turbine. Since a tidal turbine can be subjected to tidal current in combination with waves, it would be worthwhile as well to explore this effect. In the following section, therefore, the efficiency performances of the three model turbines were investigated experimentally by testing them in a towing tank under the combined effect of steady current and waves.

Experimental setup

The experiments were conducted in the Kelvin Hydrodynamic Lab (KHL), Strathclyde University by using their towing tank facility which is 76m in length, 4.6m in width and 2.5m in depth. As shown in Figure C-1, one end of the tank is equipped with a variable-water-depth, computer-controlled four-flap absorbing wave-maker generating regular or irregular waves over 0.5m height while the opposite end is fitted with a high quality variable-water-depth sloping beach, with reflection coefficient typically less than 5% over the frequency range of interest.

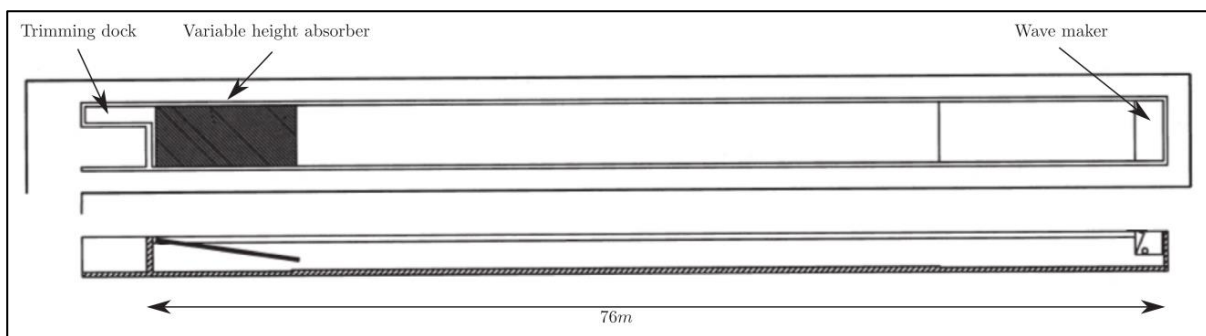


Figure C-1 Schematic of the KHL towing tank

As briefly reviewed in Chapter 2, the towing tank of KHL is equipped with a self-propelled Kempf and Remmers towing carriage with a maximum speed of 5m/s on which an open water dynamometer can be attached to drive turbine models. The open water dynamometer that KHL uses is an in-house built dynamometer driven by a 900W AC motor decelerated by a 10:1 gear box, which is limited to a maximum of 300rpm and was specially designed for tidal turbine

testing. To get rid of electrical noise, the cases of the motor and the whole body are connected to earth. The torque and thrust are measured by a torque and thrust transducer with the capability to measure 2000N of thrust and 50Nm of torque. The frictional torque of the system was also measured with the same methodology with a dummy mass in the water. All of the signals and power supplies are all transferred through a multi-channel slip ring. A general view of the dynamometer and model fitting on the towing carriage can be seen in Figure C-2. A sonic wave probe fitted onto the carriage was used to measure the encounter frequency of the waves. All of the measurement data was acquired at 137 Hz as the sample frequency.

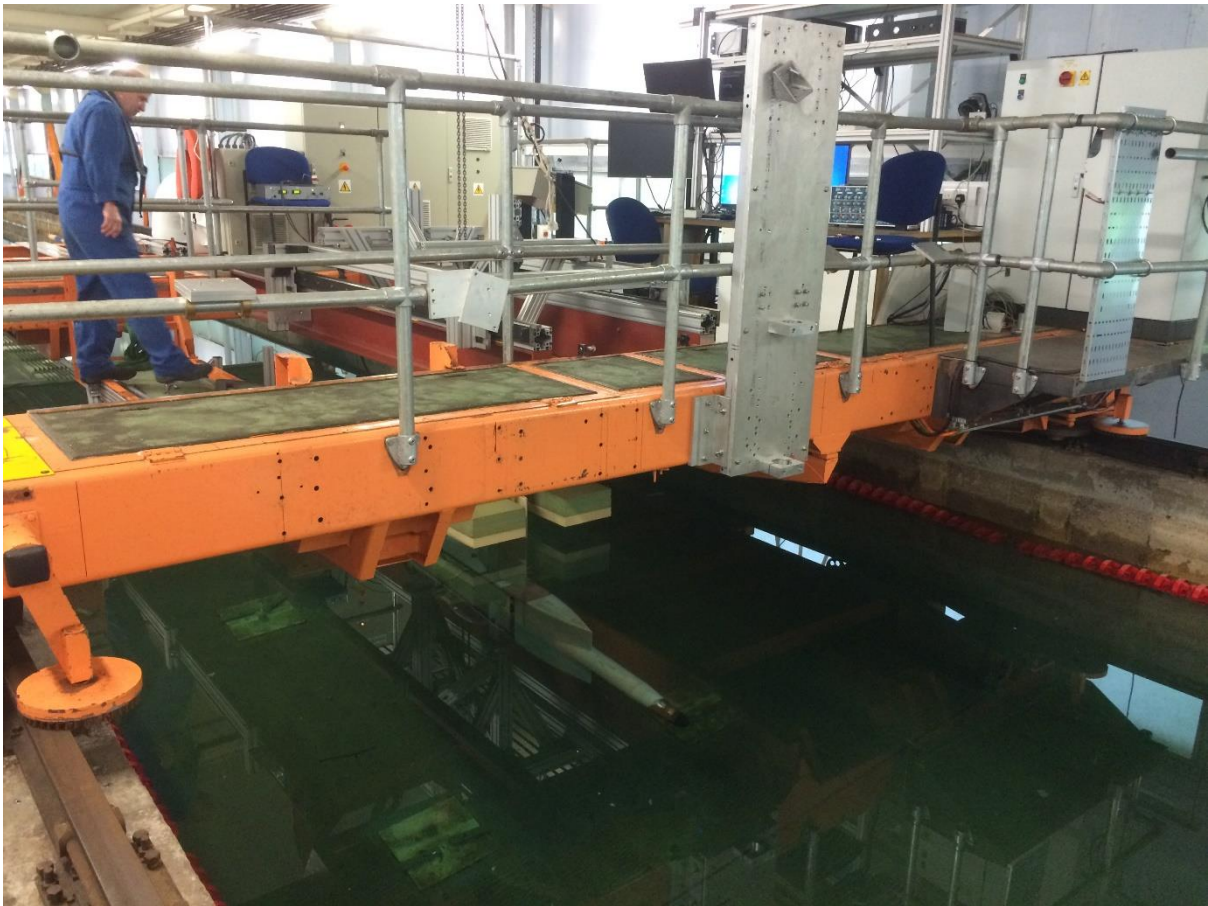


Figure C-2 Turbine model and dynamometer fitting onto the towing carriage

By taking advantage of the large cross section of the towing tank and capacity of the dynamometer one could have tested larger diameter model turbines (e.g. with a diameter of 0.8-1.0m). However, this was not viable in this study due to economic reasons and hence the existing three, 400mm diameter models that had been tested in the cavitation tunnel were again used in the towing tank with a 1.1m shaft submergence.

Due to the limitations of the slip ring, the speed of the turbine was maintained fixed at 250RPM during the tests to maximize the Reynolds number. This meant changing the towing carriage speed for the desired TSRs to be achieved. Nevertheless, the Reynolds number range could only reach at 0.15×10^5 which was significantly lower than the one in the cavitation tunnel. This comparative limitation was accepted because the typical Reynolds number range for towing tank tests varied between 0.14×10^6 and 0.17×10^6 while the range in the cavitation tunnel was between 0.08×10^6 to 0.5×10^6 . The effect of the waves on the performance of the turbines was investigated and analysed based on the relative comparison of the performances measured in the towing tank tests only.

Despite the above limitation, the uncertainty level of the towing tank tests was well controlled with 0.3% for the TSR, 1.1% for the C_p and 0.2% for $C_t/10$ which were based on 7 individual tests for $TSR=4$. In addition, all of the test runs were repeated twice for the uncertainty checks.

Test matrix

The initial set of the tests with the three model turbines involved the open water performance measurements in steady current (i.e. calm water). In these experiments the mean pitch angle of the turbines was set at 4° and the tests were conducted to further validate the effect of the tubercles as well as to check on the Reynolds number effect. The test matrix for these experiments is shown in Table C-1.

Table C-1 Test matrix for Reynolds number test and open water performance test

TSR	RPM	V(m/s)	Re
Reynolds number test			
4	50	0.262	29,317
4	100	0.524	58,634
4	150	0.785	87,950
4	200	1.047	117,267
4	250	1.309	146,584
Open water performance test			
1	150	3.142	144,433
2	250	2.618	169,643
2.5	250	2.094	158,993
3	250	1.745	152,897
3.5	250	1.496	149,101
4	250	1.309	146,584
5	250	1.047	143,568
6	250	0.873	141,903

The next set of the experiments involved the performance measurements with the same model turbines in waves: firstly in regular waves with two different wave amplitudes and over a range of frequencies within the equipment limitation; and secondly in irregular waves defined by three different JONSWAP wave spectra. The associated test matrix for these experiments in waves is given in Table C-2. The table also indicates the corresponding full-scale conditions of the tested JONSWAP spectra for the 20m diameter turbine discussed in Section 5.4.

Table C-2 Test matrix for regular and irregular wave test

Regular wave tests							
TSR	N (RPM)	V (m/s)	Re	Wave Amplitude (m)	Wave Frequency (Hz)		
4	250	1.309	146,584	0.05	0.3~0.9		
4	250	1.309	146,584	0.1	0.3~0.9		
Irregular wave tests							
Sea State	TSR	N (RPM)	V (m/s)	Re	JONSWAP, Hs (m)	JONSWAP, Tp (s)	
NO.1	4	150	0.785	87,950	0.15	1.581	
NO.2	4	150	0.785	87,950	0.25	2.214	
NO.3	4	150	0.785	87,950	0.3125	2.372	
Full-scale (corresponding) conditions of Irregular wave test (Dia=20m, Shaft submergence=55m)							
Sea State	TSR	N (RPM)	V (m/s)	Re	JONSWAP, Hs (m)	JONSWAP, Tp (s)	Return period
NO.1	4	21.01	5.50	3.08E+07	7.5	11.18	1 year
NO.2	4	21.01	5.50	3.08E+07	12.5	15.65	10 year
NO.3	4	21.01	5.50	3.08E+07	15.625	16.77	100 year

During the irregular wave tests, 250 wave encounters were guaranteed by multi runs depending on the conditions. Therefore slower carriage speed was used to reduce the tank time and only two turbines were tested which were the reference turbine (Ref) and biomimetic turbine with full tubercles (Sin8). Modelling of the irregular waves was carried out based on the specified significant wave height H_s , peak wave period T_p and spectral peakedness parameter $\gamma=3.3$ in the JONSWAP spectrum given by Equation C-1. The three tested JONSWAP spectra were plotted as shown in Figure C-3.

$$S(f) = \alpha H_s^2 T_p^{-4} f^{-5} \exp\left[-1.25\left(\frac{f}{T_p}\right)^4\right] \gamma^{\exp\left[-\left(\frac{f}{T_p}\right)^{-1}\right] / 2\sigma^2} \quad \text{Equation C-1}$$

where, $S(f)$ is the spectral wave energy density distribution; f is the wave frequency (Hz); f_p is the peak wave frequency (Hz), $1 / T_p$; $\sigma = 0.09$ for $f > f_p$ and $\sigma = 0.07$ for $f < f_p$; and

$$\alpha = \frac{0.0624}{0.230 + 0.0336\gamma - 0.185 / (1.9 + \gamma)}$$

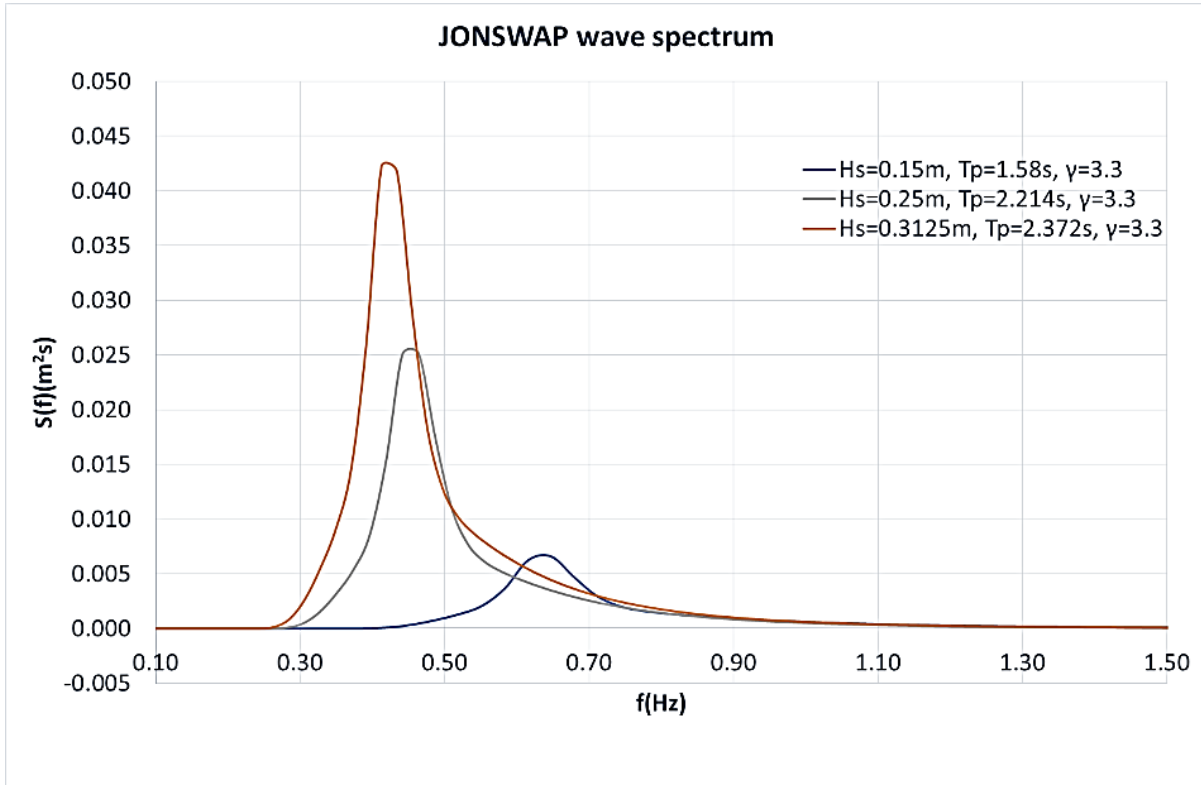


Figure C-3 JONSWAP wave spectra generated in model tests

Results and discussions

Reynolds number effect

In order to analyse the effect of the Reynolds number, the three turbines were tested with five different Reynolds numbers at $TSR = 4$. Based on the measured torque and thrust, the analysed C_p and $C_t/10$ are presented in Figure C-4. As shown in this figure, the values of C_p and $C_t/10$ rise with the increasing Re . However, these coefficients for the turbines with tubercles, “Sin2” and “Sin8”, are less sensitive to the change in Re number compared to the reference turbine, “Ref”, especially for C_p . This was possibly because the waviness caused by the tubercles on the leading edge was tripping the laminar flow to move into the transition or turbulent regime.

Because of the limited Reynolds number that could be reached in these tests, the maximum Re condition was used in the following performance tests. However, the Reynolds number effect still had to be born in mind even with the use of the maximum Re number. Having said that these tests clearly demonstrated more stable performance for the biomimetic turbine as the power generation efficiency was not dependent on the incoming velocity.

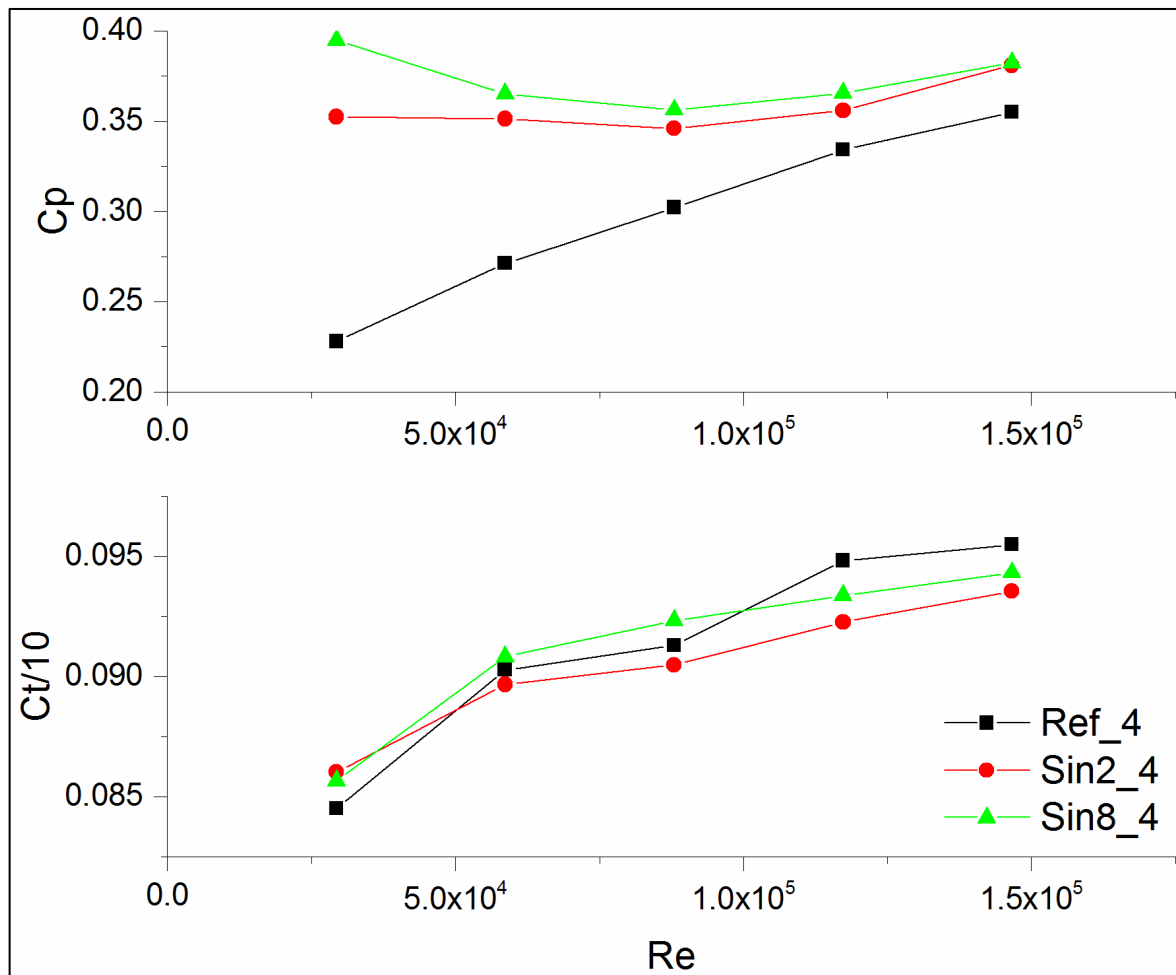


Figure C-4 Results of Reynolds number effect test

Open water performance tests in the towing tank

The three models were tested to analyse their open water performances. The test results are shown in Figure C-5. Because of the limited Re number, the coefficients of Cp and Ct/10 showed significantly lower performance (20% for the peak Cp) compared to the test results in the cavitation tunnel as shown in Figure 5-10. This might not only be because of the significant difference in the Reynolds number but also because of the blockage ratio between the two facilities. However, due to the nature of the relative comparisons, as stated earlier in Section 5.7.1, only the performance results of the tests conducted in the towing tank were compared and discussed in the following.

As shown in Figure C-4, even though the magnitudes of the results from the two facilities demonstrated certain levels of disparity, the same trend in the effect of the tubercles on the results of the towing tank test based performances can be observed: in other words, the tubercles still improved the performance in the low TSR region without compromising the peak C_p ; Sin8 showed the best performance with a slightly shifted C_p curve compared with the reference turbine; the general performance of Sin2 was very close to the reference turbine but also with the improved performance in low TSRs.

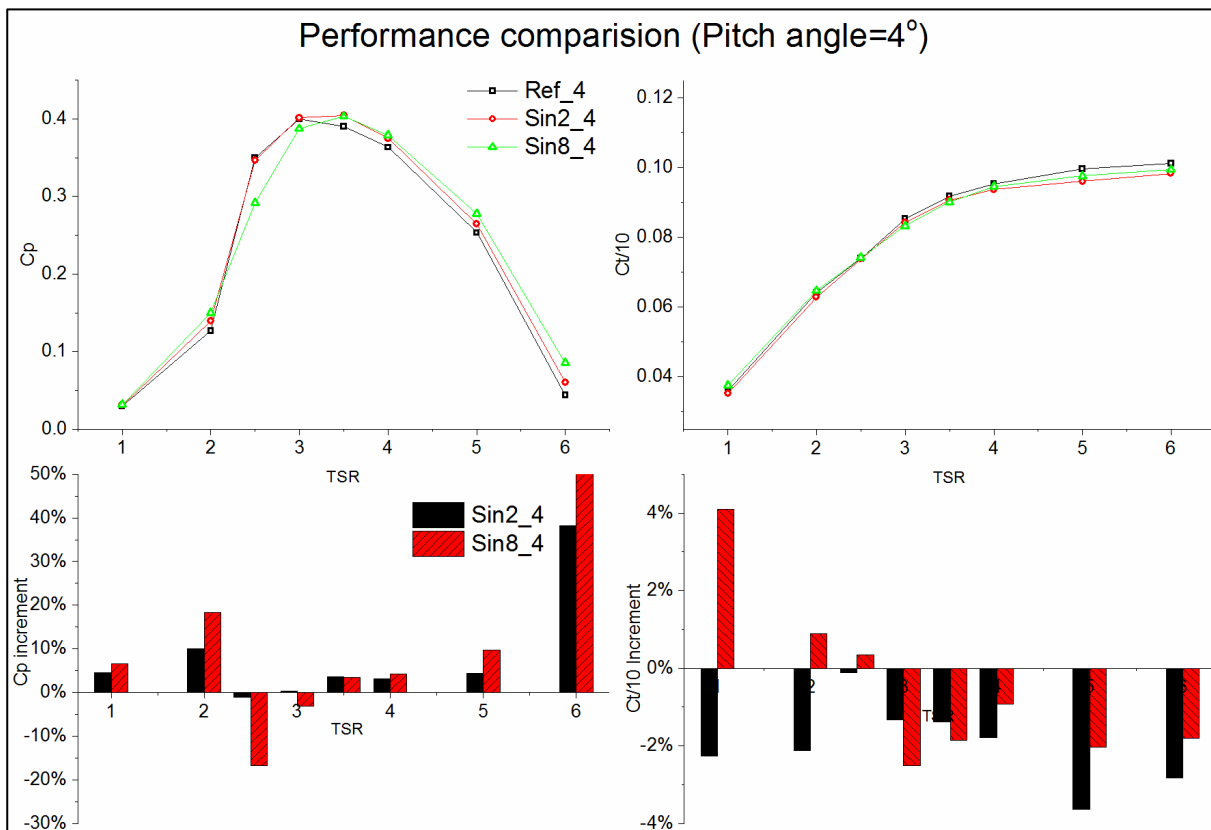


Figure C-5 Test result of open water performance in the towing tank

Open water performance tests in regular waves

Following the open water performance tests in calm water, the same tests were conducted in regular waves with two different wave amplitude (0.05m and 0.1m) and over a range of incoming wave frequencies (0.3-0.9Hz). As shown in Table 5-17, all of the wave tests were carried out for $TSR=4$, $RPM=250$ and $V=1.309m/s$. The time history of the wave height, torque and thrust of the turbines were recorded and then the peak amplitude Fast Fourier transfer analysis (FFT analysis) was applied using the Hanning window function.

Typical time history records and FFT analyses of a sample test run are shown in Figure C-6. As shown in this figure, the regular wave, with a distinct encounter frequency generated

significant fluctuation on the torque and thrust records. One can also observe two further peaks in the torque and thrust around the 1st blade passing frequency (12.5Hz) and shaft rotating frequency (4.17Hz), which might be caused by the shaft friction and non-uniform incoming flow. However, these two peaks were very stable throughout all of the tests even with different wave frequencies. Therefore, in order to identify the fluctuation caused by the wave action, which may cause fatigue failure for the tidal turbine, the peaks of the torque and thrust at encounter wave frequencies were extracted.

Uncertainty analysis for the wave test

The uncertainty levels were also checked by repeating the tests four times with the reference turbine for the test runs in waves with an amplitude of 0.1m and wave frequency of 0.5Hz. As shown in Table 5-18, the results of the measurements for the torque and thrust at the same encounter frequencies were quite repeatable with small values of standard deviation.

Table C-3 Uncertainty analysis of the wave test

Real Carriage Speed (m/s)	Real TSR	Encounter Frequency (Hz)	Torque Fluctuation Amplitude (NM)	Thrust Fluctuation Amplitude (N)	Average Cp	Average Ct/10
1.30713	4.005728	0.69978	0.679986	17.160794	0.384556	0.97679
1.30729	4.005229	0.69978	0.674702	17.089281	0.385723	0.97423
1.3072	4.005507	0.69978	0.671198	17.147577	0.386217	0.977304
1.30712	4.005758	0.69978	0.675299	16.868419	0.387079	0.977287
Percentage of standard deviations (%)			0.53%	0.79%	0.27%	0.15%

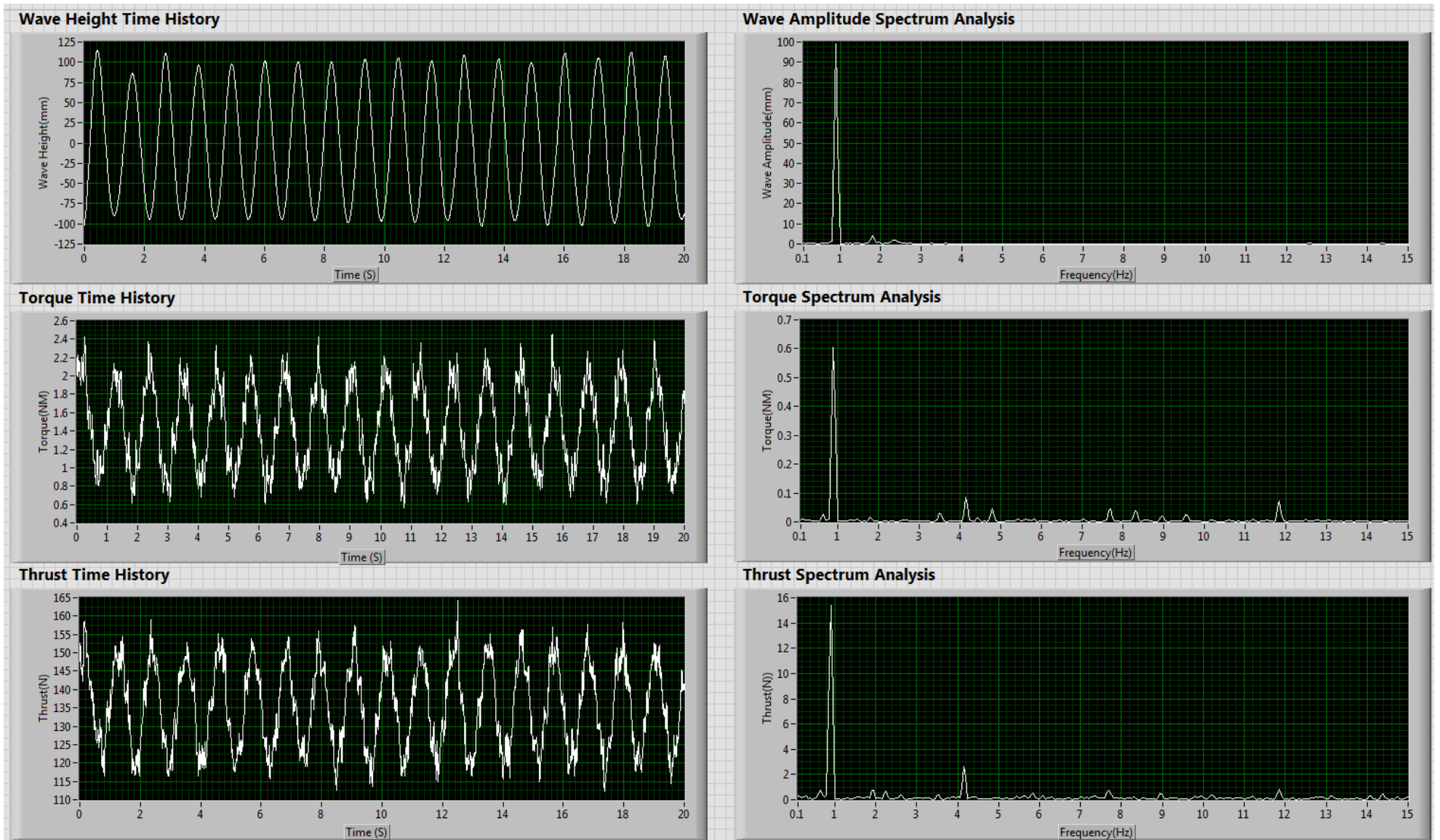


Figure C-6 Time history and FFT analysis for the regular wave test

Effect of regular wave action on the open water performance of the turbines

The analysed results of the time averaged power coefficient (C_p) and thrust coefficient ($C_t/10$) for each encounter frequency tested are presented in Table C-4 and Table C-5 for the wave amplitude of 0.05m and 0.10m, respectively. These coefficients were normalized against the corresponding C_p and $C_t/10$ values in calm water for the same tip-speed ratio, $TSR=4$.

Table C-4 Normalized time average C_p and $C_t/10$ in regular wave test at wave amplitude=0.05m and $TSR=4$

Encounter wave frequency (Hz)	Normalized Averaged $C_t/10$			Normalized Averaged C_p		
	Ref	Sin2	Sin8	Ref	Sin2	Sin8
1.54952	1.00260	0.99059	1.00012	0.99261	0.98216	0.99944
1.34957	1.00563	1.00025	1.00947	1.00231	0.99761	1.01657
1.09965	1.00854	1.00866	1.00910	1.00960	1.01437	1.02035
0.89971	1.01450	1.00971	1.01304	1.03353	1.02217	1.02716
0.69978	1.01718	1.01222	1.01078	1.04775	1.02091	1.01681
0.54982	1.01280	1.01074	1.00498	1.02144	1.02608	1.00144
0.39987	1.00794	1.00893	1.00205	1.01362	1.02345	1.00472
Calm water	1	1	1	1	1	1

Table C-5 Normalized time average C_p and $C_t/10$ in regular wave test at wave amplitude=0.1m and $TSR=4$

Encounter wave frequency (Hz)	Normalized Averaged $C_t/10$			Normalized Averaged C_p		
	Ref	Sin2	Sin8	Ref	Sin2	Sin8
1.54923	0.99165	0.99783	1.00036	0.9819	0.99761	0.9982
1.29958	1.00666	1.00414	1.00280	1.00555	1.00891	1.00514
1.09965	1.01034	1.00614	1.00826	1.01625	1.01939	1.01617
0.89971	1.01810	1.01641	1.01559	1.03896	1.04049	1.03551
0.69978	1.02375	1.01515	1.01665	1.05632	1.04570	1.04519
0.54982	1.01436	1.01525	1.00778	1.04811	1.04999	1.03546
0.39987	1.01151	1.00677	1.00106	1.04986	1.04357	1.02837
Calm water	1	1	1	1	1	1

As it can be seen in Table C-4, the impact of the waves on the $C_t/10$ of all three turbines was very limited within 2%, while the impact on the C_p was slightly larger but still within 5%. Meanwhile, the reference turbine appeared to be relatively more sensitive to the wave action (with a maximum of 4.8% increase in C_p) while the turbines with tubercles were less sensitive with a maximum of 2.6% increase in C_p for the Sin2 and 2.7% for the Sin8, respectively. This

performance enhancement could be because of the turbulent flow generated by the action of small waves.

A similar form of performance enhancement was also observed with bigger waves, as shown in Table C-5. However the differences in performance change between the reference turbine and the turbines with tubercles were smaller: a maximum of 5.6% C_p enhancement for the reference turbine and 5.0% and 4.5% for the Sin2 and the Sin8 respectively. The impact of the wave effect on the thrust coefficient, $C_t/10$, was even smaller; within 2.5% for all three turbines.

Based on the above results, it can be seen that the effect of wave action on the performance of the turbine can be beneficial in terms of performance enhancement, but this enhancement is limited to within 5%, depending on the wave condition.

Effect of regular wave action on open water performance fluctuations of turbines

Apart from the impact on the average performance, the fluctuation of the torque and thrust could be a concern with regard to the performance of a tidal turbine. The fluctuation in torque is a concern for the quality of the generated power while the fluctuation in thrust is a concern for the supporting structure. In order to further illustrate this aspect, Table C-6 and Table C-7 are included. In these tables, the percentage of C_p and $C_t/10$ fluctuation amplitude against the mean C_p and $C_t/10$ values, for the same wave condition, are presented for the two different wave amplitudes tested. As it can be seen in the tables, the amplitudes of both C_p and $C_t/10$ increased with increasing wave amplitude and decreasing wave frequency. Significant fluctuation can be observed with all three turbines, even more than 50% in C_p and a maximum of 30% in $C_t/10$. The Sin2 turbine generally showed a higher level of fluctuation while the Sin8 turbine had the lowest fluctuation. However the differences in the fluctuations between the models were relatively small.

In Figure C-7 the torque and thrust amplitudes of the three turbines are compared against each other over the encounter frequency range tested. As shown in this figure the amplitudes of the torque and thrust of the Sin8 turbine were generally lower than those of the other two turbines. This was more obvious in the thrust while the torque of the Sin8 turbine was similar to the reference turbine. Up to 4% lower thrust can be achieved with the Sin8 turbine compared to the Ref turbine in the most extreme condition (Wave Amplitude=0.1, Encounter Wave Frequency=0.39987Hz).

Table C-6 Percentage of Cp and Ct/10 fluctuation in regular wave test at wave amplitude=0.05m

Encounter wave frequency (Hz)	Percentage of Ct/10 fluctuation			Percentage of Cp fluctuation		
	Ref	Sin2	Sin8	Ref	Sin2	Sin8
1.54952	2.2%	2.6%	2.1%	5.0%	5.4%	4.5%
1.34957	3.0%	3.5%	2.9%	6.3%	7.1%	6.0%
1.09965	4.8%	4.9%	4.6%	10.1%	10.4%	9.6%
0.89971	7.2%	7.7%	7.0%	15.2%	15.5%	14.3%
0.69978	7.9%	8.3%	7.8%	16.1%	16.4%	16.0%
0.54982	11.9%	12.6%	11.6%	24.5%	25.0%	23.7%
0.39987	13.9%	14.7%	14.0%	28.0%	28.8%	28.2%

Table C-7 Percentage of Cp and Ct/10 fluctuation in regular wave test at wave amplitude=0.1m

Encounter wave frequency (Hz)	Percentage of Ct/10 fluctuation			Percentage of Cp fluctuation		
	Ref	Sin2	Sin8	Ref	Sin2	Sin8
1.54923	3.8%	4.0%	4.0%	8.4%	8.2%	8.3%
1.29958	6.6%	7.0%	6.4%	13.5%	14.1%	13.1%
1.09965	10.5%	10.9%	10.1%	21.7%	22.3%	20.9%
0.89971	14.7%	15.5%	14.2%	29.9%	30.8%	28.9%
0.69978	16.4%	17.3%	15.9%	33.0%	34.0%	31.4%
0.54982	23.6%	25.0%	23.0%	47.3%	48.5%	45.9%
0.39987	28.6%	30.0%	27.9%	56.9%	58.2%	55.4%

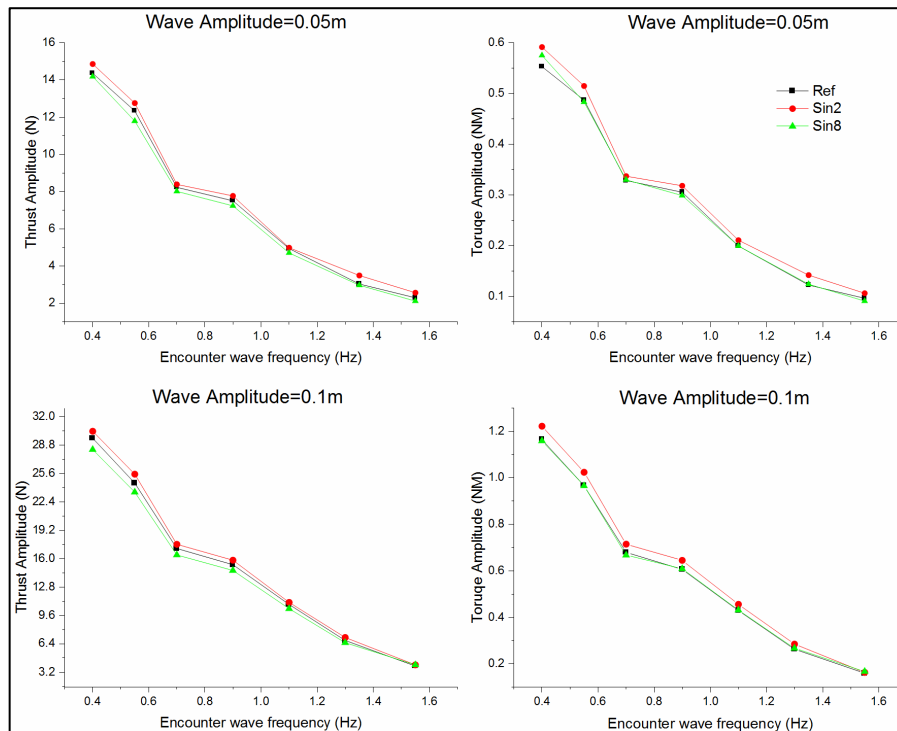


Figure C-7 Amplitudes of torque and thrust in regular waves

Open water performance tests in irregular wave tests

Having completed the performance tests in regular waves, the Ref turbine and Sin8 turbine were tested in irregular head waves which were generated based on the earlier described JONSWAP wave spectra. Due to the limited tank time available, these tests concentrated on the slower carriage speed ($V= 0.785$ m/s) and a single turbine speed, $N=150$ RPM.

Figure C-8 shows a typical time history of the wave profile generated in the tank for $H_s= 0.15$ m; $T_p=1.581$ s. The wave calibration against the encounter wave frequency is shown in Figure C-9.



Figure C-8 Sample of JONSWAP wave profile ($H_s=0.15$ m, $T_p=1.581$ s)

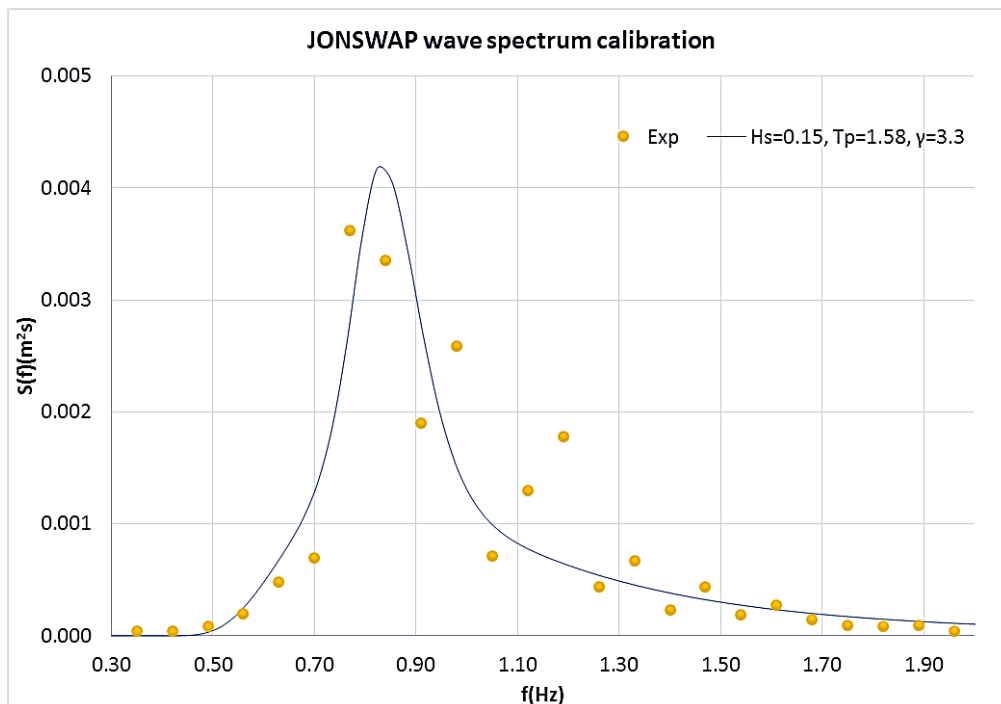


Figure C-9 Wave spectrum calibration against encounter wave frequencies ($H_s=0.15$ m, $T_p=1.581$ s)

Figure C-10 presents the full time history records and peak amplitude FFT analyses of the wave profiles as well as the torque and thrust responses of the Ref turbine for the test condition of $H_s=150\text{mm}$; $T_p=1.581\text{s}$, $N=150\text{RPM}$ and $V=0.785\text{m/s}$. A closer look at the FFT analyses indicates that apart from the major torque and thrust peak around 0.833 Hz , which corresponds to the encounter frequency for the maximum energy in the wave spectrum (at $T_p= 1.581\text{s}$), there is another local peak at 2.5Hz which corresponds to the shaft rate (150 rpm).

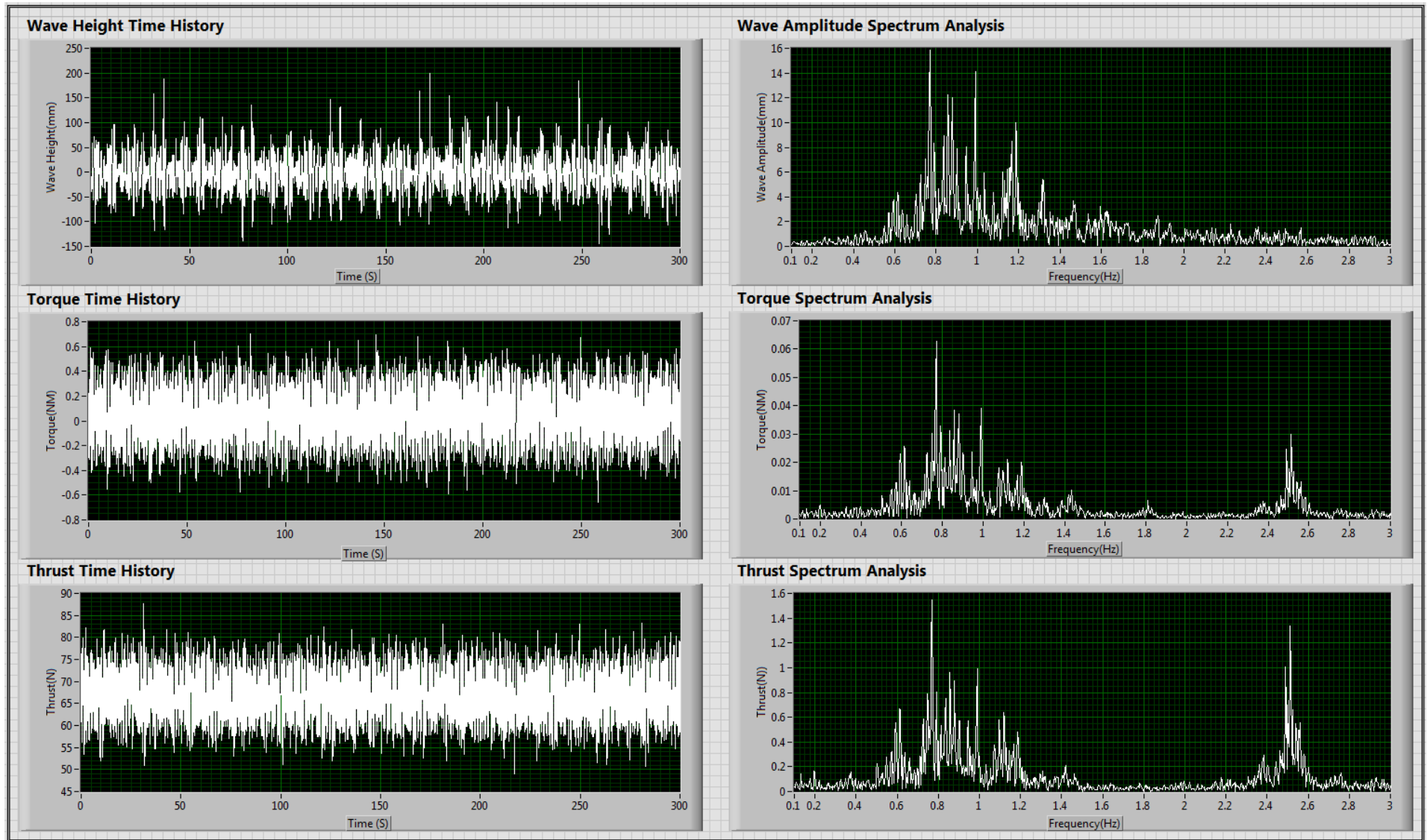


Figure C-10 Time history and FFT analysis for the irregular wave test ($H_s=150\text{mm}$; $T_p=1.581\text{s}$, $N=150\text{RPM}$ and $V=0.785\text{m/s}$)

Effect of irregular wave action on open water performance of turbines

The analysis was first conducted with regard to the time averaged performance to identify the wave effect on the power generation. The time averaged performance normalized against the performance in calm water is presented in Table C-8.

Table C-8 Normalized time average Cp and Ct/10 in irregular waves (JONSWAP)

JONSWAP Hs	JONSWAP Tp	Normalized Averaged Ct/10		Normalized Averaged Cp	
		Ref	Sin8	Ref	Sin8
(m)	(s)				
0.15	1.581	1.0157	0.9959	1.0512	1.0156
0.25	2.214	1.0144	0.9963	1.1039	1.0469
0.3125	2.372	1.0148	1.0012	1.1320	1.0755
Calm water		1	1	1	1

As it can be seen, the variation of the averaged Ct/10 overall is very limited (within 2%), and with Sin8 is even smaller, limited to within 1%. The average Cp could be improved by the irregular waves, however this might be because of the wave generated turbulence. This phenomenon could also be seen in the regular wave test. The performance of the Ref turbine was improved by a maximum of 13.2% under the condition “Hs=0.3125m and Tp=2.372s”, but the baseline Cp was only 30% in the calm water test at this condition (150RPM), limited by the Reynolds effect, whilst it was 35.6% for the Sin8. With the increased Reynolds number in full-scale conditions, this kind of enhancement might not exist. However because the variation for the Sin8 turbine caused by the wave effect was very limited compared to the Ref turbine, a more stable power generation performance from the Sin8 can be expected.

Effect of irregular wave action on performance fluctuations of turbines

In order to clarify the effect of the wave action on the force fluctuations, the significant values (1/3) of torque and thrust were obtained through FFT analysis. The results are presented in Table C-9.

Table C-9 Percentage of significant values of thrust and torque fluctuation in irregular waves (JONSWAP)

JONSWAP Hs	JONSWAP Tp	Percentage of significant thrust fluctuation (1/3)		Percentage of significant torque fluctuation (1/3)	
		Ref	Sin8	Ref	Sin8
(m)	(s)				
0.15	1.581	35.69%	36.16%	80.66%	76.73%
0.25	2.214	66.60%	71.01%	148.77%	143.32%
0.3125	2.372	80.06%	80.04%	174.62%	159.12%

The results in Table C-9 indicate severe force fluctuations in both torque and thrust. In terms of the torque, the fluctuation of the Sin8 turbine was smaller compared to the Ref turbine, especially under the 100-year conditions ($H_s=0.3125m$, $T_p=2.372s$), which indicated around 10% less. However for the thrust, Sin8 showed slightly higher values under the 1-year and 10-year conditions ($H_s=0.15m$, $T_p=1.581s$ and $H_s=0.25m$, $T_p=2.214s$), but similar levels of fluctuation can be observed under the 100-year conditions.

Response Amplitude Operator (RAO) for turbine performance

During the analysis of the wave effect on the turbine performance it came to the attention of the Author that there are no recommendations or discussions on how to define the Response Amplitude Operators (RAO) or the Transfer Functions for the performance of a tidal turbine. These definitions have been thoroughly investigated and used in the ship motion context and, as such, the ship can be regarded as a linear system and the input to the system is the ocean waves and the output from the system is the motion response. However whether the turbine system can be regarded as a linear system, as shown in Figure C-11, to predict the response as torque or thrust in waves is yet to be concluded (Barltrop *et al.*, 2006; de Jesus Henriques *et al.*, 2014; Tatum *et al.*, 2016). In order to quantify the RAO for the tidal turbine system, the following equation was formulated as below in Equation C-2.

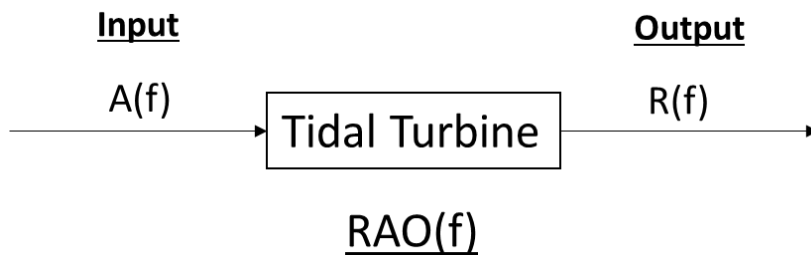


Figure C-11 Linear turbine response to the wave action

$$RAO(f) = \frac{R(f)}{A(f)} \quad \text{Equation C-2}$$

Where $RAO(f)$ is the response amplitude operator for given wave frequencies, f ; $R(f)$ is the response amplitude spectrum of the turbine system; $A(f)$ here is the wave amplitude spectrum. Subscripts Q and T will be used to specify the torque or the thrust, respectively.

RAO in regular waves

In order to investigate the above problem, the Ref turbine was chosen. The RAO analysis for the torque and thrust of this turbine in regular waves is shown in Figure C-12. As shown in the figure, the response of the torque and thrust is strongly linear with the wave amplitude, as the curves of $RAO_Q(f)$ and $RAO_T(f)$ with two different wave amplitudes, 0.05m and 0.1m as noted after the underscore in the legend, almost overlap.

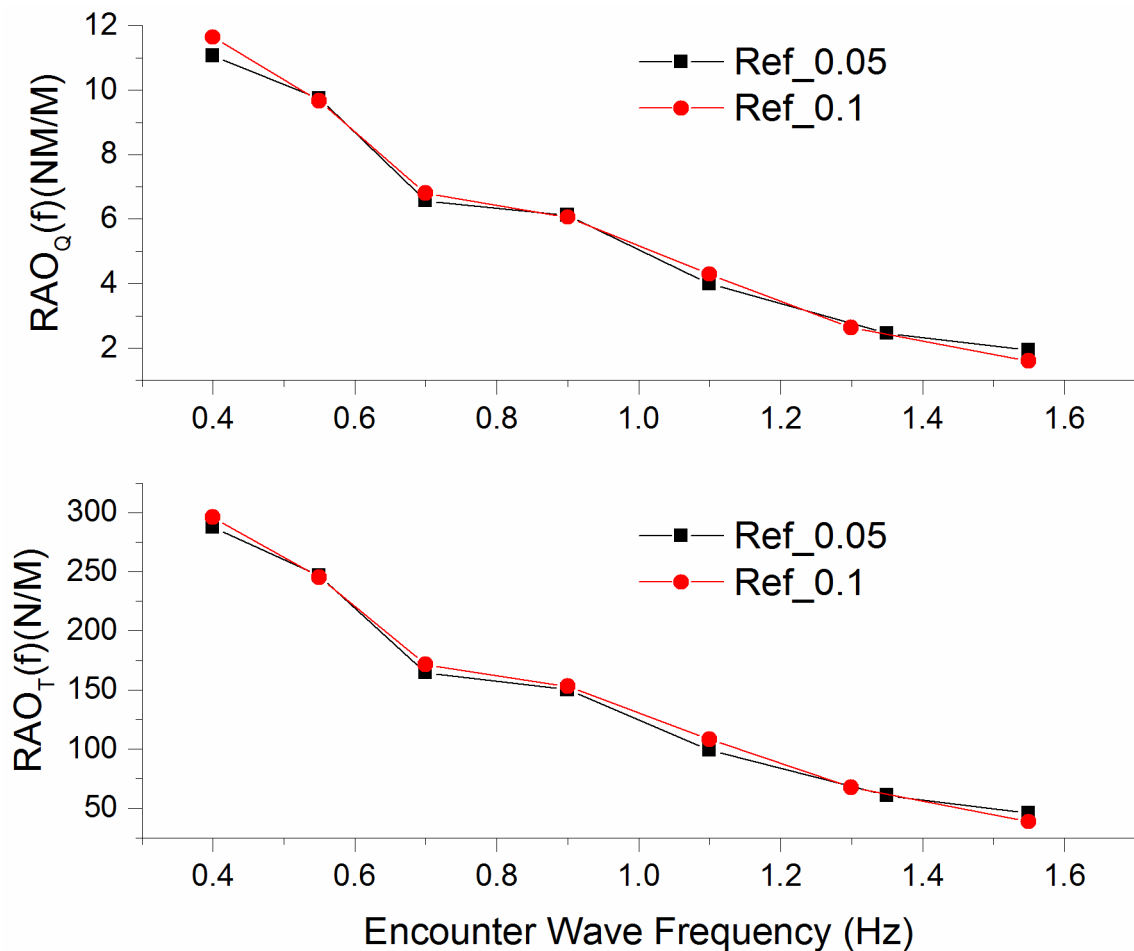


Figure C-12 RAOs of the reference turbine in regular waves with 250rpm

The comparisons of RAO for thrust and torque for the three turbines are presented in Figure C-15 and Figure C-16, respectively, for two different wave heights. In the top right corners of these figures a closer look at the thrust and torque for 0.1m wave amplitude is also included for the sake of easier comparison. The legend is named by “Model name_ Wave height_ RPM”, as “Ref_0.1_250”. From these figures, it can be seen that the Sin8 turbine displayed the lowest RAOs in both torque and thrust while the Sin2 turbine showed the highest.

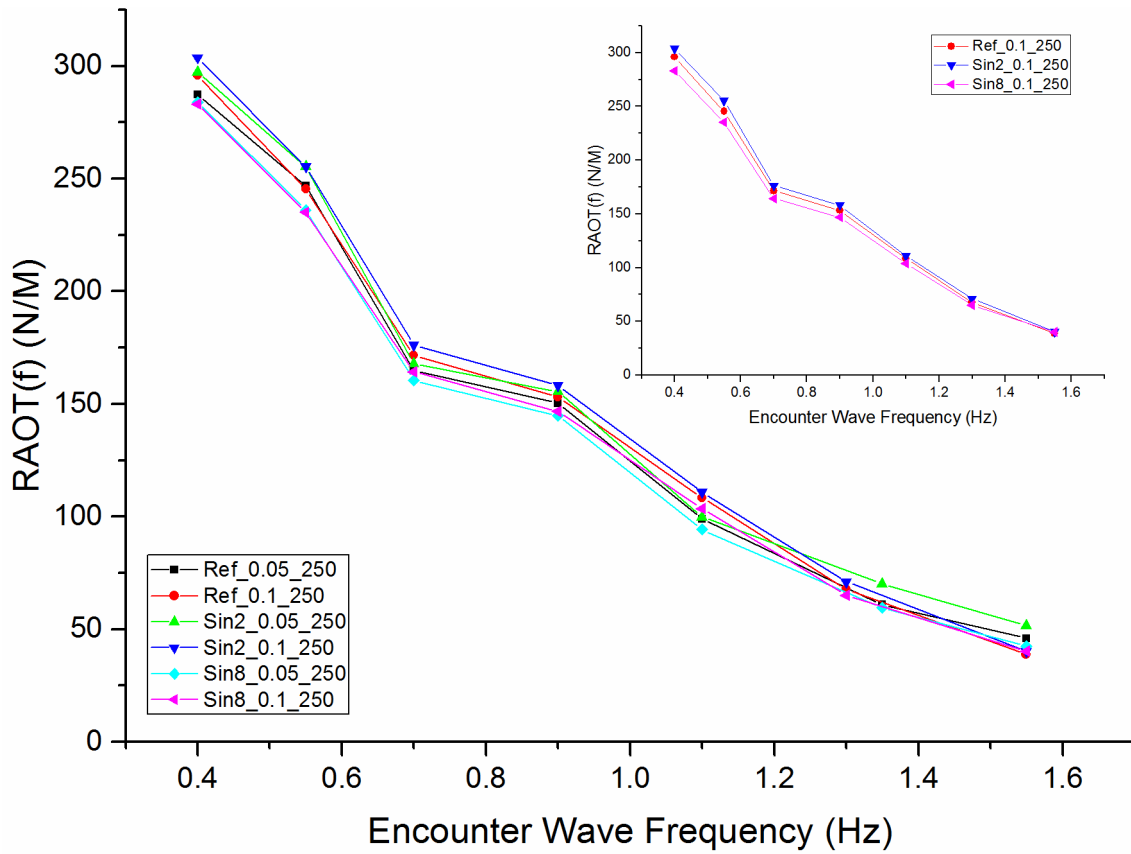


Figure C-13 Comparison of thrust RAO in the regular waves with 250RPM

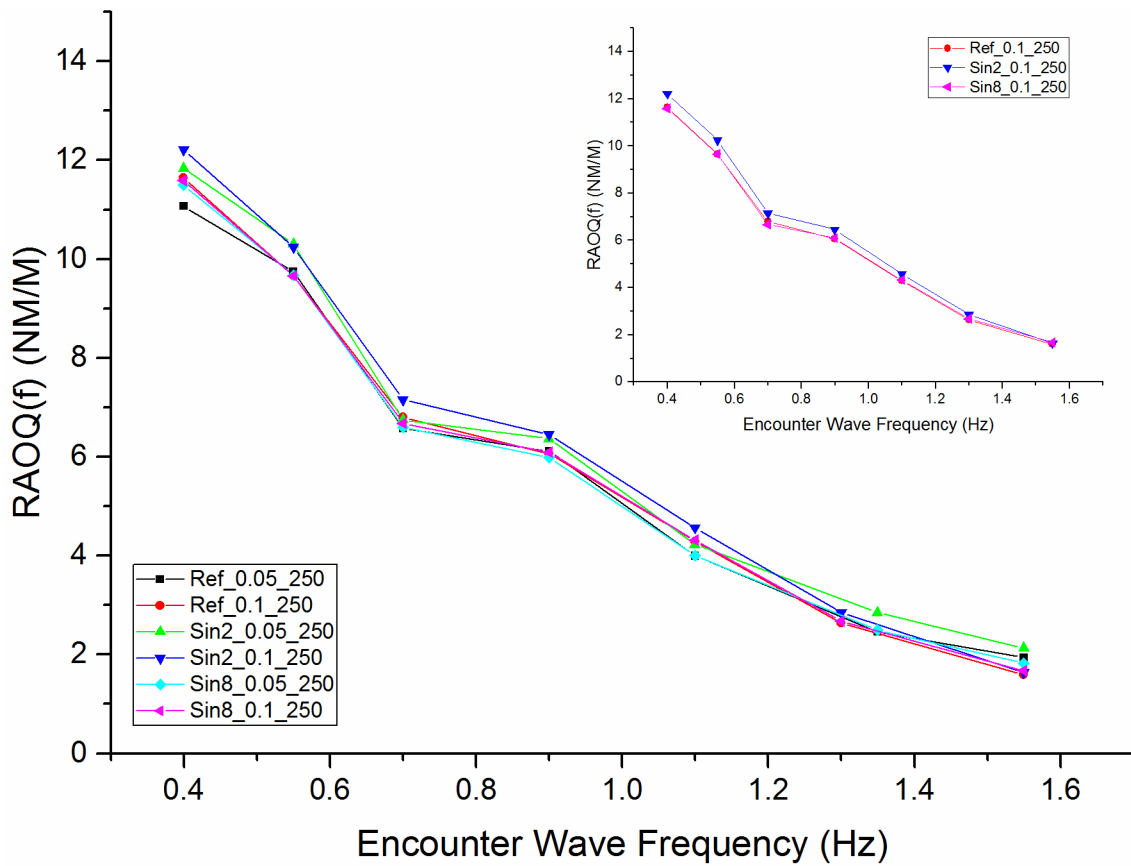


Figure C-14 Comparison of torque RAO in regular waves with 250RPM

RAO in irregular waves

According to the principle of superposition, irregular waves can be described as a linear superposition of an infinite number of simple, regular harmonic wave components. In this sense, the RAO(f) can also be derived from the response spectrum obtained in the irregular wave test. If the linear assumption is applied to the turbine system, the RAO(f) measured in the regular wave tests and that derived from the irregular wave tests should be close to each other. Therefore, this assumption was tested and results are shown in Figure C-15 in which all of the tests were conducted at the same carriage speed and RPM for the Ref turbine. In these figures, the lines correspond to the RAO in regular waves while the dots correspond to the RAO derived from the motion response spectra. For the irregular wave tests, three different JONSWAP wave spectra were used. As it can be seen from these figures the RAO(f)s derived from these tests, over the majority of the data, show reasonable correlations which further validate the hypothesis of the principles of superposition and linear response, as applied to the tidal turbine.

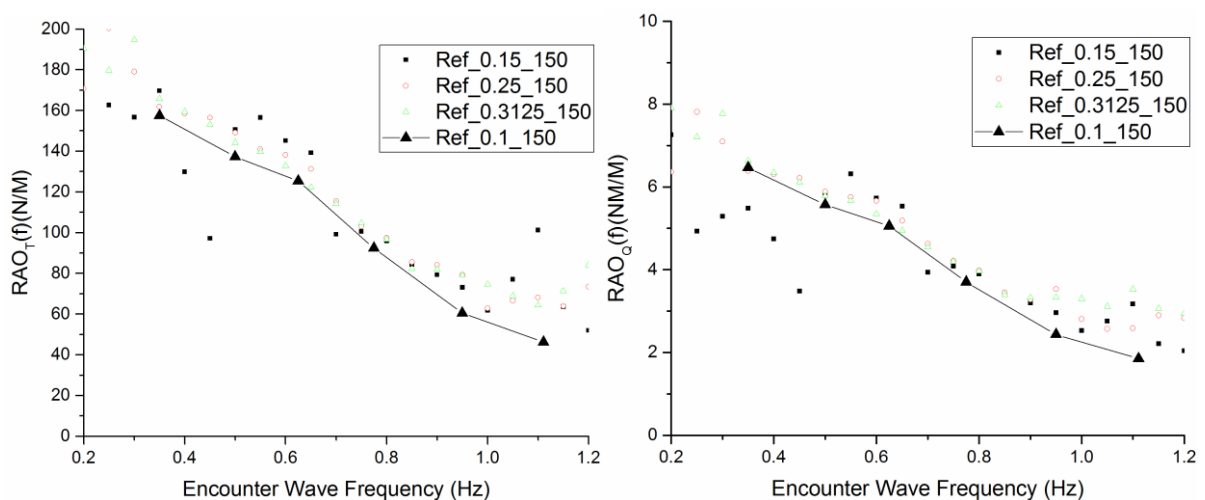


Figure C-15 RAO(f) of thrust (left) and torque(right) derived from regular and irregular wave test with 150RPM

Critical speed effect

However, a closer look at the details of the test results for the derived RAO(f)s with different towing speeds and hence different RPM shows significant differences. As it is shown in Figure C-164, in spite of the same TSR (0.126), wave height (0.1m) and encounter frequencies, the RAO(f)s achieved at 1.309m/s and 250rpm are much higher than the result in 0.785m/s and 150rpm. As it was commonly experienced in the full-scale when the turbine is operating under

various current speeds, this raised the question of what the RAOs for tidal turbines are under different current speeds.

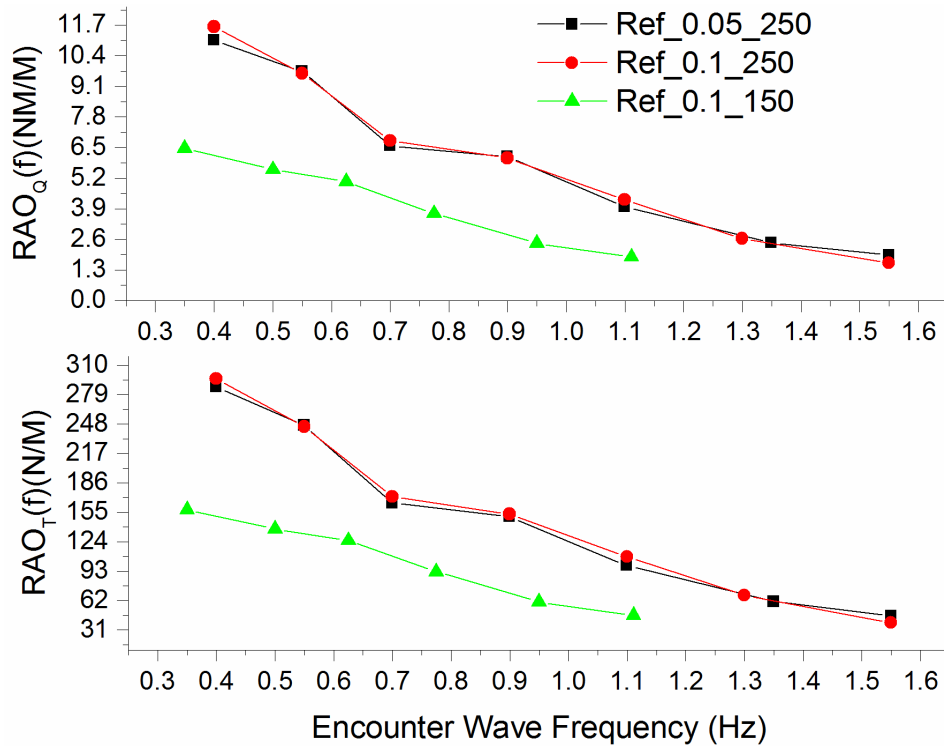


Figure C-16 RAO(f) of torque (top) and thrust(bottom) tested at different towing speeds

As it has generally been acknowledged in wave theory, by ignoring the effect of wave diffraction, the wave action can be simplified and assumed to be mainly causing cyclic velocity fluctuation at a certain level of water depth. Based on this assumption, the thrust (T) and torque (Q) of turbine model can be expressed by the thrust and torque coefficients, C_T and C_Q , as follows:

$$T = C_T * \frac{1}{2} \rho A_T V^2 \quad \text{Equation C-3}$$

$$Q = C_Q * \frac{1}{2} \rho A_T V^2 R \quad \text{Equation C-4}$$

If the above assumed cyclic velocity fluctuation in the axial direction has an amplitude of ΔV while C_T is assumed to remain the same (in spite of the changes in TSR based on the open water performance tests shown in Figure C-5) the thrust would fluctuate with an amplitude of ΔT , as given by Equation C-5.

$$\Delta T = C_T * \frac{1}{2} \rho A_T [(V + \Delta V)^2 - V^2] \quad \text{Equation C-5}$$

(However, the above assumption made for the thrust cannot be applied to the torque since the variation in the torque coefficients is significant)

Using Equation C-3 and Equation C-5, the velocity fluctuation can be calculated as shown in Equation C-6.

$$\Delta V = V * \left(\sqrt{\left(\frac{\Delta T}{T} + 1 \right)} - 1 \right) \quad \text{Equation C-6}$$

The predicted results of ΔV , based on Equation C-6, for the two sets of regular wave test data with two different carriage speeds, but at the same wave height, are shown in Figure C-17. As it can be seen in this figure, the simplified correction made for the effect of waves can justify the fact that the main effect of the waves on the turbine performance can be expressed by the contribution in the current speed due to the longitudinal component of the wave particle velocity. This is of course very much dependant on the depth of submergence of the turbine since the effect will be more significant (due to e.g. diffraction, etc.) and complex as the turbine gets closer to the free surface.

The above simplified theory has already been applied to calculate the response amplitude caused by the different wave spectra combined with varied current speeds (Barltrop *et al.*, 2006). In fact Barltrop *et al.* modelled the effect of the orbital wave velocities on the blade forces of a HATT by using a BEM model and achieved close agreement between the predictions and experimental results in regular waves.

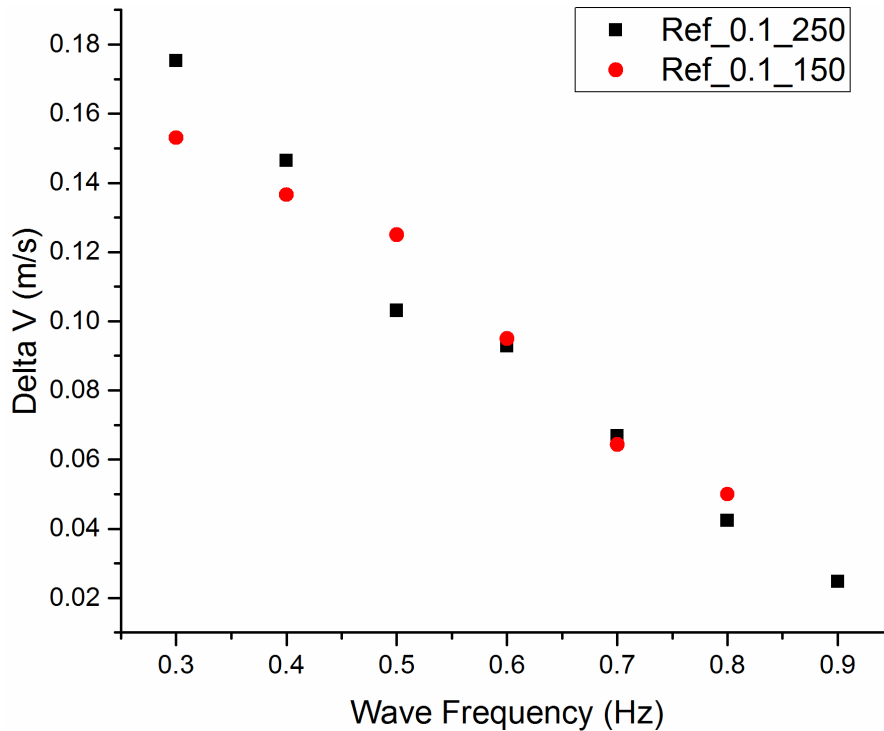


Figure C-17 ΔV against the wave frequency as calculated based on two regular wave test data with two different carriage speeds

Concluding remarks on hydrodynamic performance of turbines under the effect of wave-current interaction

Based on the analysed results of the experimental performance tests in waves which were conducted in the KHL with the three model turbines, the following further remarks can be concluded:

1. The Reynolds number range experienced in the towing tank tests was significantly lower than the range in the cavitation tunnel tests, which led to great disparity between the magnitudes of the performance results obtained from the two different facilities. However, the models with the leading-edge tubercles appeared to be less sensitive to the change in the Reynolds number compared to the reference turbine. This can be attributed to the potential early triggering of turbulent flow on the turbine blades with the tubercles.
2. A relative comparison of the open water performance of the three turbines tested in calm water, in the KHL, further confirmed the main findings of the ECT tests where the benefits of leading-edge tubercles have been demonstrated, especially at low TSRs.

3. The effect of waves on the averaged magnitude of the C_p and $C_t/10$ coefficients of the three turbines was not as significant as the effect on the fluctuation amplitudes of the same coefficients. Amongst the three turbines, the lowest fluctuation was experienced with the Sin8 turbine which also generated the highest power.
4. The RAOs for the torque and thrust data, based on the regular wave tests, displayed a reasonably linear relationship with the wave height under the same current speed. The Sin8 turbine presented the lowest RAOs over the range of frequencies tested, in both torque and thrust, while the Sin2 turbine displayed the highest.
5. A further check on the RAOs derived from the response spectra of the irregular wave tests displayed reasonable correlations with the RAOs which were obtained from the regular wave tests. This has further supported the applicability of the superposition principle of the regular wave RAOs for different frequency ranges to obtain the responses in irregular waves for the prediction of tidal turbine performance.
6. The fluctuating effect of the waves on the performance of a turbine can be included in a simplified manner with a correction in the current speed through the longitudinal component of the orbital wave velocity.